Université du Québec
Institut National de la Recherche Scientifique (INRS)
Centre Energie Matériaux Télécommunications (EMT)

ADVANCING BIOMEDICAL SECOND HARMONIC GENERATION IMAGING THROUGH MACHINE LEARNING FOR IMAGE PROCESSING AND ENHANCEMENT

By

Arash Aghigh

A thesis submitted for the achievement of the degree of Doctor of Philosophy (PhD) in Energy and Materials Sciences

Jury Members

Président du jury et Examinateur interne	Jinyang Liang INRS-EMT
Examinatrice externe	Caroline Boudoux Polytechnique Montréal
Examinatrice externe	Claire Lefort Université de Limoges
Directeur de recherche	François Légaré INRS-EMT

REMERCIEMENTS

To my esteemed supervisor François, your guidance, expertise, and mentorship have been invaluable in completing this thesis. Your belief in my potential and your commitment to excellence have shaped my academic endeavours and personal growth. I am genuinely grateful for the opportunity to learn from you, and for your profound impact on my professional development.

To Gaetan and Heide, your expertise and assistance have contributed significantly to the success of this thesis. Your willingness to share knowledge and offer guidance has been instrumental in overcoming obstacles and achieving milestones. I extend my heartfelt gratitude for your invaluable contribution to this work.

To all the dedicated INRS staff members, your collective efforts have created an environment conducive to learning, exploration, and innovation. From administrative support to technical assistance, each member of the INRS community has played a crucial role in my academic journey. I sincerely thank all those who have contributed to the enriching experience of pursuing my Ph.D. at INRS.

To my dearest wife, Justine, you have been my steadfast source of love, support, and inspiration throughout this challenging, yet rewarding journey. Your patience, understanding, and encouragement have been the bedrock upon which I built my academic pursuit. This thesis is as much yours as it is mine, and I dedicate it to you with all my heart.

To my parents and sister, your unwavering belief in my abilities and unconditional love has been my constant motivation. Your sacrifices, encouragement, and enduring support have brought me through the highs and lows of this academic journey. This thesis is a testament to the values you instilled in me, and the dreams you helped me chase.

To my best friend and brother Alborz, your friendship has been a source of strength and rejuvenation in moments of doubt and fatigue. Your camaraderie, laughter, and genuine concern provided solace during the most challenging times. This thesis is a tribute to our bond and to the countless memories that have sustained me throughout this doctoral expedition.

Arash Aghigh

RÉSUMÉ

Cette thèse explore l'intégration de la microscopie par génération de seconde harmonique (SHG) avec des techniques d'apprentissage automatique pour améliorer les capacités d'imagerie et d'analyse, en s'attaquant aux limitations liées à la résolution, au bruit et à la vitesse d'acquisition. La microscopie SHG, une méthode d'imagerie non linéaire, offre des avantages uniques pour l'étude des structures biologiques non centrosymétriques. Les travaux présentés dans cette thèse élargissent les applications de la microscopie SHG dans la recherche biomédicale grâce à des innovations en traitement d'image, en classification et en amélioration d'image. La première partie de cette thèse propose une revue exhaustive du développement historique, des principes théoriques et des modalités avancées de la microscopie SHG. Une attention particulière est accordée à ses applications en imagerie neuronale et en analyse des structures biologiques, établissant une base solide pour les recherches expérimentales ultérieures. En s'appuyant sur ces connaissances, une étude des tissus glandulaires mammaires combine l'imagerie SHG et SHG résolue en polarisation (P-SHG) avec des réseaux neuronaux convolutifs pour automatiser la classification des tissus touchés par des tumeurs et étudier l'optimisation des paramètres d'apprentissage automatique dans le contexte de la microscopie SHG. Cette approche met en évidence des variations structurelles significatives dans le microenvironnement tumoral, offrant des perspectives sur les processus de remodelage tissulaire. Pour répondre aux défis posés par les faibles rapports signal/bruit en imagerie SHG, la thèse applique des modèles d'apprentissage profond, tels que CARE 2D et Noise2Void 2D, pour améliorer la qualité des images. Ces modèles réduisent efficacement le bruit tout en préservant l'intégrité structurelle, permettant ainsi une imagerie de haute qualité avec une puissance laser réduite et minimisant les dommages photoniques aux échantillons biologiques. En outre, ce travail aborde le besoin d'une imagerie plus rapide en utilisant des réseaux antagonistes génératifs super-résolution améliorés (ESRGANs). Cette approche innovante accélère l'imagerie P-SHG à l'échelle complète des glandes mammaires, reconstruisant des images haute résolution à partir de données basse résolution tout en maintenant des détails structurels essentiels. La réduction du temps d'imagerie améliore considérablement l'efficacité de la microscopie SHG, la rendant plus adaptée aux études à grande échelle ou sensibles au temps.

Dans l'ensemble, ces travaux démontrent le potentiel transformateur de la combinaison de la microscopie SHG avec des techniques avancées d'apprentissage automatique. Ces innovations améliorent la qualité d'imagerie, réduisent le temps d'analyse et élargissent l'accessibilité de la

SHG pour l'étude des structures biologiques complexes. Elles ouvrent la voie à des applications plus larges en recherche biomédicale et en diagnostics cliniques. Les perspectives incluent le développement de systèmes d'imagerie multimodale, l'optimisation des modèles d'apprentissage profond pour des tissus diversifiés et la standardisation des techniques SHG pour une intégration dans les flux de travail cliniques.

Mots-clés: Microscopie SHG, imagerie résolue en polarisation, apprentissage automatique, modèles d'apprentissage profond, imagerie biomédicale, réduction du bruit, amélioration d'image, microenvironnement tumoral, réseaux antagonistes génératifs (GAN), diagnostics cliniques.

ABSTRACT

This thesis explores the integration of second harmonic generation (SHG) microscopy with machine learning techniques to enhance imaging and analysis capabilities, addressing limitations in resolution, noise, and imaging speed. SHG microscopy, a nonlinear imaging method, provides unique advantages for studying non-centrosymmetric biological structures. The work presented advances SHG microscopy's applications in biomedical research through innovations in image processing, classification, and enhancement. The first part of this thesis provides a comprehensive review of the historical development, theoretical principles, and advanced modalities of SHG microscopy. Emphasis is placed on its applications in neuronal imaging and biological structure analysis, establishing a strong foundation for subsequent experimental research. Building on this knowledge, a study of mammary gland tissues combines SHG and polarization-resolved SHG (P-SHG) imaging with convolutional neural networks to automate the classification of tumor-affected tissues and study machine learning parameter tuning in the context of SHG microscopy. This approach reveals significant structural variations within the tumor microenvironment, offering insights into tissue remodeling processes. To address challenges posed by low signal-to-noise ratios in SHG imaging, the thesis applies deep learning models, including CARE 2D and Noise2Void 2D, to improve image quality. These models effectively reduce noise while preserving structural integrity, allowing for high-quality imaging at reduced laser power and minimizing photodamage to biological samples. Additionally, this work addresses the need for faster imaging by employing enhanced super-resolution generative adversarial networks (ESRGANs). This innovative approach accelerates whole-sample P-SHG imaging of mammary gland tissues, reconstructing high-resolution images from low-resolution data and maintaining critical structural details. The reduction in imaging time significantly improves the efficiency of SHG imaging, making it more suitable for time-sensitive or large-scale studies. Collectively, the findings demonstrate the transformative potential of combining SHG microscopy with advanced machine learning techniques. These innovations enhance imaging quality, reduce analysis time, and expand the accessibility of SHG for studying complex biological structures.

This work paves the way for broader applications of SHG microscopy in biomedical research and clinical diagnostics. Future directions include the development of multimodal imaging systems, refinement of deep learning models for diverse tissues, and standardization of SHG techniques for integration into clinical workflows.

Keywords: Second Harmonic Generation (SHG) Microscopy, Polarization-Resolved Imaging, Machine Learning, Deep Learning Models, Biomedical Imaging, Noise Reduction, Image Enhancement, Tumor Microenvironment, Generative Adversarial Networks (GANs), Clinical Diagnostics

SOMMAIRE RÉCAPITULATIF

Un aperçu de la microscopie SHG

Au cours des deux dernières décennies, la microscopie par génération de seconde harmonique (SHG) est devenue une méthode clé pour l'imagerie optique, avec de nombreuses applications dans les sciences des matériaux et biomédicales. Les avancées dans le développement de technologies laser ultra-rapides fiables et robustes ont été essentielles pour améliorer les techniques de microscopie optique non linéaire [48], en particulier dans l'imagerie biomédicale. Des microscopes clés en main ont été développés en utilisant ces sources laser et sont maintenant largement utilisés dans les laboratoires de recherche. La microscopie SHG impose que la structure d'intérêt soit non-centrosymétrique [19], ce qui la rend très sensible aux protéines filamenteuses dans les échantillons biologiques [48,87]. Bien que cette exigence limite l'application du SHG à quelques structures seulement, c'est aussi une force clé car les signaux sont très spécifiques et offrent des images à contraste élevé. La microscopie SHG présente plusieurs avantages par rapport à l'imagerie par fluorescence : elle est basée sur un contraste endogène (c'est-à-dire que le contraste provient de l'échantillon lui-même et non d'un colorant ou d'un fluorophore). Enfin, contrairement à la fluorescence, le SHG est exempt de photoblanchiment (le signal généré n'est pas limité dans le temps) et se produit instantanément (pas de limitation sur le taux de répétition du laser) [14].

Cette thèse vise à relever un défi crucial dans le domaine de l'imagerie biomédicale : surmonter les limitations actuelles de la microscopie SHG grâce à l'intégration de techniques d'intelligence artificielle (IA). Les objectifs spécifiques de cette recherche sont d'améliorer la qualité des images, de permettre une analyse automatisée et d'élargir les applications cliniques de la microscopie SHG. En explorant de nouvelles approches basées sur l'IA pour le traitement d'images, la classification et l'acquisition, ce travail cherche à repousser les limites du possible avec la microscopie SHG et à ouvrir la voie à son adoption plus large dans la recherche et les contextes cliniques.

Un aperçu historique exhaustif du SHG a été donné dans le premier article de cette thèse ; nous nous concentrerons donc uniquement sur les étapes clés au fil des ans : l'observation du SHG pour la première fois en 1961 [23], la combinaison du SHG avec la microscopie optique en 1974 [25], la première microscopie biologique SHG en 1986, et la découverte des capacités d'imagerie biomédicale de la microscopie SHG [31]. En 1990, Denk et al. ont introduit la microscopie par balayage laser à fluorescence par excitation à deux photons (TPEF) en utilisant des lasers pulsés et un microscope confocal modifié [32]. À la suite du succès de la TPEF en 1996, la microscopie par excitation à trois photons a été démontrée [33]. La modalité SHG a été combinée avec la TPEF au début des années 2000 dans de nombreuses études [36-38]. Depuis lors, par suite des progrès des lasers à mode bloqué commercialement disponibles et des microscopes multiphotoniques conviviaux [39], le SHG est devenu une méthode puissante pour l'imagerie optique et biomédicale à haute résolution spatiale multimodale.

La région 700–1000 nm est utilisée par le SHG pour minimiser l'absorption des biomatériaux (eau et hémoglobine) [37]. Il est important de noter que d'autres "fenêtres" optiques répondant à ce critère sont disponibles (se référer à la Figure 2 de l'article 1). En utilisant des longueurs d'onde plus longues, telles que 1000–1300 nm, la diffusion peut être limitée, conduisant à une augmentation de la profondeur de pénétration dans les tissus [14], bien que cela se fasse au détriment d'une résolution spatiale réduite. Malgré les similitudes, les techniques SHG et TPEF sont fondamentalement basées sur des processus différents. Dans le SHG, la conversion de fréquence est réalisée par des états virtuels sans transfert net d'énergie au système. Cela contraste avec la TPEF, qui implique un transfert de population de l'état électronique fondamental vers des états électroniques excités (se référer à la Figure 2 de l'article 1). Ces origines différentes conduisent à des propriétés radicalement différentes et souvent complémentaires, ce qui explique la popularité croissante de la microscopie SHG.

Propriétés du signal SHG et microscopie SHG dans les échantillons biologiques

Le signal SHG est caractérisé par l'hyperpolarisabilité et la susceptibilité non linéaire du second ordre. La condition de symétrie de Kleinman simplifie notre compréhension de ces propriétés [19]. Ainsi, la microscopie SHG peut fournir des aperçus sur les structures moléculaires et macromoléculaires des tissus.

La microscopie SHG est particulièrement efficace pour l'imagerie du collagène, une protéine majeure dans le tissu conjonctif. Elle a été appliquée avec succès à l'imagerie de divers tissus, y compris les tendons [31] et le cartilage [72] (voir Figure 5 de l'article 1). De plus, elle peut visualiser d'autres protéines, comme la myosine [48], offrant des aperçus sur les mécanismes cellulaires et la structure des microtubules [122].

La microscopie SHG est essentielle dans les études neuroscientifiques, en particulier l'imagerie des microtubules. Les microtubules (MTs) sont des composants cellulaires vitaux, et la microscopie SHG a été utilisée pour étudier leur polarité et structure pendant les différentes phases de la division cellulaire [125] (voir Figure 21 de l'article 1). Cette technique a montré un grand potentiel pour explorer divers aspects et mécanismes des MTs et des maladies associées.

Techniques avancées de microscopie SHG

Il existe une multitude de méthodes de microscopie SHG avancées, et nous allons brièvement introduire chaque modalité dans cette section. Pour plus d'informations, veuillez-vous référer à l'article 1.

La SHG résolue en polarisation (P-SHG) combine la microscopie SHG avec la polarimétrie pour améliorer la visualisation des structures complexes, comme les fibrilles de collagène. Cette technique mesure divers paramètres, y compris l'orientation et l'anisotropie des fibrilles, et a été appliquée dans diverses études biomédicales [52]. (Voir Figures 8 et 9 de l'article 1).

La microscopie SHG en champ large illumine toute la zone d'intérêt simultanément et améliore considérablement le débit d'imagerie. Cette méthode utilise traditionnellement des impulsions à haute énergie, mais prend également en compte les dommages photo-induits sur les cellules vivantes, conduisant à des adaptations telles que des impulsions de faible énergie pour l'imagerie en direct (voir Figures 17 et 18 de l'article 1) [83].

La SHG Interférométrique (I-SHG) et la I-SHG Rapide sont des techniques avancées dans le domaine de la microscopie SHG, une technique d'imagerie optique non linéaire. L'I-SHG améliore les capacités de la microscopie SHG traditionnelle en incorporant des méthodes interférométriques, qui fournissent des informations structurelles et d'orientation supplémentaires concernant les échantillons biologiques, en particulier au niveau moléculaire [71]. Cette méthode est particulièrement utile pour étudier des structures, comme le collagène, dans les tissus (voir Figures 13 et 14 de l'article 1) [71].

La I-SHG Rapide ou I-SHG en un seul balayage est une évolution de l'I-SHG visant à augmenter considérablement la vitesse d'imagerie. Ceci est crucial pour les applications nécessitant des observations en temps réel ou quasi réel, comme les processus biologiques dynamiques. Tout en maintenant les avantages de l'I-SHG, la I-SHG Rapide optimise le processus d'imagerie pour une acquisition de données plus rapide, la rendant plus adaptée aux scénarios d'imagerie en temps réel et en direct [75]. Ces deux techniques représentent des avancées significatives en microscopie SHG, élargissant leurs applications en recherche biomédicale en fournissant des capacités d'imagerie plus détaillées et rapides (Voir Figure 1-8 de la thèse) [75].

Perspectives de la microscopie SHG

Au cours des deux dernières décennies, la microscopie SHG est apparue comme un outil inestimable en bioimagerie et neuroimagerie. Elle a été largement utilisée pour étudier des structures biologiques non centrosymétriques. Malgré ces avancées, des défis demeurent dans l'interprétation pleinement quantitative des images SHG en raison de la nature cohérente du processus impliqué. Les avancées futures en microscopie SHG visent à améliorer la résolution spatiale, la profondeur d'imagerie et à s'aventurer dans le domaine spectroscopique. Cependant, le coût élevé et la complexité de l'équipement, ainsi que le besoin de formation spécialisée, limitent son utilisation généralisée dans la pratique biomédicale courante [2]. Les avancées récentes dans la technologie laser, y compris le passage vers des lasers à fibres et à semi-conducteurs plus robustes et efficaces, devraient simplifier et réduire le coût des microscopes SHG, élargissant potentiellement leurs applications biomédicales. Les avancées logicielles et informatiques en microscopie, y compris le traitement rapide des images et les applications d'apprentissage automatique, ont amélioré les capacités d'imagerie [131]. Cependant, il est nécessaire de standardiser et d'unifier les processus d'imagerie à travers les laboratoires pour assurer la reproductibilité et la portabilité. Malgré ces défis, la SHG et autres modalités de microscopie optique non linéaire continuent d'offrir des aperçus précieux qui ne sont pas facilement disponibles avec les techniques d'imagerie optique traditionnelles linéaires ou incohérentes. Les avancées technologiques en cours, telles que l'apprentissage profond, devraient encore améliorer ces modalités, les rendant plus simples et plus accessibles pour un large éventail d'applications scientifiques et médicales. Il est donc nécessaire d'explorer les concepts de l'apprentissage profond et leur chevauchement avec la microscopie SHG [2].

Cette thèse est structurée autour de quatre articles interdépendants, chacun abordant des aspects spécifiques de ces objectifs :

1. Le premier article fournit une revue complète de la microscopie SHG, établissant une base solide pour les recherches ultérieures.
2. Le deuxième article se concentre sur l'application de techniques d'apprentissage profond pour la classification des images SHG des tissus des glandes mammaires, démontrant le potentiel de l'IA dans l'analyse automatisée des images.
3. Le troisième article évalue la performance de deux techniques de débruitage basées sur l'IA, CARE 2D et N2V 2D, pour améliorer la qualité des images SHG de différents tissus.

4. Le quatrième article introduit une nouvelle approche pour l'imagerie P-SHG de l'ensemble de l'échantillon, utilisant des réseaux antagonistes génératifs pour améliorer la résolution des images tout en réduisant considérablement le temps d'imagerie.

Ces articles collectivement démontrent comment l'intégration de l'IA peut surmonter les limitations actuelles de la microscopie SHG et étendre ses applications dans la recherche biomédicale et la pratique clinique.

Aperçu de l'apprentissage profond et de son impact sur la microscopie SHG

L'apprentissage profond (*Deep Learning*, DL) s'inspire des mécanismes complexes de traitement des données observés dans le cerveau humain, en particulier de sa capacité à apprendre sans règles prédéfinies, en se basant plutôt sur d'importants ensembles de données pour établir des liens entre les données d'entrée et des étiquettes spécifiques. La clé dans ce domaine est l'utilisation de réseaux neuronaux artificiels (ANNs), où chaque couche offre des interprétations uniques des données [133-135]. Le DL a révolutionné la microscopie et l'analyse d'image, améliorant la précision et l'analyse rapide d'images complexes, et offrant des perspectives auparavant difficiles à atteindre. Son adaptabilité et sa capacité à découvrir des modèles subtils dans les données en font une force transformatrice en microscopie, avec le potentiel de redéfinir notre compréhension du monde microscopique [133–136]. Les architectures d'apprentissage profond pour l'analyse d'image impliquent divers algorithmes sophistiqués. Les réseaux neuronaux *feed-forward* ou perceptrons multicouches (MLPs) sont fondamentaux pour de nombreux modèles modernes de DL. Ces réseaux, inspirés des systèmes neuronaux humains, impliquent un flux de données unidirectionnel de l'entrée vers la sortie sans boucles de rétroaction (voir Figure 1-13 de la thèse) [137–140]. Les réseaux neuronaux convolutifs (CNNs) (voir Figure 1-14 de la thèse) et les réseaux neuronaux récurrents (RNNs) sont des architectures essentielles. Les CNNs sont spécialisés pour les données en grille comme les images, tandis que les RNNs gèrent les données séquentielles en capturant les dépendances temporelles [141–145].

Les réseaux antagonistes génératifs (GANs) représentent une variante unique des ANNs comprenant un générateur et un discriminateur, tous deux formés simultanément. Ces réseaux sont largement utilisés dans l'adaptation de domaine et la génération d'image, en particulier dans l'analyse d'image médicale [147–149].

Analyse d'images médicales utilisant l'apprentissage automatique : Le DL joue un rôle crucial dans l'analyse d'images médicales. La classification d'image, la réduction du bruit et l'amélioration de la résolution sont des domaines critiques où le DL contribue de manière significative. Diverses architectures, telles que les CNNs et les GANs, ont été efficacement appliquées dans ces domaines [150–165]. L'apprentissage par transfert dans l'analyse d'image est essentiel pour l'imagerie médicale, abordant les problèmes de pénurie de données et réduisant les besoins en ressources. L'apprentissage par transfert avec les CNNs implique de transférer les connaissances de tâches précédemment acquises à de nouvelles, particulièrement pour la classification d'image médicale [166, 167].

Les métriques de qualité d'image sont vitales pour évaluer l'efficacité du DL dans les analyses d'images. Des techniques telles que l'indice de similarité structurelle (SSIM) (voir Figure 1-16 de la thèse) et ses variantes, l'erreur quadratique moyenne (MSE) et le rapport signal sur bruit de crête (PSNR) sont des métriques couramment utilisées. Ces métriques fournissent une mesure quantitative de la qualité de l'image, qui est cruciale pour le succès des techniques d'analyse d'image [168–181].

Applications du DL en imagerie biomédicale

Le DL a considérablement enrichi l'imagerie biomédicale. Des études sur l'imagerie biomédicale SHG, la réduction du bruit en tomographie par cohérence optique (OCT) et les méthodes de classification dans le diagnostic du cancer du sein ont montré l'impact du DL dans ce domaine (Voir Figure 1-17 de la thèse) [182–186]. Malgré ses avancées, le DL en microscopie fait face à des défis tels que la rareté des données, l'interprétabilité des décisions des modèles et les barrières d'accessibilité. Aborder ces limitations est crucial pour de nouvelles avancées dans ce domaine [187, 188].

Énoncé du problème général de la thèse

La microscopie SHG est un outil puissant en imagerie biomédicale, permettant l'observation détaillée de structures non centrosymétriques telles que le collagène et de nombreux autres échantillons biologiques. Malgré ses capacités, la microscopie SHG sous-utilise les avancées en intelligence artificielle (IA) et en apprentissage automatique, qui pourraient révolutionner ses applications. Cette thèse vise à combler cette lacune en introduisant l'IA dans divers aspects de la microscopie SHG pour surmonter les limitations actuelles. L'IA et l'apprentissage automatique ont transformé de nombreux domaines, des véhicules autonomes à la médecine personnalisée. Ces technologies ont le potentiel d'automatiser des tâches complexes, d'améliorer le traitement des données, de fournir des aperçus plus profonds et d'améliorer les analyses d'images. Cependant, leur application en microscopie SHG reste minimale, représentant une opportunité significativement manquée pour les avancées en imagerie biomédicale.

Article 1 : La microscopie de génération de seconde harmonique : un outil puissant pour l'imagerie biologique

Énoncé du problème de l'article 1

Le domaine de la microscopie SHG a considérablement évolué au fil des ans, offrant des aperçus sans précédent dans divers domaines scientifiques, en particulier dans l'étude des structures et fonctions neuronales. Cet article de revue est principalement motivé par le besoin de consolider l'important éventail de publications de recherche de notre laboratoire, qui contribue collectivement à la compréhension de la microscopie SHG et de ses modalités avancées. Cet article fournit un aperçu complet du développement historique et des fondements théoriques de la microscopie SHG, offrant ainsi une base solide pour les nouveaux chercheurs et les experts dans le domaine. L'un des objectifs clés de cette revue était de servir de point de départ solide pour les futurs étudiants et chercheurs qui entament leur revue de littérature dans ce domaine. En résumant et en synthétisant la littérature existante, cet article vise à faciliter une entrée plus aisée dans le domaine, permettant aux chercheurs de saisir rapidement les concepts fondamentaux et la progression historique de la microscopie SHG. Cette compréhension fondamentale est cruciale pour permettre aux chercheurs de se plonger plus facilement et avec plus de contexte dans des études et des domaines d'intérêt spécifiques. En outre, cet article se concentre de manière significative sur l'application de la microscopie SHG dans les études neuronales. De nombreuses études ont utilisé la microscopie SHG pour démêler les complexités des structures et fonctions neuronales, contribuant immensément à notre compréhension du système nerveux. Cependant, ces études ont été dispersées dans diverses publications, rendant difficile pour les chercheurs d'accéder à un corpus de connaissances consolidé. Cet article de revue aborde cette lacune en compilant et en passant en revue toutes les études significatives de microscopie SHG dans la recherche neuronale menées au fil des ans. En fin de compte, cette revue récapitule non seulement les contributions pivotales de notre laboratoire et d'autres dans le domaine, mais ouvre également la voie à de futures explorations et découvertes en microscopie SHG et études neuronales.

Sommaire de l'article 1

Dans le discours précédent, nous avons examiné en profondeur la microscopie SHG et ses variantes avancées, comprenant une analyse complète des fondements techniques et des applications dans divers domaines scientifiques. Étant donné la couverture étendue de ces aspects, il n'est ni nécessaire ni bénéfique de réitérer ces détails dans le manuscrit actuel. Au contraire, notre focus se tournera exclusivement vers l'application de la microscopie SHG dans les études neuronales, un domaine bourgeonnant de potentiel et d'innovation. De plus, nous explorerons également l'avenir de la microscopie SHG tel qu'énoncé dans cet article.

La microscopie SHG a considérablement avancé notre compréhension du système nerveux, en particulier dans l'étude détaillée des neurones et des microtubules. Dans le monde complexe des neurosciences, les neurones, avec leur structure complexe comprenant le soma, les dendrites et les axones, jouent un rôle pivot dans le traitement et la transmission de l'information (voir Figure 19 de l'article 1). Bien que les méthodes traditionnelles telles que l'électrophysiologie aient été essentielles pour étudier l'activité neuronale, elles sont limitées par leur nature invasive et la portée étroite des réseaux de neurones qu'elles peuvent étudier.

La microscopie SHG émerge comme une alternative puissante et non invasive, permettant une observation plus complète des réseaux neuronaux. Cette technique contourne les limitations des méthodes traditionnelles, permettant un examen plus large et moins intrusif des fonctions neuronales. Une avancée notable dans la microscopie SHG est l'utilisation de colorants SHG, tels que FM 4–64. Ces colorants ont considérablement amélioré le rapport signal sur bruit en imagerie, facilitant une visualisation plus claire des activités neuronales, y compris l'observation des potentiels d'action et leur propagation à travers les structures neuronales (voir Figure 20 de l'article 1).

L'application de la microscopie SHG va au-delà des neurones pour étudier les microtubules, des composants cruciaux dans le maintien de l'intégrité cellulaire et la régulation du trafic intracellulaire. Composés de dimères d'α- et β-tubuline, les microtubules possèdent une polarité distincte essentielle à leur fonction. La microscopie SHG a été particulièrement efficace pour explorer la structure et la fonction de ces microtubules. Elle a éclairé leur nombre, leur organisation et leur polarisation au sein des neurones, contribuant grandement à notre compréhension de leur rôle dans les activités neuronales (voir Figure 1-11 de la thèse). La technique a fourni de nouveaux aperçus sur la polarité des microtubules, révélant une polarité uniforme dans les axones, en contraste avec la polarité plus complexe et moins définie observée dans les dendrites.

Les avancées technologiques et méthodologiques en microscopie SHG ont été substantielles. Les progrès récents incluent des améliorations dans la technologie laser et l'incorporation de méthodes computationnelles telles que l'apprentissage automatique, qui ont amélioré les capacités et l'efficacité de l'imagerie SHG. Cependant, la technique fait encore face à des défis, en particulier le besoin d'équipements coûteux et d'une formation spécialisée. Malgré ces obstacles, les innovations en cours devraient rendre la microscopie SHG plus accessible et polyvalente pour les applications biomédicales.

Le domaine évolue vers la standardisation des processus d'imagerie pour garantir la reproductibilité et la portabilité dans différents environnements de recherche. Alors que la microscopie SHG devient plus accessible et rentable, elle est prête à devenir une partie plus intégrante de la recherche biomédicale de routine et du diagnostic clinique.

Cette revue complète établit une base solide pour les études ultérieures, identifiant les domaines clés où l'intégration de l'IA pourrait considérablement améliorer les capacités de la microscopie SHG.

Article 2 : Microscopie non linéaire et classification par apprentissage profond pour les études de l'environnement microscopique des glandes mammaires

Énoncé du problème de l’article 2

Le problème principal abordé par cette étude était le défi d'imager et d'analyser avec précision et efficacité les changements structurels dans les glandes mammaires murines, en particulier dans le contexte du développement tumoral. Les techniques d'imagerie traditionnelles, bien qu'efficaces dans une certaine mesure, ne parviennent souvent pas à capturer les changements complexes dans la composition et la structure des tissus, tels que les agrégations de collagène et les modifications des orientations fibrillaires autour des sites tumoraux. Cette limitation entrave une compréhension complète du microenvironnement tumoral et de son impact sur les tissus environnants. Pour surmonter ces défis, cette étude a introduit une approche intégrée utilisant la microscopie SHG et P-SHG automatisée. Ces techniques d'imagerie avancées sont censées fournir des aperçus plus détaillés et précis sur les changements structurels au sein des glandes mammaires influencés par la croissance tumorale. Cependant, l'efficacité de ces techniques pour distinguer entre les glandes naïves et celles portant des tumeurs, en particulier en ce qui concerne les fibres de collagène plus fines, reste à évaluer et à optimiser systématiquement. Bien que des méthodes existantes, telles que CurveAlign, offrent des aperçus précieux, elles nécessitent une inspection manuelle et peuvent manquer des détails plus fins.

De plus, cette étude a cherché à combler le fossé dans l'analyse d'image automatisée pour ces types d'images de microscopie. Cette étude propose l'utilisation d'un programme personnalisé pour l'analyse d'image P-SHG et d'un modèle d'apprentissage profond supervisé pour les images SHG afin d'améliorer la détection et la classification des changements structurels. Les méthodes utilisées ont été comparées aux modèles et méthodes établis.

Sommaire de l’article 2

Au cours de la dernière décennie, des avancées significatives ont été réalisées dans la compréhension de l'environnement tumoral, en se concentrant particulièrement sur les interactions entre les cellules tumorales, les cellules immunitaires, les cellules stromales et la matrice extracellulaire (ECM), avec un accent sur le rôle du collagène dans la progression du cancer du sein. L'arrangement du collagène, en particulier à la frontière entre la tumeur et le stroma, est lié à la progression, à l'invasion et à la métastase du cancer du sein. Les Signatures Collagènes Associées aux Tumeurs (TACS) sont classifiées en trois types en fonction de leur arrangement, fournissant des aperçus sur le potentiel métastatique des tumeurs.

La coloration histologique et la microscopie polarisante à cristaux liquides sont courantes mais ont une résolution et une analyse quantitative limitées. La microscopie SHG s'est imposée comme une méthode de premier plan pour l'imagerie du collagène, offrant une meilleure résolution, une phototoxicité réduite et une facilité de préparation des échantillons. La SHG est essentielle pour étudier la restructuration du collagène dans divers cancers, y compris le cancer du sein, des ovaires, de la prostate et du poumon.

La P-SHG surmonte les limitations de la SHG traditionnelle et fournit des informations structurales détaillées sur les fibres de collagène. L'imagerie et l'analyse d'images P-SHG avancées ont amélioré notre compréhension de la distribution et de l'asymétrie des fibrilles. Ces avancées en microscopie SHG et P-SHG ont considérablement amélioré notre compréhension des composants structurels de l'environnement tumoral, en particulier en relation avec le collagène, offrant de nouveaux aperçus sur la progression du cancer et des cibles thérapeutiques potentielles.

L'analyse d'image utilisant la microscopie SHG et P-SHG a évolué pour identifier des caractéristiques détaillées du collagène. L'intégration de l'apprentissage profond automatise l'analyse d'image, bien que des défis subsistent dans le traitement de petits ensembles de données.

Des souris femelles BALB/c, conformes aux directives du Conseil canadien de soins aux animaux et approuvées par l'Université McGill, ont été utilisées pour la préparation des tissus. L'étude a impliqué à la fois des glandes mammaires naïves et porteuses de tumeurs. Les échantillons ont subi un processus de préparation détaillé, incluant l'encapsulation dans la paraffine, la coupe, la déparaffinisation, la réhydratation et une préparation finale pour la microscopie. L'installation d'imagerie SHG a utilisé un microscope inversé personnalisé avec balayage laser, employant un laser Ti: Sa mode verrouillé pour l'éclairage. Le système comprend un tube photomultiplicateur pour la détection de l'émission SHG et des filtres spécifiques pour l'isolation du signal. Un plateau de balayage motorisé à grande vitesse a facilité l'imagerie de grandes zones d'échantillons.

Pour la microscopie P-SHG, des étapes supplémentaires ont été prises pour ajuster la polarisation linéaire du faisceau laser et capturer des images dans différents états de polarisation. Ce processus a été contrôlé par un programme Python personnalisé, tandis que le script MATLAB a traité les images P-SHG (voir Figures 1 et 2 de l'article 2).

La classification d'image dans cette étude a été exécutée en utilisant des architectures séquentielles personnalisées et MobileNetV2. Un ensemble de données relativement petit d'images de glandes mammaires, incluant des échantillons naïfs et porteurs de tumeurs, a été amélioré à l'aide de techniques d'augmentation de données, telles que le retournement, la rotation et le zoom. Le processus de classification a impliqué l'entraînement de l'ensemble de données sur vingt-cinq époques, et la performance du modèle a été évaluée en enregistrant la précision et la perte sur différents ensembles de données d'entraînement et de test. Cette méthodologie complète vise à tirer parti des techniques d'imagerie avancées et de l'apprentissage profond pour l'analyse détaillée et la classification des échantillons de glandes mammaires dans les études sur les tumeurs (voir Figures 5 et 6 de l'article 2).

Dans la phase d'imagerie SHG, des zones significatives des glandes mammaires à la fois naïves et porteuses de tumeurs ont été méticuleusement imagées. Ce processus a révélé des différences structurelles distinctes ; les glandes naïves présentaient des structures ductales bien définies, tandis que les glandes porteuses de tumeurs montraient des signaux SHG diminués, indiquant la présence de tumeurs. Particulièrement aux bords de la tumeur, le collagène agrégé formait une barrière, une constatation cohérente avec des recherches précédentes suggérant le rôle du collagène dans l'entrave à la propagation des tumeurs (voir Figure 3 de l'article 2).

Pour une analyse plus détaillée, les méthodes P-SHG et CurveAlign ont été employées. La technique P-SHG, à travers un processus long impliquant l'imagerie de zones plus petites avec des pas de balayage plus fin, fournit des détails complexes sur l'orientation des fibres de collagène à la frontière entre la tumeur et le stroma, ce qui est crucial pour comprendre les risques d'invasion locale et de métastase. L'étude a constaté que la P-SHG offrait des aperçus plus détaillés sur les fibres de collagène plus fines que CurveAlign, qui manquait parfois ou surestimait les orientations des fibres dans les régions de signal dimère (voir Figure 4 de l'article 2).

Dans le domaine de la classification d'image pour la microscopie SHG, cette recherche s'est aventurée dans l'apprentissage profond et les techniques d'apprentissage par transfert en utilisant un modèle séquentiel personnalisé et le modèle MobileNetV2. Le prétraitement des images SHG a été suivi par un entraînement sur ces modèles. L'étude a abordé les défis de travailler avec un petit ensemble de données en employant des stratégies d'augmentation de données et en ajustant les paramètres du modèle pour atténuer le surapprentissage. Malgré ces efforts, la taille limitée de l'ensemble de données a conduit à des degrés variables de performance du modèle, comme en témoignent les précisions et les courbes de perte d'entraînement et de test. L'analyse a conclu que, bien que les modèles personnalisés adaptés à des ensembles de données spécifiques puissent être efficaces, ils sont limités par les données disponibles.

En revanche, l'apprentissage par transfert avec des architectures plus complexes telles que MobileNetV2 offre des avantages potentiels mais risque également le surapprentissage en raison de la profondeur et de la complexité de ces réseaux, en particulier lorsqu'on travaille avec de petits ensembles de données. Cette analyse complète souligne les compromis entre le temps d'imagerie, la précision et les défis inhérents à l'application de techniques computationnelles avancées à des ensembles de données d'imagerie biologique.

Après l'analyse de la variation des paramètres, le modèle optimal pour l'ensemble de données de l'étude s'est avéré être un partage de données à 30% avec un *dropout* de 0,2 et trois couches d'augmentation de données, atteignant une précision de test de 73%. Une limitation notable est la vitesse d'imagerie, indiquant la nécessité de nouvelles avancées technologiques (voir tableaux 1-4 de l'article 2).

Cette étude a également mis en évidence le potentiel de combiner l'analyse P-SHG avec la classification d'images et l'imagerie en champ large dans la recherche sur le cancer. Cette approche fournit des aperçus précieux sur la formation et le remodelage du collagène dans la matrice extracellulaire (ECM), ce qui est crucial pour comprendre la progression du cancer.

Cette étude démontre le potentiel de l'apprentissage profond pour améliorer l'analyse des images SHG, ouvrant la voie à des applications cliniques plus larges et à une détection plus précise des tumeurs.

Article 3 : Apprentissage profond pour la restauration d'image en microscopie de génération de seconde harmonique – une approche pour réduire la puissance laser et les dommages sur l'échantillon.

Énoncé du problème de l'article 3

Le principal défi abordé dans cette étude est l'état relativement naissant des applications de l'apprentissage profond en microscopie, en particulier dans le contexte de la restauration d'image pour les images SHG à faible rapport signal sur bruit (SNR). Actuellement, il existe un écart significatif dans l'application des techniques d'apprentissage profond avancées pour améliorer et restaurer les images SHG souffrant d'un faible SNR. Cet écart limite l'utilité de la microscopie SHG pour fournir des aperçus clairs et détaillés sur les structures et processus biologiques, en particulier dans les cas où il est difficile d'obtenir des images de haute qualité en raison de contraintes techniques telles que la puissance du laser ou la qualité de la préparation des échantillons. Cette étude vise à être pionnière dans l'application de deux techniques de restauration d'image basées sur l'apprentissage profond, CARE 2D et Noise2Void (N2V) 2D, sur les images SHG à faible SNR. Ces techniques ont montré des promesses dans d'autres contextes d'imagerie mais n'ont pas encore été systématiquement appliquées et évaluées dans le domaine de la microscopie SHG. En mettant en œuvre ces techniques, cette étude a cherché à améliorer la qualité des images SHG dans deux cas exemplaires, démontrant ainsi leur utilité potentielle dans une variété de scénarios d'imagerie biologique.

Le premier cas impliquait l'investigation de l'effet de la concentration en glycérol sur les images SHG lors de la fixation de poissons zèbres. Ce cas donne des aperçus sur la façon dont la qualité de l'image peut être compromise pendant la préparation des échantillons et comment l'apprentissage profond peut atténuer ces effets. Le second cas se concentre sur l'imagerie des images à faible puissance laser des tissus musculaires de deux souches de poissons zèbres, dont une souche qui modélise l'amyotrophie spinale et la barrière de la matrice extracellulaire autour d'une glande mammaire de souris porteuse de tumeur. Ces cas sont particulièrement difficiles en raison de problèmes inhérents de faible SNR et sont donc idéaux pour évaluer l'efficacité de CARE 2D et N2V 2D dans l'amélioration de la qualité de l'image. Pour évaluer quantitativement le succès de ces techniques de restauration d'image, cette étude a utilisé la moyenne SSIM et le PSNR comme métriques de contrôle de la qualité. Ces métriques comparent les images restaurées (prédites) aux images de vérité terrain (GT) à haut SNR, fournissant une mesure claire de l'amélioration et de la fidélité. En essence, cet énoncé de problème souligne le besoin de techniques de restauration d'image avancées dans le domaine de la microscopie SHG pour surmonter les limitations posées par un faible SNR, permettant une visualisation plus claire et plus détaillée des échantillons biologiques.

Sommaire de l'article 3

La microscopie SHG, un outil significatif tant en imagerie médicale que non médicale, dépend fortement du rapport signal sur bruit (SNR) pour la qualité d'image. Le SNR est affecté par des facteurs tels que la puissance du laser, le temps d'exposition et les propriétés de l'échantillon. Ajuster la puissance du laser est un acte d'équilibre ; une puissance plus élevée améliore le signal SHG mais risque d'endommager l'échantillon. Différents échantillons présentent des forces de signal SHG variables ; par exemple, les tissus riches en collagène montrent des signaux forts, tandis que d'autres, comme les microtubules, ont des signaux intrinsèquement faibles, conduisant à un faible SNR et à une obscurité potentielle de la structure de l'échantillon sous le bruit.

Les avancées en apprentissage profond ont introduit de nouvelles techniques de restauration d'image en microscopie pour améliorer la qualité d'image en réduisant le bruit et les distorsions. Ces techniques incluent *Noise to Ground Truth* (N2GT), *Noise to Noise* (N2N) et *Noise to Void* (N2V). N2GT utilise une image de référence sans bruit pour la comparaison, N2N emploie une autre image bruyante au lieu d'une image de référence, et N2V repose sur les propriétés statistiques du bruit dans une seule image. La qualité des images débruitées est couramment évaluée à l'aide de métriques telles que le SSIM et le PSNR, qui mesurent la similarité et la qualité des images traitées par rapport aux images originales. Malgré ces développements, l'application de l'apprentissage profond pour la restauration d'image en microscopie SHG à faible SNR est encore un domaine émergent, offrant un potentiel pour des recherches futures et l'amélioration des techniques de microscopie SHG.

La méthodologie de l'étude a impliqué la préparation d'échantillons de tissus à la fois de poissons zèbres et de souris, suivie d'une imagerie avancée en microscopie SHG et d'une restauration d'image utilisant des techniques d'apprentissage profond.

Pour la préparation des tissus, des poissons zèbres adultes de type sauvage et hétérozygotes smn+/− ont été maintenus dans des conditions contrôlées, et des embryons ont été collectés et stadiés. Un génotypage a été réalisé pour différencier entre les larves de type sauvage, hétérozygotes et homozygotes. Les larves de poisson zèbre de 5 jours après la fécondation ont été fixées, rincées et montées pour la microscopie SHG. De même, des souris BALB/c femelles ont été utilisées pour des études de tumeurs murines avec des échantillons porteurs de tumeurs obtenus à partir d'injections orthotopiques de cellules 4T1. Après la période de croissance, les échantillons ont été fixés, inclus, sectionnés et préparés sur des lames.

Le dispositif d'imagerie SHG comprenait un microscope inversé à balayage personnalisé équipé d'un laser Ti: Sa à verrouillage de mode. Ce dispositif a permis un contrôle précis de la puissance du laser et des ajustements fins de la mise au point et du positionnement de l'échantillon. Le signal SHG collecté a été détecté à l'aide d'un tube photomultiplicateur et a été isolé à l'aide de filtres spectraux. Un programme Python personnalisé a été utilisé pour l'acquisition du signal et la synchronisation, et les données brutes ont été visualisées à l'aide de Fiji-ImageJ (voir Figure 1 de l'article 3).

La restauration d'image a été réalisée en utilisant les modèles CARE 2D et N2V 2D. Ces modèles ont été entraînés sur Google Colaboratory en utilisant la boîte à outils ZeroCostDL4Mic. L'entraînement impliquait d'utiliser différents nombres d'époques et de patchs d'image pour les échantillons de cancer de la glande mammaire et de poissons zèbres. Le modèle N2V 2D, qui repose sur un apprentissage auto-supervisé, a subi un entraînement prolongé pour apprendre efficacement et éliminer les motifs de bruit. Le modèle CARE 2D, quant à lui, a eu moins d'époques de formation. L'augmentation des données et des paquets Python essentiels, tels que TensorFlow, Keras et NumPy, étaient intégraux au processus de formation, accéléré par un GPU Tesla T4 sur les serveurs Google.

Dans la section résultats et discussion, l'accent a été mis sur l'évaluation de l'impact des méthodes de fixation sur la qualité d'image en microscopie SHG et l'efficacité des modèles d'apprentissage profond, CARE 2D et N2V 2D, pour la restauration d'image.

L'étude a commencé par évaluer les niveaux de bruit dans les images de microscopie SHG en fonction de la teneur en glycérol dans les solutions de fixation utilisées pour les échantillons de poissons zèbres. Trois concentrations différentes de glycérol ont été testées, révélant une corrélation directe entre la concentration de glycérol et le bruit dans les images finales. Les résultats ont indiqué qu'un minimum de 50% de glycérol était optimal pour maintenir la qualité de l'image sans perturber le processus de fixation. Pour les échantillons avec des concentrations plus élevées de glycérol, le modèle N2V 2D a réussi à restaurer les images, récupérant efficacement les informations structurelles des muscles du poisson. Cette constatation était significative, suggérant que des outils d'apprentissage profond tels que N2V 2D pourraient potentiellement compenser des compositions chimiques sous-optimales lors de la préparation des échantillons, réduisant ainsi le besoin de traitements répétés des échantillons et économisant du temps et des ressources (voir Figures 2 et 3 de l'article 3).

Dans la phase suivante de l'étude, les modèles CARE 2D et N2V 2D ont été appliqués aux images SHG de glandes mammaires porteuses de tumeurs. Nous avons créé des images SHG avec différents SNR en ajustant la puissance d'entrée du laser. Pour les images à SNR plus élevé, CARE 2D a amélioré les détails et la netteté, a amélioré le contraste et a révélé des détails complexes de la structure des limites de collagène autour de la tumeur. Cependant, dans les cas de SNR extrêmement bas, CARE 2D a entraîné des hallucinations, créant des structures artificielles qui n'étaient pas présentes dans les images originales. L'hallucination fait référence à un phénomène observé dans les systèmes d'IA, en particulier dans le domaine de la génération et de la reconnaissance d'images, où l'IA produit ou interprète des données visuelles d'une manière qui s'écarte significativement des résultats précis ou attendus. Cette déviation n'est pas due à une erreur aléatoire mais est une conséquence des limites inhérentes et des biais des données de formation, des algorithmes et de l'architecture sous-jacente de l'IA. Les hallucinations de l'IA surviennent lorsque le modèle infère des motifs, des objets ou des caractéristiques dans une image qui ne sont pas présents ou sont significativement déformés par rapport à leur représentation réelle. Ce phénomène est souvent attribué au surapprentissage, où le modèle d'IA est excessivement entraîné sur un ensemble de données limité et devient ainsi trop sensible à des motifs ou bruits spécifiques inhérents à cet ensemble de données. En conséquence, lorsqu'il est présenté avec de nouvelles données inconnues, le modèle pourrait "voir" des éléments ou des motifs qui correspondent à sa formation mais n'existent pas objectivement dans les données d'entrée.

L'efficacité des modèles a été évaluée quantitativement à l'aide de métriques, telles que le mSSIM et le PSNR. Le modèle CARE 2D a montré une amélioration substantielle de la qualité d'image pour le cas de puissance de 30 mW, avec des augmentations notables des valeurs mSSIM et PSNR. En comparaison, pour le modèle N2V 2D, les améliorations du mSSIM étaient significatives, en particulier pour les cas de puissance de 30 mW et 70 mW, bien que les valeurs PSNR variaient (voir Figures 4 et 5 ainsi que le tableau 1 de l'article 3).

L'étude a également exploré l'application de ces modèles aux images SHG de structures musculaires de poissons zèbres, en comparant les souches de type sauvage et smn-/-. CARE 2D a tendance à lisser les structures musculaires, entraînant la perte de caractéristiques musculaires distinctes. Cependant, il a amélioré l'intensité SHG, en particulier à des réglages de puissance plus élevés. N2V 2D, d'autre part, a préservé les détails structurels des muscles plus efficacement dans tous les cas, le rendant le choix préféré pour les études se concentrant sur la morphologie musculaire et les changements structurels, malgré sa capacité inférieure à restaurer l'intensité SHG par rapport à CARE 2D (voir Figure 6 et tableau 2 de l'article 3).

En conclusion, cette étude a trouvé que CARE 2D était plus adapté pour débruiter les échantillons avec un SNR plus élevé, comme les glandes mammaires porteuses de tumeurs, en raison de sa capacité à améliorer la netteté et les détails de l'image. En revanche, N2V 2D est préférable pour préserver les structures musculaires naturelles dans les échantillons de poissons zèbres, en particulier dans les cas où la morphologie musculaire et l'intégrité structurelle sont cruciales. Le choix entre CARE 2D et N2V 2D dépend des besoins spécifiques de l'étude, équilibrant le besoin d'améliorations détaillées contre la préservation des structures naturelles.

Un aspect essentiel de cette étude était la gestion de la puissance laser d'entrée en imagerie SHG pour minimiser les dommages potentiels sur l'échantillon, ce qui entraîne souvent une réduction du SNR de l'image. La recherche a souligné qu'une diminution substantielle de la puissance laser d'entrée (jusqu'à 70%) est réalisable sans perdre le signal SHG et est particulièrement bénéfique pour la transition des échantillons fixes aux échantillons vivants. En tirant parti de l'apprentissage profond, il est possible de réduire considérablement la puissance d'entrée sans compromettre le signal SHG.

Cette recherche comparative fournit des informations cruciales sur l'efficacité des techniques de débruitage basées sur l'IA pour différents types de tissus, contribuant à l'amélioration globale de la qualité d'image en microscopie SHG.

Article 4 : Accélérer l'imagerie de génération de seconde harmonique résolue en polarisation avec des réseaux génératifs antagonistes super-résolution améliorés

Énoncé du problème de l’article 4

Le principal défi abordé dans cette étude est la nécessité d'augmenter significativement la vitesse d'imagerie de la microscopie P-SHG, en particulier pour les échantillons de glandes mammaires entières. Dans l'état actuel de la microscopie P-SHG, l'acquisition d'images haute résolution nécessite souvent un compromis entre la vitesse d'imagerie et la qualité des images. Des images de haute qualité sont généralement obtenues à un rythme plus lent, ce qui n'est pas toujours réalisable, en particulier dans des études nécessitant une imagerie rapide de grands échantillons ou lors de processus biologiques sensibles au temps. Pour surmonter cette limitation, cet article propose une nouvelle application des Réseaux Génératifs Adversaires Super-Résolution Améliorés (ESRGAN) pour améliorer la qualité des images P-SHG de basse qualité. L'objectif principal était d'explorer si ESRGAN pouvait être efficacement utilisé pour maintenir une qualité d'image acceptable tout en accélérant considérablement le processus d'imagerie. En capturant initialement des images de qualité inférieure à un rythme plus rapide puis en appliquant ESRGAN pour l'agrandissement, cette étude vise à atteindre un équilibre entre la vitesse d'imagerie et la qualité de l'image.

La méthodologie de recherche comprit l'acquisition d'images SHG de haute qualité d'échantillons de glandes mammaires entières pour établir un repère de qualité. L'étude s'est ensuite concentrée sur la prise rapide d'images P-SHG de moindre qualité de l'ensemble de l'échantillon et l'application d'ESRGAN pour améliorer ces images. Cette étape est cruciale pour démontrer la faisabilité de cette approche dans des scénarios d'imagerie pratiques. Pour évaluer l'exactitude et l'efficacité de cette méthode, cette étude a impliqué une analyse comparative. Des images P-SHG de haute qualité de zones sélectionnées de différents échantillons ont été capturées pour servir de références. Ces images ont été comparées aux résultats des images P-SHG améliorées pour évaluer dans quelle mesure le processus d'agrandissement compensait la qualité initiale inférieure des images. De plus, cette étude emploie les évaluations de métriques de qualité mentionnées précédemment pour garantir que l'intégrité structurelle des images originales est raisonnablement maintenue après l'agrandissement. Il est impératif de vérifier que, bien que le processus d'imagerie soit accéléré, les images agrandies fournissent toujours des représentations fiables et précises des tissus des glandes mammaires.

Sommaire de l’article 4

La glande mammaire, essentielle pour la production de lait après l'accouchement, subit des changements significatifs sous l'influence des hormones. Sa structure comprend deux composants principaux : l'épithélium mammaire et le stroma. Bien que le développement de l'épithélium mammaire soit bien compris, celui du stroma l'est moins. Le stroma mammaire inclut diverses cellules, telles que les adipocytes, les fibroblastes, les cellules immunitaires, et des composants de la matrice extracellulaire (ECM), tels que le collagène et les laminines. Ces composants jouent un rôle crucial dans le développement et la fonction des glandes mammaires. Par exemple, pendant la puberté, l'expansion stromale permet la croissance des adipocytes et l'orientation des fibres de collagène en préparation pour la morphogenèse épithéliale. Ce processus est influencé par les œstrogènes, qui favorisent l'expansion de l'épithélium le long de ces fibres, conduisant à une architecture glandulaire mature.

La microscopie SHG est devenue la méthode privilégiée pour l'imagerie du collagène dans les tissus, offrant des avantages tels que la haute résolution spatiale, la réduction de la phototoxicité et la facilité de préparation des échantillons. Cette méthode non invasive est particulièrement efficace pour détecter les changements du collagène fibrillaire dans les glandes mammaires. Pour surmonter certaines des limitations de la microscopie SHG, telles que les interférences dans les études d'orientation des fibres, la P-SHG a été développée, combinant les avantages de la SHG et de la polarimétrie. La P-SHG est très précieuse pour étudier la structure du collagène, en particulier dans la recherche sur la glande mammaire. Cependant, les méthodes SHG et P-SHG peuvent être coûteuses et chronophages, en particulier pour les grands échantillons.

Pour relever ces défis, des modèles basés sur les Réseau Antagoniste Génératif (GAN), en particulier ESRGAN, ont été utilisés pour l'agrandissement des images. Les GAN impliquent deux réseaux neuronaux en compétition : un générateur qui crée des données ressemblant à de vraies données et un discriminateur qui distingue entre les données réelles et générées. Avec le temps, cela conduit à la génération de données de haute qualité et réalistes. ESRGAN, une approche d'apprentissage profond pour la super-résolution d'image, se concentre sur la capture de caractéristiques d'image de haut niveau à travers une fonction de perte perceptuelle, améliorant ainsi la qualité des images agrandies.

Dans cette étude, la préparation des échantillons a impliqué la sélection de souris à différents stades de développement de la glande mammaire et leur euthanasie humaine. Les glandes mammaires ont été récoltées, étirées à leur forme originale sur des lames de verre et fixées à l'aide du fixatif de Carnoy. Après la fixation, les tissus ont été réhydratés, colorés pour mettre en évidence l'épithélium mammaire, puis déshydratés à nouveau. Les échantillons préparés ont été imagés pour une analyse numérique, en se concentrant sur divers aspects des glandes mammaires.

Les échantillons préparés ont ensuite été imagés à l'aide d'un dispositif de boîte lumineuse et de caméra, avec une clé de mesure pour standardiser la comparaison entre les échantillons. L'analyse numérique de ces images, en se concentrant particulièrement sur les branches épithéliales, les bourgeons terminaux et l'architecture globale, a été réalisée à l'aide du logiciel ImageJ.

Le dispositif d'imagerie pour cette étude a utilisé des techniques de microscopie avancées, en particulier la microscopie SHG et sa variante P-SHG. Le microscope à balayage inversé personnalisé à laser a employé un laser à fibre YB à verrouillage de mode avec des réglages spécifiques pour la durée d'impulsion, la fréquence de répétition et la puissance moyenne pour optimiser la qualité d'imagerie. Le processus d'imagerie inclut des ajustements dans le contrôle de la puissance et la mise au point à l'aide d'une combinaison de moteurs mécaniques et piézoélectriques. Le signal SHG a été collecté et filtré à travers une série de filtres spectraux pour isoler des longueurs d'onde spécifiques d'intérêt. Le dispositif d'imagerie a été contrôlé et synchronisé à l'aide d'un programme Python personnalisé, permettant une acquisition efficace d'images SHG de haute qualité (voir Figure 1 de l'article 4).

Pour l'imagerie P-SHG de qualité inférieure, le dispositif a été modifié pour inclure une plaque demi-onde motorisée, permettant la rotation de la polarisation linéaire du faisceau laser. Cela a permis de capturer des images dans divers états de polarisation. En revanche, l'imagerie P-SHG de haute qualité implique l'imagerie de régions d'intérêt aléatoires à l'aide d'un objectif différent pour une résolution améliorée.

Pour relever les défis de la qualité d'image, cette étude a utilisé plusieurs modèles d'agrandissement basés sur l'ESRGAN. Ces modèles comprennent Ultrasharp_4X, ESRGAN_Nomos2K, 4X_Remarci et 4X-UniScaleV2_Sharp. L'agrandissement a été facilité par le programme ChaiNNer. Un agrandissement guidé utilisant PixTransform avec des images SHG de haute qualité servant de référence a également été effectué. Ce processus a impliqué des itérations avec différents modes de séparation de canaux et a été accéléré à l'aide d'un GPU RTX 3060Ti. L'approche complète dans la préparation des échantillons, la configuration d'imagerie et l'agrandissement d'image souligne la méthodologie rigoureuse employée dans cette étude pour assurer une analyse détaillée et précise du développement de la glande mammaire.

L'intégration des images histologiques avec leurs homologues en imagerie SHG a fourni une vue complète de la microstructure tissulaire. Cette approche était particulièrement bénéfique pour offrir une compréhension plus holistique de l'architecture tissulaire et aider dans le processus d'agrandissement en assurant la fidélité structurelle dans les images SHG améliorées (voir Figure 2 de l'article 4).

Des comparaisons ont été effectuées entre les images SHG originales de haute qualité et leurs versions de basse qualité, suivies par une analyse des images agrandies. Les images de haute qualité, avec une résolution de 1800×800 pixels, affichaient une quantité significative de détails et de clarté. Cependant, la capture de ces images haute résolution est chronophage, nécessitant environ 18 minutes par image. Cela était préoccupant, en particulier pour l'imagerie P-SHG, qui nécessitait plusieurs images et pouvait potentiellement endommager les échantillons en raison d'une exposition prolongée au laser. À l'inverse, les images originales de basse qualité, avec une résolution de 225×100 pixels, étaient capturées beaucoup plus rapidement, mais manquaient de détails et de netteté (voir Figure 3 de l'article 4).

Pour résoudre ces problèmes, des techniques d'agrandissement d'image ont été utilisées, en particulier le modèle Ultrasharp_4X basé sur l'ESRGAN. Ce modèle a été choisi en raison de sa capacité à améliorer efficacement la résolution de l'image tout en maintenant l'intégrité structurelle. En appliquant ce modèle, la résolution de l'image a été améliorée à 3600×1600 pixels. Cependant, le processus d'agrandissement introduit une certaine dégradation de qualité, nécessitant des mesures de contrôle de qualité détaillées.

Le contrôle de qualité implique d'évaluer les images agrandies à l'aide de diverses métriques, telles que l'évaluateur de qualité d'image naturelle (NIQE), l'évaluateur de qualité d'image perceptuelle (PIQE), la similarité structurelle multi-échelle (MS-SSIM), le Rapport Signal sur Bruit Maximal (PSNR) et l'erreur quadratique moyenne normalisée (NRMSE). Ces métriques indiquent que les images agrandies, bien qu'elles ne soient pas identiques aux images originales de haute qualité, ont maintenu un haut niveau de fidélité et ont réussi à améliorer les images (voir tableau 1 et 2 de l'article 4).

L'étude a également inclus une analyse P-SHG, en utilisant initialement des mesures CurveAlign pour déterminer la faisabilité d'analyser des images de basse qualité. Il a été constaté que, bien que les images de basse qualité résolussent des alignements significatifs de fibres, elles manquaient de détails (voir Figure 4 de l'article 4). L'agrandissement de ces images s'est avéré plus efficace, améliorant la résolution des alignements et des orientations de fibres plus fines. Les images P-SHG ont été capturées à divers états de polarisation et traitées à l'aide d'un script MATLAB pour analyser l'orientation des fibres. Cette analyse a confirmé que les détails d'orientation dans les images agrandies étaient précis, offrant une méthode fiable pour améliorer les images de basse qualité pour une analyse P-SHG détaillée (voir Figure 5 de l'article 4).

Notre analyse a fait un bond significatif dans l'imagerie P-SHG en réduisant le temps d'imagerie de 4,5 heures à 13,5 minutes, réalisant ainsi une réduction de temps de plus de 95%. Cette efficacité a été réalisée grâce à la sélection stratégique du modèle "ultrasharp_4X", qui fait partie de l'ESRGAN pour l'agrandissement des images. Ce modèle a été préféré en raison de son haute-fidélité aux images originales, contournant les complications rencontrées lors de l'utilisation d'images de haute qualité comme références pour l'agrandissement.

L'un des avantages les plus significatifs de cette méthode accélérée est la réduction drastique de l'exposition au laser des échantillons. Cet aspect est crucial pour préserver l'intégrité des spécimens biologiques sensibles, car une exposition prolongée au laser peut entraîner des dommages photo-induits. Par conséquent, notre méthode ne protège pas seulement la qualité de l'échantillon, mais permet également des périodes d'observation prolongées sans risque de modifier leurs propriétés.

De plus, le besoin réduit d'imagerie haute résolution dans de nombreuses applications nous a permis de reconsidérer les composants optiques de notre configuration. Cela a conduit à l'adoption d'objectifs et de systèmes d'imagerie plus économiques, rendant la technologie plus accessible et réduisant les coûts globaux.

La validité de notre approche d'imagerie accélérée a été évaluée de manière approfondie en comparant les images P-SHG générées en utilisant notre méthode avec celles produites en utilisant des techniques conventionnelles et chronophages. Ces comparaisons ont confirmé que notre processus plus rapide produisait constamment des résultats similaires aux caractéristiques originales de l'échantillon (voir Figure 6 de l'article 4).

En résumé, notre recherche sur l'imagerie P-SHG marque une avancée notable dans le domaine, non seulement en termes d'efficacité temporelle, mais aussi en réduisant les risques d'exposition de l'échantillon et en abaissant les barrières économiques. Ce progrès ouvre de nouvelles possibilités pour l'utilisation généralisée de l'imagerie P-SHG dans diverses applications scientifiques et de recherche, favorisant l'innovation et la découverte.

Cette approche novatrice utilisant les GANs pour l'imagerie P-SHG représente une avancée significative dans l'amélioration de l'efficacité et de l'accessibilité de la microscopie SHG, avec des implications importantes pour la recherche biomédicale et les applications cliniques.

Conclusion

La série d'études présentée englobe une gamme d'approches et de méthodologies innovantes dans le domaine de la microscopie SHG et de ses applications, chacune abordant des défis uniques et faisant avancer notre compréhension et nos capacités en imagerie biologique.

Dans le Projet 1, une revue complète de la microscopie SHG, en particulier dans les études neuronales, a été établie comme une ressource vitale pour les chercheurs dans le domaine. En consolidant et contextualisant une richesse de recherches, cette revue a non seulement souligné les avancées historiques et théoriques en microscopie SHG, mais a également fourni un guide fondamental pour les recherches futures, particulièrement bénéfique pour ceux qui sont nouveaux dans le domaine.

L'exploration dans le Projet 2 de l'orientation des fibres de collagène et des défis des petits ensembles de données dans les glandes mammaires a démontré le potentiel d'intégration de techniques d'imagerie avancées, telles que la microscopie SHG et P-SHG automatisées, avec des méthodes d'apprentissage profond. Cette approche a montré des promesses pour surmonter les limitations des techniques d'imagerie traditionnelles, permettant une analyse plus détaillée et efficace des changements structurels dans les microenvironnements tumoraux.

Dans le Projet 3, l'application des techniques d'apprentissage profond pour le débruitage d'images SHG à faible SNR représente une avancée significative dans la restauration d'image en microscopie. L'utilisation des techniques CARE 2D et N2V 2D a ouvert de nouvelles possibilités pour améliorer la qualité d'image dans des scénarios difficiles, tels que l'imagerie à faible puissance laser des tissus musculaires de poissons zèbres et des glandes mammaires de souris porteuses de tumeurs. L'application réussie de ces techniques peut révolutionner l'approche de restauration d'image en imagerie biologique haute résolution.

Enfin, l'accent mis dans le Projet 4 sur l'accélération de l'imagerie P-SHG en utilisant le modèle ESRGAN pour l'agrandissement d'image aborde un besoin critique en imagerie biologique : l'équilibre entre la vitesse et la qualité. En démontrant qu'il est possible d'acquérir rapidement des images de basse qualité puis de les améliorer grâce à des techniques d'agrandissement avancées, cette étude ouvre la voie à des processus d'imagerie plus efficaces, en particulier dans les études sur de grands échantillons ou les processus biologiques sensibles au temps.

Collectivement, ces études mettent en évidence la nature dynamique et évolutive de la microscopie SHG et de ses applications. Elles soulignent l'importance des approches interdisciplinaires qui combinent des techniques d'imagerie avancées avec des méthodes computationnelles pour relever les défis complexes rencontrés en imagerie biologique. Les aperçus et méthodologies développés à travers ces projets contribuent non seulement au domaine de la microscopie SHG, mais ont également des implications plus larges pour l'étude des structures et processus biologiques. Alors que nous continuons à repousser les limites de ce qui est possible en microscopie et en analyse d'image, ces études serviront sans aucun doute de références fondamentales pour guider les recherches futures et l'innovation dans ce domaine vital.

En conclusion, cette thèse démontre le potentiel transformateur de l'intégration de la microscopie SHG avec des techniques avancées d'IA. Les résultats mettent en évidence des améliorations significatives dans la qualité d'imagerie et les capacités analytiques, suggérant un avenir où ces technologies seront intégrales à la recherche biomédicale et aux applications cliniques. Les travaux futurs devraient se concentrer sur le raffinement de ces méthodes pour une accessibilité plus large et une précision diagnostique améliorée. Cela pourrait inclure le développement de modèles d'apprentissage automatique pour des échantillons biologiques plus diversifiés, l'exploration de leur intégration dans les flux de travail cliniques, et le développement de systèmes d'imagerie SHG rentables et conviviaux pour améliorer l'accessibilité dans divers contextes de soins de santé.

TABLE OF CONTENTS

LIST OF FIGURES

LIST OF TABLES

LIST OF EQUATIONS

LIST OF ABBREVIATIONS

AI	Artificial intelligence
AUC	Area under the curve
CARS	Coherent anti-Stokes Raman spectroscopy
CCD	Charged coupled device
CNN	Convolutional neural network
CW	Continuous wave
CW-SSIM	Complex wavelet structural similarity index
DC	Dichroic mirror
DCDC	Double core, double-clad
DFG	Difference frequency generation
DIC	Differential interference contrast
DL	Deep learning
DLAM	Deep learning autofluorescence harmonic microscopy
ECM	Extracellular matrix
EM	Electron microscopy
EOM	Electro optic modulator
FR-IQA	Full reference image quality assessment
FT	Fourier transform
GAN	Generative adversial network
GDP	Guanosine diphosphate
GT	Ground truth
GTP	Guanosine triphosphate
HWP	Half-wave plate
IQA	Image quality assessment
KDP	Monopotassium phosphate
LD	Linear dichroism
MAP	Microtubule-associated proteins
MLP	multilayer perceptron
MSE	Mean squared error
MS-SSIM	Multi-scale structural similarity index

MT	Microtubules
NA	Numerical aperture
NIQE	Natural image quality evaluator
OCT	Optical coherence tomography
OR	Optical rectification
PALM	Photo-activated localization microscopy
PIQE	Perception based image quality evaluator
PMT	Photomultiplier tube
PSA	Polarization state analyzer
PSG	Polarization state generator
PSI	Phase-shifting interferometry
PSNR	Peak Signal-to-Noise Ratio
QWP	Quarter-wave plate
RNN	Recursive neural network
SFG	Sum frequency generation
SHG	Second harmonic generation
SNR	Signal to noise ratio
SSIM	Structural Similarity Index
STED	Stimulated emission depletion
STORM	Stochastic optical reconstruction microscopy
TACS	Tumor associated collagen signature
TL	Transfer learning
TPEF	Two-photon excitation microscopy
WGAN	Wasserstein generative adversial network

1 INTRODUCTION AND LITERATURE REVIEW

The synergy between microscopy, biophotonics, and the study of biological samples through light interaction is rooted in a historical journey dating back to Janssen's microscope invention in 1585 [1]. This remarkable journey has evolved into a vital photonics subbranch known as biophotonics. Over the centuries, scientific pioneers such as Robert Hooke and Antoine von Leeuwenhoek made significant strides in the 17th century using microscopes to examine various biological samples [1]. Since then, microscopy and biophotonics have progressed through numerous iterations and advancements. Notable improvements include refining optical elements, advancements in light sources, innovations in detection methods, and enhancements in sample-preparation techniques [2]. In the upcoming sections, we will explore different nonlinear microscopy iterations and their roles in studying biological samples. Notably, the integration of artificial intelligence (AI) into SHG microscopy has significantly expanded its applications and improved its analytical capabilities. Recent advances have focused on overcoming limitations, such as noise reduction and image enhancement. This has paved the way for broader applications in biomedical research, offering new opportunities for exploring complex biological phenomena.

This thesis addresses a critical challenge in biomedical imaging: overcoming the limitations of SHG microscopy by integrating AI techniques. This research aims to enhance image quality, enable automated analysis, and expand the clinical applications of SHG microscopy. By exploring novel approaches to image processing, classification, and acquisition, this study sought to push the boundaries of what is possible with SHG microscopy and pave the way for its broader adoption in research and clinical settings. The document is structured around four interrelated articles, each addressing specific aspects of these objectives. Following this introduction, we present a comprehensive background of SHG microscopy and AI in imaging, followed by detailed summaries and analyses of the four core articles. The thesis concludes with a synthesis of the overall findings and their implications for the field, demonstrating how the integration of AI and SHG microscopy can revolutionize biomedical imaging.

1.1 History of optical microscopy

The importance of microscopy cannot be overstated in various fields, including biology, health, microfabrication, nanofabrication, and materials science. The nuances of microscopy, including its strengths and limitations, are delicately balanced by factors such as contrast mechanisms, spatial resolution, field of view, acquisition speed, penetration depth, and applicability in vivo [3]. At the core of microscopy techniques is the pivotal concept of contrast mechanisms. These mechanisms pivot on how materials respond when probed by light, electron beams, or fine points, thereby revealing variations in structure and composition [3]. Diverse microscopy methods employ a spectrum of contrast mechanisms primarily favored in biological studies, including light, electron absorption, and fluorescence. Each mechanism provides distinct insights into material structure and properties [3]. Spatial resolution, a defining factor, dictates the ability of a technique to discern intricate details. Optical microscopy typically achieves a resolution of 1 micron, yet some methods surpass the diffraction limit, pushing the resolution below 100 nm [3].

In the realm of microscopy, the field of view and image acquisition speed have immense significance. A generous field of view aids in locating intriguing details, whereas swift image acquisition is vital, especially when investigating dynamic structures in living organisms [2]. Despite the unique challenges in capturing rapid movements, the ability to image living organisms in real-time is a hallmark of optical microscopy.

In 1846, Zeiss unveiled the world's first commercial optical microscope in Jena, Germany, starting a fascinating journey [4]. This method meticulously aligns an objective and an eyepiece with the sample to observe an enlarged image directly. Illuminating the sample from behind allowed the light to pass through before collection by the objective. The absorption and diffusion of light within the sample form the basis for image contrast, with a theoretical resolution limit of approximately 200 nm [3]. Optical microscopy was confined to thin tissue slices because thicker samples scattered light. In 1903, Köhler introduced a dark-field microscope to address some of the scattering problems encountered by the original microscope [5]. In dark-field microscopy, the sample is illuminated to prevent direct capture of light by the lens, gathering diffused or reflected light from specific structures within the sample and enhancing the contrast [5]. Subsequent innovations included the phase-contrast microscope unveiled by Zernike in 1935 [6] and the differential interference contrast (DIC) microscope introduced by Nomarski in 1952 [7]. These methods rely on the interaction between index variations in the material and the phase shift of the light wavefronts, quantifiable through an interference phenomenon. While these innovations aimed to improve the contrast and resolution in bright-field microscopy, they have limitations, including low-intensity images and poor effective resolution. The overarching challenge was adapting microscopy for less-controlled in vitro samples while enhancing light penetration without introducing degradation [8].

The turning point arrived in 1955 when Minsky introduced the confocal scanning microscope [9]. His invention remained unappreciated until the invention of lasers in 1960, which provided a stable and bright light source for scanning microscopy. The first laser scanning microscope was debuted in the late 1960s using a He-Ne laser [10]. This innovation marked a shift to point-by-point illumination and efficient light filtering, eventually coining the term "confocal microscope" in 1977 [11]. The primary advantage of a confocal microscope is its exceptional axial resolution, which is achieved by selectively collecting the signal from a specific plane within the imaged material [12]. Confocal microscopy is frequently paired with fluorescence microscopy, particularly in biological imaging. This technique involves attaching fluorophores to specific structures for differentiation using sequential filters. These fluorophores are optimized for efficient light conversion, reduced required light intensity, and minimized thermal damage to biological tissues [13]. However, fluorescence microscopy grapples with photobleaching, where the efficiency of fluorophores diminishes with prolonged exposure to light and phototoxicity owing to direct interactions between light and cells [14].

Several techniques have emerged to overcome the optical resolution limit imposed by light diffraction. An overview of these methods is provided in Figure 1-1. STED microscopy was pioneered by Hell et al. in 1994 and achieved a spatial resolution below 100 nm in fluorescence microscopy [15]. STED employs an excitation beam for fluorescence, and a secondary beam shifts towards the red spectrum, using a donut-shaped irradiance profile to de-energize fluorescent molecules [15,16]. Stochastic techniques, including Photoactivation Localization Microscopy (PALM) [17] and Stochastic Optical Reconstruction Microscopy (STORM) [18], can achieve similar spatial resolutions. These super-resolution methods are primarily applied to biological samples, necessitating staining, dyes, or controlled concentrations of fluorescent proteins for sub-diffraction image reconstruction. While image acquisition relies on a diffraction-limited optical microscope in the case of STED or sophisticated image reconstruction techniques in PALM/STORM, these innovations pave the way for exploring previously inaccessible domains, notably the intricate interior of cells, including compact nuclei [8].

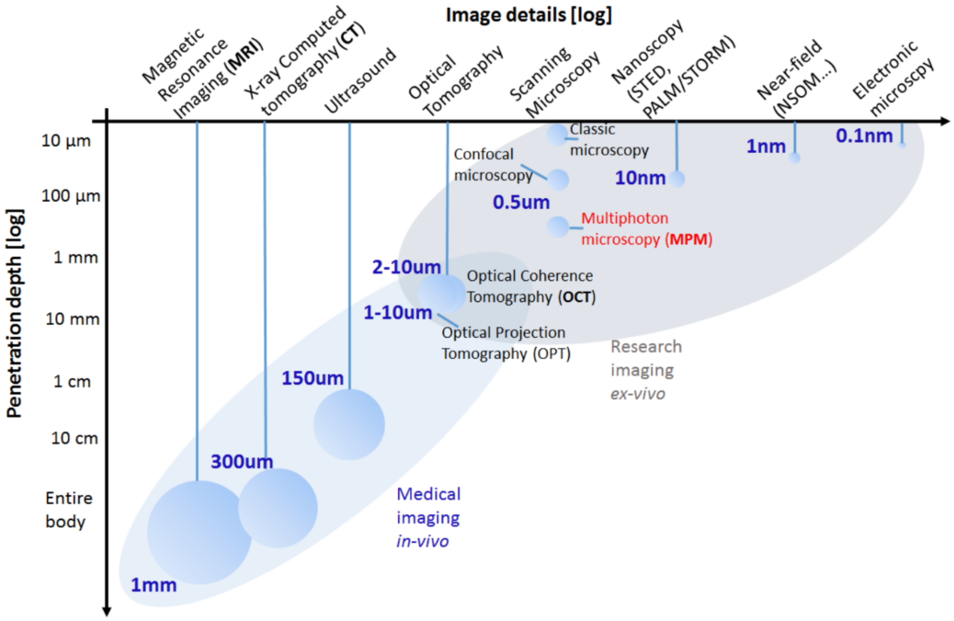

Figure 1-1: Resolution and penetration depth of several medical imaging techniques. Extracted from [8].

The 1990s are considered a key milestone for nonlinear microscopy, which is discussed in the next section on the history of second harmonic generation microscopy and its physical characteristics.

1.2 Nonlinear optics and process

The following sections detail nonlinear processes and microscopy, starting with the history and physical principles.

1.2.1 Nonlinear microscopy history

The theoretical prediction of two-photon absorption by Goeppert-Mayer in 1931 set the stage for significant developments [19]. Three decades later, in 1960, Theodore Maiman's creation of a ruby laser [20], based on the foundational work of Schawlow and Townes in 1958 [21], marked a turning point for microscopy, specifically nonlinear microscopy. Almost immediately after these breakthroughs, various nonlinear optical techniques began to emerge. In 1961, Franken et al. observed the frequency doubling of a ruby laser in a quartz crystal, marking the birth of second harmonic generation (SHG) microscopy [22]. The following year, Bloembergen and Pershan clarified the SHG equations and explained the fundamental principles governing light-matter nonlinear interactions with a thorough examination of Maxwell's equations [23].

In 1974, Hellwarth and Christensen combined SHG with optical microscopy by focusing a laser on potassium deuterium hydrogen phosphate (KDP) crystals [24]. However, this method relied on robust SHG converters because the entire field was illuminated with a continuous-wave (CW) laser. In 1977, Sheppard et al. imaged quartz using a scanning SHG microscope that detected a nonlinear optical signal [25]. Simultaneously, through electron microscopy (EM), Parry and Craig revealed that collagen fibrils in tissues such as tendons possess mixed polarity, with neighboring fibrils pointing in opposite directions [26]. This discovery was later confirmed using a combination of atomic and piezoelectric force microscopy [27,28]. In 1978, Roth and Freund conducted comparative measurements between the SHG signal of a reference quartz sample and that of a rat-tail tendon. They discovered that the SHG signal was significantly lower (3-4 orders of magnitude) in the biological sample than in the reference material, emphasizing the potential of using SHG measurements in vivo [29]. Finally, in 1986, Freund and Deutsch became pioneers in performing SHG microscopy of biological samples, demonstrating that the macroscopic polar structure in tendons arose from a network of fine structures, specifically collagen fibrils, within the entire tissue volume [30]. This groundbreaking work illustrated the viability of using SHG microscopy for biomedical imaging. In 1990, Denk et al. introduced two-photon excitation fluorescence (TPEF) laser scanning microscopy utilizing pulsed lasers and a modified confocal microscope [31]. Denk initially employed a high-repetition-rate dye laser emitting femtosecond pulses for the experiment. However, the 1980s and the 1990s saw the emergence of Titanium Sapphire lasers, which provided ideal femtosecond light sources for nonlinear optical microscopy.

Following the success of TPEF, three-photon excitation microscopy was first demonstrated in 1996 [32]. Although SHG predates TPEF microscopy, it experienced a period of relative obscurity before being reintroduced in 1998 [33,34] and subsequently integrated with TPEF in the early 2000s in numerous studies [2,35–37]. With advancements in commercially available mode-locked lasers and user-friendly multiphoton microscopes [38], SHG has emerged as a powerful tool for high spatial resolution optical imaging, contributing significantly to multimodal imaging. In recent years, these nonlinear optical microscopy methods have been substantially enhanced and adapted, making them commonplace in laboratory settings. The next significant advancement in this field will involve harnessing these microscopy techniques for diagnostics, paving the way for their clinical utilization and integration into the medical field.

1.3 Nonlinear processes

This section discusses the physical processes and properties of nonlinear optics and SHG in further detail. Most concepts covered in this section are based on Boyd's Nonlinear Optics book [39], which is strongly recommended for further information on this topic.

1.3.1 Second harmonic generation theory and principles

To understand SHG, we must first examine how electron behaves when excited by an incoming photon. The electron travel depends on the strength of the excitation photon and can be described in two cases (illustrated in Figure 1-2): if the excitation energy is low, the electron's trajectory can be approximated as a parabolic path, rendering the process linear. This linear excursion is often called elastic, which is analogous to mechanical systems [39]. However, in a strong exciting field, a more significant part of the electron potential is traversed, leading to a nonlinear or inelastic oscillation of the electron or electron assembly. An illustrative example of this phenomenon is SHG, which is a component of the Fourier decomposition of the anharmonic response of an electron excited by a powerful electromagnetic field. This inelastic oscillation of electrons results in partial "transmission" of the excitation field. This process causes a change in the fundamental frequency of the electron motion by inducing one of its harmonics. This phenomenon can be attributed to the electric field oscillating at a high frequency when interacting with a molecular structure, repeatedly inducing a molecular dipole [39].

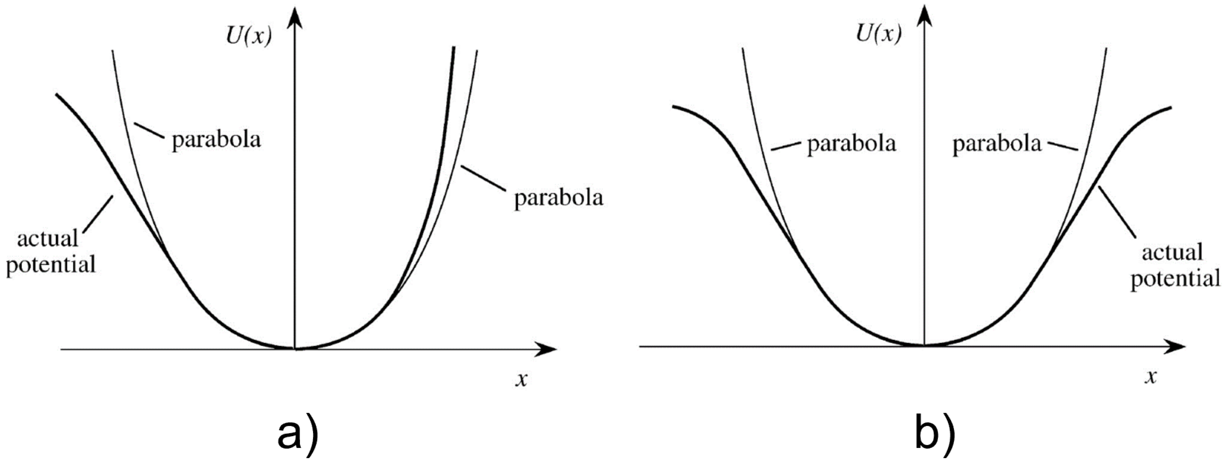

Figure 1-2: Potential energy function $U(x)$ vs electron position x for (a) non-centrosymmetric and (b) centrosymmetric media. Extracted from [39].

For such a conversion, the medium must allow vibrations at these specific frequencies. Owing to symmetry considerations, any medium with a center of symmetry will eliminate all the Nth harmonics, where N is an even number. This property is a crucial factor for understanding and predicting the behavior of nonlinear optical processes. For further clarification, we can mathematically examine the molecular response to an external electric field [39]:

$$P = P^{(0)} + \alpha E + \beta EE + \gamma \mathrm{EEE} + \cdots \qquad 1.1$$

Here, E represents the incident electric field, and α, β, and γ represent the first-, second-, and third-order hyperpolarizabilities, respectively. The first term, $P^{(0)}$, represents the permanent dipole of the molecule. The second term corresponds to the linear response, and the third term accounts for second-order nonlinear interactions such as sum and difference frequency generation [39]. The fourth term describes third-order nonlinear effects, which encompass phenomena such as two-photon absorption [40], third harmonic generation [41], Kerr effect [42], self-phase modulation [43], cross-phase modulation [44], and stimulated Raman scattering [45]. Molecules capable of generating SHG are distinguished by their high hyperpolarizability β, which is intricately linked to their structural symmetry [46].

On a macroscopic scale, SHG is characterized by the nonlinear susceptibility, $\chi^{(2)}$, which arises from the coherent summation of the individual hyperpolarizabilities of harmonophores within a given volume. The connection between the molecular and macromolecular nonlinear responses can be defined as follows [47,48]:

$$\chi^{(2)} = N_s < \beta > \qquad 1.2$$

Here, N_s represents the density of molecule S, and $< \beta >$ represents the average orientation of the first hyperpolarizability [39]. Various processes can be described to elucidate the interactions between two electromagnetic fields of frequencies ω_1 and ω_2 within a medium that exhibits a non-zero value $\chi^{(2)}$:

Second Harmonic Generation 1 (SHG 1):

$$P(\omega_1 + \omega_1) \propto \chi^{(2)} E_1^2 \qquad 1.3$$

Second Harmonic Generation 2 (SHG 2):

$$P(\omega_2 + \omega_2) \propto \chi^{(2)} E_2^2 \qquad 1.4$$

Sum Frequency Generation (SFG):

$$P(\omega_1 + \omega_2) \propto 2\chi^{(2)} E_1 \ E_2 \tag{1.5}$$

SHG is a unique case of SFG in which the two frequencies are the same.

Difference Frequency Generation (DFG):

$$P(\omega_1 - \omega_2) \propto 2\chi^{(2)} E_1 \ E_2^* \quad \text{or } P(\omega_2 - \omega_1) \propto 2\chi^{(2)} E_2 \ E_1^* \tag{1.6}$$

Optical Rectification (OR):

$$P(\omega_1 - \omega_1 = 0 \ \& \ \ \omega_2 - \omega_2 = 0) \propto 2\chi^{(2)}(E_1 \ E_1^* + E_2 \ E_2^*) \tag{1.7}$$

OR is a unique case of DFG, in which the two frequencies are the same, resulting in static polarization [39].

The energy level diagrams for the SHG, a degenerate case of SFG, and DFG are shown in Figure 1-3.

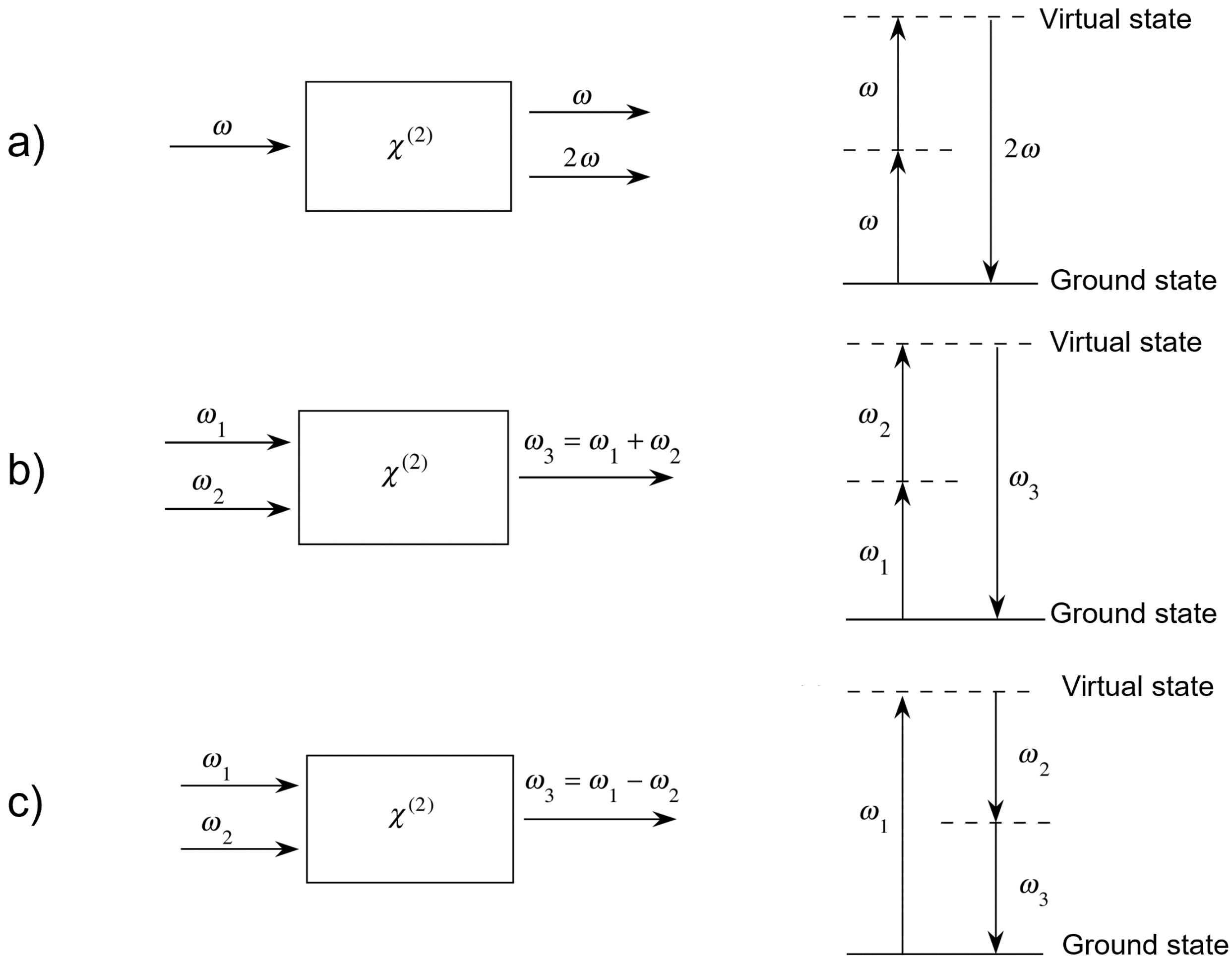

Figure 1-3: Geometry of interaction and energy level interaction for a) SHG, b) SFG (degenerate case) and c) DFG. Extracted from [39].

1.3.2 Hyperpolarizability and second-order nonlinear susceptibility

The orientation of the dipoles in a material can vary from being entirely random, as in amorphous materials, to being highly organized, as in crystalline materials. Amorphous centrosymmetric materials have a $\chi^{(2)}$ value of zero because on average, their dipoles do not prefer any orientation. On the other hand, crystalline materials can have a non-zero $\chi^{(2)}$, but only when their dipoles align in a specific preferred direction. However, it is essential to note that some crystalline materials might still have a $\chi^{(2)}$ value of zero if their dipoles point in opposite directions, despite being organized. A material with a non-zero $\chi^{(2)}$ is referred to as non-centrosymmetric (meaning it lacks an inversion center), whereas a material with zero $\chi^{(2)}$ is called centrosymmetric (with an inversion center). Figure 1-4 clearly illustrates the difference between centrosymmetric and non-centrosymmetric materials.

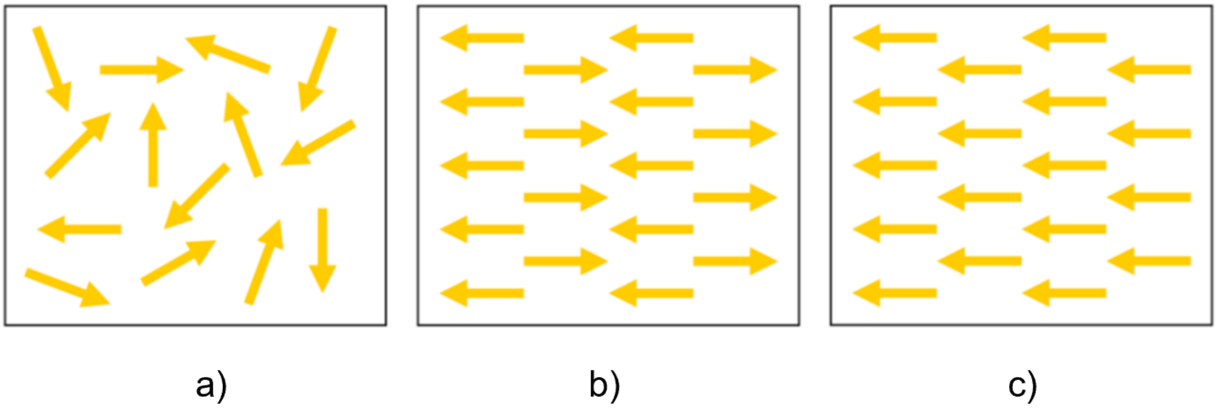

Figure 1-4: Dipole orientation in different material: a) amorphous centrosymmetric, b) crystalline centrosymmetric, and c) non-centrosymmetric. Only a non-centrosymmetric material has a non-zero nonlinear susceptibility. Extracted from [49].

SHG can only occur in non-centrosymmetric materials because they possess a non-zero $\chi^{(2)}$. When an electromagnetic wave passes through a material, its dielectric polarization signifies the oscillation of dipoles within the material. When the wave electric field is strong, the nonlinear terms in the dielectric polarization become significant [39]. These terms cause the dielectric polarization to oscillate at new frequencies that differ from the original electromagnetic wave. Consequently, there are dipoles in the material oscillating at these new frequencies. As oscillating dipoles emit radiation, electromagnetic waves oscillating at these new frequencies are generated and observed outside the material. The harmonic generation process is coherent. The oscillation of the dipole moments in the material instantaneously follows the electromagnetic wave. As a result, a phase relationship exists between the generated electromagnetic wave and the original wave. This phase relationship also explains why centrosymmetric materials do not produce second harmonics. There is destructive interference between the signals generated by adjacent dipoles with opposing dipole moments. Even in non-centrosymmetric materials, the coherent nature of SHG and this phase relationship can lead to destructive interference effects that reduce the efficiency of converting the original wave into SHG [39].

Another crucial aspect to consider in SHG is the tensor nature of $\chi^{(2)}$, which adds complexity to this phenomenon. The $\chi^{(2)}$ tensor is of the third rank and has twenty-seven elements ($\chi^{(2)}_{ijk}$). In most cases, owing to material symmetries, several tensor elements are either negligible or zero and only a few elements are significant. In such cases, the formula can be significantly simplified by considering only the contributions of the significant elements of the $\chi^{(2)}$ tensor. For general

SHG, or when the Kleinman symmetry condition is satisfied, the $\chi^{(2)}$ tensor can be expressed using contracted notation [39]:

$$d_{il} = \begin{bmatrix} d_{11} & d_{12} & d_{13} & d_{14} & d_{15} & d_{16} \\ d_{21} & d_{22} & d_{23} & d_{24} & d_{25} & d_{26} \\ d_{31} & d_{32} & d_{33} & d_{34} & d_{35} & d_{36} \end{bmatrix} = \frac{1}{2}\chi_{\mathrm{ijk}}^{(2)} \tag{1.8}$$

Thus:

$$\begin{bmatrix} P_x\ (2\omega) \\ P_y\ (2\omega) \\ P_z\ (2\omega) \end{bmatrix} \propto \begin{bmatrix} d_{11} & d_{12} & d_{13} & d_{14} & d_{15} & d_{16} \\ d_{21} & d_{22} & d_{23} & d_{24} & d_{25} & d_{26} \\ d_{31} & d_{32} & d_{33} & d_{34} & d_{35} & d_{36} \end{bmatrix} \begin{bmatrix} E_x^2(\omega) \\ E_y^2(\omega) \\ E_z^2(\omega) \\ 2E_y(\omega)E_z(\omega) \\ 2E_x(\omega)E_z(\omega) \\ 2E_x(\omega)E_y(\omega) \end{bmatrix} \tag{1.9}$$

1.3.3 Coherence length and phase matching

Let us examine the wave equation with nonlinear polarization [39]:

$$\nabla^2\mathbf{E} - \frac{1}{\epsilon_0 c^2}\frac{\partial^2\mathbf{D}^{(1)}}{\partial t^2} = \frac{1}{\epsilon_0 c^2}\frac{\partial^2\mathbf{P}^{NL}}{\partial t^2} \tag{1.10}$$

The wave equation must hold for all frequency components of the electric field, including those at 2ω. To define the outgoing field, we express this as [39]:

$$E(2\omega) = A_3(z)\mathrm{e}^{\mathrm{j}(k_3 z - 2\omega t)} \tag{1.11}$$

where $k_3 = \frac{n_3 2\omega}{c}$ and $n_3^2 = \epsilon^{(1)}(2\omega)$, and n_3 represents the refractive index at the frequency 2ω.

By substituting these earlier definitions into the one-dimensional wave equation, it transforms into [39]:

$$\frac{\mathrm{d}^2 A_3}{\mathrm{d}z^2} + 2\mathrm{j}k_3\frac{\mathrm{d}A_3}{\mathrm{d}z} = -\frac{4d_{\mathrm{eff}}\,(2\omega)^2}{c^2}A_1A_2\mathrm{e}^{\mathrm{j}(2k-k_3)z} \tag{1.12}$$

The slowly varying envelope approximation was employed, allowing us to neglect the first term in this equation compared to the second term. Consequently, we have [39]:

$$\frac{\mathrm{d}A_3}{\mathrm{d}z} = \frac{2\mathrm{j}d_{\mathrm{eff}}\,(2\omega)^2}{k_3 c^2}A_1A_2\mathrm{e}^{\mathrm{j}\Delta kz} \tag{1.13}$$

Where $\Delta \mathrm{k} = 2\mathrm{k} - \mathbf{k}_3$, denotes the phase-matching vector. Assuming the amplitudes of the pump fields, A_1 and A_2, remain constant, a straightforward integration over the medium's length from zero to L helps us derive a solution to this equation and, consequently, calculate the generated sum-frequency intensity (I_3) [39]:

$$I_3 = 2n_3\epsilon_0 c|A_3|^2 = \frac{8n_3\epsilon_0 d_{\mathrm{eff}}^2(2\omega)^4|A_1|^2|A_2|^2}{k_3^2c^3}\left|\frac{\mathrm{e}^{j\Delta kL}-1}{\Delta k}\right|^2, \qquad 1.14$$

$$I_3 \propto |A_1|^2|A_2|^2\mathrm{sinc}^2\,(\Delta kL/2).$$

It is important to note that in the context of SHG, typically, only one laser is used: thus, A_1 = A_2. Consequently, the intensity of the second harmonic generated depends on the square of the fundamental laser intensity. When dealing with a wave mixing process in a nonlinear medium of length L, the intensity of the output wave also depends on the product ΔkL. Figure 1-5 illustrates the behavior of I_3 relative to this factor [39].

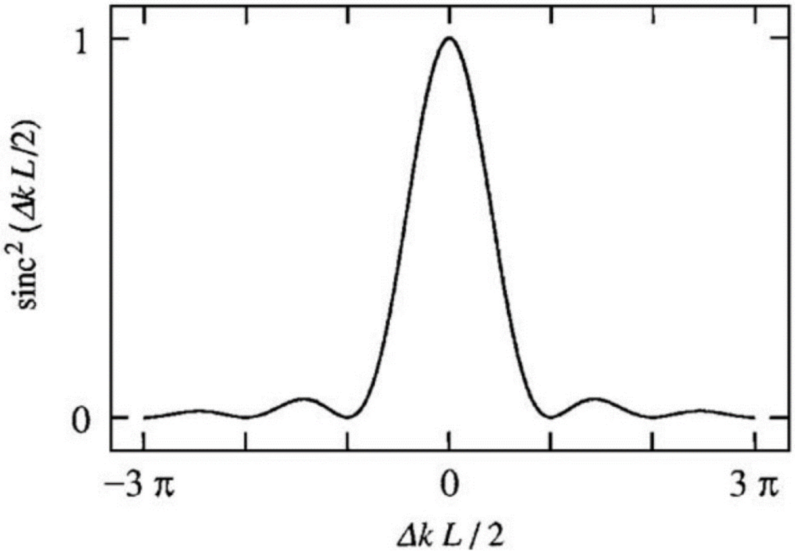

Figure 1-5: Effect of phase matching on the efficiency of SHG. Extracted from [39].

This phenomenon arises because the generated intensity results from the sum of the intensities produced by all the dipoles encountered along the length of the medium. If the light from the first excited dipole has traversed a distance within the material that causes it to acquire a phase shift of π relative to the exciting wave, the light produced at that new location will interfere destructively with the first one, and the power returns to the ω waves. When the pump intensity is infinite, two scenarios emerge. First, if $\Delta k = 0$, the output intensity continually increases with L. Otherwise, it varies spatially in a periodic manner with coherence length $4L_{coh}$, where $L_{coh} = \pi/\Delta k$. Therefore, for a given Δk, constructive interference reaches its maximum when the medium's length equals L_{coh}, hence the term "coherence length." If the pump intensity is finite, I_3 varies spatially, regardless of Δk, and the amplitude or maximum value is dictated by equation 1.14. Consequently, achieving efficient SHG requires approaching the ideal condition of $\Delta k = 0$, which signifies perfect phase-matching. One method for phase matching involves the use of a birefringent medium [39]. Another technique for achieving phase matching is temperature control. Some crystals, such as lithium niobate, exhibit high temperature-dependent birefringence and phase-matching can be achieved by varying the temperature [39].

To summarize, for a medium to have a non-zero $\chi^{(2)}$ and facilitate SHG, it must consist of molecules with a non-zero β and be organized on a scale more prominent than the wavelength of the light to achieve phase matching [39]. Consequently, the signal obtained in SHG can provide insights into the organization and structure of imaged materials [40]. For instance, by manipulating the polarization of the incident and detected beams, it is possible to determine d_{eff} for the considered geometry and investigate the ratios between the different elements of the $\chi^{(2)}$ tensor [50]. In a medium such as biological tissue, the interaction length, which corresponds to the focal volume length in microscopy, is typically much smaller than the coherence length. This phenomenon makes the generation of second harmonic signals relatively straightforward [51]. Finally, when SHG is measured in reflection rather than transmission, the phase-matching vector must be larger as $\mathbf{k}_3$ changes sign ($\Delta \mathrm{k} = 2\mathrm{k} - \mathbf{k}_3$), leading to a shorter coherence length and different phase-matching conditions [39].

1.4 Advanced SHG microscopy methods

Advanced techniques, such as polarization-resolved SHG (P-SHG), interferometric SHG (I-SHG), and wide-field SHG, are pivotal in expanding the capabilities of bioimaging. Each technique has unique advantages. P-SHG enhances the visualization of complex structures by measuring parameters such as the alignment and anisotropy of fibrils, as observed in collagen studies [2]. I-SHG provides additional structural and orientation information at the molecular level, which is crucial for understanding biological samples, such as tissues and cells. Wide-field SHG increases the imaging throughput by illuminating the entire sample area simultaneously, balancing the energy input with the need to minimize photodamage [2].

1.4.1 Polarization resolved SHG microscopy

Polarization resolved second harmonic generation (P-SHG) combines the advantages of SHG microscopy, offering high specificity and contrast, with the sensitivity to molecular alignment provided by polarimetry [2]. Typically employed in examining collagen, this technique offers a more precise depiction of the intricate hierarchical structures within fibrils in the imaging plane. The pioneering application of P-SHG in biological samples occurred in 2002 when Stoller and colleagues conducted their initial experiments on rat-tail tendon fascia [52]. By collecting various linear polarization scans in both the axial and transverse planes, they discovered that the SHG signal strongly responded to the polarization of the incident laser light source, enabling the determination of collagen fibril orientation. When light travels through a medium, its polarization characteristics can be described using either Stokes vector formalism [53] or Jones vector formalism [54]. Jones vector formalism is applicable to fully polarized light, in which the entire state can be represented via the amplitude and phase of oscillations in two electric field vector components that lie within the plane of polarization. In contrast, Stokes vector formalism is used for partially polarized light [55].

P-SHG has become increasingly prevalent in biomedical research, providing a valuable means of analyzing protein structures. Prior to this method, scientists relied on cryo-electron microscopy [56] and X-ray crystallography [57], which are often hindered by laborious and intricate sample preparation processes. Consequently, these methods are not practical for live or dynamic samples, let alone those involving living animals [58]. Various techniques have been used to explore the structural dynamics of proteins. Nuclear magnetic resonance and Forster resonance energy transfer are among them [2]. Nuclear magnetic resonance is a powerful technique that can provide valuable information about the structure and dynamics of proteins in solution. However, this method has several limitations [58]. For example, it requires large samples and can be time-consuming and expensive. Forster resonance energy transfer involves the energy transfer between two fluorescent molecules attached to distinct parts of the protein. This can provide information about the distance and orientation between two molecules, which can be used to deduce information about the protein structure [58]. Although these techniques are valuable, they offer lower spatial resolution and reduced sensitivity than other methods [58].

P-SHG offers a simple and cost-effective solution for analyzing untouched samples. With only a few additions to a standard SHG microscope setup, P-SHG can be utilized without complex and expensive equipment [58]. The examination of collagen changes linked to aging [59], keratoconus cornea [60], and lung cancer-related alterations in collagen structure [61] are some areas in which P-SHG has proven useful.

Most of the theoretical background stated below is based on [62,63]. Let us consider the collagen fibrils as an example. The second harmonic response of the medium depends on its second-order nonlinear susceptibility tensor, $\chi^{(2)}$. The tensor indicates how the polarizability of the medium P_i changes with an electric field $E(\omega)$:

$$P_i = \chi_{ij}^{(1)} E_j + \chi_{ijk}^{(2)} E_j E_k \tag{1.15}$$

Collagen fibrils have a cylindrical shape and follow Kleinman symmetry, the tensor $\chi^{(2)}$ has only two independent components:

$$\chi_{xxx} \quad , \; \chi_{xyy} = \chi_{xzz} = \chi_{yxy} = \chi_{zxz} = \chi_{yyx} = \chi_{zzx} \tag{1.16}$$

Where x is along the fiber axis, and the second harmonic polarizability is:

$$\begin{aligned} P_x \; (2\omega) &= \chi_{xxx}^{(2)} E_x^2 + \chi_{xyy}^{(2)} E_y^2 + \chi_{xyy}^{(2)} E_z^2, \\ P_y \; (2\omega) &= 2\chi_{xyy}^{(2)} E_x E_y \\ P_z \; (2\omega) &= 2\chi_{xyy}^{(2)} E_x E_z \end{aligned} \tag{1.17}$$

A linear polarization laser travelling in the z-direction creates an angle μ with the collagen fibril in the xy plane, as shown in Figure 1-6.

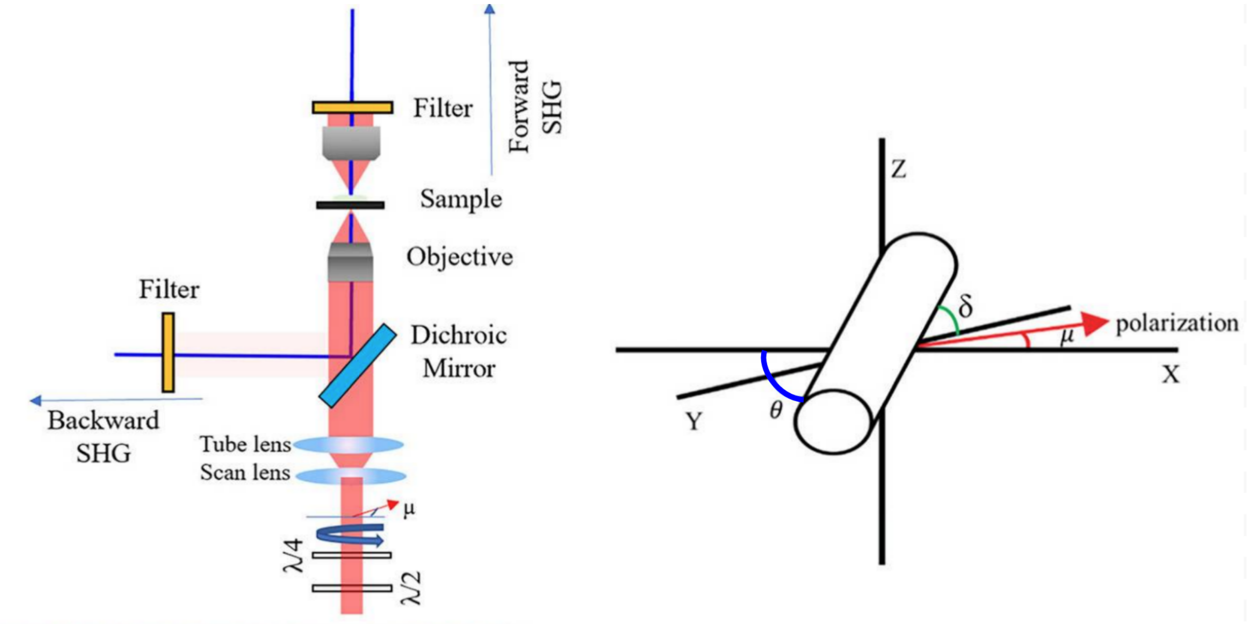

Figure 1-6: Diagram of a standard P-SHG microscope with a sample in focus. A half-wave plate and quarter-waveplate adjust the polarization of the input laser. The laser made an angle with the collagen fibril in the focus in the xy-plane. The collagen fibril has an angle θ with the laboratory axis and a tilt δ, which is assumed to be zero for simplicity in this case. Adapted from [63].

Considering that the electric field and fibril lie in the same focal plane, the electric field is given by:

$$E_x = E_0 \cos\mu \ , \qquad E_y = E_0 \sin\mu \tag{1.18}$$

Substituting 1.18 back into 1.17, considering the angle between the collagen fiber and the laboratory axis, and factoring out the anisotropy parameter $\rho = \frac{\chi^{(2)}_{xxx}}{\chi^{(2)}_{xyy}}$, we have:

$$\begin{aligned} P_x\ (2\omega) &\propto \cos^2(\mu-\theta) + \sin^2(\mu-\theta) \\ P_y\ (2\omega) &\propto 2\cos(\mu-\theta)\sin(\mu-\theta) \end{aligned} \tag{1.19}$$

Moreover, the total SHG intensity becomes:

$$I_{SHG}(\mu) = K[A\cos(4\mu-4\theta) + B\cos(2\mu-2\theta) + 1] \tag{1.20}$$

A and B are related to susceptibility components, K is the average number of photons detected, and θ is the angle of the collagen fiber in the focal plane. By applying a fit or Fourier transform to 1.20, the primary orientation of the fibrils (θ) can be determined by changing the angle μ [62,63]. The utilization of 3D Fourier Transform Second Harmonic Generation (FT SHG) has provided a unique avenue for directly extracting orientation information from intensity images through the analysis of spatial patterns. This innovative approach is useful for distinguishing between isotropic and anisotropic regions within biological tissues [64]. However, it is essential to acknowledge that the efficacy of this method can be influenced by the presence of interference from SHG patterns, which occasionally obscure the actual underlying material structure. To complement FT SHG, a specialized software tool named CurveAlign [65] was developed. CurveAlign demonstrates its advantages, mainly when SHG filaments exhibit high clarity or when interference patterns do not mask the intriguing features of the physical structure of the material. Moreover, for more versatile applications in similar situations, there is a valuable ImageJ plugin called OrientationJ [66,67]. Although both methods have their merits and strengths, they cannot resolve highly complex structures.

1.4.2 Interferometric SHG microscopy

The coherent nature of SHG offers valuable insights into the samples but presents certain limitations. As described in earlier studies, the patterns observed in SHG images result from complex interferences [68,69]. These interferences can introduce significant imaging artifacts, mainly depending on the microscopic configuration [69], and potentially obscure the underlying structure, which is particularly relevant in biological specimens [69]. Within the focal volume, the interaction of dipoles with opposing or matching polarities leads to destructive or constructive interference, resulting in regions with low or high SHG signals. Therefore, SHG images often exhibit both bright and dark regions, which may not directly correspond to the actual distribution of the harmonophores. Thus, it is essential to assess local polarity within a sample to obtain precise quantitative information [69].

It is noteworthy that a polarity inversion, represented by a change in the $\chi^{(2)}$ sign induces a π phase shift in the emitted SHG signal; consequently, the signal phase retains information about the polarity within the sample, which can be mapped for each pixel in the image. This is typically achieved through interferometry, with Interferometric Second Harmonic Generation (I-SHG) initially proposed in 2004 to facilitate phase measurements in a scanning SHG microscope [70]. Subsequently, this technique was applied to examine tendons in 2013 [71] and cartilage in 2015 [72].

The I-SHG method employs direct phase measurements to probe the relative polarity of harmonophores. This technique involves the combination of two SHG signals, one from a reference nonlinear crystal positioned before the microscope (reference SHG) and the other from the sample being analyzed (sample SHG), which are then interfered with. As both SHG beams are spatially and temporally coherent, the total intensity of the detector follows the widely recognized two-wave interferometry equation [8,49]:

$$I = I_{ref} + I_s + 2\sqrt{I_{ref} I_s} \cos\left(\varphi_s - \varphi_{ref}\right) \tag{1.21}$$

Where I_s and φ_s (and I_{ref} and φ_{ref}) represent the intensity and phase of the sample (reference) SHG beam, respectively. The images obtained by I-SHG microscopy do not directly provide φ_s . In an image, each pixel has a signal that follows equation 1.21. To extract the optical phase of the imaged area, a cosine function must be interpolated at each pixel using images captured at different reference phases. To interpolate a cosine, at least three points are required. Two points are insufficient for this function, because two solutions with distinct phases can pass through them. Therefore, we require a combination of at least three images taken at different reference phases to interpolate the optical phase correctly at each pixel. A larger number of images implies a larger number of points, which allows us to perform better interpolation and improves the accuracy of the optical phase φ_s found at each pixel [8,49].

Interferograms can be captured when the phase difference between the sample and reference SHG beams is tweaked. The argument of the cosine (relative phase) and its multiplicative factor (interferometric contrast) can be extracted by analyzing the experimental curve and fitting it accordingly. This technique is commonly referred to as phase-shifting interferometry (PSI) [2]. A simple and practical method that can be applied to process images and solve this interpolation is to use pairs of I-SHG images. To eliminate the constant term, two π-phase-shifted raw images are subtracted as follows [73]:

$$\begin{aligned} I(0) - I(\pi) &= \left[I_{ref} + I_s + 2\sqrt{I_{ref} I_s}\, cos\left(\varphi_s - \varphi_{ref}\right)\right] \\ &- \left[I_{ref} + I_s + 2\sqrt{I_{ref} I_s}\, cos\left(\varphi_s - \varphi_{ref} - \pi\right)\right] \\ I(0) - I(\pi) &= \left[2\sqrt{I_{ref} I_s}\, cos\left(\varphi_s - \varphi_{ref}\right)\right] - \left[-2\sqrt{I_{ref} I_s}\, cos\left(\varphi_s - \varphi_{ref}\right)\right] \\ I(0) - I(\pi) &= 4\sqrt{I_{ref} I_s}\, cos\left(\varphi_s - \varphi_{ref}\right) \end{aligned} \tag{1.22}$$

The experimental cosine is fitted to determine the amplitude and relative phase of each pixel, which produces phase and interferometric contrast maps. This operation isolates the interferometric contrast by eliminating the term $I_{ref} + I_s$ from the image signal [8,49]. It also amplifies the interferometric contrast term by a factor of two. The new image contains only interferometric contrast, and its pixels have positive and negative counts. Thus, the image obtained after subtraction clearly shows the sign and intensity of interferometric contrast. If I_{ref} is much higher than I_s , this image processing step is beneficial because it isolates the interferometric contrast from the rest of the signal to amplify the SHG signal. A visual representation of this process is shown in Figure 1-7.

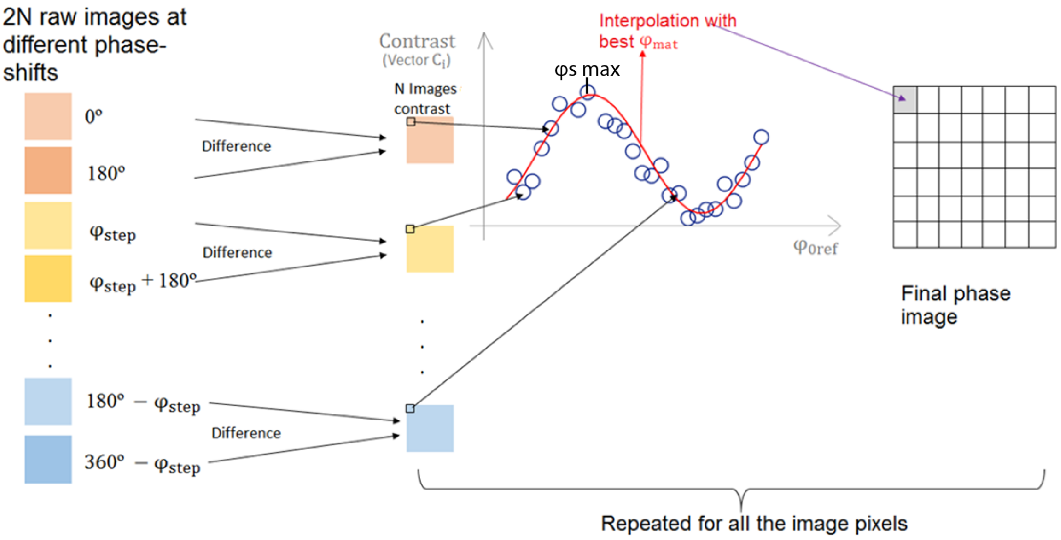

Figure 1-7: Diagram of the algorithm for finding the relative I-SHG phase. The 2N original images were paired and subtracted to obtain the N contrast images. The intensity of each pixel depends on a cosine function of the phase shift of the interferogram, which can be interpolated to obtain optical phase and interferometric contrast images. Extracted from [73].

Various methods can be employed to adjust the phase difference between the two SHG signals, including a gas cell, changes in distance, a rotating glass plate [74], and more advanced techniques, such as using an electro-optic phase modulator (EOM) [75], as depicted in

Figure 1-8.

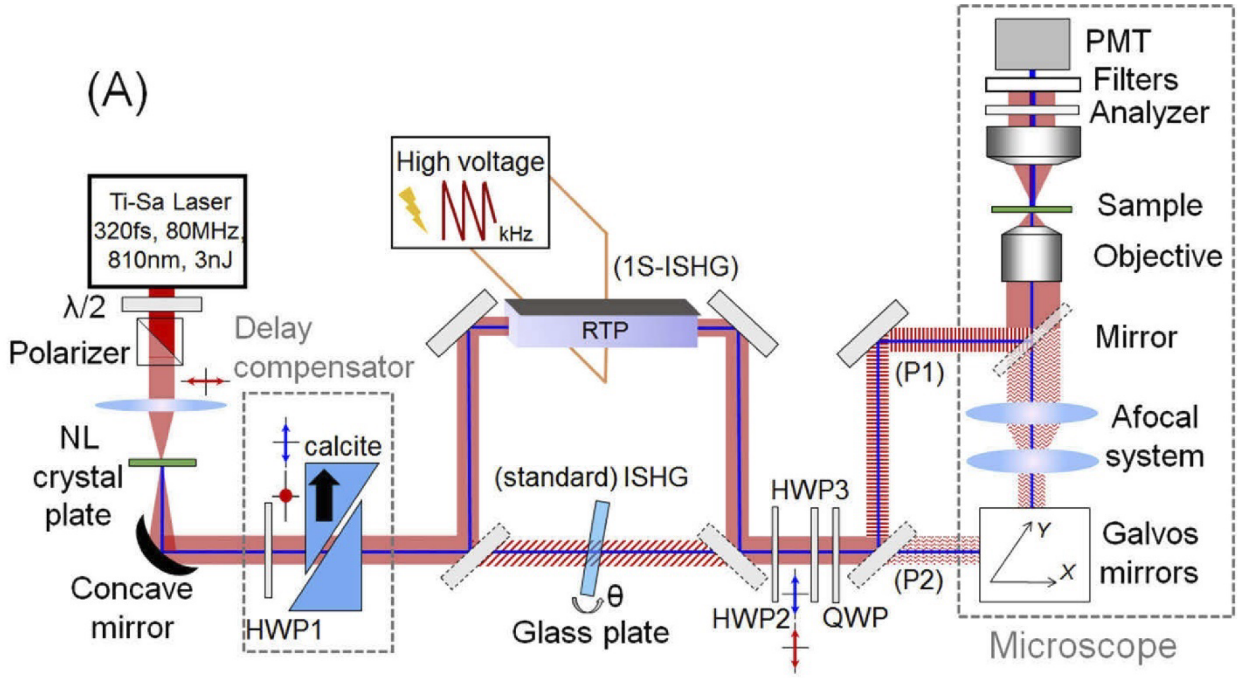

Figure 1-8: Diagram of an advanced I-SHG setup. The setup was designed modularly to choose between different pathways for image acquisition: P1 for sample scanning with a motorized stage and P2 for laser scanning using galvos. A common-path interferometer can pass through a phase scanner (EOM) or a standard phase shifter (a rotating glass plate). The phase scanner modulated the phase difference between the two beams, whereas the phase shifter adjusted the phase offset. The beams are directed to the objective (P1) by mirrors or galvos for conventional laser scanning (P2). Stage-scanning mode was used when the beams directly reached the objective. The stage moved the sample in the X- and Y-directions. The grey rectangles with solid or dashed outlines are mirrors that can be flipped. HWP1&2: half-wave plate at 810 nm, full-wave plate at 405 nm. HWP3 is a half-wave plate at 810 nm and 405 nm, and QWP is a quarter-wave plate for the same wavelength. Extracted from [75].

In conclusion, I-SHG microscopy has proven to be a powerful technique for enhancing the visualization of non-centrosymmetric structures in biological tissues. By overcoming the limitations of complex interferences in SHG images, I-SHG allows for more precise characterization of biopolymers such as collagen. As we transition from the intricacies of I-SHG, we explore the capabilities of Wide-field SHG microscopy. This technique offers the advantage of high-speed imaging, capturing entire frames simultaneously, which is particularly beneficial for dynamic studies and large-scale tissue characterization. However, it also presents its challenges, which we explore in the following section.

1.4.3 Wide-field SHG microscopy

Scanning SHG imaging is a well-established technique that has been successfully used in numerous applications. However, it faces a significant limitation in terms of imaging throughput, which refers to the number of detected photons per frame per second. Two primary strategies can be considered to address this limitation: enhancing the scanning speed and parallelizing photon emission. With some success, improvements in the scanning speed have been explored using acousto-optic deflectors [79] and resonant scanners [80]. Nonetheless, these methods are constrained by the dwell time required to accumulate sufficient photons to produce a measurable signal.

In contrast, wide-field SHG microscopy represents the ultimate parallelization approach, as it allows for the simultaneous illumination of the entire area of interest with signals detected by a pixelated detector [76,77]. Wide-field SHG imaging differs from the conventional point-by-point method by employing higher-energy pulses, enabling frame-by-frame capture over larger areas. This approach facilitates real-time video rate imaging. However, a trade-off is accompanied by wide-field imaging because it limits the penetration depth.

Lasers with a repetition rate of a few kilohertz are commonly employed in these applications [78]. In addition, the development of more sensitive CCD cameras can significantly enhance the performance of wide-field SHG. Temporal focusing is occasionally utilized to mitigate the out-of-plane illumination inherent to wide-field techniques and to improve the axial resolution as shown in Figure 1-9. This setup incorporates a "temporal lens," where the pulse frequencies are scattered at the back-focal plane of the microscope objective [79,80]. This causes each frequency to travel at a distinct angle and to recombine at the focal point. Before reaching the focal plane, spatial chirping increases the effective pulse duration beyond the Fourier-limited value, thereby reducing the peak power when the pulse is not in the focal plane. Notably, this technique has also been applied in scanning multiphoton imaging, allowing video rate acquisition despite using a point-scanning scheme [81].

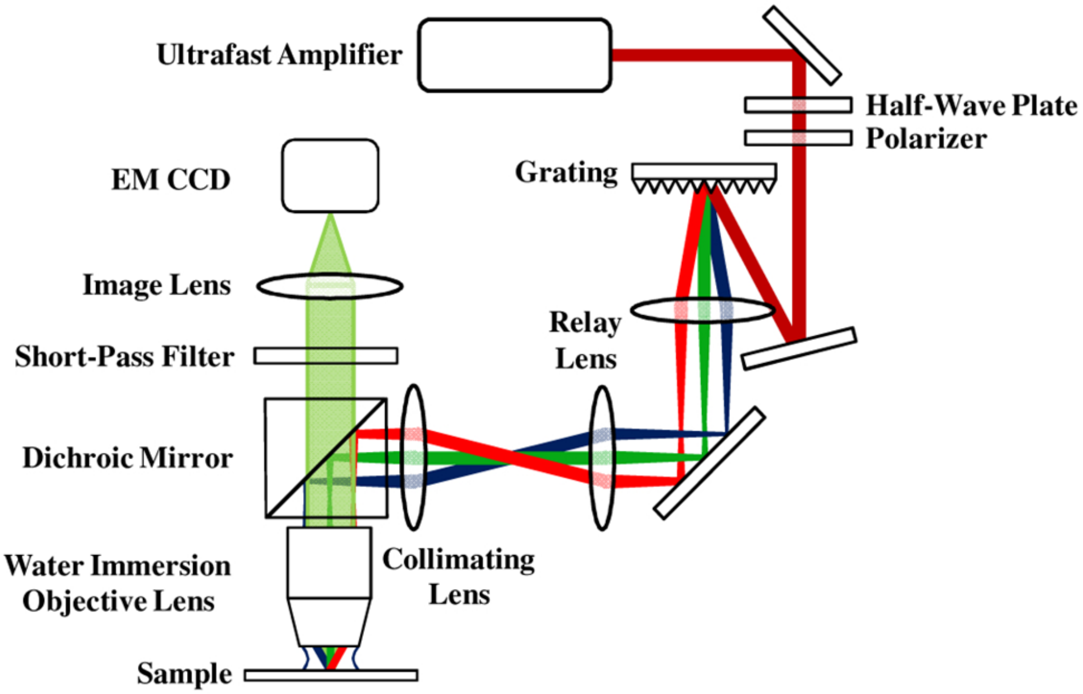

Figure 1-9: Example of a wide-field SHG imaging system with spatiotemporal focusing. A microscope system uses three main components to generate spatiotemporal focus: a high-NA objective lens, a collimating lens, and a diffraction grating [79,80]. The laser pulse hits the grating and is split into different spectral components. The collimating lens then aligns these components and travels along its optical axis. The high-NA objective lens directed them to the sample from various angles. The spectral components recombine in phase at the focal plane, forming a short pulse with high peak power. This pulse enables efficient multiphoton excitation of the sample [79,80]. Extracted from [82].

Given the vulnerability of living cells, it is crucial to exercise caution to prevent photodamage. Various studies have examined light-induced damage using wide-field SHG microscopy across different cell lines. These investigations have been instrumental in delineating a range wherein pulse energy, and consequently heat deposition, remains beneath the damage threshold for the samples [83]. In recent advancements, a high-repetition-rate (in the MHz range) wide-field SHG microscope has been developed for live imaging of contracting muscle tissue. Remarkably, this system employs laser pulses with exceptionally low pulse energy, hovering around 60 nJ per pulse [83].

1.5 SHG microscopy in biological samples

In this section, we discuss the application of SHG microscopy to different biological samples, starting with collagen. Figure 1-10 shows the essential components of SHG microscopy.

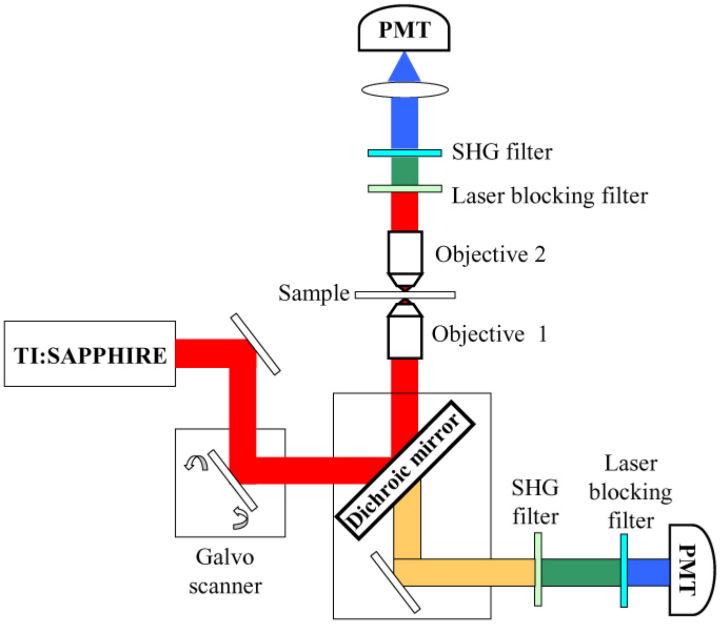

Figure 1-10: Laser scanning SHG microscopy system with forward and backward SHG detection. In this case, the laser source, a Ti: Saph laser, illuminated and scanned the sample using a galvo mirror scanner system. Subsequently, the input laser was filtered out, and the forward and backward SHG signals from the sample were collected using PMTs. Extracted from [84].

1.5.1 SHG microscopy in collagen

Collagen, a vital structural protein found in various connective tissues, is crucial, constituting approximately one-third of an organism's total protein mass [29]. Connective tissues encompassing a diverse range of biological tissues are characterized by an extracellular matrix that separates cells. This matrix consists of a ground substance, viscous fluid, and collagen and elastic fibers maintained by specialized fibroblast cells [85]. Collagen in the form of fibers imparts the necessary mechanical properties for tissue functionality. These connective tissues primarily support, connect, or segregate different tissues in an organism, with additional functions depending on the specific tissue [85]. Collagen molecules consist of three identical helical chains forming a triple helix at the molecular level. Various types of collagen, particularly types I and II, create well-organized fibrils observable by SHG microscopy [86,87].

In contrast, non-fibrillar collagen, such as type IV collagen, which forms sheets in specific tissue layers, cannot be visualized using SHG microscopy [35]. The introduction of SHG microscopy to biological tissue imaging dates back to the pioneering work of Freund et al. in 1986, specifically in rat-tail tendons [30]. These tendons exhibit a highly organized multi-scale structure primarily composed of type I collagen. More recently, SHG microscopy has been applied to visualize the fascia [68] and monitor tendon healing processes [84]. The polar structures of fibrillar collagen types I and II enable the generation of strong SHG signals. Consequently, this technique examines collagen fiber organization at the micrometre scale in connective tissues without staining, making it especially valuable for collagen-rich tissues.

The tropocollagen molecule has three identical helices, resulting in C3 rotational symmetry. Freund et al. suggested that the structural arrangement of type I collagen in tendons could be represented by either C∞ or cylindrical symmetry when averaged over dimensions approximately equal to the wavelength of light [30]. Rocha-Mendoza and his team investigated the molecular basis of non-centrosymmetry in the tropocollagen molecule, which in turn, applies to collagen [88]. The investigation conducted by the researchers focused on fibrils extracted from rat tail tendons, which are primarily composed of type I collagen. Their findings revealed that this collagen molecule's $\chi^{(2)}$ encompasses both achiral and chiral contributions, with the chiral effects attributed to the elements represented by $\chi_{\mathrm{ijk}}^{(2)}$ (where i ≠ j ≠ k) [88].

Furthermore, the study leveraged vibrational sum frequency spectroscopy (SFG-V) to demonstrate that the achiral contribution originates from the non-centrosymmetric orientation of methylene groups in the rings of Proline and Hydroxyproline amino acids, projecting outward from the tropocollagen helix [89]. Additionally, the study highlighted the presence of hydrogen bonds between the nitrogen, hydrogen segment of glycine, and carbon and oxygen segment of proline in the X position of an α chain. This interaction, which is essential for binding the three α chains, establishes a helical scale at the center of the helix, resulting in a supramolecular nonlinear chiral contribution. It is necessary to note that assuming C∞ symmetry, as is common in such studies, simplifies the collagen fibril into a cylinder, leading to omission of the chiral contribution. Typically, Kleinman symmetry is assumed in fibrillar collagen. While this assumption holds [90], some debate exists because the second harmonic wavelength in their research (400 nm) significantly differs from the first electronic transition in tendons at approximately 310 nm. Chu et al. pointed out that the resonance frequencies of muscle fibers (around 310 nm and 550 nm) closely align with the second harmonic wavelength of their laser at 615 nm [91]. Consequently, the SHG intensity changes with respect to the angle between the collagen fiber and polarization of the incident light, and this change varies depending on the detected polarization. P-SHG derives the anisotropy parameter and applies a Fourier transform [92].

The multifaceted roles of collagen in connective tissues, its structural and molecular characteristics, and its interactions with light and imaging techniques are subject to extensive research, contributing to our understanding of this fundamental protein.

1.5.2 SHG microscopy in muscle

The sarcomere is a structural unit composed of two distinct protein filaments, actin and myosin [93,94]. These filaments work together to enable muscle contractions. Muscle tissues are characterized by a high concentration of myosin, and the interpretation of SHG images of these tissues is well established. Extensive research using electron microscopy has yielded a deep understanding of the nanoscale structure of muscle tissues [95,96]. In striated muscles, myosin molecules cluster to create thick filaments, whereas actin forms thin filaments. These myosin molecules have opposing orientations within each half of the thick filament. The movement of thick filaments along thin filaments enables contraction or relaxation of the sarcomere. Muscles consist of numerous sarcomeres arranged end-to-end, which enables their contraction.

Multiple SHG microscopy studies have revealed that myosin is responsible for the signal within muscle tissue [48,86,91,97–101]. More precisely, it has been demonstrated that the signal originates from the tail of the myosin molecule with the head having minimal influence [97,102].

The contribution of myosin to SHG is significantly greater—approximately three orders of magnitude higher—than that of actin [103].The SHG signal arises from C-N peptide bonds, which are present in all proteins. However, the substantial difference in SHG intensity between the two major muscle proteins suggests key structural distinctions. For constructive interference and strong SHG generation, two levels of molecular organization are required: first, peptide bonds must be arranged in a helical structure, and second, these helices must be sufficiently aligned within the protein. While actin contains α-helices, their varied orientations result in weak SHG signals. In contrast, myosin possesses long and well-ordered α-helices within the thick filament, which amplify the SHG response [103].

Owing to the bipolar nature of thick filaments, one or two SHG signal bands are occasionally observed per sarcomere [104,105]. The signal intensity is typically lowest at the M-line, where myosin molecules switch their orientation, causing destructive interference in the SHG response [94]. This characteristic striation pattern has been exploited in SHG microscopy to non-invasively monitor sarcomere organization and structural integrity in both healthy and diseased muscle tissues [94].

Studies have demonstrated that the polarization dependence of SHG can be used to distinguish different conformational states of myosin within muscle fibers, such as relaxed, rigor, and actively contracting states [94,103] . Quantifying this polarization-dependent SHG response through the tensor component ratio (γ) enables detailed assessment of structural changes in myosin filaments during contraction. Notably, myosin filaments in rigor exhibit a higher γ ratio compared to the relaxed state, suggesting conformational differences that may involve tilting or bending of the myosin rod domain [94,103].

This ability of SHG to probe molecular interactions in myofibrils makes it a valuable tool for studying muscle physiology and pathology. SHG imaging has been successfully used to assess myofibrillar disruptions in muscular dystrophy [104] and serves as a powerful diagnostic tool for detecting sarcomere disarray in various muscle diseases.

1.5.3 SHG microscopy in neurons

The nervous system is an essential organ in living organisms and plays a crucial role in processing and transmitting information [105]. Receptive extensions of the neuron are termed dendrites, where most incoming signals are consolidated [106]. Signals are transmitted through components called axons. A neuron may possess multiple dendrites but always has only one axon. At the end of the axon, terminals and synapses exist that contain neurotransmitters essential for chemical communication between neurons.

Traditionally, the exploration of neuronal mechanisms has hinged on electrophysiology, which involves the insertion of electrodes into neurons to gauge electrical potentials and currents. This method is heralded as the standard for unraveling the intricacies of neuronal activity and has been instrumental in unearthing insights into neuron functionality. However, this approach needs to be revised. First, it is an invasive procedure and poses considerable challenges when applied to living organisms [107]. Furthermore, despite recent advancements, patch clamping is burdened by its capacity to collect data from only a restricted number of neurons, substantially inhibiting the examination of neuronal networks [108].

Optical techniques have surfaced as desirable alternatives to overcome these limitations, affording the requisite flexibility to complement the electrophysiological measurements. TPEF and SHG microscopy have been extensively applied in neuroscience and are experiencing growing favor owing to their ability to provide complementary insights into the distinctive facets of neuronal structures. Although many SHG microscopy investigations have traditionally been grounded in the use of endogenous cellular properties, the utilization of SHG dyes has also been explored in various studies [109–113].

Dombeck et al. harnessed the FM 4–64 SHG dye, showcasing a notable enhancement in the signal-to-noise ratio (SNR) compared to conventional fluorescent probes [111]. Using the same dye, Nuriya et al. achieved a pioneering milestone by revealing the ingress of action potentials into dendritic spines [112]. Subsequently, they elucidated the SHG response to an action potential and meticulously traced its propagation from the soma to axons [114]. Concurrently, Nemet et al. posited that all-trans-retinal chromophores are viable candidates for SHG imaging of neuronal membranes [110]. Jiang et al. demonstrated that the limitations in the signal-to-noise ratio, as observed in prior studies, could be circumvented through photon counting detection [115]. They subsequently revealed that the potential-sensing capacity of FM 4–64 originates from electrooptical mechanisms [113].

In neuroscience, SHG microscopy has proven to be a valuable tool for investigating microtubules (MTs), which are fascinating structural elements. MTs are vital cytoskeletal filaments with diverse functions, including preserving cellular integrity, regulating intracellular trafficking, and playing critical roles in cell division [116–119]. These tubular structures, composed of α- and β-tubulin dimers, form linear protofilament polymers when these dimers bind head-to-tail [119,120]. Importantly, MTs exhibit intrinsic polarity, with all protofilaments aligned parallel and all dimers within the filament sharing the same orientation [120].

Numerous studies have investigated how MTs generate SHG [121–123]. Recent research [122] underscores the significance of factors such as number, organization, and polarization in shaping the SHG signal produced by MTs, as illustrated in Figure 1-11 [123].

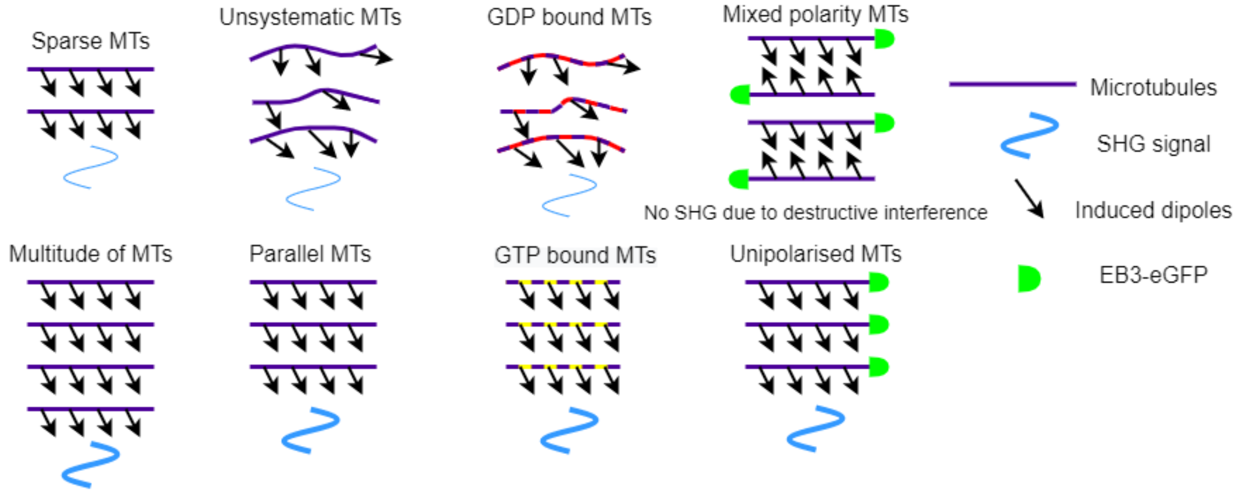

Figure 1-11: Several factors influence the SHG signal's strength in neurons. Number, parallelity, and polarity all play essential roles in the strength of the SHG signal. Moreover, guanosine triphosphate (GTP)-bound MTs have been shown to have stronger SHG than guanosine diphosphate (GDP)-bound MTs. Extracted from [123].

Although MT polarity was not the central focus of these studies, subsequent insights have emerged through the deployment of the "protein plus" method, which tags microtubule-associated proteins (MAP) with a fluorophore, allowing the tagged MAP to bind to the positive end of MTs [118,124]. Combining this approach with SHG microscopy revealed that MTs within axons exhibit well-defined and consistent polarity, with the minus end directed towards the cell body and the positive end extending towards axon terminals where neurotransmission occurs [118]. However, it is essential to note that this method relies on fluorescent markers and is invasive. Additionally, investigations into the effects of the commonly used paraformaldehyde fixation method revealed a significant loss of SHG signal, suggesting alterations in protein conformation [123]. In contrast, the polarity of MTs in dendrites still needs to be understood and structured more rigorously [116]. Although previous studies have hinted at a potential mixture of polarities within dendrites [121] and the presence of polarity domains [122], these observations remain hypothetical and require thorough characterization for verification. This raises intriguing questions about why axons exhibit uniform polarity while dendrites do not, and whether this mixed polarity holds functional relevance. SHG, particularly I-SHG, presents a promising avenue for exploring the mechanisms underlying dendrites and the significance of their polarity in neural function.

In a distinct domain of biology—embryogenesis—SHG microscopy has proven invaluable for providing time-lapse images of the various phases of cell division. Notably, SHG intensity changes have facilitated the study of mitotic spindles, which comprise highly organized MTs, in different embryo types, including Caenorhabditis elegans, zebrafish, mice, rats, and sea urchins [125]. In a groundbreaking study using I-SHG, Bancelin et al. successfully mapped the polarity of MTs within mitotic spindles during cell division in zebrafish embryos [126]. They observed changes in MT polarity at various stages of cell division, studying the dynamic alignment and polarity of MT networks. This research illustrates the power of I-SHG microscopy and its potential for investigating dendritic polarity and other neuronal processes. In a broader context, SHG and advanced SHG microscopy techniques are versatile tools with promising potential for the in-depth exploration of various facets and unknown mechanisms related to MTs and associated diseases [123,126,127].

1.6 The future of SHG imaging

Over the past two decades, SHG microscopy has firmly established itself as an indispensable tool in bioimaging and neuroimaging. Numerous studies have demonstrated its potential for investigating the non-centrosymmetric biological structures mentioned in this thesis. Innovative techniques have evolved over the years to minimize invasiveness, enhance imaging throughput through wide-field imaging, and develop specialized SHG probes [2]. These advances have continually expanded the frontiers of SHG imaging to new domains and structures. In this dynamic landscape, both conceptual and technological progress in SHG microscopy continue to shape the evolving field of biophotonics. Innovations aimed at enhancing spatial resolution through coherent structured illumination [128] and post-processing methods such as pixel reassignment [129] and changing optical properties via adaptive optics [130,131] exemplify rapid advancements in the field.

However, despite these strides, complete quantitative interpretation of SHG images remains a challenging endeavor because of the coherent nature of the process. While different SHG approaches contribute to this puzzle, a comprehensive integration of these techniques within a single instrument could provide a definitive solution to this enduring challenge. Moreover, expensive equipment and specialized training requirements hinder the adoption of SHG microscopy in routine biomedical practice. This limitation is particularly evident in advanced SHG techniques that rely on state-of-the-art optical implementations and complex hardware systems. However, recent advancements in laser technology have led to a shift from traditional Ti: sapphire lasers to more robust and cost-effective fiber and semiconductor lasers [132]. These developments are expected to open new avenues for the biomedical applications of SHG microscopy. The advancement of endoscopic SHG has also contributed to the broader application of this technology, offering the potential for the in vivo imaging of organs, as exemplified in Figure 1-12 [133].

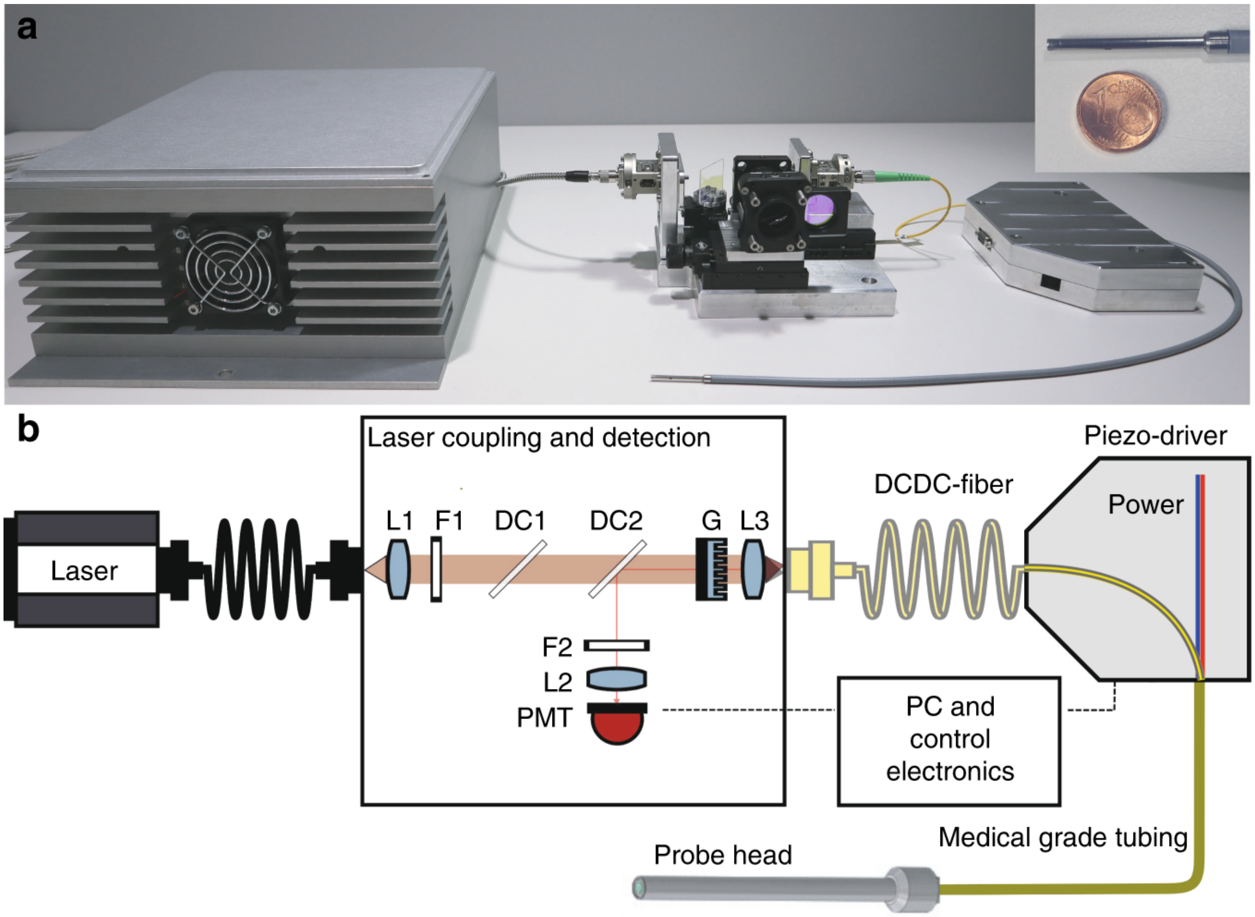

Figure 1-12: a) The nonlinear endomicroscopic fiber probe and laser coupling unit. The probe head contained an optical fiber and cables connected to the piezo scanner. b) The fiber laser generates pump and Stokes beams for coherent anti-Stokes Raman scattering (CARS) imaging. The laser beam was collimated by a lens and filtered by a long-pass filter to remove four-wave mixing noise, and its power was controlled by a short-pass dichroic mirror (DC1). A linear diffractive grating (G) and lens (L3) couple the beams into a double-core, double-clad (DCDC) fiber. Nonlinear signals from the sample (CARS, SHG, and TPEF) were collected by the outer cladding of the DCDC fiber and detected by a photomultiplier tube (PMT) after the desired nonlinear signal was selected using a bandpass filter (F2). Extracted from [133].

In addition to hardware enhancements, significant progress has been made in software analysis and computational approaches to enhance the imaging capabilities in microscopy. Improved processing capabilities through graphical processing units and field-programmable gate arrays have accelerated the data analysis. Moreover, machine learning, a transformative force in various fields including image processing, has been used in SHG microscopy. Standardization and unification of imaging processes are becoming increasingly essential to ensure reproducibility and portability across different laboratories, as current imaging systems tend to be unique and customized in each setting. Despite the challenges and limitations discussed, SHG and nonlinear optical microscopy techniques offer a wealth of information that is not readily accessible using traditional linear or incoherent optical imaging methods. With ongoing advancements in optics, machine learning, and laser technology, nonlinear imaging modalities have become more sophisticated and accessible, offering new horizons for applications in fundamental science and medical research.

Machine learning can further enhance the SHG microscopy and image analysis. These technologies can automate image interpretation, assist in quantifying SHG signals, and provide insights that may be challenging to manually extract. The following section delves into machine learning concepts and their applications in SHG microscopy, shedding light on the exciting potential of combining it with this powerful imaging technique. The combination of SHG microscopy and machine learning enhances our ability to explore the intricacies of biological structures and enables novel diagnostic and therapeutic applications. Mixing artificial intelligence with SHG microscopy promises to open new horizons for research, diagnostics, and patient care in bioimaging and neuroimaging as technology advances.

1.7 Deep learning in microscopy

Deep Learning (DL) is inspired by the intricate data-processing mechanisms observed in the human brain. DL's inherent ability to learn without relying on predefined human-crafted rules distinguishes it. Instead, it harnesses extensive datasets to establish connections between the input data and specific labels. DL is constructed by integrating numerous layers of algorithms, known as artificial neural networks (ANNs), each of which provides a unique interpretation of the data they receive [134–136]. DL has emerged as a revolutionary tool in microscopy and image analysis. By continually refining its algorithms through iterative learning, DL has shown remarkable performance in the field of microscopy, enabling the precise and rapid analysis of intricate images and providing previously challenging insights. Its adaptability and capacity to uncover subtle patterns within data makes DL a transformative force in the world of microscopy and image analysis, with the potential to reshape how we explore and understand the microscopic world [137].

1.7.1 Deep learning architecture for image analysis

As image datasets become increasingly complex and the demand for robust decision-making systems increases, the need for more sophisticated algorithms is justified. Many different architectures are available for deep learning; however, we describe the most prominent networks in this section.

The basis for numerous modern deep learning models is feed-forward neural networks, commonly referred to as multilayer perceptrons (MLPs), which take cues from human neural systems in a general manner [138,139]. They are termed "feed-forward neural networks" because they strictly involve data flowing in a unidirectional manner from the input to the output without any feedback loop from the output back into the model [140]. An example of such a model is shown in Figure 1-13.

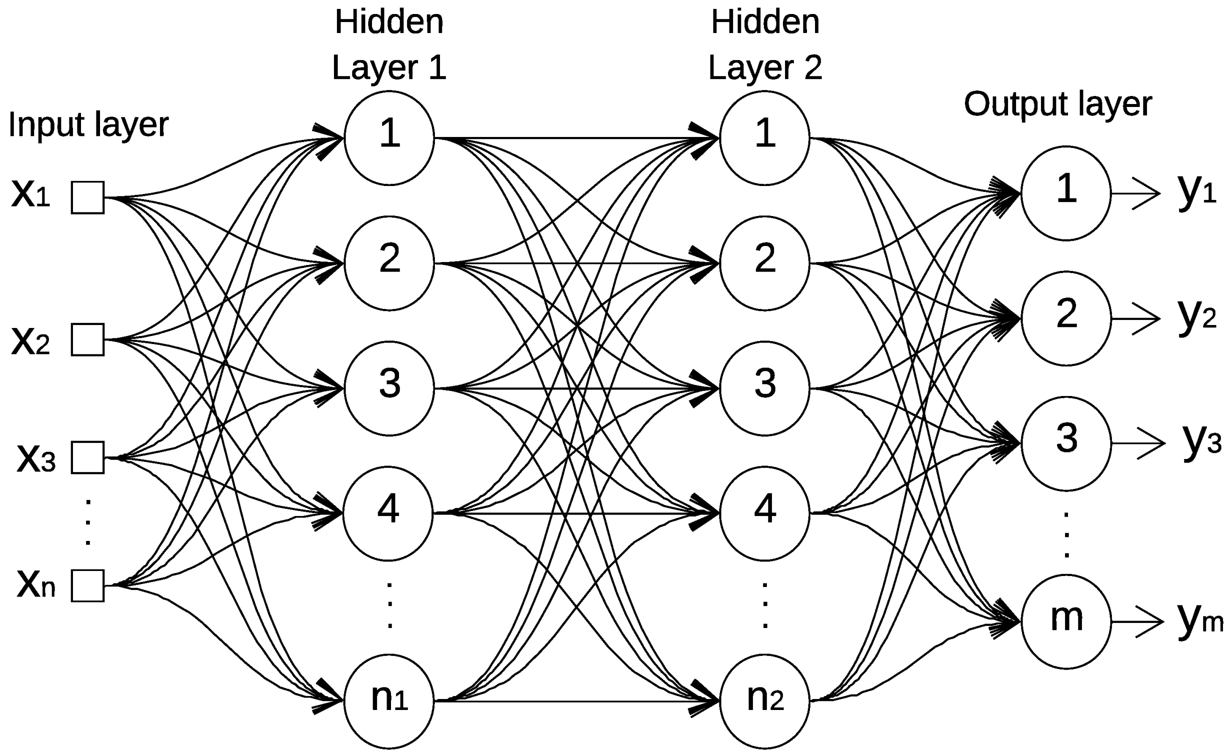

Figure 1-13: An example of an MLP with an input layer, two hidden layers, and an output layer. Extracted from [141].

A convolutional neural network (CNN) [142] represents a variation of an MLP designed explicitly for processing grid data, such as images. In contrast to MLPs, CNNs inherently consider the spatial details in images [136].

Standard neural networks such as MLPs have inherent limitations when dealing with sequential data [143]. In contrast, recurrent neural networks (RNNs) feature neurons that extend over time, allowing them to capture temporal dependencies [143]. Furthermore, RNNs incorporate hidden layers that introduce memory into a network over time. RNNs can be structured in three distinct architectures to address the challenges posed by sequential data. The one-to-many RNN architecture comprises a single input neuron and a sequence of output neurons, which are commonly used in tasks such as image captioning [144]. The many-to-one RNN architecture involves multiple input neurons and a single output neuron, and is typically used for text classification [145]. The many-to-many RNN architecture entails multiple input and output neurons, which are often employed in tasks such as machine translation [146]. Despite these advancements, RNNs still need to be explored in biophotonics in comparison with MLPs and CNNs. Figure 1-14 highlights a CNN network with two pooling and convolutional layers.

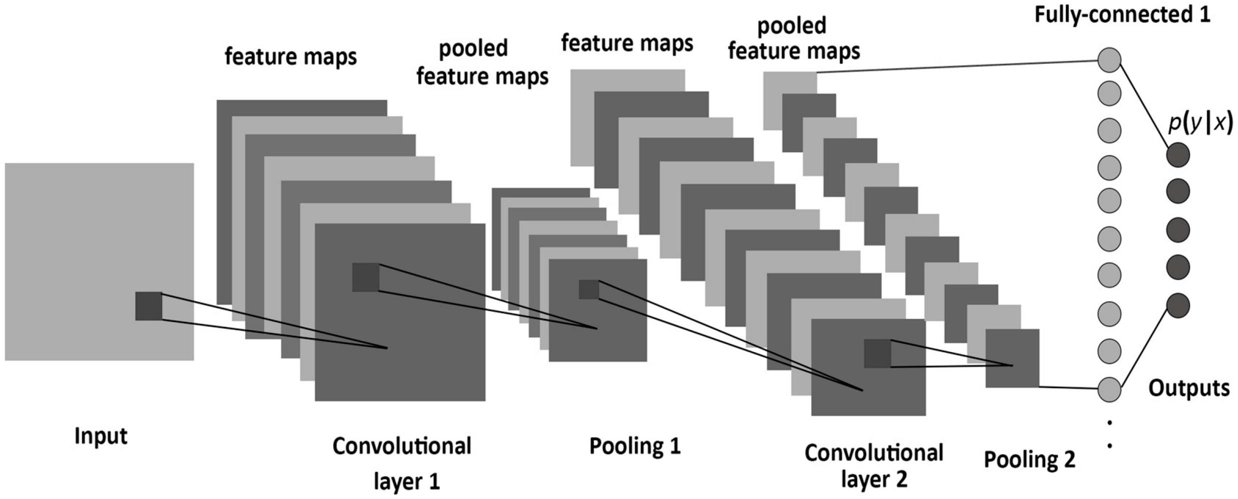

Figure 1-14: Example of a CNN. The difference between a CNN and MLP is that a CNN contains convolutional and pooling layers. Extracted from [147].

A generative adversarial network (GAN) represents an ANN's unique variant comprising two key components: a generator and discriminator (illustrated in Figure 1-15) [148]. The two networks are simultaneously trained. The input to the generator can be either a random noise vector or an actual image. The generator is a differentiable function, often represented by an MLP or autoencoder, that maps the input to an output. The primary objective of the generator is to learn the distribution to approximate the prior distribution from which the input data are drawn. The generator output is designed to visually resemble actual data such as images. In addition to the generator output, an actual input image is provided to the discriminator. This adversarial training is accomplished by optimizing the loss function, which is optimized using the backpropagation technique. During back-propagation, the gradient computed from the loss function is propagated from the discriminator to the generator, enabling the update of the generator parameters [148].

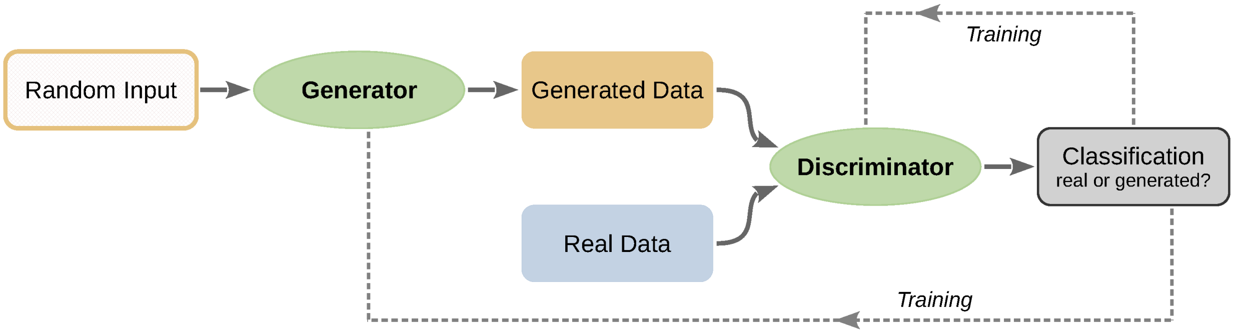

Figure 1-15: Architecture of a GAN network. The generator learns to produce realistic data that resemble actual data, whereas the discriminator evaluates the authenticity of the data. Extracted from [149].

Training a GAN presents specific challenges. First, achieving convergence for both networks is complex owing to their simultaneous training [150]. Additionally, the early convergence of the discriminator can easily distinguish generated images from real images. This is because the discriminator gradient approaches zero, providing minimal guidance to the generator for further training [150]. After several iterations, when convergence between the two networks is achieved, the generator can produce highly realistic images that are challenging to identify as "fake" images by the discriminator [148]. Adversarial training of GANs has gained popularity in both industrial and academic research because of its potential for domain adaptation and image generation. In the next section, we will examine these architectures applied to medical image analysis and how each network has helped move the research forward to reach the goal.

1.7.2 Medical image analysis with machine learning

DL can be immensely useful given the complexity of medical image analysis and acquisition. In this section, we detail some of the applications in which DL has been able to help biomedical imaging research.

Image classification: Instead of pixel-wise prediction, image-level classification assigns a single label to each input image. Supervised learning networks, particularly CNNs, are powerful tools for microscopic image classification [151]. However, unsupervised feature learning has been effectively applied to various computer vision tasks and holds promise for medical imaging [152,153]. A common approach for image classification is to utilize neural networks as classifiers that provide direct predictions for individual images. Alternatively, networks trained on extensive datasets can be feature extractors, generating data representations that are fed into other classifiers. Deep learning has the potential to transform image analysis, automate tasks, such as image classification and segmentation, and reduce the need for manual data inspection [154–

157]. This approach has applications in SHG microscopy for various medical domains, including lymphedema [154], ovarian tissue [129,155], and breast cancer [156,158]. However, when dealing with smaller datasets such as those often encountered in medical imaging, applying deep learning can present challenges that require specific measures to ensure the accuracy of the trained model [159]. Gao et al. conducted CNN experiments to investigate the effects of hyperparameters, data augmentation, and image foreground masks on the classification performance. Their experiments also revealed that CNNs, when pretrained on a significantly larger dataset and fine-tuned on a smaller related dataset, achieved higher accuracy than those trained from scratch on a smaller dataset [160]. In a different approach, Chen et al. used a fully connected neural network for a label-free cell classification [161].

Image denoising: Deep neural networks are versatile for various input-output scenarios, including image enhancement by using noisy or low-resolution images as input and using generative networks to produce images with the desired resolution or noise level as the output. These networks can learn from high-resolution images, reduce artifacts, and preserve features without excessive smoothing. GANs are commonly employed to maintain high-frequency features. A variation of GANs, known as Wasserstein generative adversarial networks (WGANs), use the Wasserstein distance as a loss function and have successfully enhanced the resolution of OCT images [162]. Another approach uses edge-sensitive conditional generative adversarial networks (cGANs) to mitigate speckle noise effectively [163]. Deep learning has also been introduced to restore microscopy images, focusing on enhancing the image quality while avoiding the creation of hallucinations. Among the various image restoration techniques to eliminate noise, Noise to Ground Truth (N2GT) involves noise removal by comparing an image to a reference image (ground truth). However, it has limitations owing to the need for ground-truth images [164]. Noise to Noise (N2N) focuses on denoising by comparing a noisy image to another with a higher SNR [165]. Noise to Void (N2V) removes noise by training a deep neural network to learn the statistical properties of noise and signal within a single image without requiring image pairs [166]. These diverse approaches offer valuable tools for enhancing the image quality across various microscopy applications and are the basis for Article 3 of this thesis.

Transfer learning in image analysis: Transfer learning (TL) with CNNs aims to enhance the performance of a new task by leveraging previously acquired knowledge from similar tasks [167,168]. This approach has contributed significantly to medical image analysis by addressing data scarcity issues, saving time, and conserving hardware resources. Transfer learning using CNNs involves transferring knowledge at the parameter level. Well-trained CNN models utilize the learned parameters of their convolutional layers for new tasks in the medical domain. Specifically, in the context of transfer learning with CNNs for medical image classification, a model is trained to classify medical images (target task) by leveraging generic features learned from natural image classification (source task), where labels are available in both domains [167].

Image resolution enhancement: In the previous section, we discussed how GAN architectures could be effectively utilized for image denoising and resolution enhancement. Although improving the signal-to-noise ratio is crucial for image interpretation, it can also be enhanced by increasing the number of collected images [140]. However, the resolution of the obtained image is often restricted owing to technical limitations such as the diffraction limit. Various advanced technical solutions enable imaging beyond the diffraction limit, which falls under the category of super-resolution imaging. In addition to these technical solutions, overcoming the diffraction limit is feasible through image-processing techniques, particularly deep learning. This GAN-based approach achieves super-resolution while simultaneously reducing image noise [140].

Although all methods have helped with medical imaging in one way or another, the accuracy of the generated images and the output are of utmost importance for the integrity of the experiments. Image quality metrics play a pivotal role in image analysis, particularly in deep learning. They are crucial for several reasons, contributing to the success and effectiveness of image analysis techniques, which will be explored in the next section.

1.7.3 Image quality metrics

Image quality assessment (IQA) has attracted significant attention over the last three decades. This heightened interest can be attributed to the widespread availability of digital images that are routinely acquired, compressed, transmitted, restored, and edited by the public [169]. IQA methods have now become instrumental in developing and evaluating imaging devices, serving as indispensable tools to gauge the extent to which various distortions and operations impact an image. Current IQA approaches can be categorized into two primary groups: subjective and objective methods [170]. Subjective methods rely on quality scores provided by human experts, whereas objective methods leverage mathematical models to estimate perceived image quality automatically, aligning with human observation. Objective methods can be further classified into three main categories based on the availability of a reference image: No-Reference IQA (NR-IQA) or "blind," Reduced-Reference IQA, and Full-Reference IQA (FR-IQA) [169]. The FR-IQA techniques assess the visual quality of a target image in relation to a reference image, which is the optimal quality. Applying FR-IQA methods to microscopy can be challenging because of the typical absence of reference images [171].

In contrast, NR-IQA methods evaluate image quality solely based on the information within the tested image, making them well suited for use with microscopy images [172–174]. However, it is worth noting that most established NR-IQA methods have been designed considering the characteristics of natural images captured by digital cameras. Owing to the nature of imaged scenes and acquisition mechanisms, microscopy images possess unique characteristics that may lead to unpredictable results when applying traditional NR-IQA metrics [169].

1.7.4 Full-reference image quality metrics

This section explores the most popular FR-IQA metrics currently used for DL applications. The classification of objective image quality metrics is based on the presence of an original, undistorted image, which serves as a comparison standard for a distorted image. The predominant approaches are categorized as full references, in which a complete reference image is presumed to be accessible [171]. However, obtaining a reference image in practical scenarios may not be feasible, necessitating a no-reference or "blind" quality assessment approach. Alternatively, there exists a third type of method in which the reference image is only partially available, taking the form of a set of extracted features that serve as supplementary information for evaluating the quality of the distorted image, referred to as reduced-reference quality assessment [175]. The simplest IQA method is the mean squared error metric.

The Mean Squared Error (MSE) is a widely used metric in image processing and signal analysis, serving as a quantitative measure of the discrepancy between an original and a reconstructed or processed image [176]. The MSE provides a numerical representation of the overall distortion or error, calculated by averaging the squared differences between the corresponding pixel values of the two images. A lower MSE value indicates a closer match between the original and processed images, signifying a higher fidelity. Although MSE is a straightforward and computationally efficient metric, it has limitations, such as being sensitive to outliers and not aligning with human perceptual differences [176]. Despite these drawbacks, MSE remains a fundamental tool for evaluating the quality of image reconstructions and is commonly employed in optimization processes, such as those related to image compression and restoration algorithms [176].

The Peak Signal-to-Noise Ratio (PSNR) is another widely utilized metric in image and video quality assessment, complementing MSE. While MSE measures the average squared difference between the corresponding pixels of an original and processed image, PSNR provides a more interpretable and perceptually relevant measure by considering both the magnitude of the error and the maximum possible signal strength [177]. The PSNR is calculated as the ratio of the peak signal power to the mean squared error, expressed in decibels (dB). The peak signal power represents the maximum possible intensity value that the pixels can have, which is typically constrained by the image's bit depth. As such, the PSNR considers the dynamic range of the image, offering a normalized measure of quality [177]. One notable advantage of the PSNR is its straightforward interpretation. Higher PSNR values corresponded to lower distortion, reflecting a closer resemblance between the original and processed images. This metric is widely used in various applications, including image and video compression, where it aids in assessing the impact of compression algorithms on the visual quality. Despite its advantages, the PSNR has certain limitations. Similar to MSE, it is sensitive to minor errors and may not align perfectly with human perception [177]. High PSNR values do not always guarantee superior visual quality, particularly when considering the intricacies of the human visual system. For example, PSNR may not accurately capture the impact of compression artifacts on the subjective visual experience. When comparing PSNR to MSE, it is crucial to recognize that PSNR builds upon MSE by incorporating the signal-to-noise ratio aspect [177]. PSNR provides a more normalized and perceptually relevant measure, considering the dynamic range of the images being compared. However, both metrics share the fundamental limitation of being sensitive to pixel-wise differences, without accurately reflecting human perceptual judgments [177].

The Structural Similarity Index (SSIM) and its variants, such as the Multi-scale Structural Similarity Index (MS-SSIM) [178] and Complex Wavelet Structural Similarity Index (CW-SSIM) [179], represent advancements in image quality assessment that address some of the limitations of traditional metrics, such as MSE and PSNR [180].

SSIM, introduced by Wang et al., assesses the perceived quality of an image by considering the structural information, luminance, and contrast [175]. Unlike MSE and PSNR, which focus on pixel-wise differences, SSIM incorporates the elements of human visual perception. It operates by dividing the image into local regions and evaluating the similarity of the structures within these regions, as seen in Figure 1-16. The resulting index ranges from -1 to 1, where 1 indicates perfect similarity [175].

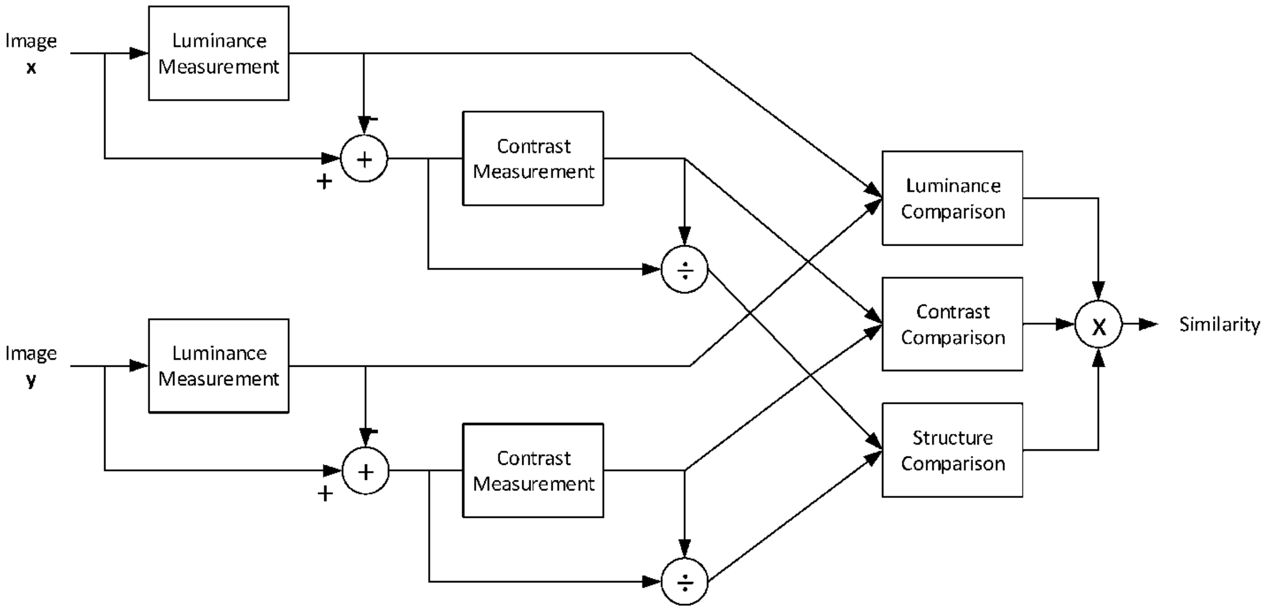

Figure 1-16: SSIM process for comparing the similarity between two images. The luminance, contrast, and structure were compared and reflected in the similarity index results. Extracted from [181].

MS-SSIM extends SSIM by incorporating multi-scale processing. This involves generating multiple scales of an image, applying SSIM at each scale, and combining the results [178]. This accounts for the variations in perception at different scales, making MS-SSIM more robust in capturing local and global structural information [178]. CW-SSIM introduces complex wavelet transforms to better model the sensitivity of the human visual system to spatial frequencies [179]. CW-SSIM can capture intricate details and textures in images better by employing complex wavelets, accurately reflecting the perceived quality [179]. Comparing SSIM and its variants to traditional metrics, such as MSE and PSNR, reveals significant advantages. SSIM-related metrics align more with human perception when considering structural information and texture details [180]. They are less sensitive to compression artifacts and other distortions that may not be perceptually noticeable. Consequently, SSIM metrics often provide a more reliable measure of the image quality. However, they still have some limitations, particularly in scenarios where a reference image may not be available or when the quality degradation is severe [182].

1.7.5 No-reference image quality metrics

No-reference metrics or blind metrics do not require a reference image for comparison and are particularly valuable in situations where obtaining a pristine reference image is challenging or impossible [172]. These metrics leverage statistical models, machine learning, or other sophisticated approaches to estimate image quality without direct comparison with the original.

As technology evolves, the demand for accurate, efficient, and reference-free image quality assessments continues to increase. No-reference metrics represent a promising avenue in this direction, overcoming some of the challenges posed by traditional metrics, and providing more flexibility in evaluating image quality across diverse applications and scenarios [172].

The Natural Image Quality Evaluator (NIQE) is a prominent example of a no-reference image-quality metric designed to assess the perceptual quality of natural images without requiring a reference image for comparison [183]. Introduced by Mittal et al., NIQE leverages statistical modelling and analyses of natural scene statistics to estimate the image quality [183]. This metric is based on the premise that natural images exhibit certain statistical regularities, and deviations from these norms can indicate image distortions or artifacts. NIQE has found applications in various fields, including image and video processing, where it offers an efficient and automated means of evaluating the quality of images in situations where obtaining reference images may be impractical or unfeasible. NIQE, being a no-reference metric, represents a departure from traditional approaches, such as MSE and PSNR, which require a pristine reference image. Instead, NIQE analyzes the statistical properties inherent in natural images, such as texture, edge, and luminance variations [172]. By quantifying deviations from these statistical norms, the NIQE provides an objective measure of image quality that aligns with human perceptual judgments. Its versatility makes NIQE suitable for image quality assessment across various applications, including image compression, denoising, and other image-processing tasks [172,183].

The Perceptual Image Quality Evaluator (PIQE) is another noteworthy example of a no-reference image quality metric, offering a different approach to NIQE. PIQE relies on a machine learning model trained on a large dataset of images to predict perceptual image quality [184]. Unlike NIQE, which is rooted in the statistical analyses of natural image properties, PIQE takes advantage of the learning capabilities of a neural network to discern features indicative of image quality [184]. This allows PIQE to adapt to a broader range of image contents and quality variations. PIQE has demonstrated effectiveness in various applications, including the evaluation of compressed images and the assessment of the impact of distortions on perceived quality [184]. A comparison of NIQE and PIQE reveals nuanced differences in their methodologies. While NIQE leans on statistical regularities in natural images, PIQE harnesses the power of machine learning to infer perceptual qualities [174]. The choice between the two may depend on the specific requirements of a given application and nature of the images under consideration. We have covered DL and the most popular metrics used to validate the results, in the next section, we will examine how DL and these metrics overlap with biomedical microscopy, and how they can help advance biomedical SHG microscopy and its applications.

1.7.6 DL application in biomedical imaging and SHG biomedical imaging

There are many instances where DL has enriched biomedical imaging, and in this section, we will discuss SHG and non-SHG biomedical imaging enhanced by such techniques.

In one study, Hall et al. proposed a new algorithm for real-time collagen fiber alignment quantification for SHG imaging [185]. Their algorithm evaluated the Fourier transform magnitude of image symmetry using a single parameter, the fiber alignment anisotropy, ranging from 0 (randomized fibers) to 1 (perfect alignment). The proposed model enables real-time application and quantification [185].

Optical coherence tomography (OCT) encounters challenges posed by coherent noise, specifically speckle noise, which degrades the contrast and detailed structural information in OCT images [186]. This in turn imposes significant limitations on OCT's diagnostic capabilities. Qui et al. proposed an innovative denoising method for OCT images in a study. To train and evaluate denoising deep learning models, they generated label images by averaging 50 frames of registered B-scans acquired in a single direction [186]. Their novel method excels in preserving detailed structural information in the retinal layers and enhances perceptual metrics in human visual perception [186].

In another study, to counter noise in two-photon microscopy, Lee et al. proposed a novel approach based on DL [187]. They addressed suboptimal image quality due to various noise factors, including blur, white noise, and photobleaching in two-photon microscopy, with a novel algorithm rooted in deep CNNs [187]. The proposed model comprises multiple U-nets, each targeting noise removal at different scales and contributing to the performance enhancement through a coarse-to-fine strategy. Notably, the constituent CNNs fully utilize 3D convolution operations, allowing the model to facilitate end-to-end learning without requiring pre/post-processing [187].

In a recent study, Kistenev et al. applied DL image classification to lymphedema tissue analysis [154]. This study encompassed thirty-six image samples from patients in the second stage of lymphedema and forty-two image samples from healthy individuals. This examination specifically focused on the papillary layer of the skin. Notably, the study identified disorganization in the collagen network and an elevation in the collagen/elastin ratio within lymphedema tissue, indicative of heightened fibrosis severity. To characterize the images, edge detection, the histogram of oriented gradients method, and a machine-learning-based predictive model for diagnosis were used. Integrating "ensemble learning" in the classification process yielded a 96% accuracy in validating the data from the testing set [154].

In ovarian cancer studies, Huttunen et al. demonstrated that deep learning techniques can effectively classify multiphoton microscopy images of unstained reproductive tissues [155]. Using four pretrained convolutional neural networks, they fine-tuned the models with over 200 murine tissue images. These images were based on combined SHG and TPEF contrast to enhance tissue visualization. With this approach, they were able to accurately label tissue as either healthy or associated with high-grade serous carcinoma, with a sensitivity of over 95% and specificity of 97% [155].

In wide-field P-SHG applications, Mirsanaye et al. demonstrated a DL-based classification method for breast cancer diagnostics by examining collagen fibers in the ECM (Figure 1-17) [156]. This study demonstrated the application of high-throughput widefield P-SHG microscopy for whole-slide imaging of breast tissue microarrays. The obtained P-SHG parameters were utilized for classification, distinguishing between tumor and normal tissue with accuracy and an F1-score of 94.2% and a 6.3% false discovery rate. Subsequently, the trained classifier accurately predicted the tumor tissue with 91.3% accuracy, 90.7% F1-score, and 13.8% false omission rate [156].

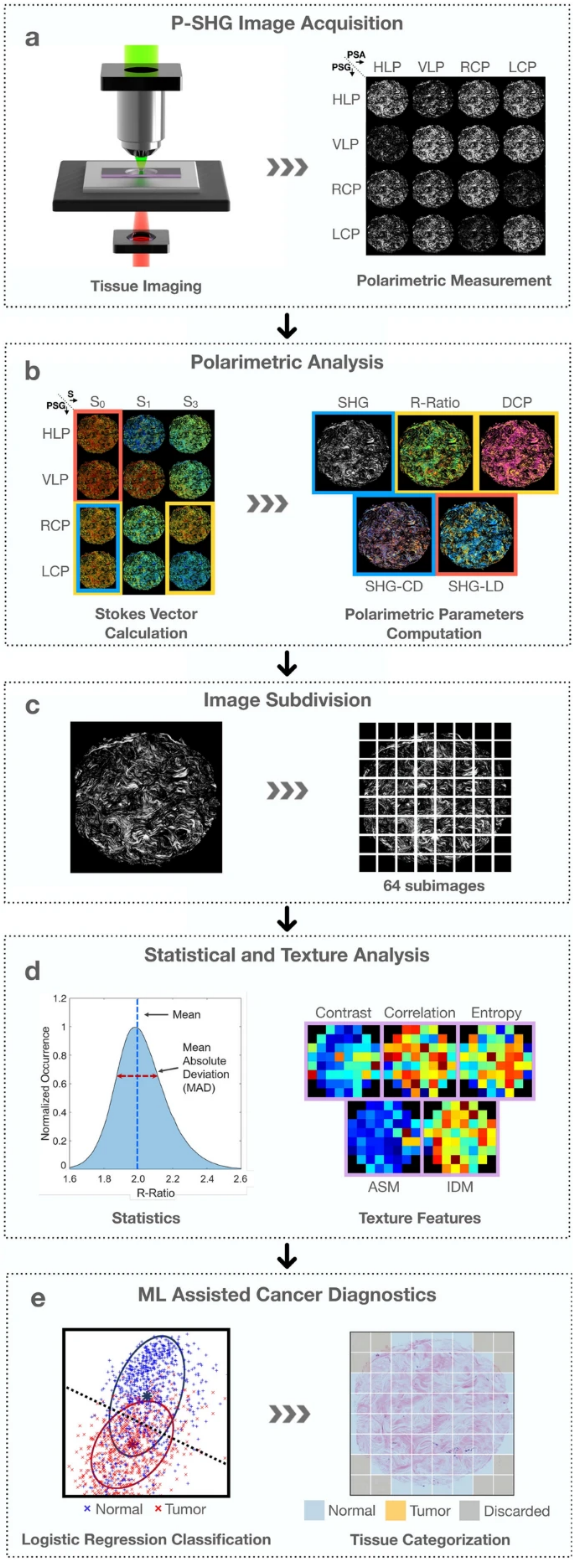

Figure 1-17: Imaging and classification steps for a wide-field P-SHG microscope. (a) The sample was imaged at 16 different combinations of polarization states set by a polarization state generator (PSG) and polarization state analyzer (PSA). (b) SHG Stokes vector components were computed from the images to obtain polarimetric parameter images. (c) Polarimetric images were divided into sixty-four smaller images, enabling

high-resolution texture analysis and statistical significance testing. (d) The mean and mean absolute deviation of the polarimetric parameters and texture parameters (contrast, correlation, entropy, angular second moment, and inverse difference moment) were calculated for each smaller image. (e) A logistic regression classifier is trained using polarimetric and texture parameters to predict whether the tissue is normal or tumorous. Extracted from [156].

To improve laser scanning microscopy, Shen et al. introduced deep learning autofluorescence harmonic microscopy (DLAM) [157]. DLAM aims to improve the speed, field of view, and image quality using attention-guided networks. Their study showcases the label-free large-field imaging of clinicopathological tissues with better spatial resolution and efficiency [157].

Therefore, we can see how advancements in different areas of DL can benefit different studies and microscopic techniques. Despite these advancements, it is essential to acknowledge that there are still certain shortcomings and challenges associated with applying deep learning to microscopy. These limitations are thoroughly discussed in the subsequent section, shedding light on areas that require further attention and refinement.

1.7.7 Deep learning in microscopy shortcomings

The biophotonics field faces challenges related to the systematic accessibility of data and the scarcity of open repositories, posing a significant hurdle for utilizing deep learning in biophotonics data analysis owing to insufficient data availability. Deep learning models inherently rely on large datasets, and data inadequacy risks overfitting, resulting in poor generalizability to new datasets [188].

Understanding how DL models make decisions is crucial for medical imaging and modern healthcare systems. It is essential to ascertain whether deep neural networks base their predictions on biomolecular information rather than being influenced by background effects or image noise. At times, this distinction can be quite challenging to researchers, which is considered one of the drawbacks of using such methods [140]. DL holds significant potential for clinical healthcare, yet it faces challenges in standardization compared with established radiological or histopathological techniques [140]. The absence of an international consensus on evaluating the performance of biophotonics devices hampers data reproducibility, making machine learning models trained on such data less dependable. Enhancing the quality of clinical studies, promoting data comparisons across different laboratories and systems, encouraging open databases, and enabling quantitative comparisons between different models are pivotal for developing robust computational models [140]. DL techniques are formidable analytical tools for microscopy, demonstrating superior performance compared to traditional image processing pipelines.

Although DL technology has sparked enthusiasm and innovation, the demand for robust and compatible resources to train DL networks creates an accessibility barrier that is particularly challenging for inexperienced users to overcome [189]. This hurdle involves the availability of high-performance computing and extends the expertise required for practical DL model training. Bridging this accessibility gap is crucial for empowering a broader user base by leveraging the capabilities of DL in microscopy and fostering the widespread adoption of these advanced analytical tools [189].

2 OVERVIEW OF RESEARCH ARTICLES

This thesis delves into integrating artificial intelligence into SHG microscopy to enhance its application in biomedical imaging. It is structured around four interrelated articles, each contributing uniquely to the overarching thesis's objectives. This section provides a comprehensive overview of each article, detailing its title, objectives, hypotheses, methodological approach, and relationship with other articles to form a coherent whole that addresses the general objectives of the thesis.

2.1 General thesis objectives

The primary aim of this thesis was to address the inherent limitations of SHG microscopy, thereby enhancing its capability for accurate and practical biomedical imaging. The specific objectives include:

Enhancing image quality: Machine learning techniques are implemented to reduce noise and improve resolution, thereby enhancing the effectiveness of SHG microscopy in clinical and research applications.

Enabling Automated Analysis: Employing automated analysis to minimize human error and increase efficiency in the processing and interpretation of biomedical images.

Expanding Clinical Applications: Extending the potential applications of SHG microscopy in clinical settings by improving its imaging capabilities, aiding in diagnosing and studying various diseases.

The following sections present summaries of the four articles that form the core of this thesis. Based on the above background information, these articles address specific challenges in SHG microscopy. Each article summary includes the study's objectives, methodological approach, key findings, and relation to the overall thesis goals.

2.2 Article summaries

2.2.1 Article 1: “Second harmonic generation microscopy: a powerful tool for biological imaging”

Objective: This article provides an overview of the historical development and theoretical basis of biomedical SHG microscopy, tracing its evolution from its early discovery in nonlinear optics to its modern applications in biomedical imaging. It explores key technological advancements and advanced imaging modalities that have expanded SHG's capabilities in biological research. By synthesizing these developments, this review serves as a comprehensive resource for new researchers entering the field, offering insights into the foundational principles and the latest innovations in SHG microscopy.

Hypotheses: This study hypothesizes that SHG microscopy's intrinsic ability to selectively visualize non-centrosymmetric structures provides unparalleled insights into select biological structures. It highlights the unique advantages of SHG microscopy in visualizing complex biological systems. Unlike fluorescence-based techniques, which rely on external labeling agents, SHG generates contrast through intrinsic molecular properties, making it particularly suited for imaging non-centrosymmetric structures such as collagen, myosin, and microtubules. This label-free, specific imaging approach allows researchers to study structural organization, and disease progression in a minimally invasive manner. These properties position SHG as an indispensable tool in biomedical imaging, neuroscience, and tissue diagnostics, with the potential for further enhancement through emerging computational techniques.

Methodological Approach: This article conducts a comprehensive literature review to synthesize historical, theoretical and experimental research on SHG microscopy across various biological fields. It consolidates data from neuroscience, cancer imaging, tissue analysis and extracellular matrix studies to present an interconnected picture of the current state of SHG technology, identifying its strengths and areas needing improvement. This synthesis provides a crucial rationale for integrating computational technologies to address identified limitations.

Relation to Thesis Objectives: This article sets the foundation for this thesis, providing a detailed account of SHG microscopy's strengths, challenges, and potential for enhancement through computational approaches. It identifies key areas where AI-driven methods, such as deep learning-based denoising and GAN-based super-resolution, can improve SHG imaging quality, reduce acquisition time, and enhance automated analysis.

Key Findings: This review confirms that SHG microscopy excels in imaging non-centrosymmetric biological structures, with significant applications in neuronal pathways, collagen networks, and myosin filaments. Unlike fluorescence microscopy, SHG provides high spatial resolution without photobleaching, making it ideal for long-term live imaging of delicate tissues. However, several challenges persist, including signal interference and resolution constraints. These findings emphasize the need for advanced denoising, enhanced resolution, and computational post-processing techniques to further enhance SHG's imaging quality.

Support for Hypotheses: The findings support the hypothesis that SHG microscopy is indispensable for studying complex biological systems, owing to its unique imaging properties. Moreover, this review highlights specific areas where deep learning can mitigate SHG's current limitations, including noise reduction, resolution enhancement, and real-time image interpretation. These insights reinforce the broader objective of integrating computational techniques to optimize SHG imaging for biomedical applications.

Novel Contributions: This article consolidates current knowledge and offers a comprehensive overview of SHG microscopy. By identifying key technological gaps, such as signal optimization, imaging speed, and real-time analysis, it establishes a roadmap for future innovations, particularly in AI-enhanced imaging applications.

Comparison with Existing Research: This article reaffirms prior findings on SHG's advantages while introducing new perspectives on improving its capabilities, contributing significantly to the existing literature on SHG microscopy.

This comprehensive review sets the stage for subsequent studies by identifying key areas in which DL can significantly enhance the SHG microscopy capabilities.

2.2.2 Article 2: "Nonlinear microscopy and deep learning classification for mammary gland microenvironment studies"

Objective: This study explores the application of deep learning techniques to classify SHG images of naïve and tumor-bearing murine mammary gland tissues. By leveraging supervised learning and transfer learning with the MobileNetV2 architecture, this research aims to improve the accuracy and efficiency of automated tissue classification. The study specifically evaluates how deep learning models can enhance SHG-based cancer diagnostics by detecting subtle ECM modifications associated with tumor progression. Additionally, it assesses the feasibility of deep learning classification with a highly limited dataset, reflecting the real-world constraints of SHG image acquisition. Given that deep learning models typically require large-scale datasets, this study investigates optimization strategies, including data augmentation and transfer learning, to improve model generalization and prevent overfitting.

Hypotheses: This study hypothesizes that deep learning models can accurately classify SHG images by detecting collagen organization patterns and subtle ECM modifications that distinguish naïve from tumor-bearing tissues. Given SHG's unique ability to visualize collagen fibrillar architecture, deep learning algorithms can enhance image-based diagnostics by identifying tumor-associated collagen signatures (TACS) that are difficult to quantify through traditional manual analysis. Additionally, the study investigates whether transfer learning can improve classification accuracy in small SHG datasets, addressing the common challenge of limited training data in biomedical imaging.

Methodological Approach: This study employs a supervised deep learning approach to classify SHG images of naïve and tumor-bearing murine mammary glands. The classification task is performed using a custom CNN and transfer learning with MobileNetV2, a lightweight neural network architecture optimized for image recognition. To mitigate the challenges of small dataset size, the study implements data augmentation techniques, including rotation, flipping, and zooming, to artificially expand the training dataset. The performance of the model is evaluated using accuracy, precision, recall, F1-score, and area under the curve (AUC) metrics. Additionally, this study investigates overfitting and underfitting challenges, optimizing hyperparameters such as dropout rate, data split ratio, and number of convolutional layers to improve model generalization.

Relation to Thesis Objectives: This article contributes to the thesis objective of enhancing SHG microscopy through deep learning-based automation. By demonstrating that CNNs can accurately classify small SHG image datasets, it supports the broader goal of reducing manual intervention in SHG-based diagnostics.

Key Findings: This study demonstrates that deep learning models significantly improve SHG image classification, distinguishing between naïve and tumor-bearing mammary gland tissues with an optimal test accuracy of 73%. However, classification performance is highly dependent on dataset size and preprocessing techniques. The study found that data augmentation improved model robustness, but excessive augmentation led to overfitting in some cases.

Support for Hypotheses: The findings validate the hypothesis that CNNs can accurately classify SHG images, confirming that deep learning models can detect fine structural variations in collagen organization that differentiate tumor-bearing from naïve tissues. The results support the thesis objective of developing AI-driven methods for automated SHG image interpretation.

Novel Contributions: This study identifies key challenges in applying deep learning to SHG image classification, particularly small dataset constraints, model generalization issues, and hyperparameter sensitivity. It systematically examines how transfer learning, data augmentation, and dropout optimization influence model performance, providing a roadmap for future AI-driven SHG imaging approaches.

Comparison with Existing Research: Compared with traditional classification methods, this study offers insight into accuracy, efficiency, and the unique challenges of applying CNNs to SHG image analysis with a very small dataset. Unlike conventional deep learning studies in biomedical imaging, which typically rely on large datasets, this study evaluates classification performance under realistic low-data conditions, reflecting practical constraints in SHG imaging. The limited number of training images posed significant challenges in model generalization, leading to issues such as overfitting, data imbalance, and sensitivity to hyperparameter selection. However, this study demonstrates that parameter optimization and data augmentation can help mitigate these limitations, making AI-based SHG classification feasible even in low-data scenarios.

Building on the foundation established in Article 1, this study demonstrated the practical application of AI in enhancing SHG image analysis.

2.2.3 Article 3: “A comparative study of CARE 2D and N2V 2D for tissue-specific denoising in second harmonic generation imaging”

Objective: This study evaluates the performance of two deep learning-based denoising techniques, Content-Aware Image Restoration (CARE 2D) and Noise-to-Void (N2V 2D), in improving the SHG image quality of different tissue types, including tumor-bearing murine mammary glands and zebrafish muscle structures. Beyond general noise reduction, this study explores the impact of glycerol concentration on SHG image noise and how deep learning can be used to restore image quality when fixation-induced artifacts are present. Additionally, it investigates low-power SHG imaging, assessing whether denoising models can compensate for the reduction in laser power, which is critical for reducing photodamage and enabling live imaging applications.

Hypotheses: This study hypothesizes that both CARE 2D and N2V 2D will effectively reduce noise in SHG images while preserving critical structural details, thereby improving the visualization and analysis of biological structures. Given that CARE 2D is a supervised model trained with ground-truth images, it is expected to provide strong noise suppression, contrast enhancement, and intensity restoration. However, since it relies on paired training data, its performance may be limited in cases where noise originates from fixation chemicals or sample preparation artifacts. Since N2V 2D does not require explicit ground-truth training, it is expected to outperform CARE 2D in situations where noise is introduced due to fixation chemicals and sample preparation-related artifacts. However, because it learns noise patterns from the input images themselves, it may be less effective in enhancing overall contrast compared to CARE 2D.

This study also examines whether deep learning-based denoising can compensate for low-laser-power SHG imaging by restoring image clarity without compromising structural integrity. The hypothesis is that deep learning models can effectively restore structural details under low-power conditions, thereby making SHG microscopy a more viable tool for live imaging applications where reducing photodamage is critical.

Methodological Approach: This study applied CARE 2D and N2V 2D models to SHG images of murine mammary gland tumors and zebrafish muscle tissues. Performance was assessed using the modified Structural Similarity Index Metric (mSSIM) and Peak Signal-to-Noise Ratio (PSNR). In addition to standard noise reduction evaluation, the study analyzed the impact of glycerol fixation on SHG image noise by testing how different concentrations of glycerol (50%, 80%, and 100%) affected image quality. This experiment aimed to determine whether deep learning models could restore image clarity when images were degraded by improper fixation. Another critical aspect of the methodology involved a low-power SHG imaging experiment, where laser power was reduced by 70% to evaluate the effectiveness of deep learning models in compensating for weaker signals. The study also examined tissue-specific denoising performance by comparing the ability of the models to restore collagen fiber structure in tumor-bearing mammary glands and preserve fine muscle fiber details in zebrafish tissues.

Relation to Thesis Objectives: By focusing on deep learning-based SHG image restoration, this study aligns with the thesis objective of enhancing SHG microscopy through AI-driven methods. It contributes to improving the versatility of SHG as a biomedical imaging tool by demonstrating how denoising models can compensate for imaging limitations caused by low laser power and sample fixation inconsistencies. The results establish the feasibility of applying deep learning for low-power SHG imaging, reinforcing the broader objective of expanding SHG's applicability beyond fixed samples and making it a viable tool for real-time imaging in biological research.

Key Findings: The study demonstrates that both CARE 2D and N2V 2D improve SHG image quality, but their effectiveness is highly dependent on tissue type, signal-to-noise ratio (SNR), and imaging conditions. CARE 2D performs well in moderate-SNR images, delivering strong noise suppression and improved contrast. However, in very low-SNR cases, the model generates hallucinated structures, which misrepresent biological features . This limitation suggests that while CARE 2D is effective in well-structured images, it may not be reliable when the original signal is extremely weak, as it can create artifacts rather than reconstruct missing information accurately. N2V 2D, in contrast, excels at preserving muscle structures in zebrafish samples. Unlike CARE 2D, it avoids over-smoothing and maintains the natural appearance of fine biological structures, even though it does not enhance SHG intensity to the same degree. At low laser power, CARE 2D was better at matching high-intensity reference images of ECM, whereas N2V 2D was superior in preserving structural integrity, particularly in muscle tissues. Another important finding is that glycerol concentration significantly affects SHG noise levels, with higher concentrations leading to increased signal degradation. Because CARE 2D requires paired reference images for training, it could not be applied in these cases. However, N2V 2D effectively restored images affected by high glycerol content, making it the preferred choice for denoising when sample preparation inconsistencies impact SHG image quality. These findings indicate that while no single model is universally superior, CARE 2D is preferable for structured tissues with moderate SNR due to its strong contrast enhancement. In contrast, N2V 2D is more effective in preserving structural integrity when noise stems from fixation artifacts or low SNR conditions. The choice between CARE 2D and N2V 2D depends on the specific imaging conditions and the need for either intensity restoration (CARE 2D) or fine-detail preservation (N2V 2D).

Support for Hypotheses: The findings support the hypothesis that both CARE 2D and N2V 2D effectively reduce noise in SHG images while preserving critical structural details, though their performance depends on imaging conditions and tissue type. CARE 2D demonstrated strong noise suppression, contrast enhancement, and intensity restoration, particularly in structured tissues with moderate-to-high SNR, such as the extracellular matrix of tumor-bearing mammary glands. However, in low-SNR conditions, it introduced artificial structures (hallucinations), particularly within tumor boundaries, suggesting that it may misrepresent biological features when the original signal is weak. In contrast, N2V 2D, performed better in conditions where noise was introduced due to fixation chemicals and sample preparation inconsistencies, effectively restoring images affected by high glycerol concentrations while preserving fine structural details, especially in muscle tissues. Although it did not enhance SHG intensity to the same extent as CARE 2D, it avoided over-smoothing and maintained structural integrity more reliably in complex biological structures. Both models were effective in compensating for low-laser-power SHG imaging, with CARE 2D excelling in intensity restoration and N2V 2D preserving fine morphological details, confirming their potential for enhancing SHG microscopy while reducing photodamage in live imaging applications. However, at extremely low power, both models showed diminished performance, indicating that deep learning-based restoration has limitations when the SHG signal is excessively weak.

Novel Contributions: This study presents one of the first direct comparisons of CARE 2D and N2V 2D in SHG microscopy across different tissue types, providing valuable insights into the strengths and limitations of these denoising models. It introduces deep learning based compensation for low laser power SHG imaging, a concept that has significant implications for live-cell imaging and photodamage reduction. Additionally, the study demonstrates that deep learning can correct fixation-induced artifacts in SHG images, suggesting applications beyond noise reduction in cases where sample preparation inconsistencies affect imaging quality. By identifying tissue-specific denoising preferences, this work also provides practical guidelines for selecting appropriate deep learning models based on image characteristics and research objectives.

Comparison with Existing Research: This study advances previous research by providing a comprehensive evaluation of deep learning-based denoising models in SHG microscopy and expanding upon prior studies that have focused on single-method applications. The study also introduces deep learning for low-power SHG imaging, a concept that has not been widely explored in prior research. By demonstrating that AI-based denoising can compensate for imaging constraints related to laser intensity and fixation artifacts, this study broadens the applicability of deep learning in SHG microscopy, reinforcing the importance of tailored model selection based on specific imaging conditions.

While Article 2 focuses on image classification, this study expands on image quality enhancement, addressing another key challenge identified in Article 1.

2.2.4 Article 4: “Accelerating whole-sample polarization-resolved second harmonic generation imaging in mammary gland tissue via generative adversarial networks”

Objective: This article introduces a novel approach to whole-sample P-SHG imaging, utilizing ESRGAN to upscale low-resolution images while significantly reducing imaging time. P-SHG imaging provides valuable insights into collagen fiber orientation and ECM organization, but traditional high-resolution imaging methods require extended acquisition times and increased laser exposure, leading to potential photodamage. The goal of this study is to determine whether deep learning-based techniques can serve as a viable alternative by preserving image quality while improving acquisition speed.

This study systematically evaluates different ESRGAN variants to determine which model best balances image sharpness, structural accuracy, and computational efficiency for P-SHG imaging. Since resolution enhancing methods can introduce unwanted artifacts or distort fine image details, it is critical to assess which ESRGAN model is best suited for SHG microscopy applications.

Hypotheses: This study hypothesizes that ESRGAN can improve P-SHG imaging resolution under reduced acquisition time conditions without compromising image quality. It investigates whether ESRGAN can accurately reconstruct fiber orientation information and ECM structures, maintaining analytical reliability for P-SHG studies. Another key hypothesis is that certain ESRGAN variants will perform better than others, with specific architectures preserving texture and structural integrity more effectively in SHG imaging applications.

Methodological Approach: This study applied ESRGAN to low-resolution SHG and P-SHG images and evaluated its effectiveness using image quality assessment (IQA) metrics, including Structural Similarity Index (SSIM), Peak Signal-to-Noise Ratio (PSNR), and Mean Squared Error (MSE). Since different ESRGAN variants exist, this study tested multiple architectures to determine the most suitable model for mammary gland SHG imaging, balancing resolution improvement with artifact suppression and computational efficiency. In addition to evaluating general image quality, the study conducted a detailed analysis of fiber orientation data and texture features, assessing whether ESRGAN-upscaled images retained the essential structural characteristics needed for quantitative P-SHG analysis. The upscaled images were compared to high-resolution ground-truth images to determine whether ESRGAN could serve as a reliable alternative to direct high-resolution acquisition.

Relation to Thesis Objectives: This article directly aligns with the thesis's goal of enhancing SHG microscopy through machine learning-based image enhancement. By demonstrating that deep learning-based image enhancement can reduce acquisition time while maintaining image quality, this study contributes to making SHG imaging more efficient, cost-effective, and less resource-intensive. The work also complements GAN-based approaches explored elsewhere in this thesis, reinforcing the broader objective of leveraging AI-driven solutions to optimize SHG image acquisition and analysis.

Key Findings: The study demonstrates that ESRGAN successfully reduces imaging time while maintaining high image quality and analytical accuracy, making it a viable tool for improving P-SHG imaging efficiency. ESRGAN exhibits superior structural preservation, contrast enhancement, and reduced artifacts, enabling accurate fiber orientation analysis in upscaled images. The model successfully reconstructs ECM structure and fiber orientation details, ensuring that upscaled images retain key biological features necessary for P-SHG analysis. One of the critical findings was that not all ESRGAN variants performed equally well for SHG imaging applications. Certain ESRGAN variants introduced undesirable artifacts, such as over-smoothing, texture loss, and edge distortions, while others failed to preserve fine details in fiber orientation data. The study identified the most suitable ESRGAN architecture, which provided the best balance between sharpness, structural accuracy, and computational efficiency for P-SHG imaging. The ability to select the optimal ESRGAN variant enhances the practical implementation of this method in biomedical imaging. Another key finding was that ESRGAN allows for a significant reduction in imaging time, demonstrating its potential to minimize acquisition time in P-SHG imaging. This advancement makes SHG microscopy more cost-effective and accessible, enabling high-quality imaging without the need for extended acquisition times.

Support for Hypotheses: The findings confirm the hypothesis that GAN-based super-resolution can improve imaging resolution under reduced acquisition time conditions while preserving image quality. ESRGAN successfully reconstructed collagen fiber orientation and ECM structures, ensuring that critical biological information was retained in upscaled images. The results also confirmed that imaging time could be reduced without sacrificing image clarity, supporting the idea that deep learning-based super-resolution can mitigate photodamage in P-SHG imaging. The study further validated the hypothesis that certain ESRGAN variants performed better than others, with specific architectures proving more effective at preserving texture and structural integrity while minimizing upscaling artifacts, reinforcing their potential as a practical alternative to direct high-resolution imaging in SHG microscopy.

Novel Contributions: This research presents a novel application of GAN-based resolution enhancement in biomedical SHG imaging, demonstrating a method that balances image quality, acquisition speed, and structural accuracy in P-SHG imaging. By systematically evaluating different ESRGAN variants, this study provides a clear framework for selecting the most effective architecture for SHG applications, reducing the risk of artifact introduction while maximizing resolution improvements. The ability to reduce acquisition time without sacrificing analytical accuracy offers a practical solution for overcoming cost and time constraints in high-resolution SHG imaging, making advanced imaging techniques more accessible to the biomedical research community.

Comparison with Existing Research: This study builds upon existing research by applying GAN-based upscaling specifically to P-SHG imaging. Unlike previous approaches that rely on direct high-resolution acquisition, this study demonstrates that GAN-based models can reduce the need for extensive imaging time and laser exposure, making P-SHG imaging more practical for long-term studies and live imaging applications. The work also contributes to the broader field of biomedical imaging by highlighting the importance of selecting the proper resolution-enhancing model to achieve optimal results, providing a structured approach for implementing AI-driven methodologies in SHG microscopy.

2.3 Thematic cohesion across articles

The four articles presented in this thesis are intricately connected through their collective focus on enhancing second harmonic generation (SHG) microscopy. Article 1 provides the theoretical and historical context and sets the foundation for the entire research. It offers insights into the existing capabilities and limitations of SHG microscopy, highlighting the need for technological advancements. Building on this foundation, Article 2 focuses on image classification and employs deep learning techniques to improve the accuracy of identifying different tissue types. Automated image analysis demonstrated how CNNs can transform SHG microscopy into a more precise tool for clinical applications. Article 3 examines the effectiveness of denoising techniques, highlighting how these models can enhance image quality by reducing noise while preserving crucial structural details. These advancements are pivotal for biomedical imaging, where clarity and accuracy are essential. Finally, Article 4 explores improvements in imaging speed and resolution. This demonstrates that generative adversarial networks (GANs) can significantly reduce imaging time without sacrificing quality, making SHG imaging more efficient and accessible. Together, these articles form a unified narrative supporting the overarching thesis of advancing SHG microscopy with machine learning.

Articles 2, 3, and 4 addressed the limitations identified in Article 1 by demonstrating the capability to improve image classification accuracy, enhance image quality through denoising, and increase imaging speed without compromising quality with different ML methods. These advancements overcome key challenges in SHG microscopy, such as the need for expert interpretation, image noise interference, and lengthy acquisition times for high-quality images.

Collectively, these articles address the thesis objectives by exploring SHG microscopy and demonstrating the role of machine-learning techniques in enhancing image quality, speed, and clinical applicability. They present significant technological advancements in terms of image quality, analysis speed, and clinical applicability. This integration illustrates a holistic approach to revolutionizing SHG microscopy, aligning with the thesis's goal of making SHG a robust tool in biomedical research and clinical practice. The articles highlight the potential of overcoming current limitations, expanding SHG applications, and setting new standards for accuracy and efficiency in biomedical imaging.

This progression reflects a comprehensive approach to advancing SHG microscopy from the foundational understanding of the key limitations to implementing enhancements in image quality and speed.

2.4 Consolidated research findings

The combined results demonstrated significant advancements in image quality, automated analysis, and imaging speed in SHG microscopy. Denoising techniques (Article 3) have shown a remarkable ability to enhance image clarity while preserving crucial structural details, thereby addressing a fundamental challenge in SHG microscopy. The deep learning classification model (Article 2) demonstrated the potential for rapid, automated tissue analysis, which could significantly accelerate research and diagnostic processes. The application of GANs to P-SHG imaging (Article 4) represents a major leap forward in reducing the image acquisition time without sacrificing quality, making whole-sample imaging more feasible. Together, these advancements have brought SHG microscopy closer to widespread clinical adoption by addressing key practical limitations.

Collectively, these findings directly address the core objectives of this thesis by demonstrating how machine learning can overcome the technical limitations of traditional SHG microscopy. By integrating denoising, automated analysis, and super-resolution techniques, this research establishes a clear path for making SHG microscopy more efficient, accessible, and clinically viable. These advancements not only reinforce the potential of SHG microscopy in biomedical imaging but also lay the groundwork for its broader adoption in both research and clinical settings.

2.5 Tools and resources for DL-based microscopy enhancement

To facilitate the integration of deep learning in microscopy, several open-source tools have been developed to streamline image processing, model selection, and visualization. These tools significantly reduce the technical barrier for researchers by providing pre-trained models, user-friendly interfaces, and cloud-based platforms that do not require extensive coding expertise.

OpenModelDB (https://openmodeldb.info/) is a community-driven database of AI models for image upscaling and enhancement. It provides researchers with an accessible platform to compare, select, and download deep learning models tailored for imaging applications. By offering a variety of models, OpenModelDB enables efficient selection of AI-based solutions for SHG image processing.

CAREamics (https://github.com/CAREamics) is a deep learning framework designed for microscopy image restoration. It incorporates AI-based denoising models such as N2V 2D and CARE 2D, both of which were explored in this thesis for enhancing SHG image quality. CAREamics offers a streamlined, user-friendly approach to AI-based denoising, making it accessible to researchers.

ZeroCostDL4Mic (https://github.com/HenriquesLab/ZeroCostDL4Mic) is a Google Colab-based platform that enables researchers to apply deep learning pipelines to microscopy images without programming expertise. It provides pre-configured workflows for tasks such as image restoration, segmentation, and super-resolution, making AI-powered microscopy analysis accessible to a wider range of users. By eliminating the need for local computational resources, ZeroCostDL4Mic facilitates rapid deployment of AI techniques in biomedical imaging.

ChaiNNer (https://github.com/chaiNNer-org/chaiNNer) is a node-based, no-code AI workflow tool designed for image processing. It allows users to build complex deep learning pipelines using a visual interface rather than writing code. ChaiNNer supports a variety of AI-based image restoration and enhancement techniques, making it particularly useful for researchers looking to apply deep learning to microscopy images without extensive programming knowledge. Its modular design enables easy experimentation with different models, including upscaling, denoising, and super-resolution techniques.

Netron (https://netron.app) is an intuitive neural network visualization tool that allows researchers to analyze, debug, and optimize AI models used in SHG image processing. By providing a graphical representation of neural networks, Netron enhances model interpretability, helping users identify key parameters, adjust architectures, and fine-tune models for microscopy applications.

The integration of these tools supports this thesis's objective of enhancing SHG microscopy through deep learning while ensuring accessibility to a broad range of researchers. By leveraging platforms like ChaiNNer, Careamics, and ZeroCostDL4Mic, researchers can apply advanced AI techniques without requiring extensive coding knowledge, making deep learning more practical for SHG microscopy.

3 SECOND HARMONIC GENERATION: A POWERFUL TOOL FOR BIO-IMAGING

LA MICROSCOPIE DE GÉNÉRATION DE SECONDE HARMONIQUE : UN OUTIL PUISSANT POUR L'IMAGERIE BIOLOGIQUE

Authors :

Arash Aghigh[1], Stéphane Bancelin[2], Maxime Rivard[3], Maxime Pinsard[4],
Heide Ibrahim[1] and François Légaré[1*]

[1] Centre Énergie Matériaux Télécommunications, Institut National de la Recherche Scientifique, Varennes, Québec, Canada.

[2] Univ. Bordeaux, CNRS, IINS, UMR 5297, F-33000 Bordeaux, France

[3] National Research Council Canada, Boucherville, Québec, Canada.

[4] Institut national de recherche en sciences et technologies pour l'environnement et l'agriculture, Paris, France.

Titre de la revue ou de l'ouvrage :

Biophys Rev **15**, 43–70 (2023).

- Received 02 August 2022
- Accepted 21 December 2022
- Published 19 January 2023

https://doi.org/10.1007/s12551-022-01041-6

Contribution des auteurs :

A.A conceived and wrote this review article. A. A., S. B., M. R., and M.P. participated in drafting, section arrangement, and critical revision of the manuscript. H. I. and F. L. critically revised the manuscript for important intellectual content and approved the final version to be published.

3.1 Main article

Abstract

Second harmonic generation (SHG) microscopy is an important optical imaging technique in a variety of applications. This article describes the history and physical principles of SHG microscopy and its more advanced variants, as well as their strengths and weaknesses in biomedical applications. It also provides an overview of SHG and advanced SHG imaging in neuroscience and microtubule imaging and how these methods can aid in understanding microtubule formation, structuration, and involvement in neuronal function. Finally, we offer a perspective on the future of these methods and how technological advancements can help make SHG microscopy a more widely adopted imaging technique.

Keywords: Nonlinear microscopy, SHG, neuroimaging, interferometry, polarimetry

Introduction

Despite being tremendously powerful tools, conventional linear optical microscopes suffer from scattering and a lack of optical sectioning in thick and complex samples [190]. Over the past two decades, Second Harmonic Generation (SHG) microscopy has become a key method for optical imaging with many applications in materials and biomedical science. Advancements in the development of reliable and robust ultrafast mode-locked laser technologies have been pivotal for the improvement of nonlinear optical microscopy techniques [191–193], especially for biomedical imaging. Using these laser sources, turn-key microscopes have been developed and are now widely spread within research laboratories.

SHG microscopy imposes a requirement: the structure of interest needs to be non-centrosymmetric [39], which makes it highly sensitive to filamentous proteins in biological samples [48,87]. Otherwise, samples must be stained with appropriate SHG dyes [109]. While this requirement limits SHG application to only a few structures, it is also a key strength since the signals are highly specific and offer sharp contrast images. Beyond that, SHG microscopy has several advantages over fluorescence imaging: it is based on an endogenous contrast (i.e., the contrast arises from the sample itself and not in a e.g., a fluorophore). Lastly, unlike fluorescence, SHG is free from photobleaching (the signal generated is not limited in time) and occurs instantaneously (no limitation on the laser repetition rate) [14].

In this review, we will first provide an overview of SHG microscopy of highly organized biological structures from its history and theoretical principles to its application to various tissues. We will then focus on several advanced SHG modalities and lastly, we will discuss SHG application in neuroscience.

Second harmonic generation microscopy for biomedical imaging

In this section, we will briefly describe the history behind SHG microscopy, and we will provide a brief introduction of the principles behind the SHG signal generation and how it can be applied to biomedical research.

History

An exhaustive historical overview on SHG would start in the 19th century, during which Lord Rayleigh introduced the non-linearity of acoustic waves in his theory of sound [194,195]. In this review, we will focus on the use of laser driven SHG processes to provide imaging contrast in biological samples in parallel to the development of advanced microscopy techniques. For a more comprehensive and in-depth look into the history and development of SHG microscopy we refer to Masters and So [196].

In 1931, two-photon absorption was theoretically predicted by Goeppert-Mayer [197]. Three decades later, in 1960, the ruby laser was created by Maiman [20] based on the theoretical foundation developed by Schawlow and Townes [21]. For more details on laser invention and its fundamental impact in science and technology, we suggest the excellent review by Siegman [198]. Almost immediately after this discovery, different non-linear optical processes were observed starting with SHG in 1961, when Franken *et al*. observed frequency doubling of a ruby laser in a quartz crystal [22]. At this time, the measured SHG signal was so dim that it was famously mistaken by the *Physical Review* editor as a speck of dust. In 1962, Bloembergen and Pershan derived the SHG equations and described key principles ruling light-matter non-linear interaction through an in-depth review of Maxwell’s equations [23]. For a comprehensive and detailed explanation of the fundamentals and formulations of non-linear optics, we strongly recommend the Nonlinear Optics book [39]. As for biological samples, the first attempts to understand piezoelectric and pyroelectric effects in bone and tendon were realized in 1964 by Fukada and Yasuda [199] and in 1966 by Lang [200]. They demonstrated that tendon has a macroscopic polar structure using piezoelectric [199] and pyroelectric measurements [200], although without successfully identifying the structural origin of piezoelectric and pyroelectric effects.

In parallel, the confocal microscope, originally developed by Minsky in 1955 to image unstained neural networks of the brain [12,201], encountered a tremendous success, leading to the first implementation of laser scanning confocal microscopy in the late ’60s. In 1974, Hellwarth and Christensen already combined SHG with optical microscopy by applying a focused laser on potassium deuterium hydrogen phosphate (KDP) crystals [24]. However, this method was solely based on very strong SHG converters as the entire field was illuminated with a CW laser. In 1977, Sheppard *et al*. imaged quartz with a scanning SHG microscope using a tight focusing that allowed to detect the non-linear optical signal [25]. Simultaneously, Parry and Craig showed, using electron microscopy (EM), that collagen fibrils composing tissues, such as tendons, possess an architecture with mixed polarity with neighboring fibrils pointing in opposite directions [26]. This was later confirmed using the combination of atomic and piezoelectric force microscopy [27,28]. In 1978, Roth and Freund reported on comparative measurements between the SHG signal of a reference quartz sample and a rat-tail tendon. They found that the SHG signal was 3-4 orders of magnitude lower in the biological sample than in the reference material and already highlighted that SHG measurements could be advantageously used *in vivo* [29]. Finally, in 1986, Freund and Deutsch were the first to perform SHG microscopy of biological samples and proved that the macroscopic polar structure in the tendon arises from the network of fine structures that happen to be collagen fibrils, within the whole tissue volume [30]. In that pioneering publication, the viability of using SHG microscopy for biomedical imaging was demonstrated.

In 1990, Denk *et al*. introduced two-photon excitation fluorescence (2PEF) laser scanning microscopy using pulsed lasers and a modified confocal microscope [31]. Following the success of 2PEF, in 1996, three-photon excitation microscopy was demonstrated [202]. Although the SHG modality is older than 2PEF microscopy [31], it was forgotten for over a decade and rediscovered in 1998 [33,34] and combined with 2PEF in the early 2000s in many studies [35–37]. Since then and following the progress in commercially available mode-locked lasers and user-friendly multiphoton microscopes [203], SHG has become a powerful method for multimodal high spatial resolution optical imaging.

SHG microscopy

In the context of microscopy, 2PEF and SHG present many technical similarities, which allows to combine them easily and efficiently in the same instrument. A typical implementation of a modern SHG microscope, obtained after many experimental setup iterations, is depicted in Figure 3-1.

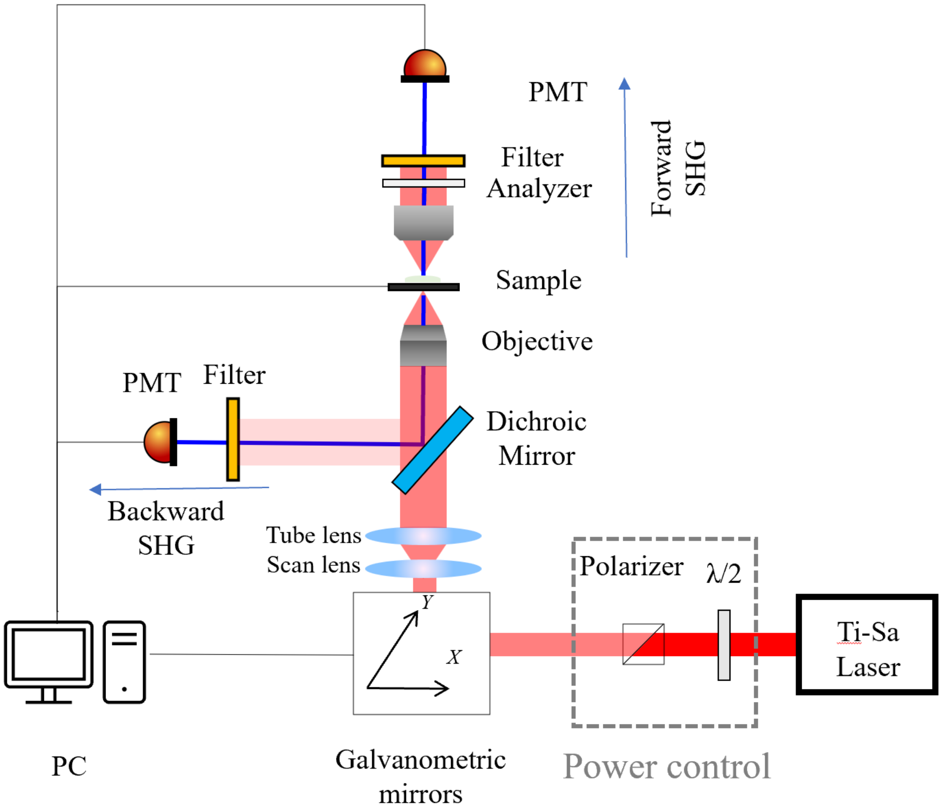

Figure 3-1: Typical SHG microscopy setup, with source, power control unit, scanning system, objective lens, and detectors. Detectors are connected to a PC that controls the microscope and synchronizes laser scanning with signal acquisition using a detector which is typically a photo multiplier tube (PMT).

Since the obtained imaging depth depends on the excitation wavelength [14,190], the employed laser is traditionally in the NIR-I region (700-1000 nm) [204] to minimize absorption from biomaterials (water, hemoglobin) [36]. It is worth noting that other optical “windows” matching this criterion are available, as indicated in Figure 3-2. Using longer wavelengths, *e.g.* NIR-2 (1000-1300 nm), allows to limit scattering and hence to increase the penetration depth in the tissues [14,190] however at the expense of a reduced spatial resolution. Despite the higher penetration depth provided by longer wavelengths, it has been shown that, at least for imaging collagenous tissues, longer wavelengths result in lower SHG signal as the hyper-polarizability tensor decreases [205]. Therefore, shorter wavelengths should still be favored for performance. Besides that, the use of long wavelength lasers (1230 nm), such as Cr:forsterite lasers, provides the opportunity to simultaneously perform SHG and third harmonic generation (THG) microscopy in the visible range, avoiding the UV absorption of biological samples [206].

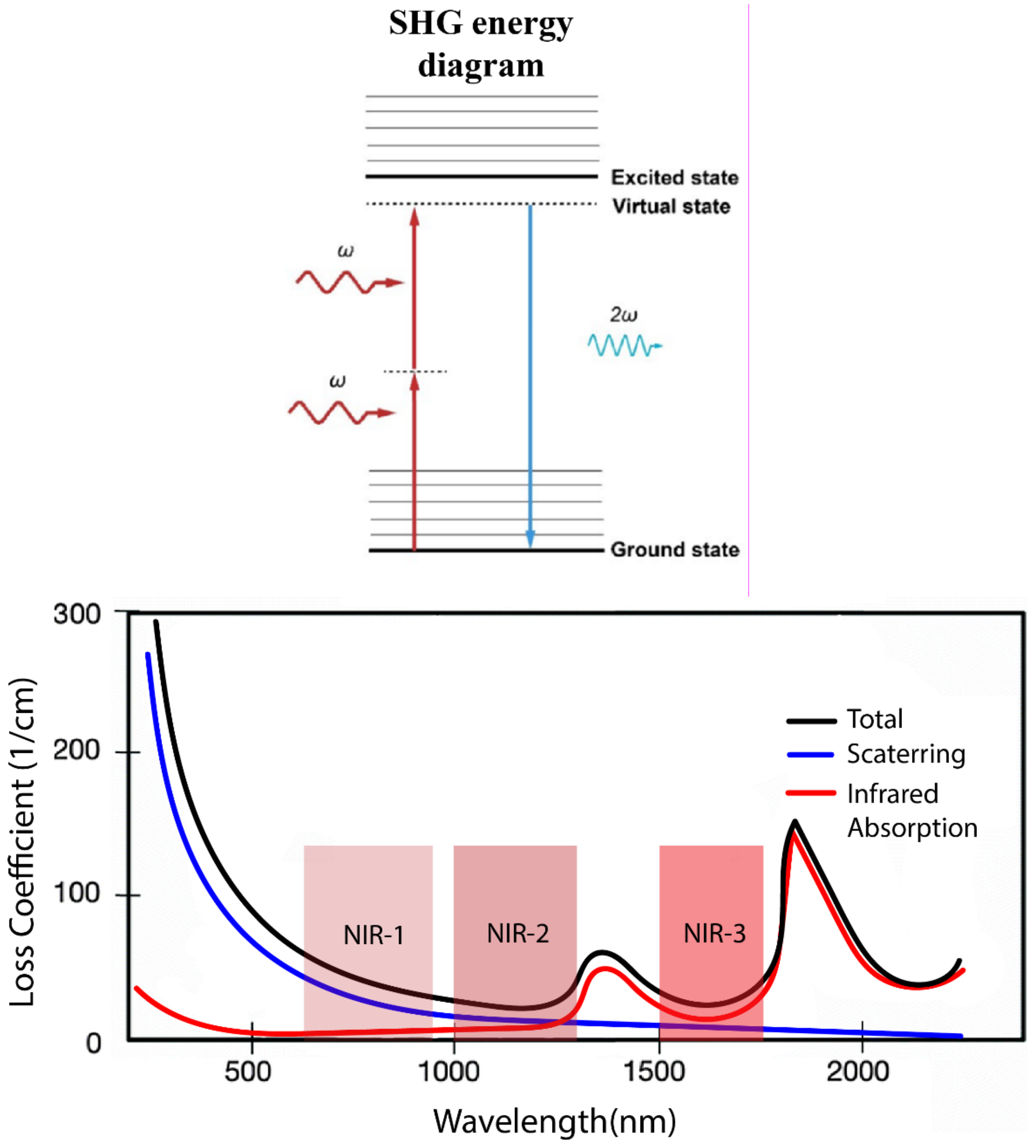

Figure 3-2: Top: energy level diagram of SHG. Two incident photons interact with the molecules (harmonophores) through virtual states, leading to the generation of a photon at 2ω, exactly twice the input frequency (ω). SHG is a parametric process, and no energy transfer occurs. Reproduced under CC BY 4.0 from [292]. Bottom: Absorption spectrum of the human skin, indicating 3 possible transparency windows. Adapted with permission from [36].

To favor the efficient generation of the non-linear optical signal, the typical pulse duration is about 100 fs at a repetition rate of a few tens of MHz [14]. High numerical aperture (NA>1) objectives are used to tightly focus the light on the sample and spatially concentrate laser pulse energy [47]. For thin samples, where the light can be detected in the forward direction (see Figure 3-1), a high numerical aperture condenser is added to efficiently collect the light [87]. Both modalities (2PEF and SHG) present a quadratic dependence of the generated signal to the input laser intensity [191], leading to an intrinsic three-dimensional spatial resolution due to the signal generation being confined in the focal volume [40].

Despite these similarities, SHG and 2PEF techniques are based on fundamentally different processes. In SHG, the frequency conversion is achieved through virtual states without a net transfer of energy to the system (Figure 3-2). This contrasts with 2PEF which involves population transfer from the electronic ground state to excited electronic states. These different origins lead to radically different, and often complementary properties that explain the rising popularity of SHG microscopy.

SHG microscopy of endogenous proteins

Second-order non-linear processes, such as SHG, can be efficiently described through an anharmonic oscillator model in which a non-linear restoring force is generated by the molecular potential. At the molecular level, SHG originates from the hyperpolarizability of peptide bonds in collagen and tubulin, usually considered as single SHG emitters [207]. Indeed, an electric field oscillating at a high frequency and reaching an harmonophore will repeatedly pull the electrons back and forth, leading to the induction of a molecular dipole [39,40,48]:

$$\boldsymbol{p} = \boldsymbol{p}^{(\mathbf{0})} + \alpha\boldsymbol{E} + \beta\boldsymbol{E}\boldsymbol{E} + \gamma\boldsymbol{E}\boldsymbol{E}\boldsymbol{E} + \cdots \qquad 3.1$$

where α is the polarizability of electrons of the peptide bond, **E** the incident electric field and β and γ the hyperpolarizabilities of the first and second order, respectively. The first term $\mathbf{p}^{(0)}$ is the permanent dipole of the molecule. The second term corresponds to the linear response, the third one defines second order non-linear interactions, such as sum and difference frequency generation [39], and the fourth term describes third order non-linear effects (*e.g.* two-photon absorption [40], third harmonic generation [41], Kerr effect [42], self-phase modulation [43], cross-phase modulation [44], and stimulated Raman scattering [45]).

As a degenerate case of sum frequency generation, SHG arises from the third term in Equation 1. Molecules capable of emitting SHG are characterized by a high hyperpolarizability β, which strongly depends on their symmetry. Indeed, in the case of a molecule having a center of symmetry, elements contributing to the molecule's hyperpolarizability cancel each other, preventing SHG formation. More generally, the generation of even harmonics is only possible in non-centrosymmetric materials.

The coherent nature of SHG implies that the signal results from interferences of individual contributions of harmonophores. Figure 3-3 illustrates the case with simple dipoles, separated by a distance negligible with respect to the wavelength of the incoming light wave. When the electric fields emitted by the two dipole moments are in phase and thus constructively interfere, the resulting SHG is coherently added (central row). In contrast, there is destructive interference when the dipole moments have opposite directions and the SHG signal vanishes [39] (bottom row).

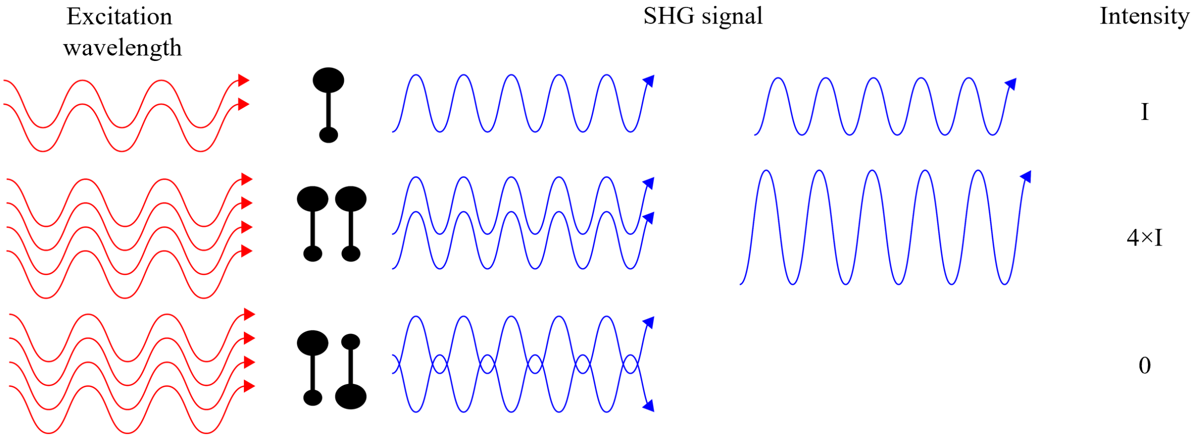

Figure 3-3: Comparison of the SHG signal from a single dipole (upper row) to the SHG from two parallel (central row) and anti-parallel dipoles (bottom row). Adapted from [208].

At macroscopic scale, SHG is described by the non-linear susceptibility $\chi^{(2)}$, which results from the coherent summation of the individual hyperpolarizabilities of all harmonophores within a volume. The relation between the molecular and macro-molecular nonlinear response is given by [47,48]:

$$\chi^{(2)} = N_S < \beta > \qquad 3.2$$

where N_S is the density of molecule S and <β> is the orientational average of the first hyperpolarizability [39]. For SHG to occur, at this scale, the medium should exhibit a $\chi^{(2)} \neq 0$ [40,47], which only happens for non-centrosymmetric macromolecular organization.

Consequently, to perform SHG microscopy in biological samples, the tissue must present a non-centrosymmetric structure both at the molecular scale ($\beta \neq 0$) and at the macro-molecular level ($< \beta > \neq 0$) as well as a high density of harmonophores. Interestingly, this constraining origin of the signal can be exploited as a contrast enhancing mechanism, since it makes the occurrence of the SHG signal highly specific to only a few biological entities, with collagen as a prime example. SHG can thus act as a unique probe of the multiscale distribution of molecules within the sample.

Properties of the SHG signal

Before discussing the properties of the SHG signal, one should have a closer look at the hyperpolarizability and second order nonlinear susceptibility.

In the general case β, and therefore $\chi^{(2)}$, are third order tensors with 27 components ($\chi^{(2)}_{ijk}$). However, depending on the symmetry of the molecules, the number of non-zero and independent components can be reduced. In this review, we will assume that the Kleinman symmetry condition holds true [39], which requires that the excitation and emission wavelength must be far from resonance, which is the case in most biological samples (e.g. collagen) [55]. Under this assumption, the last two indices of $\chi^{(2)}_{ijk}$ can be freely permuted. Thus, we can regroup the two last indices (*jk)* into a single index *l* and introduce the new tensor:

$$d_{il} = \begin{bmatrix} d_{11} & d_{12} & d_{13} & d_{14} & d_{15} & d_{16} \\ d_{21} & d_{22} & d_{23} & d_{24} & d_{25} & d_{26} \\ d_{31} & d_{32} & d_{33} & d_{34} & d_{35} & d_{36} \end{bmatrix} = \frac{1}{2}\chi^{(2)}_{ijk} \qquad 3.3$$

Note that with the Kleinman symmetry and the permutation, not all 18 components in the matrix are independent ($d_{12} = d_{26}$ and $d_{14} = d_{25}$). Considering only the second order effect in Equation 1, the dipole momentum induced by the incident laser is given by:

$$\begin{bmatrix} p_x^{(2)}(2\omega) \\ p_y^{(2)}(2\omega) \\ p_z^{(2)}(2\omega) \end{bmatrix} \propto \begin{bmatrix} d_{11} & d_{12} & d_{13} & d_{14} & d_{15} & d_{16} \\ d_{21} & d_{22} & d_{23} & d_{24} & d_{14} & d_{12} \\ d_{31} & d_{32} & d_{33} & d_{34} & d_{35} & d_{36} \end{bmatrix} \begin{bmatrix} E_x^2(\omega) \\ E_y^2(\omega) \\ E_z^2(\omega) \\ 2E_y(\omega)E_z(\omega) \\ 2E_x(\omega)E_z(\omega) \\ 2E_x(\omega)E_y(\omega) \end{bmatrix} \qquad 3.4$$

Equation 4 shows that the polarization of the input laser beam is of utmost importance since it is directly related to the tensor elements [91,209] and therefore largely determines the formation of SHG signal.

In the following case, we will use collagen as an example, but this can also be extended to other materials by considering their specific symmetry. A collagen fibril presents a cylindrical symmetry. We will make two assumptions: first that the Kleinman symmetry is applicable [55] and secondly that the chiral components of the tensor can be neglected since we do not take the out-of-focus orientation into account [55]. In this condition, the nonlinear susceptibility tensor has only two independent components which are χ_{xxx} and χ_{xyy}, where *x* is the fibrillar axis. Thus, considering that the input laser is linearly polarized and propagates along the *z*-axis, the SHG intensity in every pixel of an image is:

$$I_{SHG}(\theta, \mu) = A + Bcos(2\mu - 2\theta) + Ccos(4\mu - 4\theta) \tag{3.5}$$

where μ is the polarization angle with respect to the x axis, θ the azimuthal angle of the fibril (see schematic in Figure 3-8) with the x axis, and A, B, C are coefficients depending on the harmonophore concentration and arrangement [99]. Therefore, varying the incident polarization strongly affects the SHG intensity. This, in turn enables to probe macro-molecular organization of harmonophores within the focal volume [37]. Alternatively, the use of circularly polarized excitation light ensures that all molecules respond similarly, regardless of their in-plane orientation [40].

Since SHG is a coherent process, the phase plays a key role in the signal formation, from the molecular to the macromolecular scale. This can be clearly highlighted considering the case of SHG from bulk media. A complete description of the formalism in this case can be found in [39]. In brief, considering an incident laser beam with fixed polarization and propagation direction, and assuming the slowly varying envelop approximation, the SHG intensity can be expressed as:

$$I_{SHG} \propto |\psi|^4 L^2 \mathrm{sinc}^2\left(\frac{\Delta kL}{2}\right) = {I_{in}}^2 L^2 \mathrm{sinc}^2\left(\frac{L}{L_c}\right) \tag{3.6}$$

where ψ is the complex amplitude of the incident beam, I_{in} is the intensity of the incident laser beam, L is the length over which SHG occurs in the medium, $\Delta k = 2k_{\omega} - k_{2\omega}$ is the phase mismatch between the excitation and the emitted light (expressed as the difference of wave-vectors) and $L_c = 2/\Delta k$ is the coherence length. Consequently, when the phase-matching condition $\Delta k = 0$ is fulfilled, the SHG intensity directly scales with the square of the input laser intensity and with the square of *L*. However, if $\Delta k \neq 0$, the SHG intensity reaches a maximum value after an interaction length of $\pi L_c/2$. In that case, if the interaction length L is any longer in the material, the SHG intensity oscillates between zero and the maximum value over a spatial period of $2\pi L_c$.

In biological samples, the phase matching condition is rarely fulfilled, leading to a directionality of the SHG signal. However, ΔkL is nearly equal to zero for the forward direction since the length of interaction is small compared to L_c (few microns), due to the tight focusing. In backward direction, this is not the case since Δk is much larger and the coherence length is much shorter (a few tens of nanometer). This explains why “pure” backward SHG is always very weak. This effect will be further discussed in section II.

SHG microscopy in biological samples

One of the most ubiquitous proteins in body tissue that can be imaged using SHG microscopy is collagen, a family of proteins found in most connective tissues. At the molecular scale, collagen consists of three α-chains, called tropocollagen, which are hydrogen bonded to each other [40]. In some collagen types (mostly I and II) these triple helices spontaneously self-assemble into highly organized collagen fibrils [87] leading to very strong SHG signals [86]. In contrast, non-fibrillar collagen (*e.g.* type IV), which forms sheets in basal laminae [87], cannot be visualized with SHG microscopy [35].

The first demonstration of SHG microscopy in biological tissue has been performed using rat-tail tendons by Freund and co-workers [30]. In this tissue, collagen type I forms a highly organized multiscale structure as depicted in Figure 3-4. SHG microscopy has been used to image Achilles tendon and fascia [210]. It has also found application to monitor the healing process of tendons [211].

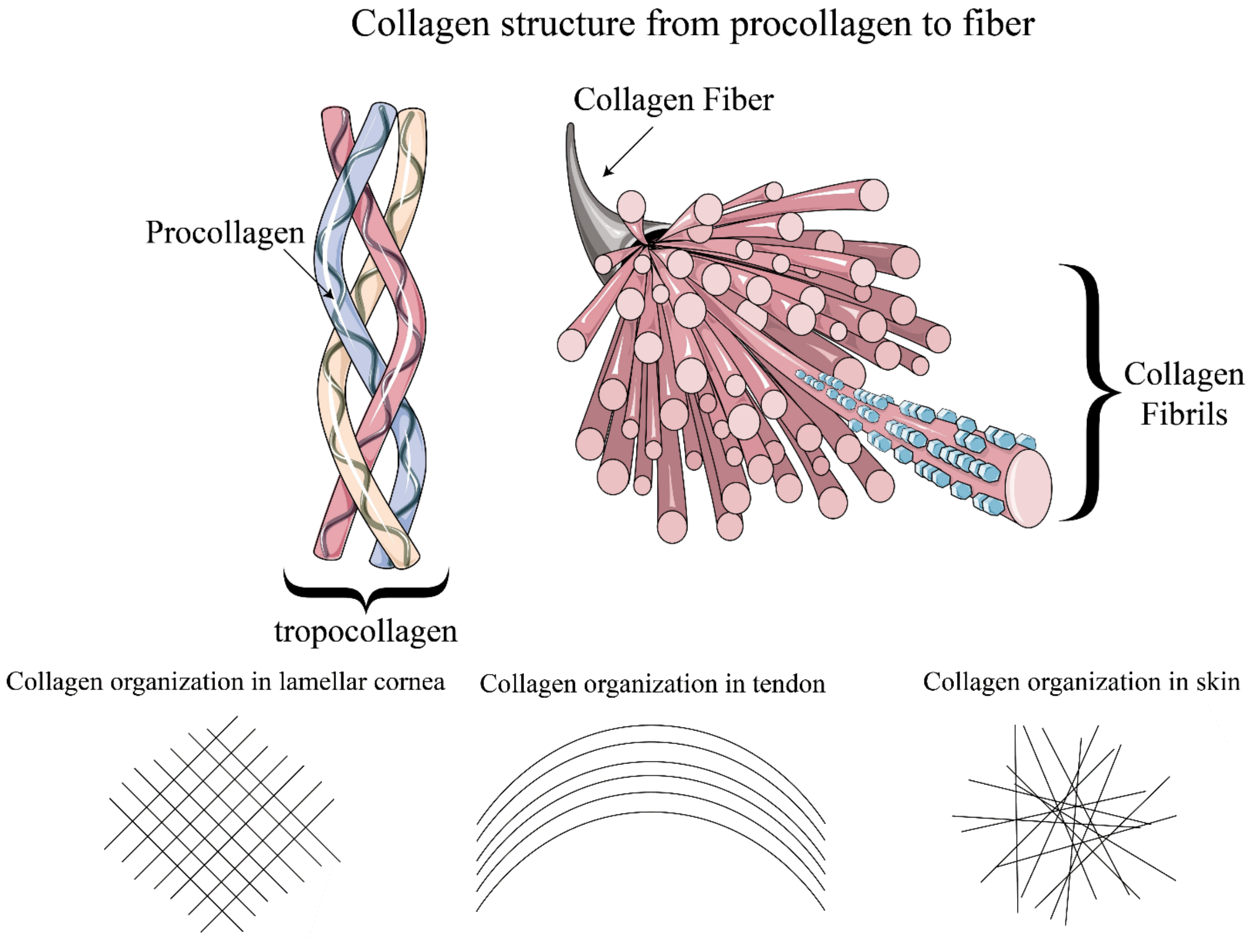

Figure 3-4: Hierarchical structure of collagen. Modified under CC BY-SA 3.0 from [212] . Bottom: Collagen organization in different biological entities [213–215].

The eye is one prominent example containing – mostly – collagen type I in two different components: the cornea and the sclera [216], which hence can be visualized using SHG microscopy. An example is shown in Figure 3-5(a) and (b). Within the cornea, the collagen is arranged in a lamellar configuration contributing to corneal transparency [216] while in the sclera, collagen fibrils are randomly packed and highly scattering [217]. Tendon and cartilage are two other tissues that have been well-studied using SHG microscopy with examples shown in Figure 3-5(c) and (d) [72,214]. The skin is another biological component that has been imaged by SHG microscopy. As an example, a recent study by Ogura *et al.* compared skin samples from humans in their young, middle and old age, reporting that the concentration of thick collagen declines with age [218] (see Figure 3-5(e) and (f)).

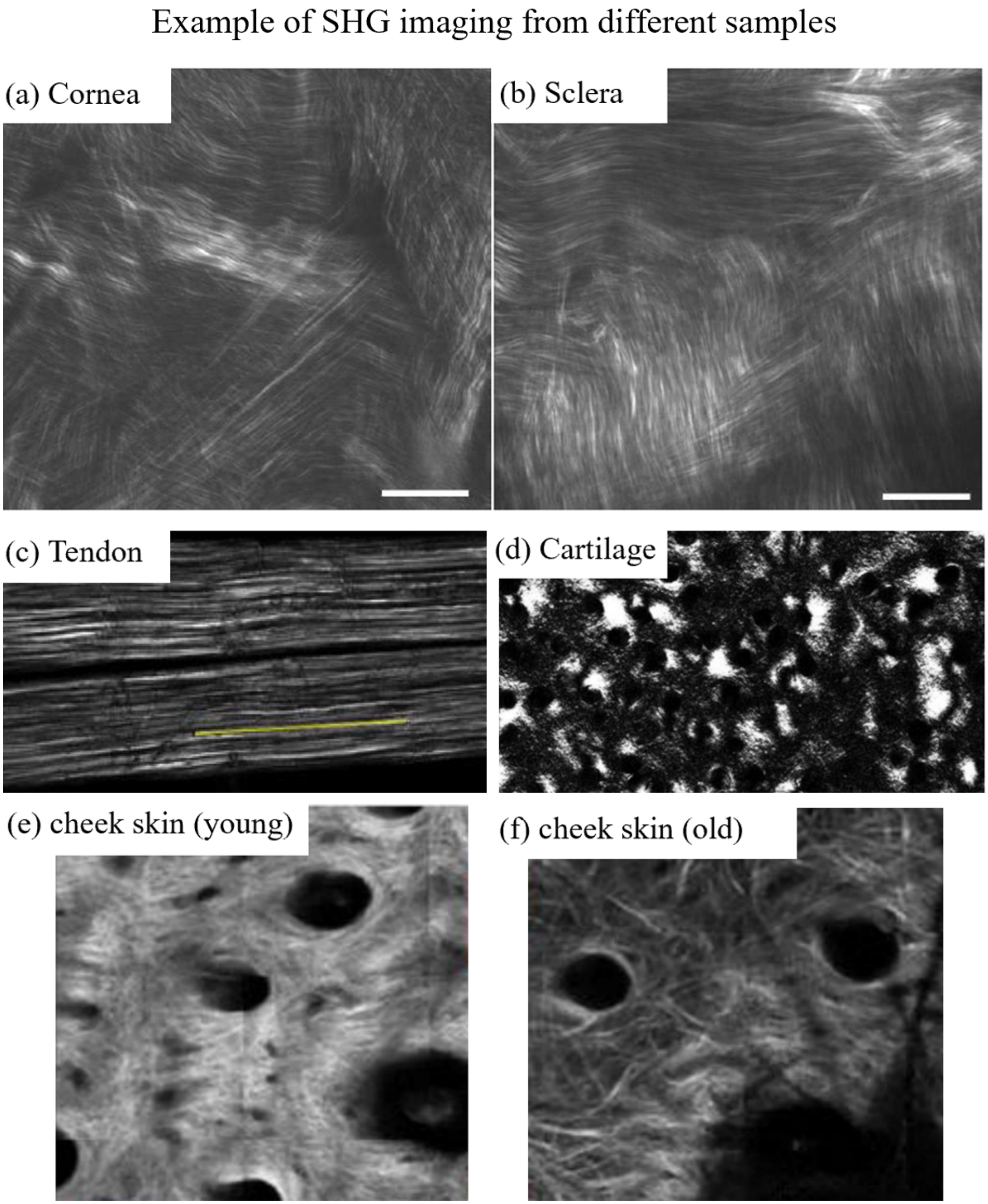

Figure 3-5: Examples of SHG images for various biological samples. SHG images from (a) cornea and (b) sclera, the scale bar is 20 µm. Extracted from [219]. (c) Tendon (500×150µm), extracted with permission from

[214]. (d) Cartilage (350×200µm), extracted with permission from [72]. SHG image of skin in young (e) vs. old age (f) (1.6×1.6mm), extracted with permission from [218].

In addition, SHG microscopy has been proven useful to image cartilage and bones [220,221], which are composed of collagen type II. This opened avenues to investigate damages of the extracellular matrix that can result in loss of structure integrity, which leads to various pathologies such as osteoarthritis. Many pathologies such as cancer can be investigated and characterized using these techniques but are beyond the scope of this review. Extensive details on these applications can be found in the literature [40,125,222,223].

Beyond collagen, other biological structures have been investigated by means of SHG microscopy. Myosin is a motor protein involved in a wide variety of functionalities, such as muscle contraction, or cellular movements that are largely influenced by the interaction between actin and myosin [224]. Therefore, the visualization of the myosin structure is bound to increase our understanding of fundamental mechano-cellular mechanisms. Mohler *et al*. first observed a strong SHG signal in mouse muscle and then confirmed in *C.elegans* that the signal arises from the heavy-chain B of myosin [48]. Studies combining SHG microscopy and 2PEF revealed enlarged lysosomes in Pompe disease and provided advanced characterization of the morphology of cardiomyocytes [101,225]. A combination of SHG and coherent anti-Stokes Raman scattering has also been used to study muscle structure [226]. More recently, wide-field SHG was applied for imaging muscle contractions, which will be briefly discussed in section II [83].

Microtubules (MTs) are another key element that can be imaged using SHG microscopy [125], allowing fascinating studies in neurosciences and developmental biology. Section III is specifically dedicated to present the recent advances of SHG microscopy for MTs studies.

Finally, beyond the study of body tissues, another application of SHG microscopy is for imaging polysaccharide chains in plants and notably in starch. Starch plays an important role in energy storage for plants and represents a major source of food for humans. In 2005 Cox et al. reported on SHG signal from cellulose and starch, which can be explained by their highly crystalline structure [227]. However, while the starch SHG signal can easily be detected at low input powers, acceptable for biological tissue imaging, cellulose was found to be a weak SHG emitter. In the same study, the authors suggested that the origin of the SHG signal in starch granules is from two polysaccharides, namely amylopectin and amylose. By performing SHG and polarization resolved SHG microscopy on starch from rice and rice flour, Zhuo et al. demonstrated that the SHG emitter in starch were only amylopectin and not amylose [228]. Building upon this study, Cisek et al. examined barley and found that wild-type amylopectin crystals generate higher SHG signal due to their long-range order [229]. On the other hand, structures containing amylose, have much lower crystalline order leading to much lower SHG emission (~20 times less) [229]. Moreover, the hydration state strongly affects the SHG intensity of starch granules [229,230]. Hydrated granules have a higher SHG intensity (Figure 3-6) due to the more ordered crystalline hydroxide and hydrogen bonds forming long-range orders, whereas ultra-dry structures have a more disordered structure [229].

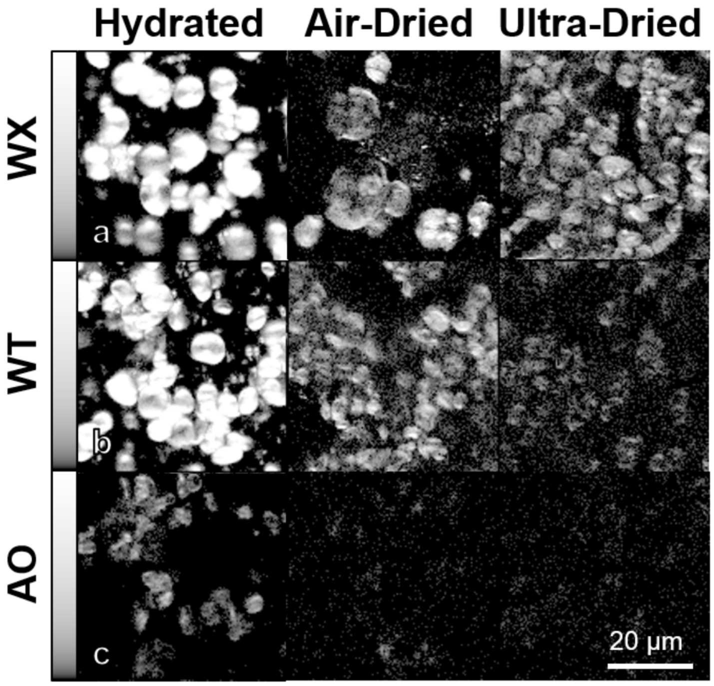

Figure 3-6: SHG imaging of three types of barley starch granules in different hydration states. a) WX (Waxy barley with only amylopectin) exhibits a very high SHG intensity even in ultra-dry conditions. b) WT (wild-type barley with ~30% amylose content) SHG signal is dimmer than in panel a) but still detectable. c) AO (amylose only barley) has the lowest SHG signal intensity among the three, which is barely detectable in ultra-dried condition. Extracted from [224].

Advanced SHG microscopy

Beyond the imaging capability, the coherent and tensorial nature of the SHG process enables us to extract additional information about the sample. This section will outline the main approaches that have been developed over the years and applied to various biological investigations.

Forward over backward second harmonic generation (F/B-SHG)

Forward over backward (also called “directional”) SHG microscopy is a method that takes full benefit from the directionality of the SHG radiation pattern. For complete description, we suggest ref. [40].

Because it is a coherent process, SHG conserves the spatial coherence of the excitation. The harmonic photons are scattered over an angle smaller than the Gaussian beam angle of the excitation. As previously mentioned, (see section I.4), perfect phase-matching is never met in SHG microscopy. The coherence length for forward SHG (F-SHG) is a few microns in most materials, which is enough for a consistent phase matching within a focal volume (not accounting for Gouy phase shift effects though). In contrast, the coherence length for backward SHG (B-SHG) is only a few tens of nanometers in most materials, which means that the B-SHG signal is always poorly phase matched. In practice, the B-SHG signal is always smaller than the F-SHG one, reaching equality only when one dipole or an extremely thin structure is excited along the propagation direction (Figure 3-7 (a-b)). The F-SHG contribution becomes much larger when many dipoles are stacked along the focal volume (Figure 3-7 (c-d)), which is usually the case in biological samples. Importantly, since the B-SHG signal is usually weak it should not be confounded with backscattered F-SHG signal. Indeed, since most biological samples are highly scattering, a significant part of the F-SHG gets scattered or reflected towards the backward direction after its generation (see Figure 3-7) [210].

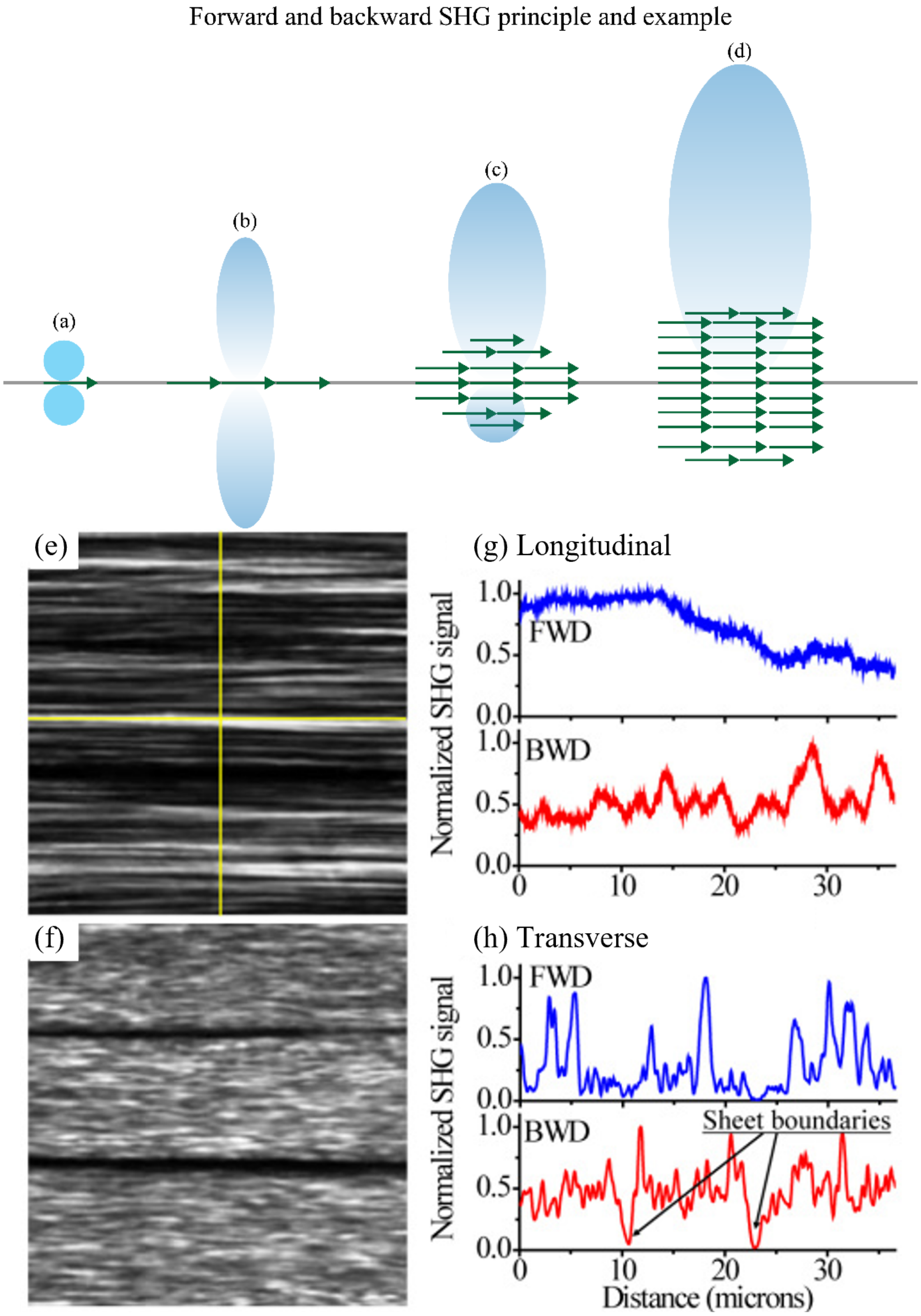

Figure 3-7: Radiation pattern for different dipole configurations in the focal volume. (a) A single dipole, indicated by the green arrow, creates equal F-SHG and B-SHG (F/B=1). (b) Several dipoles in the same plane also create the same amount of SHG signal in the forward and backward direction (F/B=1). (c) The coherent contribution of many induced dipoles packed in the optical direction will generate a strong forward SHG signal and a weak backward SHG signal (F/B>1). (d) For a bulk material, only a strong forward SHG signal is present with a negligible amount of backward SHG. Adapted under CC BY-SA 4.0 from [231]. Forward (e) and backward (f) SHG images of fascia. (g) and (h) respectively represent longitudinal and transverse intensity profiles (with respect to the fibrillar axis (horizontal axis)), as depicted by the yellow crosshair in (e), taken in forward (blue) and backward (red) direction. In the backward direction the sheet boundaries are easier to spot than in the forward SHG image. Extracted from [232].

Figure 3-7 shows an example of F/B SHG images. The F-SHG signal along the fibrils direction (longitudinal) remains exceptionally smooth (Figure 3-7 (e)), revealing that fibril bundles form domains of constant $\chi^{(2)}$ that can lead to a better fulfillment of the phase-matching condition. On the contrary, in the direction perpendicular to the fibrils (transverse), multiple/different $\chi^{(2)}$ domains boundaries are encountered, leading to rapid changes in phase-matching and high modulation of the F-SHG signal (Figure 3-7(f) and (h)). This is in agreement with the conclusion of Freund and Deutsch [30] as well as with the measurements of Parry and Craig using electron microscopy [26]. It is important to highlight that the dark lines in the collagen sheets in the forward image (e) are not due to the lack of collagen fibrils, but due to long $\chi^{(2)}$ domains whose macro-molecular structure results in poor phase-matching, leading to low signal along the full length of the domain. In contrast, since the coherence length in B-SHG is much shorter, the arrangement of the domains has almost no impact on the amount of signal generated. Therefore, the backward image is mostly uniform along the whole tissue.

Effectively, due to the different coherence lengths for F- and B-SHG, the F-SHG signal images display ordered structures whose size are on the order of λ_{SHG} (SHG wavelength), while smaller or more random structures are better revealed in B-SHG, both directions providing complementary images [40]. In the case of collagen, the F/B ratio increases either with the fibrils' diameter or when fibrils of the same polarity are bundled [49,233]. Since this ratio is usually averaged over the whole field-of-view, it quantifies the average size and global arrangement of the collagen bundles in the sample [40].

Polarization-resolved second harmonic generation (P-SHG)

P-SHG couples the benefit of SHG microscopy (high specificity and contrast) and polarimetry (sensitivity to molecular alignment). Usually applied to collagen, it can reveal more accurately the complex hierarchical structures of fibrils in the image plane. One of its first demonstrations has been realized on rat-tail tendon fascia by Stoller and co-workers in 2002 [90]. Acquiring different linear polarization scans in the axial and transverse plane, they identified that the SHG signal was highly affected by the polarization of the input laser light source, allowing the determination of the orientation of collagen fibrils. Figure 3-8 provides an example of a P-SHG system with an application example from an adult horse meniscal collagen.

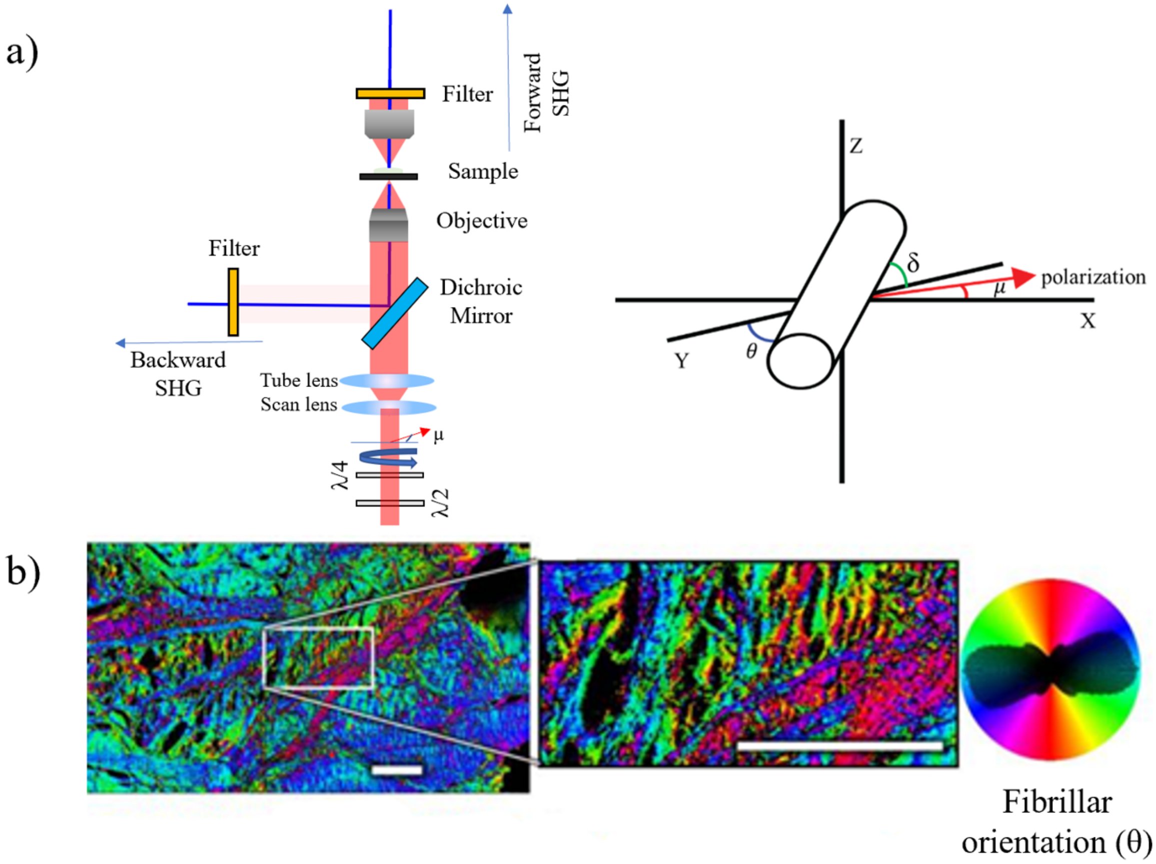

Figure 3-8: a) Schematic of a typical P-SHG microscope with sample in focus. A half-wave plate (λ/2) and a quarter-wave plate (λ/4) are used to control the pump polarization state. Adapted from [63]. b) Collagen fibril orientation in adult horse specimens measured by P-SHG. In this study, the maturation of meniscal collagen was studied in young and adult horses using P-SHG. Extracted under CC BY 4.0 from [234].

To characterize the collagen fibrils' orientation, various parameters can be measured such as the average in-plane azimuthal angle θ, in every pixel, and the anisotropy parameter ρ as indicated in the upper right corner of Figure 3-8 [234]:

$$\rho = \sqrt{\frac{I_{\parallel}}{I_{\perp}}} = \rho_0 \cos^2 \delta + 3 \sin^2 \delta \qquad 3.7$$

where $I_{\parallel}$ (resp. $I_{\perp}$) is the SHG intensity when the incident polarization is parallel (resp. orthogonal) to the fibril, δ is the out-of-plane tilt angle of the fibril and $\rho_0 = \rho(\delta = 0) = d_{33}^{(2)}/d_{31}^{(2)}$ is the anisotropy parameter for no tilt (i.e. $\delta = 0$) [235].

Alternatively, for no out-of-plane tilt, the measure of the "anisotropy parameter" r [47] can be used:

$$r = \frac{I_{\parallel} - I_{\perp}}{I_{\parallel} + 2I_{\perp}} \tag{3.8}$$

Here *r* = 0 corresponds to an isotropic orientation and *r* = 1 to the fully aligned case. In practice, r ~ 0.7 in highly aligned collagen tissue such as tendon [47]. Other parameters such as the entropy of orientation [236] or the orientation index (O.I.) [237] can also be extracted from P-SHG and some studies also reported the variance of the contrast-per-pixel as meaningful metrics for P-SHG [169].

One efficient approach to extract information from P-SHG is based on Fourier transform analysis. In that case, only the input polarization is rotated using half- and quarter-wave plates [92] (Figure 3-8). Afterwards, the relevant information can be retrieved from the P-SHG images using an analysis based on the Fourier transform of the measured intensity with respect to the input polarization angle. This method is applicable to B-SHG and backscattered F-SHG signal, making it particularly well suited for thick *in vivo* samples [92].

A more advanced modality, called PIPO (Polarization In – Polarization Out) [238], introduces an additional rotating analyzer in the detection path, in order to extract the asymmetry of fibrils distribution ς , in complement to the anisotropy ρ:

$$\varsigma = \frac{< \sin\delta >}{< \cos\delta >} \tag{3.9}$$

where <…> is the weighted average.

In the past, P-SHG emerged as a powerful tool for biomedical applications, especially to probe protein structure. Previously, cryo-EM [56] and X-ray crystallography [57] were the tools of choice for this study but both methods require complex and intensive sample preparation, preventing their use on live dynamic samples let alone on living animals [58]. Alternatively, to investigate structural dynamics of proteins, other methods have been used, such as nuclear magnetic resonance and Forster resonance energy transfer (FRET), which are more readily available but have lower spatial resolution and low sensitivity [58]. In contrast, P-SHG can be applied in pristine samples and does not rely on complex and expensive devices for analysis since it only requires adding a few optical components to a regular SHG microscope [58]. Recently, P-SHG has been used to study collagen alteration in aging [59], keratoconic cornea [60], and collagen structure alteration in lung cancer [61]. Note that high precision control of the polarization can be achieved using electro-optical modulators [52].

Circular dichroism second harmonic generation (CD-SHG)

Beyond P-SHG, the use of laser light with left- and right-handed circular polarization (LCP and RCP respectively) allows to extract the so-called circular dichroism SHG [238,239]:

$$I_{CD-SHG} = \frac{I_{(2\omega)LCP} - I_{(2\omega)RCP}}{\left(I_{(2\omega)LCP} + I_{(2\omega)RCP}\right)/2} \qquad 3.10$$

where $I_{CD\text{-}SHG}$ is obtained from subtracting two SHG images acquired with LCP and RCP, respectively. Just like circular dichroism detected in linear microscopy, CD-SHG requires an optical activity to be non-zero (which is concomitant to a chiral symmetry). Yet, non-linear CD does not mandatorily originate from the interaction between electric and magnetic dipole moments (as for linear CD) but can result from electric dipoles alone [240]. A recent study demonstrates the use of CD-SHG to investigate and characterize 3D collagen distribution. Indeed, the absolute $I_{CD\text{-}SHG}$ enables to determine whether the fibrils are oriented in the imaging plane (small $I_{CD\text{-}SHG}$ values) or out of it (high $I_{CD\text{-}SHG}$ values) [241,242] and it notably shows great promise in measuring the polarity of out-of-plane collagen fibrils. As an example, Figure 3-9 shows CD-SHG and its application in imaging human cornea.

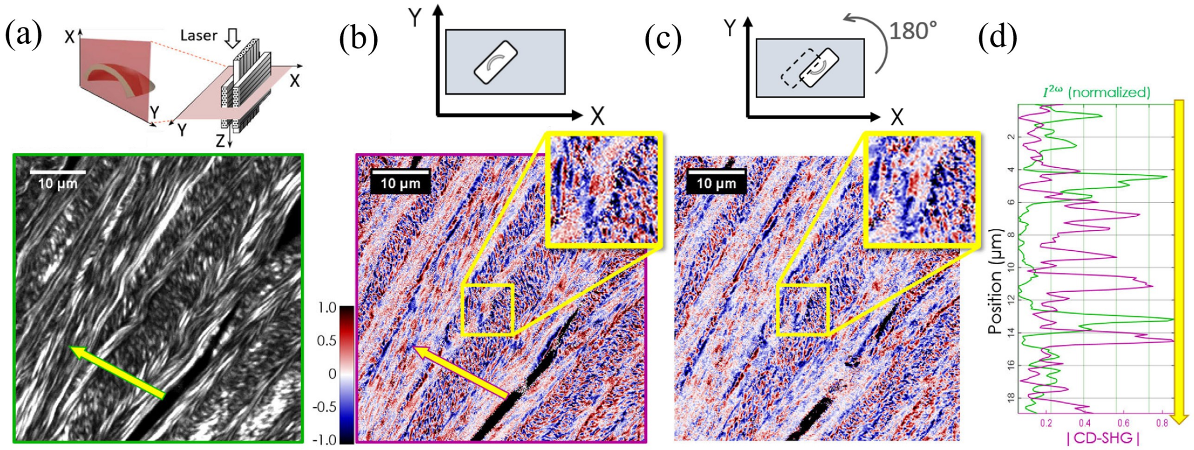

Figure 3-9: Example of CD-SHG applied in the transverse imaging of a human cornea. (a) Schematics and SHG intensity image of the cornea. (b) and (c) shows the CD-SHG imaging of the same region of the sample in two different configurations. As it is evident, the CD-SHG sign in both configurations is the same for almost 80% of the imaged pixels. Lastly, in (d) the SHG intensity profile (in green) and the CD-SHG absolute value (in magenta) are plotted along the yellow arrow shown in (a) and (b). Modified from [241].

Consequently, CD-SHG shows tremendous potential in pathological tissue diagnosis, for which disordered collagen and 3D remodeling of collagen are critical structures and processes.

Stokes vector based second harmonic generation microscopy

While changing the linear or circular input polarization state and measuring the change in SHG intensity allows to measure linear birefringence and anisotropy of the sample, this does not provide the full polarimetric response of a sample [243]. Indeed, in previously presented methods (II.2 and II.3) fully polarized light is used, represented by Jones calculus, and does not consider all states of light, namely incoherence, partially polarized and unpolarized light [243–245]. Besides the input light state, biological samples are not always well-organized and non-regular arrangements can lead to incomplete polarimetry results. For a complete description of the polarimetric response of the material Stokes-Mueller matrix formalism is better suited.

The state of polarization of light can be fully characterized through a 4×1 Stokes vector S:

$$S = \begin{bmatrix} S_0 \\ S_1 \\ S_2 \\ S_3 \end{bmatrix} = \begin{bmatrix} I_0 + I_{90} \\ I_0 - I_{90} \\ I_{45} - I_{-45} \\ I_R - I_L \end{bmatrix} \qquad 3.11$$

where I_0 is the intensity at 0^o, I_{90} is the intensity at 90^o, $I_{\pm 45}$ is the intensity at $\pm 45^o$and I_R and I_L represent the intensity at right and left polarization states. All the elements of the matrix are between -1 and +1, as they are normalized to the value of S_0. From this, vector, we can describe important polarimetric parameters such as the degree of polarization (DOP), the degree of linear polarization ($DOLP$) and the degree of circular polarization ($DOCP$) [243,244]:

$$DOP = \frac{(S_1^2 + S_2^2 + S_3^2)^{\frac{1}{2}}}{S_0}$$

$$DOLP = \frac{(S_1^2 + S_2^2)^{\frac{1}{2}}}{S_0} \qquad 3.12$$

$$DOCP = \frac{|S_3|}{S_0}$$

Stokes vector based SHG microscopy has been implemented using a four-channel-Stokes polarimeter [243], as depicted in Figure 3-10:

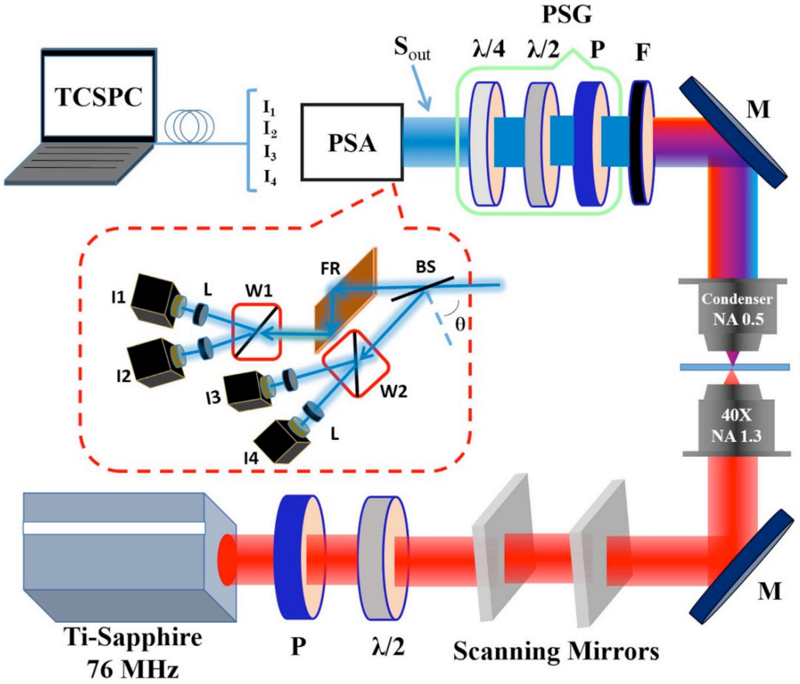

Figure 3-10: Example of a four channel-Stokes-polarimeter SHG microscopy setup. After the SHG from the sample, the signal passes through a polarization state generator consisting of a polarizer, a half-wave plate, and a quarter-wave plate before passing through a polarization state analyzer comprised of a beam splitter, a Fresnel rhomb and two Wollaston prisms. It is detected simultaneously by a time corelated single photon counting (TCSPC) system consisting of four detectors. Reproduced under CC BY 4.0 from [243].

The relation between the output Stokes matrix S_{out} and the four detected intensities is given by:

$$S_{out} = A_{4\times4}^{-1}.I = A_{4\times4}^{-1}.[I_1, I_2, I_3, I_4]^t \qquad 3.13$$

where $A_{4\times4}^{-1}$ is the polarimeter instrument matrix and I is composed of the four detected SHG intensities [243,245]. This technique has recently been used to characterize collagen fibers in adult mice tails, as shown in Figure 3-11:

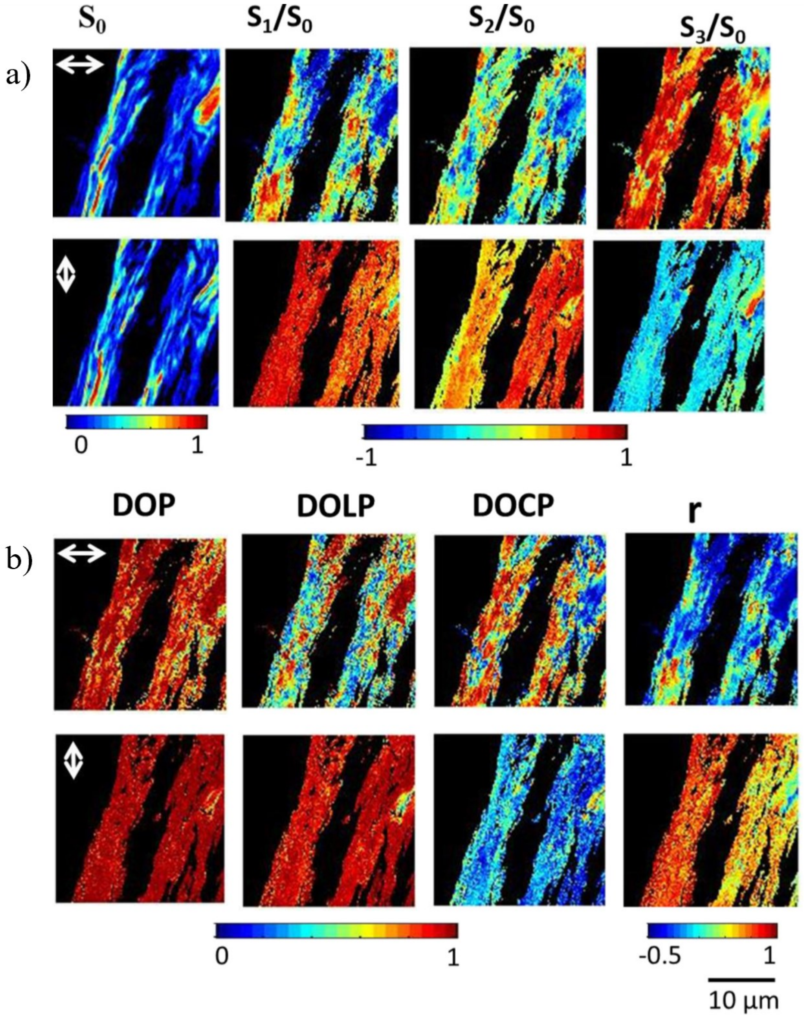

Figure 3-11: Stokes vector based SHG microscopy of collagen fibers. (a) represents the 2D Stokes vector images of the collagen fibers with vertical and horizontal input polarization. (b) shows the DOP, DOLP, DOCP and anisotropy parameter of the collagen fibers. Modified under CC BY 4.0 from [246].

One of the main drawbacks of this method is its restriction to forward detection configuration and hence thin samples [246]. In addition, this method assumes a linear relation between the incoming laser light and the SHG signal and still does not provide a complete polarimetric response of the sample [247].

A more generalized approach is the double Stokes Mueller polarimetry method (DSMP). In this method, a complete and model-independent SHG polarimetric response is represented by measuring 36 polarizations at minimum to calculate all observable laboratory-frame tensor components [247]. The relationship between the polarization of the output SHG signal and the polarization state of the input laser beam is given by the double Mueller matrix [247]:

$$S_{SHG}(2\omega) = M^{(2)} S_{in}(\omega) \tag{3.14}$$

where $S_{SHG}(2\omega)$ is the 4×1 SHG signal Stokes vector at 2ω frequency, $S_{in}(\omega)$ is the 9×1 input double Stokes vector describing the state of the two incident photon at ω frequency and $M^{(2)}$ is the 4×9 double Mueller matrix which is dependent on the nonlinear susceptibility of the material [247].

A complete characterization requires 9 polarimetric measurements for DSMP: horizontal and vertical linear polarization (HLP and VLP), right-handed and left-handed circular polarization (RCP and LCP), diagonal polarization ($\pm 45^o$), right-handed and left-handed elliptical polarization (REP and LEP) and a linear polarization at -22.5^o. The DOP is then calculated and filtered, for removing the scattering contribution, prior to calculate the double Mueller matrix of the sample. Using the six non phase matrix elements of the double Mueller matrix, the laboratory frame non-linear susceptibility tensor values can be completely retrieved. In the end, the molecular-frame orientation and non-linear susceptibility tensor ratios can be obtained by choosing a sample symmetry model. For the complete DSMP analysis and formulation please refer to [247] and [248]. An example of using the DMSP SHG technique is shown in Figure 3-12 for wall muscle in *Drosophila* larvae:

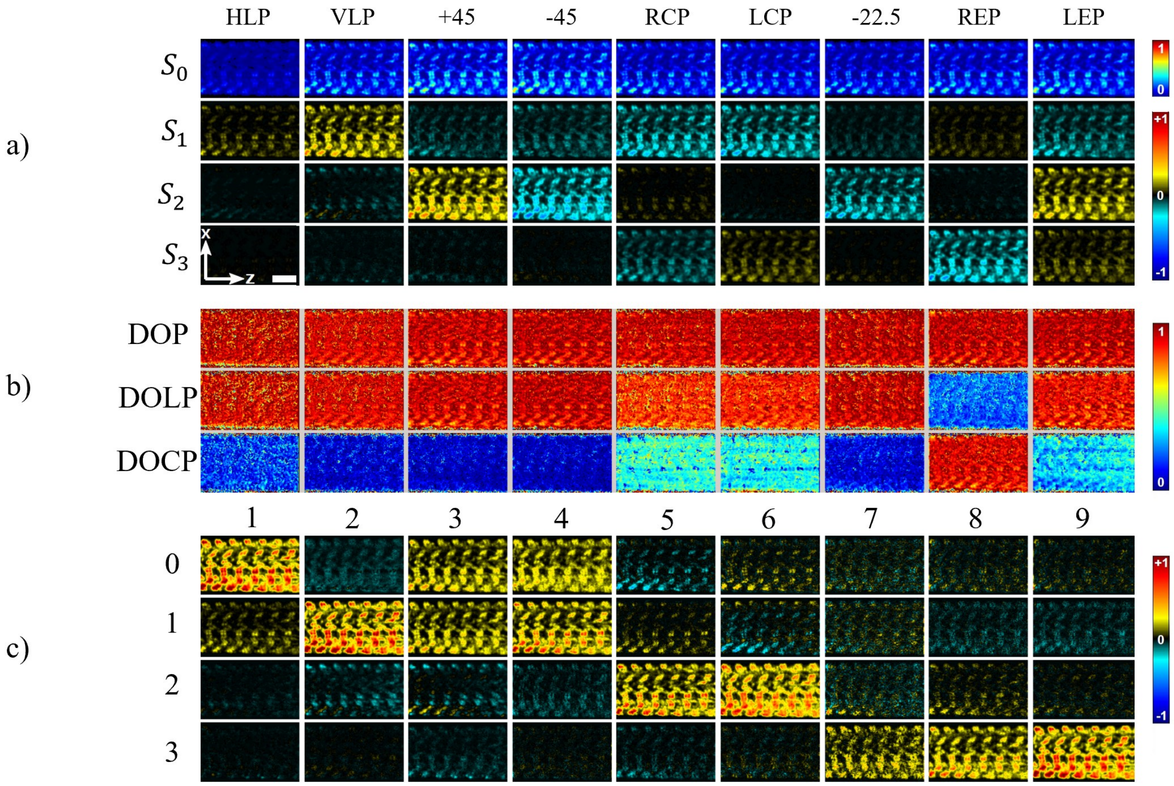

Figure 3-12: DMSP SHG images of the wall muscle of Drosophila melanogaster larva. a) Measured Stokes matrix elements. b) Maps of DOP, DOLP and DOCP. c) Double Mueller matrix elements normalized to the value obtained for χ_ZXX^((2)) from imaging. The scale bar is 10µm. Modified from [247].

Interferometric second harmonic generation (I-SHG)

While the coherent nature of SHG advantageously offers additional information about the sample, it is also a weakness since the pattern seen on SHG images results from complex interferences [68,249]. This can lead to serious imaging artifacts, depending on the microscopic arrangement [249], and eventually hide the actual underlying structure (especially in biological samples). Indeed, within the focal volume, dipoles of opposite (respectively same) polarity will destructively (constructively) interfere, leading to areas with a lower (higher) SHG signal. In the image, this results in bright and dark regions without direct correlation with the actual density of harmonophores (compare Figure 3-7 (e-f)). Hence, to extract quantitative information, it appears necessary to measure the local polarity inside the sample.

It is worth noting that an inversion of polarity (*i.e.* of the $\chi^{(2)}$ sign) leads to a π phase-shift on the emitted SHG signal (see also bottom row of Figure 3-3):

$$+\chi^{(2)} \Rightarrow e^{i0}e^{i\varphi} \Rightarrow e^{i(\varphi)}$$
$$-\chi^{(2)} \Rightarrow e^{i\pi}e^{i\varphi} \Rightarrow e^{i(\varphi+\pi)} \quad 3.15$$

Therefore, the phase of the signal keeps a signature of the polarity within the sample, which can be mapped in each pixel of the image. To do so, the most classical optical technique to record the phase of a signal is based on interferometry. While I-SHG has been originally proposed in 2004 to enable phase measurements on a scanning SHG microscope [70], it was only in 2013 that the technique was first applied to tendon [250] and later to cartilage [72].

In this method, the relative polarity of harmonophores is probed by a direct phase measurement. It relies on combining two SHG signals, one from a reference non-linear crystal placed before the microscope (reference SHG) and the second one from the sample (sample SHG), which interfere together (Figure 3-13(a)). Since both SHG beams are spatially and temporally coherent, the total intensity on the detector follows the usual two-wave interferometry equation:

$$I_{\text{SHG}} = I_{\text{s}} + I_{\text{ref}} + 2\sqrt{I_{\text{s}}I_{\text{ref}}}\cos(\varphi_{\text{s}} - \varphi_{\text{ref}}) \quad 3.16$$

where I_s and φ_s (resp. I_{ref} and φ_{ref}) represent the intensity and the phase of the sample (reference) SHG beam.

Adjusting the phase difference between the two beams enables to record the interferogram and to extract the argument of the cosine (*i.e.* the relative phase) and its multiplicative factor (the interferometric contrast) by fitting the experimental curve (Figure 3-13) [251]. This technique for fitting the cosine from many points is known as Phase-Shifting Interferometry (PSI). In brief, changing the optical path between the reference and the sample arm (Figure 3-13(b)) induces a change in the cosine argument from 0 to 2π. To remove the constant term $I_{\text{s}} + I_{\text{ref}}$, two π-phase shifted raw images are subtracted. Then, in every pixel, the experimental cosine (blue circles in Figure 3-13(d)) is fitted to determine both the amplitude (interferometric contrast) and the relative phase (φ_{mat}), the interpolated phase of the signal at each point in the material. It is the phase offset found for each interpolated cosine wave at each pixel. The procedure provides phase and interferometric contrast maps.

Various approaches can be used to adjust the phase difference between the two SHG signals, such as a gas cell, variation of distance, a rotating glass plate [74], as well as more advanced approaches, notably the use of an electro-optic phase modulator (EOM) [75]. Originally, a rotating glass plate was used to induce an optical phase shift between the reference and the sample SHGs (Figure 3-13). The refraction at different angles between the SHG and the fundamental and differences in refractive index at these two wavelengths both play a role in changing the relative optical path length between the pump and the SHG when the glass plate is rotated. For a full description of the setup and details on the technique see [75] and for a more comprehensive explanation of the phase extraction technique please refer to [242].

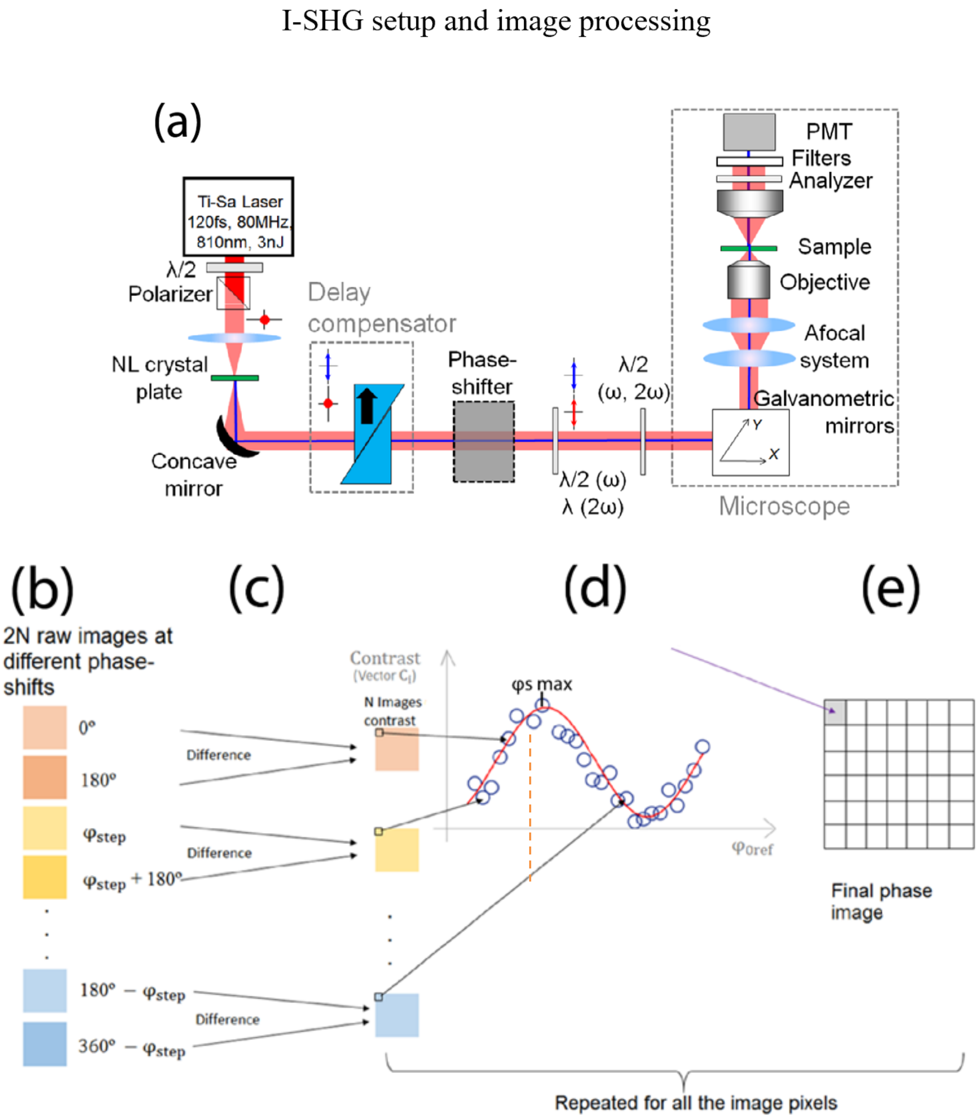

Figure 3-13: I-SHG principle. (a) Example of an I-SHG inverted microscope. The λ/2 (half-wave plate) and polarizer are used for power control and afterwards the non-linear crystal plate generates the reference SHG signal. After that, a delay compensator is used to match the optical length of the pump arm and the reference SHG arm superposed along a common path in the interferometer. The polarizations are made parallel after the phase shifter and introduced to the microscope setup for interference between the reference SHG and the sample SHG. (b-e) Schematic diagram of the algorithm for calculating the relative I-SHG phase. The 2N raw images (b) are subtracted 2 by 2 to give N contrast images (c). In every pixel, the intensity follows a cosine law

with respect to the phase-shift of the interferogram (d), which can be interpolated to find the optical phase and interferometric contrast image (e). Extracted from [8].

An example of the PSI method can be seen in Figure 3-14. In this study, Rivard *et al.* were able to reveal the bipolar structural organization of myosin using I-SHG microscopy [250]. Figure 3-14(a) displays an SHG image of muscle sarcomeres acquired in the forward direction. The following panels are raw I-SHG images taken with φ_{ref} at 105° (b), 285° (c), and 465° (d). Those were the phase shifts resulting in maximal interferometric contrast for this specific image acquisition. Panel (e) and (f) show the results of subtracting two raw I-SHG images taken at φ_{ref}= 285° and 105° (c – b) and at φ_{ref}= 465° and 285° (d – c) respectively [250]. The final phase image has been extracted from the 36 images at different reference phase (15 ° steps) that were taken during this measurement and is shown in panel (g). Lastly, (h) displays the phase histograms associated with image g), highlighting the bimodal distribution of the phase. The distribution of the phase is also represented in histograms to better show some details of the content of that image (h). These results show without ambiguity that, for each sarcomere (white band of the signal) in image (a), there are two associated $\chi^{(2)}$ domains with opposite polarities.

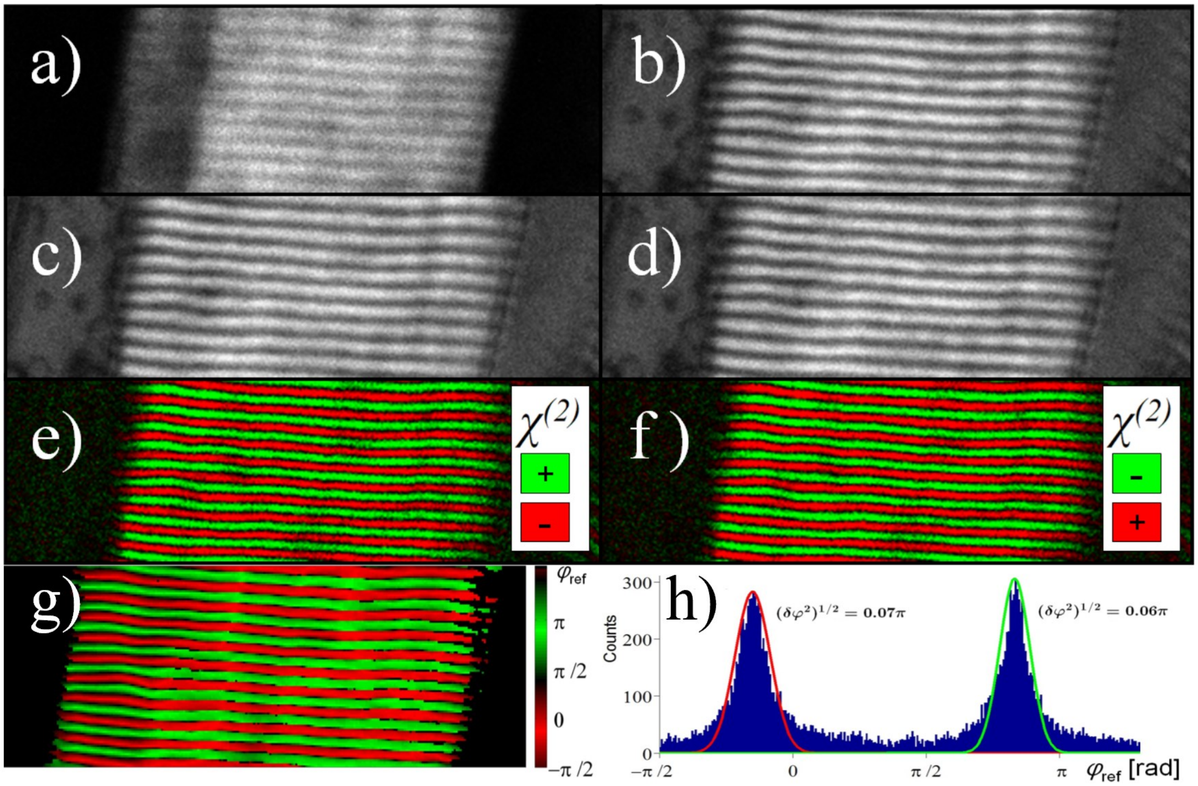

Figure 3-14: I-SHG imaging in muscle sarcomere adapted from [250]. (a) F-SHG image in the absence of a reference SHG beam. (b-d) raw I-SHG images acquired with a reference phase of 105°, 285°, and 465° respectively. (e) and (f) images resulting from the subtractions of (c) - (b) and (d) - (c). (g) depicts the relative SHG phase in the muscle and (h) the histogram of the relative SHG phase for all pixels in (g).

Fast I-SHG microscopy

Because of the optical path difference induced by scanning the laser beam inside the objective of the microscope (and the relay lenses), laser scanning microscopy is not directly applicable to I-SHG. Changing the laser angle onto the objective adds a radial phase distortion in the I-SHG images. I-SHG was thus first developed with a sample-scanning setup [250], and was later adapted to laser-scanning by correcting the phase distortion with a calibration phase map [251], which improved the imaging time by about 98%, from a few hours down to a few minutes.

However, acquiring an I-SHG image in a few minutes still imposes significant limitations in terms of temporal resolution, since it necessitates that the sample remains steady in the field of view along this time frame. Yet, in biological samples, many dynamic processes happen on a shorter time scale: for instance, monitoring cellular mitosis would require a temporal resolution below 30 seconds to properly resolve moving microtubules (MTs) [126]. Moreover, SHG from MTs is relatively weak, which additionally leads to decreased accuracy of the I-SHG measurements [75].

In this context, classical PSI is not optimal since it implies to acquire 18 images of the same zone at different phase-shifts (Figure 3-13) and leads to long dead time due to the slow speed of the mechanical phase-shifter (the glass plate). Therefore, different interferogram points used in the phase extraction (Figure 3-13(c)) are separated in time by up to a minute, which leads to significant artifacts due to instabilities.

An improved method, called single-scan I-SHG (1S-ISHG), has been recently demonstrated and consists in applying the phase-shifts within each pixel of the image, rather than between the images (Figure 3-15).

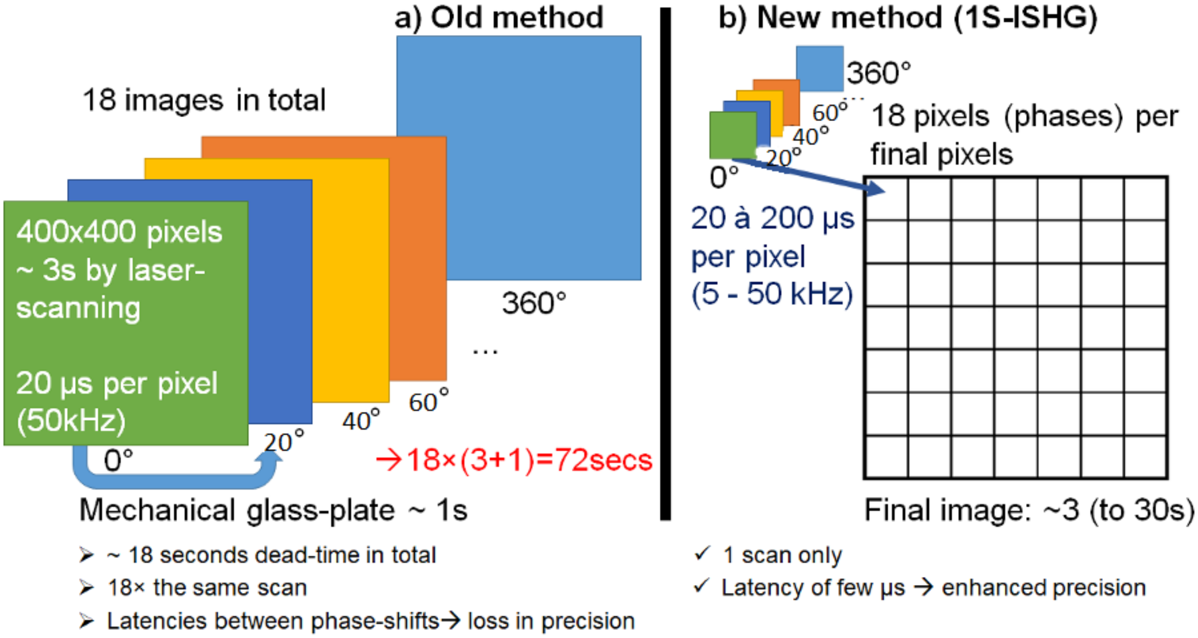

Figure 3-15: Standard (a) and fast (b) methods for phase shift in I-SHG. Extracted from [8].

To that end, the mechanical phase-shifter was replaced by an electro-optic modulator (EOM), specifically developed in collaboration with Axis Photonique Inc. (Varennes, Canada), enabling them to tune the phase-shift at high speed (up to 50 kHz). This technique results in only one scan of the area, with a settable exposure time (usually between 20 and 200 µs), ensuring only few microseconds of latency between each point of the interferogram [75]. The amount of time required to image a large area (500 µm ×100 µm) can be seen in Figure 3-16 when the fast and normal I-SHG method are used to image the central part of an adult horse meniscus.

Comparison between fast and normal I-SHG

Fast I-SHG, phase scan: 20µs, acquisition time: 25s

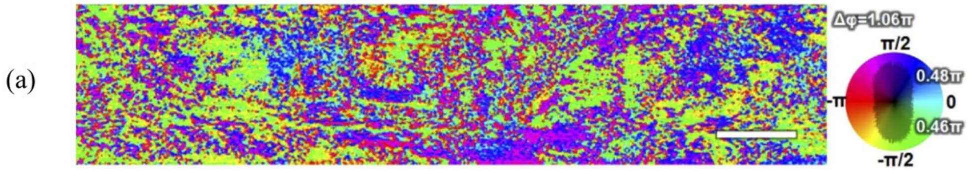

Fast I-SHG, phase scan: 200µs, acquisition time: 126s

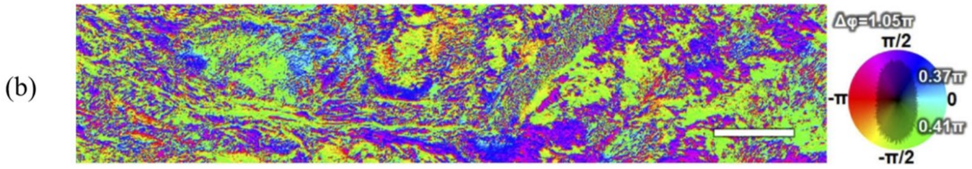

Fast I-SHG, phase scan: 2000µs, acquisition time: 495s

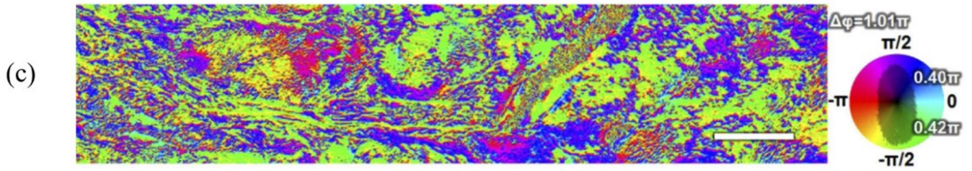

I-SHG, acquisition time: 1926s

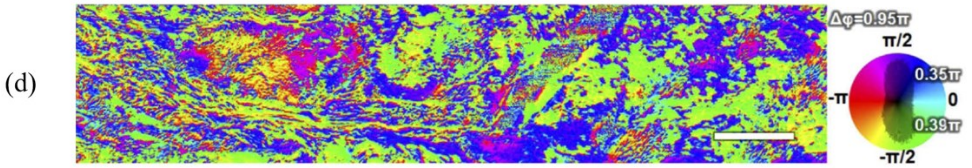

Figure 3-16: SHG phase-map of an adult horse meniscus with fast I-SHG and normal I-SHG. The scale bar is 50 µm. (a)-(c) show fast I-SHG with different phase scan durations and (d) shows the normal I-SHG at work. (a) 20 µs phase scan is acquired in ~0.5min, (b) 200 µs phase scan is acquired ~2min, (c) 2000 µs phase scan is acquired in ~8min and (d) using the normal I-SHG method, acquisition takes ~32 min. Note that reducing the phase scan duration increases the speed of acquisition, but it also increases the phase errors. Nevertheless, even the longest phase scan duration of fast I-SHG (i.e., 2000 µs) cuts the acquisition time by 25% compared to normal I-SHG which is a huge improvement overall. Adapted from [75].

Aside from the improved temporal resolution, any sample instability in the implementation would result in image distortion rather than incorrect polarity determination. Consequently, this method appears to be remarkably robust.

Wide-Field SHG imaging

Scanning SHG imaging is a well-established method which, over the years, has been successfully used for many applications. However, one of the main implementation limitations is its low imaging throughput (photons detected per frame per second). This drawback impedes its application to label-free imaging of very fast biological processes (millisecond time scale) [252]. To overcome this limitation, two strategies can be envisioned: either to increase the scanning speed or to parallelize photon emission. For scanning speed improvement, acousto-optic deflectors [253] and resonant scanners [254] have been successfully used. Yet, they remain ultimately limited by the dwell-time required to generate enough photons to obtain a recordable signal. For the latter strategy, wide-field SHG microscopy appears as the ultimate parallelization, since the complete area of interest is illuminated simultaneously and signals are detected on a pixelated detector [76,77]. Traditionally, wide-field SHG microscopy was performed using high energy (µJ) pulses from lasers operated at multi-kHz repetition rate. It has been proven that wide-field SHG microscopy improves imaging throughput by 2-3 orders of magnitude compared to scanning microscopy [76]. A typical wide-field SHG setup can be seen in Figure 3-17.

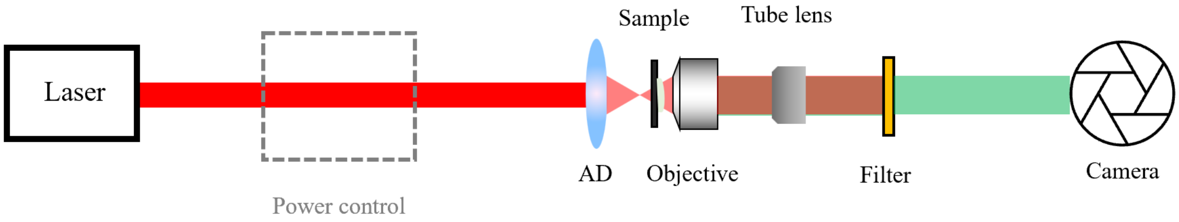

Figure 3-17: Typical wide-field SHG microscopy setup. The laser light source is in the range of 700-1100 nm. A half-wave plate and a polarizer are used for power control. An achromat doublet lens (AD) is used to focus the incoming laser beam and the sample is placed slightly above the focus to capture a larger FOV. The SHG signal is collected using an objective and a tube lens, spectrally filtered, and detected on a camera. Adapted from [255].

Due to the delicacy of living cell samples, particular care must be taken to avoid photodamage. Several studies investigated light damage in wide-field SHG microscopy for different cell lines allowing to determine a range where pulse energy and hence heat deposition remains below the damage threshold of the samples [83]. In recent advances, a high repetition rate (MHz) wide- field SHG microscope has been designed for live imaging of contracting muscle tissue that utilizes laser pulses with pulse energy as low as approximately 60 nJ per pulse (Figure 3-18).

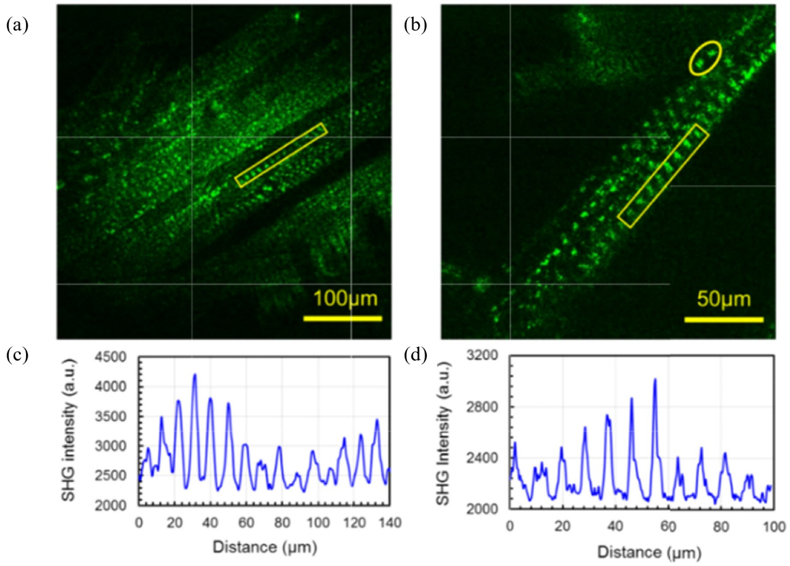

Figure 3-18: wide-field SHG images of fixed larval muscle (a) 425 µm2 and (b) 213 µm2 area with a frame integration time of 100 ms. (c) and (d) represent the SHG intensity profiles of (a) and (b) respectively from the designated regions of interests in the images. This method provides single shot imaging of large areas and is used to acquire live larvae contractions. Extracted from [255].

Lastly, holographic SHG microscopy, a variant of wide-field SHG, has been proposed to make use of the signal phase [256,257]. Other methods beside wide-field SHG microscopy also exist for improving the image acquisition speed and we suggest [258] for a recent comprehensive review of these methods.

SHG and enhanced SHG in neurons

The nervous system and neuron structure

The nervous system is a *sine qua non* organ for most living animals, responsible for information processing and transmission [105]. As depicted in Figure 3-19, neurons have a cell body called the soma, which contains the nucleus of the neuron. The receiving branches of the neuron are called dendrites, where most of the incoming signals are integrated [106]. The outgoing signal drives through a structure called the axon. Although a neuron can have many dendrites, it will always have only one axon. At the end of the axon, there are the axon terminals and synapses that contain the neurotransmitters necessary for chemical communication between the neurons.

Neuron anatomy and polarity

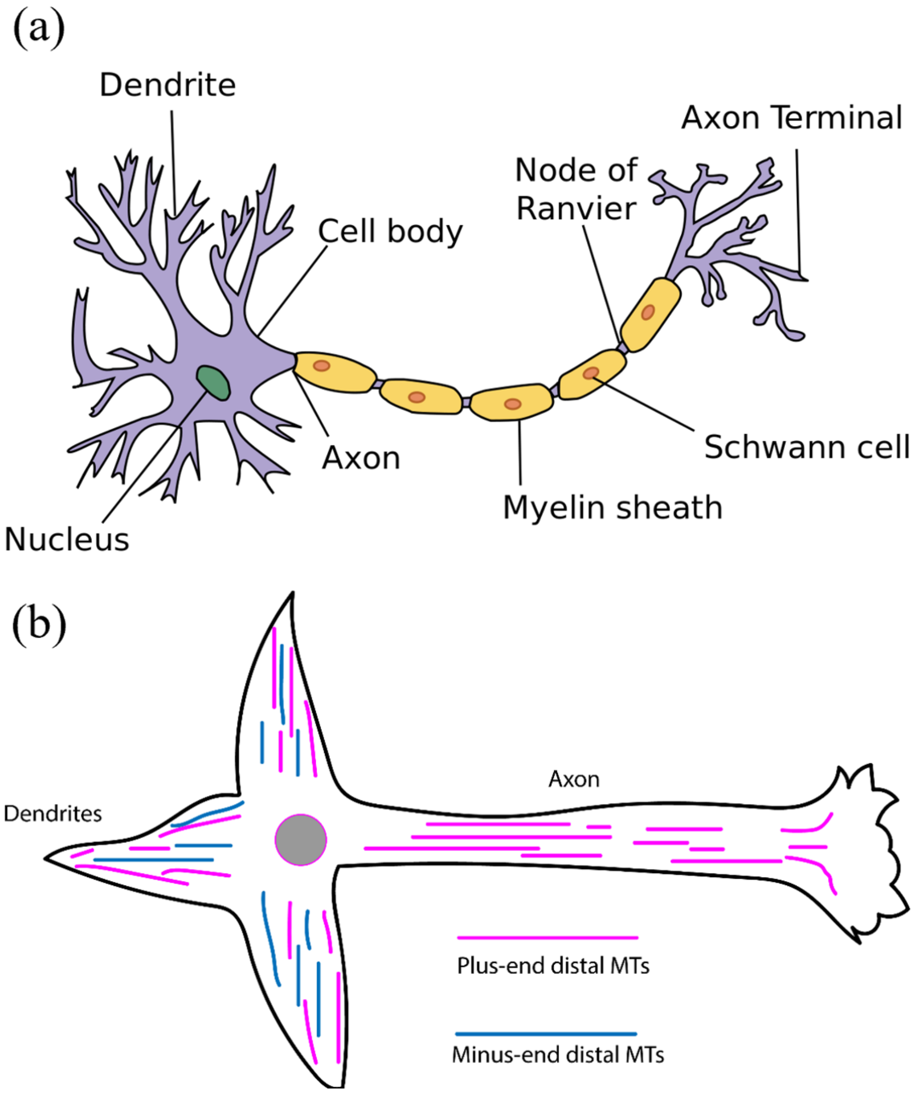

Figure 3-19: (a) Anatomy of a neuron from soma to the synapse. Extracted from [259] (. (b) Neuron polarity diagram. Adapted with permission from [260].

Studying neurons and their building components is one of the highest challenges of our times since many of their mechanisms and dysfunctions remain unknown. The following section will cover how well-suited SHG microscopy is to study these structures.

SHG microscopy in neurons

Traditionally, neuronal mechanisms have been studied using electrophysiology in which electrodes are inserted into the neurons to measure the electrical potentials and currents. This approach is considered the gold standard to study neuronal activity and has led to invaluable information about neuron functioning. Nevertheless, this approach still presents several significant limitations. Firstly, it requires a rather invasive protocol and remains challenging to use in living animals [107]. Moreover, despite recent advances, patch clamping is bounded to record data from a limited number of neurons, drastically impeding the investigation of a neuronal network [108].

To overcome such shortcomings, optical methods appear highly desirable by offering the necessary flexibility to complement such electrophysiological measurements. 2PEF and SHG microscopy have found many applications in neuroscience and are vastly gaining popularity because they provide complementary access to distinct features. Although most SHG microscopy experiments have been based on endogenous cell properties, SHG dyes have also been used in different studies [109–113]. Using FM 4-64 dye, Dombeck *et al.* demonstrated a huge improvement in signal-to-noise ratio (SNR) over fluorescent probes [111]. Using the same dye, Nuriya *et al.* were able to demonstrate for the first time that action potentials enter dendritic spines [112], and later characterized the SHG response to an action potential and its propagation from the soma to the axons [114]. In parallel, Nemet *et al.* reported that all trans retinal chromophores are suitable candidates for SHG neuronal membrane imaging [110]. Jiang *et al.* showed that the limited SNR obtained in the previous studies could be overcome (Figure 3-20) using photon counting detection [115] and later reported that the potential sensing capacity of FM 4-64 originates from electro-optical mechanisms [113].

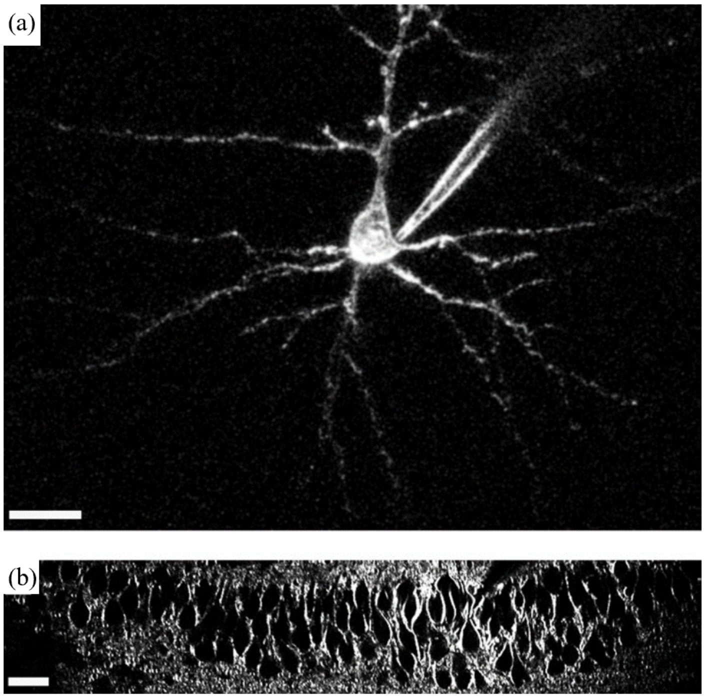

Figure 3-20: Single neuron and neuron population using FM-4-64 dye and SHG imaging. Scale bars: 20µm. (a) shows a single pyramidal neuron from a mouse visual cortex that has been injected with the dye and imaged using SHG microscopy. (b) shows a multitude of pyramidal neurons bathed and labeled by a SHG chromophore and imaged using SHG microscopy. Extracted with permission from [115].

To summarize, among many existing tools and methods for neuronal mechanism studies, optical imaging techniques can be advantageous for studying various aspects of the neurons. SHG microscopy is reliant on the cell properties for SHG signal production. In some studies, SHG dyes are necessary to further improve the SNR and the contrast in the images [110,111,113,114].

SHG microscopy in microtubules

In neuroscience, one of the interesting structures that has been investigated using SHG microscopy are microtubules (MTs). MTs are among the most important cytoskeleton filaments and their functionality encompasses the maintenance of the cell integrity and the morphology or regulation of intracellular trafficking, while also playing an important role in cell division [116–119]. MTs are structured as hollow tubes with a 25 nm outer diameter that is made of two dimers α- and β-tubulin. When these two heterodimers bind in a head-tail manner, they create a linear protofilament polymer [119,120]. MTs are fundamentally polar because all protofilaments are parallel to each other and all the dimers comprising the filament share the same orientation [120].

Many studies have focused on how MTs produce SHG [121,122,125,261]. One of the recent highlights [261] reports that the number, organization and polarization all play an important role in the formation of SHG signal from MT [261].

Although the polarity was not the focus of these studies, the MT polarity was later deduced, using the protein plus method which tags the microtubule-associated protein (MAP) with a fluorophore and the tagged MAP then binds to the positive end of MTs [118,124]. Combined with SHG microscopy, it was shown that the MTs polarity in the axons is well-defined and always the same, with the minus end pointing to the cell body and the positive end pointing to the axon terminals, where neurotransmission takes place [118]. However, this method is invasive since it uses fluorescent markers for determining the polarity of the MTs. Importantly, while paraformaldehyde is the gold standard in cell fixation, this fixation method was also investigated in this study and it causes drastic losses of SHG signal which reveals that it changes the protein conformation [261]. In contrast, MTs polarity in dendrites remains poorly characterized, but seems to be not so well-defined [116]. Even if some previous studies have suggested that there might be a mix of polarity in dendrites [121] and that domains of polarity exist among them [122], these claims remain hypothetical and a full characterization is required to verify them. Notably, many questions remain unanswered, *e.g.,* why do axons have uniform polarity, but dendrites do not? Is this mixed polarity functionally relevant? SHG and specifically I-SHG are great candidates for studying the underlying mechanisms of the dendrites and the relevance of their polarity in their operation.

Using fluorescence (red) and SHG (green) to image microtubules in neurons

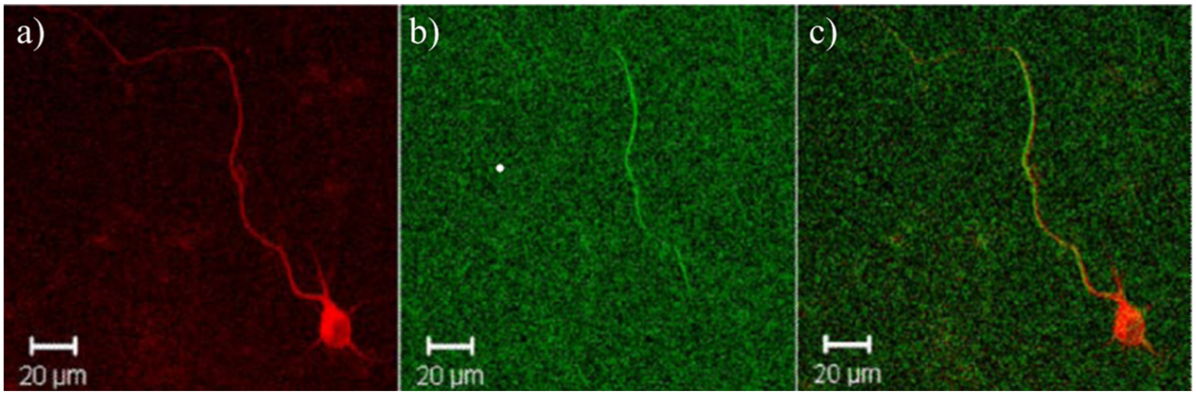

Using I-SHG to image the mitotic spindle during cell division

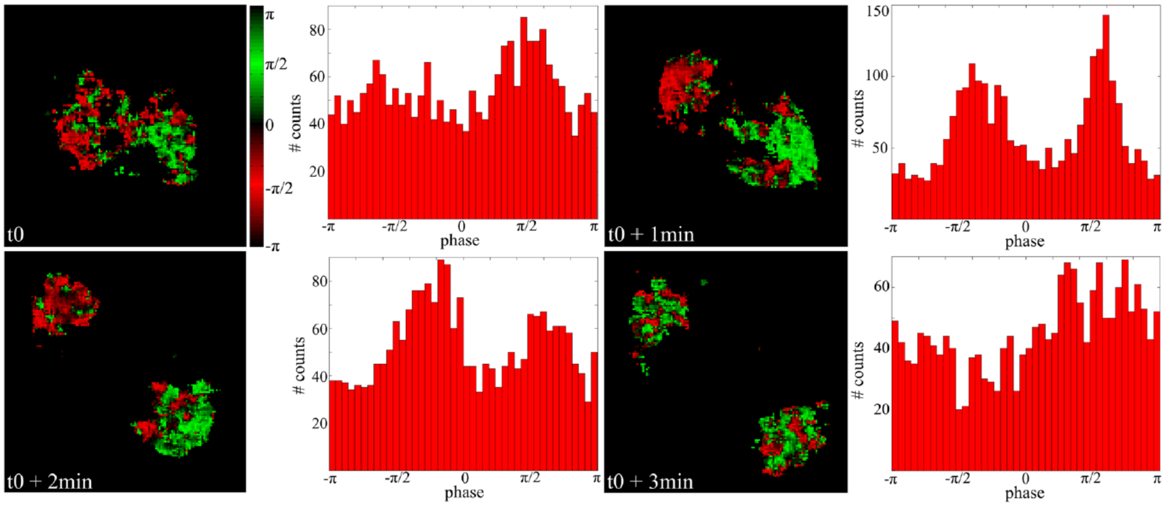

Figure 3-21: Microtubule imaging in neuron (top) and mitotic spindle (bottom). Complementation of neuron imaging using fluorescence and SHG (top). In (a), only TauRFP (tau red fluorescent protein) dye is visible in the image of the neuron. In (b), we only see the SHG image of the neuron. Finally, (c) is a combination of the fluorescence and the SHG images to benefit from both imaging techniques (Stoothoff et al. 2008). Image and histogram of SHG phase in the mitotic spindles (bottom). The red and green pixels are π-phase shifted signals. At the beginning of the metaphase (t0), the two poles are starting to have opposite polarities. At the end of the metaphase (t0+1min) and the beginning of the anaphase (t0+2min), a more uniform polarity can be seen where one pole is red and the other pole is green. At the end of the anaphase (t0+3min), a mix of red and green pixels can be seen in both poles which means that the two poles have a random polarity. Reproduced under CC BY 4.0 from [126].

Lastly, embryogenesis is an entire field in developmental biology, in which SHG microscopy has been instrumental in providing time-lapse images of the distinct stages of cell division. Specifically, SHG rises and falls have been used to investigate the dynamics of mitotic spindles, composed of highly oriented MTs, in different embryos, including Caenorhabditis elegans, zebra fish, mouse, rat and sea urchins [125]. While several methods allow to study the polarity of MTs, most of them are invasive and I-SHG microscopy appears to be a promising non-invasive alternative. In a study using the I-SHG technique, Bancelin *et al.* [126] successfully mapped the polarity of MTs forming the mitotic spindle during cell division in zebrafish embryos as shown in the bottom part of Figure 3-21. While the polarity of MTs in mitotic spindles had been previously studied indirectly with a combination of SHG and fluorescence microscopy [262], this was the first direct evidence of change in MTs polarity upon mitosis. This achievement was made possible by the advances in the I-SHG imaging speed, as discussed in section II.5. It was found that at different stages of the cell division, the SHG signal varied due to the change of alignment and polarity of the MTs' network. Bancelin *et al.* observed the SHG signal during various phases. First occurring in the pro-metaphase, the signal further increased in the metaphase and anaphase, and gradually vanished during the telophase when the mitotic spindle uncondensed. Besides the SHG intensity, they could extract the polarity of MTs during each phase. They observed that at the beginning of the metaphase and the end of anaphase, MTs had a mixed polarity revealing a more disorganized structure. In contrast, at the end of the metaphase and the beginning of the anaphase, the MTs are highly aligned with uniform polarity [126]. This study showcased the power of the I-SHG microscopy technique and how it would be advantageous to use this method for studying the polarity in dendrites and other neuronal activities. More generally, SHG and advanced SHG microscopy are versatile tools that were utilized in many MTs studies. They have shown promising potential and are a great candidate for in-depth studies of different aspects and unknown mechanisms of MTs and related diseases [126,261,263].

Conclusion and prospects

Over the past two decades, SHG microscopy has become an invaluable tool in bio-imaging and neuroimaging. Many studies illustrate its potential to investigate non-centrosymmetric biological structures such as fibrillar collagenous tissues [40], tendon [30,210,211], cartilage [220], cornea [92,219], sclera [219], fascia [68], meniscus [234], muscle [48,71,101,214,225,250], MTs [111,121,122,125,126], otoconia [264], the origin of SHG signal in neurons [121,261] and how it can a be great tool for tauopathies [263] and tubilinopathies [265]. While originally limited to point-scanning imaging of endogenous structures, over the years, many groups have demonstrated innovative approaches to minimize the invasiveness and to improve the imaging throughput, notably through wide-field imaging or the development of specific SHG probes, constantly pushing the frontier of SHG imaging into new systems and structures.

In this context, conceptual and technological advances in SHG microscopy continue to define a fast-progressing frontier in biophotonics. Aiming to improve the spatial resolution by means of coherent structured illumination [266] and utilizing post-processing methods such as pixel reassignment [128,129] , increasing the imaging depth through adaptive optics approaches [14] or pushing non-linear imaging into the spectroscopic realm using hyperspectral microscopy approaches based on sum-frequency generation [267] are all examples of this fast ongoing progress.

Despite many advances, a fully quantitative interpretation of SHG images remains elusive owing to the coherent nature of the process involved. While the different approaches presented in this review, notably F/B-SHG, P-SHG, I-SHG, CD-SHG and Stokes vector based SHG all appear as relevant pieces to this puzzle, their combination in the same instrument has yet to be done but could potentially provide a definitive answer to this long-lasting topic.

With its tremendous advantages, SHG microscopy still requires overly expensive equipment and specialized training, which impedes its larger use in routine biomedical practice. This is particularly evident for the more advanced SHG techniques that rely on state-of-the-art optical implementation and complex hardware system. The recent advancement in laser technology has led many groups to shift away from the gold-standard of Ti:Sapphire lasers towards more robust and power-efficient fiber and semiconductor lasers enabling smaller and more efficient SHG microscopes [37]. This crucial simplification and cost reduction is expected to open new perspectives for biomedical applications of SHG microscopy. Such wide application would be promoted by the progress in endoscopic SHG, which has gained popularity in recent years [268]. There are still significant technological challenges that need to be overcome to make this technology more accessible, but the efforts required to solve these technological challenges would be matched with even greater potential reward, like enabling *in vivo* imaging of organs.

Besides hardware implementation, software analysis and computational approaches for enhancing imaging capabilities have also made great strides in microscopy. These computational advancements complement the optical setups and even correct some of their flaws and shortcomings in imaging. Notably, fast image processing has been made possible in recent years thanks to improvements in graphical processing units and field-programmable gate arrays that can process large amounts of raw data at high-speed. In addition, machine learning is currently revolutionizing many fields including image processing and has naturally made its way into SHG microscopy. For example, a few groups recently ventured to develop deep learning algorithm based on neuronal networks to classify and diagnose cancer using SHG footprints [154,155,223,269].

Lastly, many current imaging systems are unique setups, customized differently in each lab [258]. A unification and standardization of the imaging process appears highly desirable for reproducibility and portability.

Regardless of the challenges and limitations we mentioned, SHG and non-linear optical microscopy imaging modalities provide a plethora of information that is not readily available with traditional linear or incoherent optical imaging techniques. With all the technological advancements in optics, machine learning and laser technology, non-linear imaging modalities are only going to get better and much simpler over time, opening new horizon for widespread applications in both fundamental science and medical applications [37].

Declarations Section

Funding

The authors acknowledge financial support from Fonds de recherche du Québec – Nature et technologies, the Natural Sciences and Engineering Research Council of Canada, the New Frontiers Research Fund, and the Canada Foundation for Innovation. A. A. thanks the NSERC CREATE program for the scholarship.

Conflict of Interest

The authors declare no competing interests.

Authors Contribution

A.A conceived and wrote this review article. A.A S.B, M.R and M.P. participated in the drafting, section arrangement, and critical revision of it. H.I and F.L revised it critically for important intellectual content and gave final approval of the version to be published. All authors read and approved the final manuscript.

Ethical Approval

Review paper, Not Applicable.

Consent to Participate

Review paper, Not Applicable.

Consent to Publish

Review paper, Not Applicable.

Data Availability

Review paper, Not Applicable

Code Availability

Review paper, Not Applicable.

4 NONLINEAR MICROSCOPY AND DEEP LEARNING CLASSIFICIATON FOR MAMMARY GLAND MICROENVIRONMENT STUDIES

MICROSCOPIE NON LINÉAIRE ET CLASSIFICATION PAR APPRENTISSAGE PROFOND POUR LES ÉTUDES DE L'ENVIRONNEMENT MICROSCOPIQUE DES GLANDES MAMMAIRES

Authors:

Arash Aghigh[1,], Samuel E J Preston[2], Gaëtan Jargot[1], Heide Ibrahim[1], Sonia V Del Rincón[2] and François Légaré[1]

[1] *Centre Énergie Matériaux Télécommunications, Institut National de la Recherche Scientifique, Varennes, Québec, Canada.*

[2] *Department of Experimental Medicine, Faculty of Medicine, McGill University, Montréal, Québec, Canada; Gerald Bronfman Department of Oncology, Segal Cancer Centre, Lady Davis Institute and Jewish General Hospital, McGill University, Montreal, Quebec, Canada.*

Titre de la revue ou de l'ouvrage :

Biomed Opt Express. 2023 May 1; 14(5): 2181–2195. Published online: 2023 April 21. Doi: 10.1364/BOE.487087

Contribution des auteurs:

A.A conceived and wrote the article and performed the experiments. S. P. provided samples for the experiments. A. A., S. P., G. J., and S. V. D. L. participated in the drafting, section arrangement, and critical revision of the manuscript. H. I. and F. L. critically revised the manuscript for important intellectual content and approved the final version to be published.

Lien entre l'article ou les articles précédents et le suivant :

This article is a continuation of a collaboration between our laboratory and the Department of Experimental Medicine at McGill University. Phosphorylation of eIF4E in the stroma drives the production and spatial organization of collagen type I in the mammary gland (DOI: 10.1016/j. matbio.2022.07.003). We aimed to investigate the possibility of using SHG microscopy and deep learning in cancer studies.

4.1 Main article

Abstract: Tumors, their microenvironment, and the mechanisms by which collagen morphology changes throughout cancer progression have recently been a topic of interest. Second harmonic generation (SHG) and polarization second harmonic (P-SHG) microscopy are label-free, hallmark, methods that can highlight this alteration in the extracellular matrix (ECM). This article uses automated sample scanning SHG and P-SHG microscopy to investigate ECM deposition associated with tumors residing in the mammary gland. We show two different analysis approaches using the acquired images to distinguish collagen fibrillar orientation changes in the ECM. Lastly, we apply a supervised deep-learning model to classify naïve and tumor-bearing mammary gland SHG images. We use transfer learning with the well-known MobileNetV2 architecture to benchmark the trained model. By fine-tuning the different parameters of these models, we show a trained deep-learning model that suits such a small dataset with 73% accuracy.

Introduction

Over the last decade, we have improved our understanding of the microenvironment in which a tumor grows; composed of co-mingling tumor cells, immune cells, stromal cells, and the extracellular matrix (ECM) [270]. Various studies have correlated the arrangement of collagen in the microenvironment surrounding the tumor with patient survival [271–277]. Collagen organization at the tumor-stroma boundary is an essential indication of breast cancer disease progression and subsequent risk of local invasion and metastasis. Studying these so-called tumor-associated collagen signatures (TACS) can help to determine the invasiveness of a breast tumor [271,278]. TACS classification sorts heterogeneous tumor-associated collagen patterns into three physically distinct types: TACS-1, representing densely packed collagen close to the tumor boundary; TACS-2, a sphere-like collagen organization around TACS-1; and TACS-3, is linear collagen pointing away from the tumor boundary [271]. Studying the underlying mechanism of the formation of these TACS (especially TACS-3) can give valuable information about the pro-metastatic features of the tumor, as locally invasive tumor cells have been shown to use radially aligned collagen fibers as migration tracks to leave the primary site [279–281]. Moreover, it has been demonstrated that collagen fiber width, length alignment, and angle provide cues for the distinction between malignant/benign tumors and patient survival [278].

Many methods are available for studying the ECM around a tumor, of which histological staining is the most common [278]. There are many stains available, but the resolution of these stains, and the inability to quantify collagen features from them, have been limiting factors for ECM studies in cancer [278]. Another method used for ECM studies is liquid crystal polarizing microscopy [282]. It is fast, not expensive and can be added to a microscope with a few optical components, but the signal processing and structure distinction are challenging [278].

To image collagen in tissues, SHG microscopy is the gold standard in imaging methods and has improved spatial resolution, limitation of phototoxicity, photobleaching, focal plane selectivity, and simple sample preparation [283]. This label-free non-invasive method provides a way to detect alterations of fibrillar collagen in the tumor microenvironment, which is impossible using other imaging techniques. SHG has played an essential role in cancer studies and has been successfully applied to assess collagen restructuring in breast [273,284,285], ovarian [286], prostate [287], and lung cancers [61]. All these studies have documented collagen morphological changes around the tumor using SHG microscopy. Nevertheless, orientation studies only based on SHG intensity can be subject to interference that masks the underlying structure [232] and make fibril orientation imaging impossible [52].

Polarization-resolved SHG microscopy (P-SHG) overcomes such limitations and combines the advantages of SHG microscopy with polarimetry [47,52,92,169]. It is used in collagen-related studies and provides accurate information about the structure of the fibrils in the imaging plane, which is highly advantageous for cancer research [288]. More advanced P-SHG microscopy systems exist, such as polarization-in, polarization-out (PIPO), that can also extract the asymmetry of fibril distribution [238] and have been successfully applied in lung [61] and breast cancer studies [289].

SHG and P-SHG image analyses have also developed over the past few years due to increasing amounts of information that can be extracted from acquired images. Collagen fiber alignment, width, length, texture, density, and TACS are all exciting metrics that can be identified using post-image-processing methods [278]. Image analysis and processing usually rely on human visual inspection for data validation. Deep learning can eliminate manual data inspection and automate image analysis, such as image classification [154–157]. Deep learning and machine learning in SHG microscopy have been applied to lymphedema [154], ovarian tissue [155,290], and breast cancer [156], to name a few. Care must be taken using these methods, as deep learning for smaller datasets can be challenging and therefore requires measures for the trained model to be accurate [159].

In this study, we imaged naïve and tumor-bearing murine mammary glands using an automated SHG and P-SHG microscopy system. From the SHG images, we identified collagen aggregations around the tumor boundary and dim SHG signal due to the tumor's takeover of a major portion of the mammary gland. Afterward, we applied our custom-written python program to analyze P-SHG images and CurveAlign to analyze SHG images to measure fibrillar orientations. CurveAlign is an effective technique for quantifying collagen fibers and can quickly extract orientation data from SHG images [291]. Nonetheless, it requires human inspection and can be prone to missing the finer fibers in images. In contrast, our automated P-SHG image analysis can resolve and detail finer collagen fibers, at the cost of requiring increased imaging acquisition time. Following this, we trained a supervised deep-learning model for the SHG images to evaluate whether we could classify naïve and tumor-bearing mammary glands using a small dataset. In this process, different data splits were tested, and other parameters of the trained model were also fine-tuned for each case to find the best possible deep learning model for our data. A comparison was made with the well-known image classification model MobilenetV2 [292].

Methodology

Tissue preparation

Female BALB/c mice were purchased from Charles River Laboratories. All animal experiments were conducted according to the regulations established by the Canadian Council of Animal Care, under protocols approved by the McGill University Animal Care and Use Committee. For the collection of naïve glands, mice were euthanized at approximately 8 weeks of age, and the 4th (inguinal) mammary gland was removed. Whole mount preparations were made using blunt tweezers to manipulate the mammary glands, spreading the tissue flat against a Superfrost microscope slide (VWR). Mounted mammary glands were then immediately placed in Carnoy's fixative (60% ethanol, 30% chloroform, 10% acetic acid) for 24 hours at 4° C, after which they were stored in 70% ethanol.

The murine tumor-bearing samples used in this study were derived from two orthotopic models: (1) injection of 4T1 cells into nulliparous mice and (2) injection of 66cl4 cells into mice in the postpartum period (an aggressive form of breast cancer). The 4T1 cells were provided by Dr. Peter Siegel's group (McGill University) and were cultured in DMEM (Wisent) supplemented with 10% FBS and antibiotics. The 66cl4 cells were provided by Dr. Josie Ursini-Siegel's group (McGill University) and cultured in RPMI (Wisent) supplemented with 10% FBS and antibiotics. Cells were maintained at a low passage number before use. For both models: 1×10^5 cells were injected into the 4th mammary fat pad, and tumors were allowed to grow for two weeks. At 14 days post-injection, mice were euthanized, and primary tumors and surrounding stroma were removed. Samples were fixed in 10% Neutral Buffered Formalin (VWR) for 48 hours at 4° C, after which they were stored in 70% ethanol.

Following fixation, naïve and tumor-bearing mammary glands were embedded in paraffin and serially sectioned (5 μm thickness). Slides were deparaffinized and rehydrated by submersion in three rounds of xylene, two rounds of 100% ethanol, one round of 95% ethanol, and one round of 70% ethanol (5 minutes per round). Rehydrated slides were rinsed for 5 minutes in distilled water. Coverslips (VWR, No. 1) were then mounted onto slides using Permount mounting medium (Fisher). Slides were allowed to dry overnight before downstream microscopy.

SHG imaging setup

SHG microscopy and P-SHG microscopy were performed using a custom laser stage scanning inverted microscope (for more details, see Figure 4-1 and Figure 4-2). A mode-locked Ti:Sa laser (Tsunami, Spectra-Physics) pumped by a 12 W Millenia Pro laser (Spectra-Physics) was used. This laser emits pulses around 810 nm and delivers 150 fs pulse duration at 80 MHz repetition rate with an average power of 2.5 W. For power control, a half-wave plate and a Glan-Thompson polarizer were used to adjust the average power to 50 mW (0.625nJ pulse energy) at the focus of the objective. Given the size of the samples to image, sample scanning using a high-speed motorized XY scanning stage (MLS203, Newton, NJ) was used. The focus was adjusted coarsely and finely with mechanical and piezoelectric motors (PI Nano-Z, USA). An air objective (UplanSApo 20X, NA 0.75, Olympus, Japan) was used for illumination. A condenser was used to collect the sample's SHG emission, which was detected by a photomultiplier tube (R6357, Hamamatsu Photonics) set at 800 V. The SHG signal was isolated by two spectral filters placed before the photomultiplier. A short pass filter that blocks any wavelength higher than 720 nm (i.e., the input laser light) is employed with a bandpass filter centered at 405 nm to filter out any residual input light. A multichannel I/O board (National Instruments) and a custom-written Python program were used for signal acquisition and synchronization. Given the sample size and the acceleration and deceleration times of the motorized scanning stage, each SHG image had an acquisition time of a few minutes. Raw data were visualized using Fiji-ImageJ (NIH, USA). For P-SHG measurements, 1000 × 1000 μm regions of interest were imaged, and for image classification, 9000 × 5000 μm whole sample images were taken.

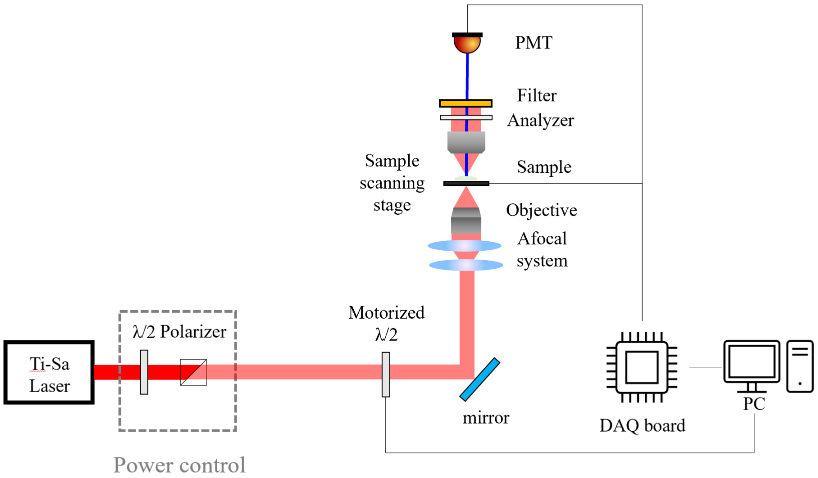

Figure 4-1: Layout of the SHG and P-SHG inverted microscope setup. When using only SHG, the motorized half-wave plate is removed. For P-SHG, the angles range from 0 to 170 degrees. The microscope and the motorized half-wave plate work under a unified custom python program for P-SHG measurements.

For P-SHG, a motorized half-wave plate was used to rotate the linear polarization of the laser beam used to acquire the images. To avoid any polarization distortion and due to the size of the sample, we used sample scanning instead of laser scanning. Images were taken for 18 polarizations states in 10-degree steps from 0 to 170 degrees. The motorized half-wave plate and the sample scanning were all synchronized with a home-built python program (for a complete description of the program, see [242]). A custom MATLAB script based on [63,236] was used for processing the P-SHG images. Fourier transform of the measured intensity about the angle is taken with a spatial fast Fourier transform algorithm. For more theoretical information about the script and how to obtain the polarization angle based on the SHG intensity, please refer to [63,236]. To summarize, the SHG intensity of collagen fibers with respect to the linear polarization angle of the input light source Ω can be written as [236]:

$$I_{SHG}(\Omega) = K[Acos(4\Omega - 4\theta) + Bcos(2\Omega - 2\theta) + 1] \qquad 4.1$$

Where A and B are associated with the susceptibility components, K is the mean number of photons detected, and θ is the collagen fiber in-plane orientation. By varying the angle Ω (i.e., using the half-wave plate to change the linear polarization of the input laser), the main direction of the fibrils (θ) can be extracted [18,19]. After a reliability test between the associated susceptibility components and the experimental data, P-SHG data can be extracted [63]. This modified MATLAB script integrates with our imaging pipeline and accepts 32-bit images [92].

In this study, we benchmark our method with CurveAlign, a well-known tool for fibrillar collagen quantification at the tumor boundary [291]. CurveAlign is a curvelet transform-based fibrillar collagen quantification platform. It consists of a few steps; first, a two-dimensional fast discrete curvelet transform is performed. Second, based on the scale of interest and the threshold of the remaining coefficients, the center and spatial orientation of each curvelet are found, and by grouping the adjacent curvelets, the local fiber orientations are estimated [293]. The simplified diagram of P-SHG and CurveAlign analysis is depicted in Figure 4-2.

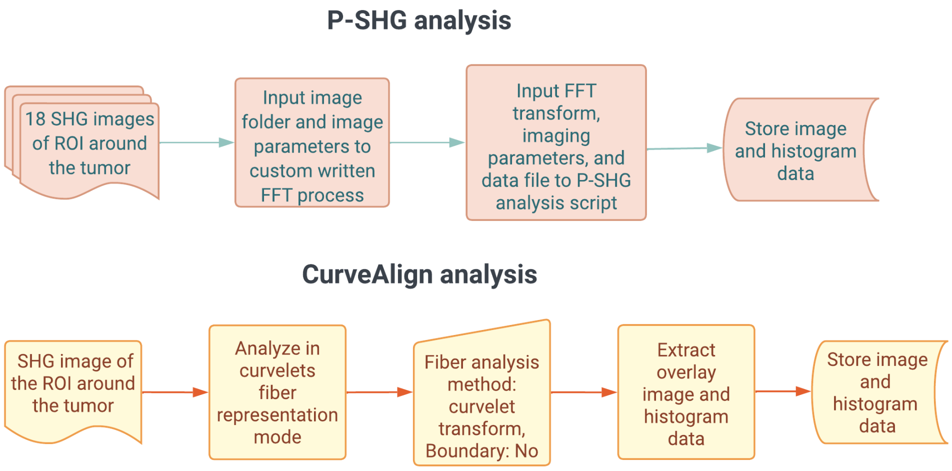

Figure 4-2: Simplified P-SHG and CurveAlign analysis flowchart. For P-SHG analysis 18 SHG images (32-bit TIFF) of the regions of interest (ROI) are taken in 10-degree steps from 0 to 170 degrees and the results (colorwheel, orientation map, anisotropy parameter map, and histogram data) are stored. For CurveAlign a single SHG image is inputted to the CurveAlign script, and the results (overlay image alongside its histogram data) is stored.

Image classification using deep learning and transfer learning

The image classification was done using TensorFlow [294], an open-source Python library developed by Google. Moreover, transfer learning was performed using the MobileNetV2 architecture since it is the most common architecture used for the image. Forty-six images comprising 28 naïve and 18 tumor bearing mammary gland samples were used. Due to the small sample size, data augmentation involving flip, rotation, and zoom was performed before the image classification. The data was trained for twenty-five epochs, and the accuracy and loss of the training and test data were recorded for a data split of 10, 20, 30, and 40% between the training and test data, and the results were plotted to determine the overall performance of the model.

Results and discussions

SHG imaging

Given the sample size, 9000 × 5000 µm area was selected to encompass most of the mammary gland and its surroundings. In this configuration, stage scanning was used for the imaging, and each image was taken over 3 min with a step size of 10 µm/pixel and 150 ms exposure time. Figure 4-3(a, b) are from naïve, non-tumor bearing, mammary glands. As can be seen, the mammary gland and its surroundings have well-defined ductal structures.

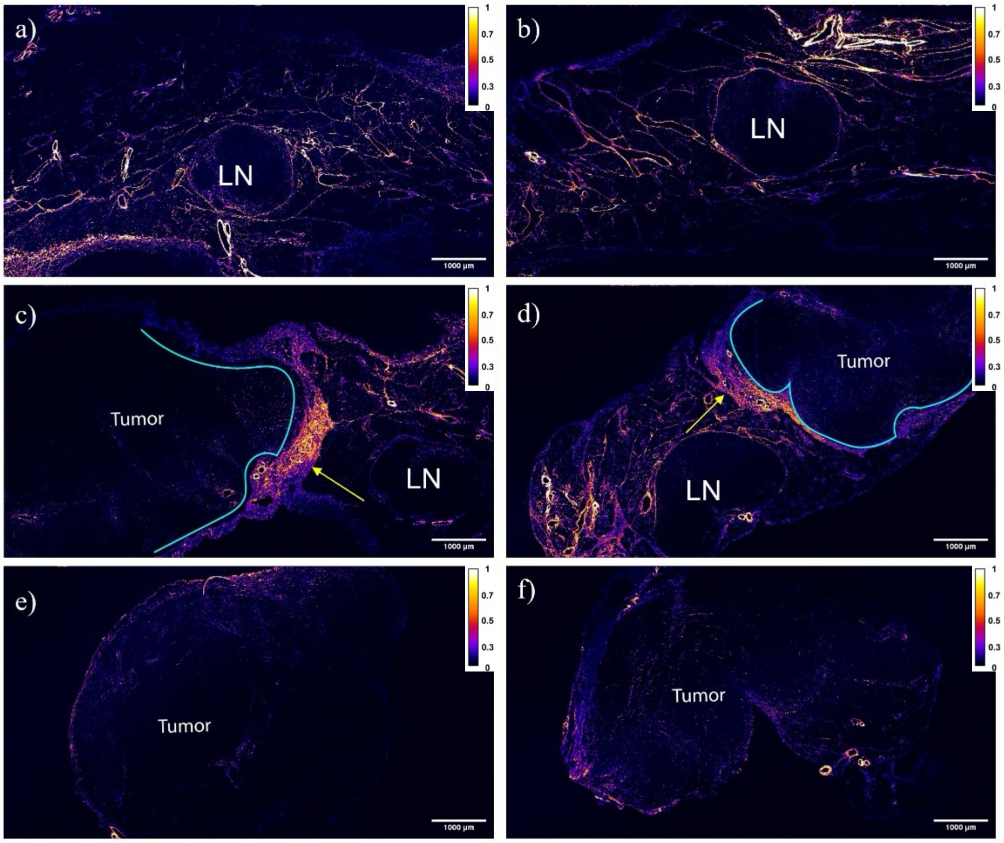

Figure 4-3: SHG images with normalized intensity calibration bars of (a, b) naïve and (c-f) tumor-bearing mammary glands. SHG microscopy can resolve the intricacies of the microenvironment. It shows that the tumor and the lymph nodes (LN) do not produce SHG signal, which leads to a loss of SHG signal as it progresses throughout the gland. Moreover, the yellow arrows in (c,d) indicate the collagen barrier formed between the tumor and the rest of the mammary gland ECM. (e,f) are more advanced cases where the tumor has taken over the majority of the mammary gland, with little normal tissue structure remaining.

The mammary gland tumors in the bottom row do not generate SHG. In Figure 4-3(c,d), the tumor edge is more pronounced, and aggregated collagen can be seen forming a barrier in the boundary between the tumor and the stroma, which is evident from the stronger SHG signal in the center of the Figure (see yellow arrow). This finding agrees with previous studies that suggest collagen deposition around a tumor can form a barrier (collagen fibers being parallel to the tumor boundaries) which provides a protective layer to physically constrain the spread of the tumor [278,295]. The fibrillar orientation and angle of the formed barriers will be addressed in later sections. In extreme cases such as Figure 4-3 (e,f), there is a very dim SHG signal since the tumor has taken over most of the mammary gland. Although the SHG intensity reveals some aspects of tumor biology, for extracting the orientation of the collagen fibrils and defining potential risk of invasion, P-SHG acquisition and image post-processing is necessary.

P-SHG and CurveAlign analysis

Restructuring of collagen fibers at the tumor-stroma junction is known to help promote local invasion and metastasis; therefore, extraction of fibrillar orientation data is essential [296]. Two approaches can be used for orientation extraction of the collagen fibrils: (i) P-SHG and extraction of angle data afterward using a custom MATLAB script or (ii) taking SHG images and processing them using CurveAlign. For P-SHG microscopy, a 1000 × 1000 μm area was chosen with a 3 μm/pixel step size and 90 μs exposure time, leading to a 4 min acquisition time for each image. For each P-SHG analysis, 18 images were taken, bringing the whole imaging process to 72 min per sample. The boundaries around the tumor of three samples were examined and afterward processed using the Fast Fourier transform process mentioned above.

To benchmark the capabilities of our P-SHG imaging and data analysis in studying the environment around the tumor boundary, CurveAlign software was used on SHG images taken from the same region of interest. Figure 4-4 provides a summary of the results obtained during this experiment:

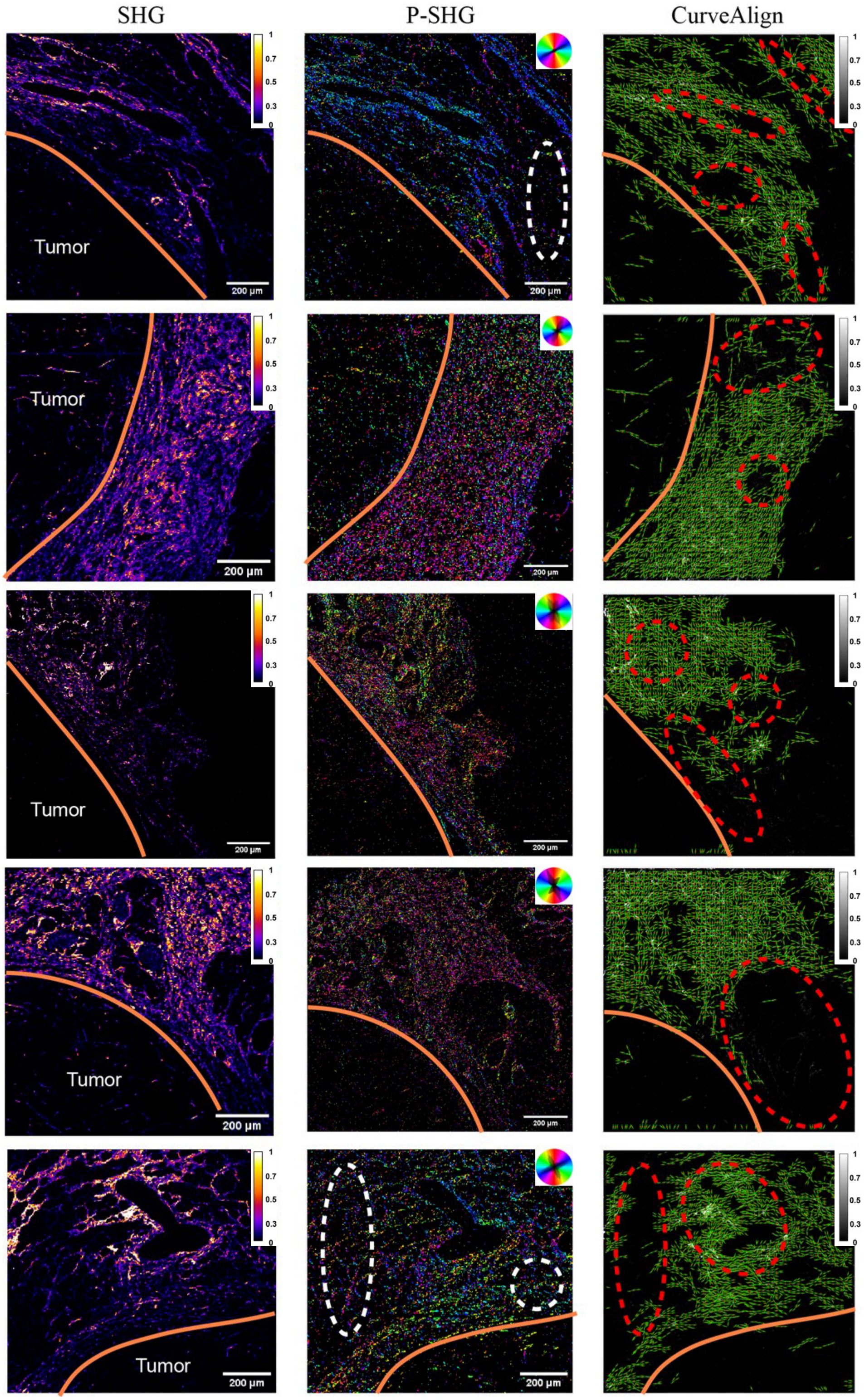

Figure 4-4: shows SHG, P-SHG, and CurveAlign analysis of 5 samples with normalized intensity calibration bar. Each row represents the same region of interest. P-SHG images are accompanied by a color wheel, with each angle (0-360 degrees) represented by a color, and the fibrillar histogram. Both approaches provide an excellent distinction between the tumor and its surroundings, although in both cases, there are some underfilling and overfilling of regions shown using white dashed lines in P-SHG and red dashed lines in

CurveAlign. As an example, in the first row, when we compare both approaches to the reference SHG image we can see that the P-SHG method is overfilling in one region indicated by the white dashed line, and there are four areas in which CurveAlign has either underfilled or overfilled indicated by the red dashed lines. Similar errors can be seen in the consecutive rows as well.

For our samples, P-SHG analysis provides orientation details for smaller and finer collagen fibers than its CurveAlign counterpart. In CurveAlign, the estimation of the orientation angle leads to insufficient detection in regions where the SHG signal is dim and overestimation in other regions (red dashed lines in Figure 4-4). Overall P-SHG analysis is more detailed, albeit noisier, and with some overfilling in different samples (white dashed lines in Figure 4-4). Overfilling in the P-SHG analysis is due to the goodness of fit (R^2) (range between 0 and 1 of the pixel intensity) that is defined during analysis. If the intensity of a pixel is lower than the goodness of fit, it will be omitted from the analysis. Therefore, it is necessary to keep the goodness of fit between 0.3-0.4 so that noisier pixels are not omitted from the analysis which would lead to overfilling of the images in some areas. We also performed multi-scale structural similarity index (MS-SSIM) (ranging from 0 to 1, with 0 being not similar and 1 being identical) by taking the SHG images used for the analyses as the ground truth (GT) and comparing the P-SHG analysis and CurveAlign analysis to the GT images and each other:

Table 4-1: MS-SSIM index of P-SHG and CurveAlign analysis

Sample No.	R^2 range of P-SHG analysis	P-SHG vs GT MS-SSIM	CurveAlign overlay vs GT MS-SSIM	P-SHG vs CurveAlign overlay MS-SSIM
1	0.4-1	0.76	0.27	0.25
2	0.4-1	0.33	0.23	0.25
3	0.4-1	0.76	0.45	0.4
4	0.4-1	0.84	0.37	0.36
5	0.4-1	0.36	0.3	0.2

Based on the results of Table 4-1, a quality metric for image similarity is a necessity to fine tune the parameters of both analysis methods. In addition, our study found that by increasing the R^2 minimum of the P-SHG analysis, the MS-SSIM between the P-SHG and CurveAlign analysis overlay image is increased (Please refer to supplementary information Table S1-S5 for more details). The solution for the underfilling and overfilling is to have a noise threshold (which our analysis method provides) that can be changed by the user based on the similarity and quality metric index between the analyzed image and GT image in the form of either a noise-free SHG image or a complementary fluorescence image. Given that P-SHG image acquisition takes 72 min compared to the 3 min of standard SHG imaging followed by the CuveAlign image processing, there is a tradeoff between imaging time and accuracy that depends on the study and experimental goals, such as boundary requirements and imaging time. To summarize, CurveAlign is a powerful image processing tool that can be used for collagen quantification around the tumor boundary but requires human inspection and high-quality SHG imaging and can miss or overfill some fiber orientations in the images. However, P-SHG imaging provides a more detailed view of the tumor microenvironment. It can resolve finer fibers but at the cost of the image being noisier and imaging acquisition being much more time-consuming. A solution for overfilling and underfilling in both methods is to introduce a similarity index metric for comparison between the analyzed image and the GT image (complementary fluorescence image or high quality SHG image) and to have flexible noise threshold metric as it varies from sample to sample.

Image classification

Image classification was performed on the data using the SHG images discussed in the previous section. SHG images of naïve and tumor-bearing mammary glands were first preprocessed in ImageJ to adjust brightness and denoise. Two models were trained for the dataset. A custom sequential model was made using the Keras library, an open-source library from Google integrated by Tensorflow, and transfer learning was performed using the MobilenetV2 model. Both models were written and trained using Google Colaboratory. Finally, to determine the effectiveness and precision of the architecture, the accuracy and loss are plotted to visualize how the models fit the data. The image processing pipeline can be seen in Figure 4-5 and the architecture of the sequential model is seen in Figure 4-6.

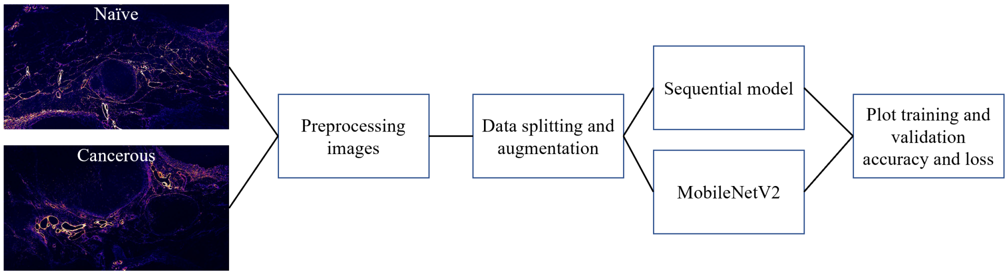

Figure 4-5: Image processing pipeline from SHG imaging to evaluate the trained model's accuracy and precision.

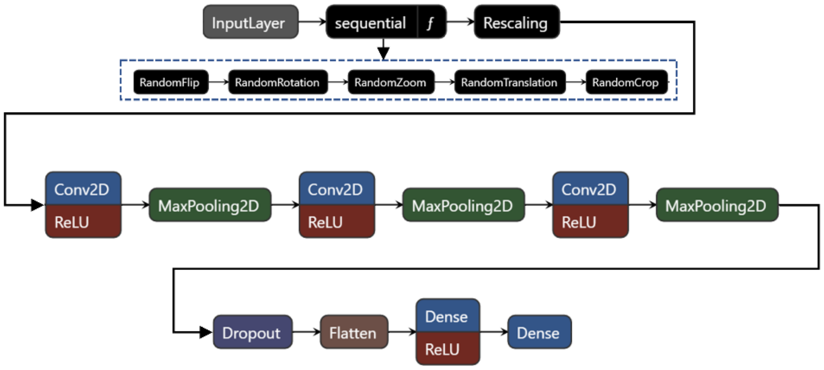

Figure 4-6: Architecture of the convolutional neural network (CNN) model built using the Keras API. The data augmentation layer (sequential) creates new training examples by applying random transformations to existing images, such as rotating, flipping, or zooming. The rescaling layer rescales the input image pixel values from the range [0, 255] to the range [0, 1]. The conv2D layer applies a convolutional operation with 16, 32 and 64 filters and Maxpooling2D reduces the spatial dimensions of the input by taking the maximum value in each 2x2 window. The Dropout layer randomly sets a fraction of the input units to zero during each training epoch (the rate is 0.2). Flatten layers flatten the output of the previous layer into a one-dimensional vector, which is fed into two dense fully connected neural network layers (Dense). We added more Conv2D and Maxpooling2D layers up to 20 layers to test how the addition of layers affected the accuracy of the classifier model.

Overall, this model consists of convolutional layers that extract features from the input image, followed by a fully connected neural network layer that makes the final classification decision. The model is trained using the Sparse Categorical Cross entropy loss function and optimized using the Adaptive Moment Estimation backpropagation algorithm.

Deep learning feasibility on a small dataset

Before we examine the efficiency of the trained model, we must define some terms used to quantify its performance. There are performance markers that are used for measuring the capability of a trained model but, for simplicity, we will perform cross-validation by splitting the data into training and test datasets, e.g., a percentage of the data will be selected as the training dataset, and the remaining percentage as the test dataset. The model uses the training data to learn from, and the test data is used for assessing the model’s performance [135]. We chose the following data split percentages: (90% training data, 10% test data), (80% training data, 20% test data), (70% training data, 30% test data) and (60% training data, 40% test data). For simplicity, they will be called 10%, 20%, 30%, and 40% data splitting, respectively.

With the definition of the data splits that will be evaluated, we can define some terms that refer to each data set. Training/test accuracy refers to how well the model fits the specified training/test data. Training/test loss assesses the model's error when learning from the training/test data. Training/test accuracy and loss are good metrics to assess the model's fit on the data. When test loss is greater than the training loss, the model is "memorizing" the training data set, and therefore its ability to be applied to unseen data is impaired [188]. This is called overfitting. There is also underfitting, in which the model needs more steps (epochs) to go through the data and be fully trained. One good indicator that can reveal many aspects of the system is the training/test loss curve, which shows how well the model performs. Each case presented in this section will be summarized in a table that shows the average training/test accuracy after 25 epochs and represented in the training/test loss curve to give a clearer picture of the model's performance.

Data augmentation and more complex architectures are unique strategies to avoid overfitting [135,297,298]. Many complex architectures solve overfitting by adding extra processing layers, but data augmentation targets the problem's root: the available training data. As in the case of image classification, the number of available data is artificially inflated by changing different aspects of the training image dataset, such as cropping, flipping, rotating, etc.[135,297,298] . All these measures mitigate overfitting.

Due to the small sample size of the data available, we also apply a variety of data augmentation such as crop, zoom, translation, and flip to inflate our dataset artificially. We also introduced a 20% dropout layer to avoid overfitting by randomly removing 20% of the nodes and their connections from our neural network, resulting in a new network architecture independent of the parent network [299]. The accuracy and loss curve of the first model can be seen below in Table 4-2.

Table 4-2: Average training and test accuracy for different data splits using a custom sequential model

Data split	Training accuracy	Test accuracy
10%	0.82	0.76
20%	0.73	0.80
30%	0.53	0.73
40%	0.69	0.74

It is evident from the data split of 10% that the test accuracy is constant, which can be due to the small test data set. Still, the training accuracy increases with each epoch, meaning the model better fits the training accuracy. In the 20% data split, we see that the accuracies are closer, and there are some epochs where the model was more accurate for the test dataset than the training set. In the 30% data split, we see a gap between the training and test accuracy, which is higher than the training accuracy. This gap could mean that the test data set is more straightforward for the model to understand than the training dataset. It could also be because the data augmentation we introduced makes it harder for the model to learn from the training dataset.

Moreover, since we are using dropout during training, in which some information from the training data is lost, it could be that consecutive layers will try making predictions based on incomplete data, thereby making it harder for the model to adapt. We will explore solutions to this problem in later sections when we change different parameters to see how it affects the trained model. There is also a gap in the 40% data split between the training and test accuracy, where the training accuracy is lower than the test accuracy.

Besides accuracy, the loss curve can provide relevant information about the model's state, whether it is fitting, overfitting or underfitting. Figure 4-7 provides the loss curve of the four data splits that were evaluated with the model:

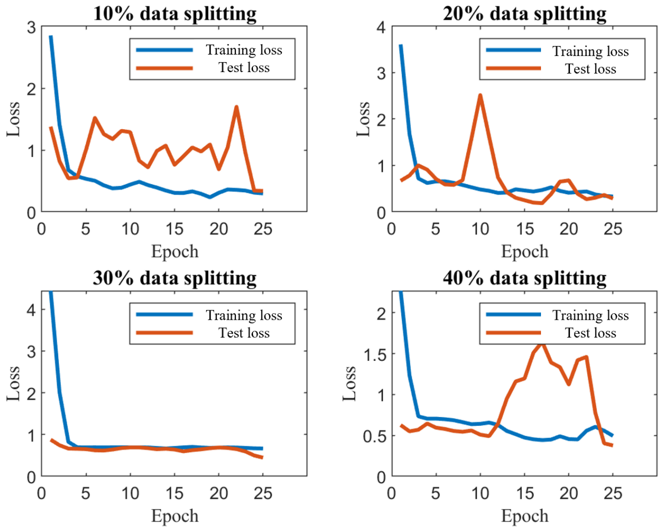

Figure 4-7: Loss curve of the model for 4 data splits. We have clear overfitting for the first data split after epoch 5, which is undesirable. The model fits the data well for 20% data splitting besides the overshoot seen at epoch 10. The best-case scenario from all the splits can be seen for 30% data splitting, where the model performs perfectly for the data provided. For the last case, we have underfitting until epoch 10, followed by overfitting.

Therefore, the test accuracy of this model, without overfitting, is 30% data splitting at approximately 73%. Based on this first investigation, we can now fine-tune other model parameters to see whether we can overcome the training and test accuracy gap. We performed receiver-operating characteristic (ROC) analysis but in the case of our data, we have 44% data bias (33 healthy cases vs. 13 cancer cases) which indicates a significant class imbalance in the data. Therefore, we implemented Precision, Recall, F1 score and area under the curve (AUC) metrics together to better understand our model accuracy. The model has a high recall (1.00), which means it can correctly identify the positive cases at the cost of having false positives. The precision of our model was low (0.3) and the F1 score of our model was 0.5. We have an AUC range of 0.51-0.55 which is expected given the high-class imbalance in the data.

Addition of more data augmentation layers and elimination of dropout

As previously mentioned, two elements, namely (i) dropouts and (ii) insufficient data, could explain the gap between the test and training accuracy. Therefore, we can introduce more data augmentation layers to the model to increase available data, eliminate the dropout in the model, and see how well it performs. The result of these changes is summarized in Table 4-3:

Table 4-3: Average training and test accuracy for different data splits using more data augmentation layers and no dropout

Data split	Training accuracy	Test accuracy
10%	0.64	0.76
20%	0.66	0.78
30%	0.65	0.79
40%	0.64	0.76

Table 4-3 shows that due to the extra layers of data augmentation implemented, the training accuracy decreases as we have made it harder for the model to learn from the training dataset. In one scenario, we also preferentially augmented the tumor bearing data to balance out the dataset. Nevertheless, the test accuracy of the model remains the same even with the elimination of dropout and having more training data. For this trained model, the 10% data splitting has underfitting until epoch 18, and afterward, the model overfits after epoch 24. Overfitting happens in many earlier epochs for the case of 20, 30, and 40% data splits. Taking the loss curve and the accuracy of this model into consideration, adding more data augmentation, and eliminating dropout does not help improve the model's performance. Experimenting with model parameters leads to the conclusion that the test accuracy of the model is sometimes higher due to the limited availability of data, and that the test data is more straightforward than the training data. Moreover, it could be beneficial to also omit some of the naïve samples to balance the dataset but given the already limited dataset, it can have a negative impact on the model's performance and therefore we decided against it.

Transfer learning using MobileNetV2

In this section, we will explore whether transfer learning with the well-established MobileNetV2 model would be the better approach. The motivation for choosing the MobilenetV2 architecture is due to its light weight and fewer number of tunable parameters as our dataset is very small. Other networks such as ResNet, Alexnet and GoogLeNet were considered but these networks are much deeper compared to MobilenetV2, with many more layers and parameters. This makes it more prone to overfitting, especially when dealing with small datasets. The deeper architectures enable the networks to capture more complex features in the data, including noise and outliers, which can hinder the model's ability to generalize to new data. As mentioned before, machine learning usually relies on the high quality and size of training data which is only sometimes readily available in real-world scenarios (SHG microscopy images are an excellent example of this problem) [155]. Moreover, training models based on small datasets are usually very application-specific and cannot be applied to other datasets. In these situations, transfer learning is appealing because researchers can leverage models trained on much bigger datasets to conform to their datasets and refine the learning process to be valid for their application [155]. Table 4-4 provides the accuracies of this model when trained using our dataset.

Table 4-4: Average training and test accuracy for different data splits using MobileNetV2

Data split	Training accuracy	test accuracy
10%	0.84	0.78
20%	0.54	0.49
30%	0.58	0.74
40%	0.49	0.33

We see that the model’s accuracy deteriorates after a 10% data split. From the loss curve, we have overfitting after epoch 4 for 10%, after epoch 8 for 20% and after epoch 12 for 40% data splits. Interestingly for MobilenetV2, we see overfitting happening for just the 10% and 40% data split cases in which overfitting happens after epochs 8 and 23. For the 20% and 30% data split, the 0.001 dropout rate in the MobilenetV2 architecture causes the training loss to fluctuate, whereas the gap between the test and training loss remains around the same size [299].

To summarize, with such a small dataset, training a simple classification network from scratch is optimal but data specific. Using transfer learning with well-known networks is a solution, but due to the complexity and number of layers present in such architectures, overfitting and underfitting are more prominent in that case.

Conclusion

In this study, SHG and P-SHG microscopy were used to study the ECM within tumor-bearing mammary glands. SHG microscopy can help identify the collagen aggregates that appear at the tumor-stroma boundary, and P-SHG microscopy is an excellent tool for analyzing collagen fibrillar orientations in the ECM. We have shown an automated SHG and P-SHG microscopy system that minimizes human intervention. We apply two image analysis methods for the collagen fibrillar orientation analysis. CurveAlign is a powerful tool that can be applied to SHG images to distinguish collagen fibrillar orientation with respect to the tumor boundary. Our custom-written P-SHG analysis method can achieve the same results with greater detail. Furthermore, deep learning and image classification can be powerful tools to differentiate between healthy and tumor-bearing samples within the limitation of a small training dataset. Therefore, if deep learning is to be used for SHG imaging, a database should be available where imaging labs worldwide can pool their images. This would help to remove data availability as a limiting problem. After investigating the variation of different parameters, the best model that showed promising results with our small dataset was the 30% data split with 0.2 dropout and three layers of data augmentation that gave a test accuracy of 73%. Another limitation in our study is the imaging speed, that requires further studies to improve. It is worth highlighting that P-SHG analysis, in conjunction with image classification and widefield imaging, has shown great promise in cancer research and provides excellent insight into the underlying mechanisms of collagen formation and remodeling in the ECM [156]. In addition, in future studies, we will explore the feasibility of adapting the machine learning approach used in this study to other tissue types. This will allow us to determine whether the approach is amenable to a wider range of applications and to identify any limitations or challenges that may arise. It will be valuable to expand this work's scope to include the analysis of metastatic lung tissue. This will let us assess the changes in collagen patterns that occur in metastatic outgrowth and potentially identify markers for early detection. Moreover, SHG and P-SHG imaging are well-established methods that have been successfully used for many years. In contrast, image analysis for these methods is still in its infancy, thereby necessitating the exploration of different analysis methods that can be used alongside these imaging techniques.

Back matter

Funding.

The authors acknowledge financial support from Canada Foundation for Innovation, Fonds de recherche du Québec–Nature et technologies, the Natural Sciences and Engineering Research Council of Canada, the New Frontiers Research Fund. A. A. thanks the NSERC CREATE program for the scholarship. Canadian Cancer Society (Grant #707140 to SVDR). SEJP was supported by a doctoral fellowship from Fonds de Recherche Québec Santé (FRQS) and the Epstein Fellowship in Women’s Health (Faculty of Medicine, McGill University).

Conflict of interest.

The authors declare no competing interests.

Data availability.

Data underlying the results presented in this paper are not publicly available but may be obtained from the authors upon reasonable request.

Acknowledgments.

The authors acknowledge technical support from Antoine Laramée.

5 A COMPARATIVE STUDY OF CARE 2D AND N2V 2D FOR TISSUE-SPECIFIC DENOISING IN SECOND HARMONIC GENERATION IMAGING

UNE ÉTUDE COMPARATIVE DE CARE 2D ET N2V 2D POUR LE DÉBRUITAGE SPÉCIFIQUE AUX TISSUS EN IMAGERIE DE GÉNÉRATION HARMONIQUE SECONDE

Authors:

Arash Aghigh[1,], Gaëtan Jargot[1], Charlotte Zaouter[2], Samuel E J Preston[3], Melika Saadat Mohammadi[1] , Heide Ibrahim[1], Sonia V Del Rincón[3], Kessen Patten[2] and François Légaré[1]

[1] Centre Énergie Matériaux Télécommunications, Institut National de la Recherche Scientifique, Varennes, Québec, Canada.

[2] Armand-Frappier Santé Biotechnologie Research Centre, Institut National de la Recherche Scientifique Laval, Québec, Canada

[3] Department of Experimental Medicine, Faculty of Medicine, McGill University, Montréal, Québec, Canada; Gerald Bronfman Department of Oncology, Segal Cancer Centre, Lady Davis Institute and Jewish General Hospital, McGill University, Montreal, Quebec, Canada.

Titre de la revue ou de l'ouvrage :

J. Biophotonics 2024, 17(6), e202300565. Published online: April 2, 2024, Doi: 10.1002/jbio.202300565

Contribution des auteurs:

A.A conceived and wrote the article and performed the experiments. C. Z. and S. P. provided samples for the experiments. M. M. assisted in data analysis. A. A., G. J., C. Z., M. M. S. P., S. V. D. L., and K. P. participated in drafting, section arrangement, and critical revision of the manuscript. H. I. and F. L. critically revised the manuscript for important intellectual content and approved the final version to be published.

5.1 Main article

Abstract.

This study explored the application of deep learning in Second Harmonic Generation (SHG) microscopy, a rapidly growing area. This study focuses on the impact of glycerol concentration on image noise in SHG microscopy and compares two image restoration techniques: Noise2Void 2D (N2V 2D, no reference image restoration) and content aware image restoration (CARE 2D, full reference image restoration). We demonstrated that N2V 2D effectively restored the images affected by high glycerol concentrations. To reduce sample exposure and damage, this study further addresses low-power SHG imaging by reducing the laser power by 70% using deep learning techniques. CARE 2D excels in preserving detailed structures, whereas N2V 2D maintains natural muscle structure. This study highlights the strengths and limitations of these models in specific SHG microscopy applications, offering valuable insights and potential advancements in the field.

Keywords: Deep learning, SHG microscopy, image restoration, myosin imaging, ECM imaging, denoising.

Introduction.

Second harmonic generation (SHG) microscopy is a powerful nonlinear optical microscopy technique that has been successfully used in medical and nonmedical imaging for years [2,37,300,301]. Image quality in microscopy crucially depends on the signal-to-noise ratio (SNR), which is the ratio of signal intensity to noise. Factors such as laser power, exposure time, and the sample itself play crucial roles in influencing the SNR. It is well known that an increase in laser power while enhancing the SHG signal risks thermal damage to the sample [14]. For example, increasing the laser power can produce a higher SHG signal but may cause thermal damage to a sample [302–304]. Therefore, finding the optimal trade-off between the laser power and achieving an acceptable SNR (i.e., having the sample structure visible with noise present) is critical. In addition to the instrumental parameters, sample type is another critical criterion that can affect the SNR in SHG microscopy. While we observed strong SHG signals from collagen rich tissues [40] and skeletal muscles [97], some samples, such as microtubules, inherently have a weak SHG signal [123]. Samples with a lower SHG signal have a low SNR, and their structure can be buried under background noise, depending on the experimental conditions.

Within the evolving landscape of SHG microscopy, deep learning is a transformative tool for classification, segmentation, and image restoration. We provide ample examples of different studies focusing on different applications. In [305] a classification application, a method for diagnosing ovarian cancer during surgery using SHG imaging and deep learning techniques is introduced. By training a convolutional neural network (CNN) on a vast dataset of SHG images, the system can differentiate between normal, benign, and malignant ovarian tissues with 99.7% accuracy. In [306] a segmentation application, the effectiveness of a U-Net CNN for improving the segmentation of collagen fibers in SHG images was demonstrated. The CNN successfully addressed the challenges posed by varying the SHG image intensity across the depths. This method consistently outperformed the traditional thresholding techniques, particularly in deeper tissue sections. Although not focused solely on SHG, [307] compared different denoising techniques to improve the quality of nonlinear multimodal images in head and neck tissue analysis. In this study, traditional methods (e.g., median filter and Gerchberg-Saxton), established deep learning networks (e.g., DnCNN), and innovative networks (e.g., Noise2Noise, MIRNet, and incSRCNN), specifically focusing on their ability to reduce noise while preserving critical image details. In another study, researchers introduced a fast large-area multiphoton exoscope (FLAME) for imaging human skin [308]. The FLAME system incorporates a deep-learning-based image restoration technique using a content-aware image restoration model (CARE) network. This approach improves the quality of the images captured by the system. These studies demonstrate the broad potential of deep learning in SHG microscopy. However, tissue-specific variations in signal intensity and the impact of preparation techniques introduce unique challenges for image restoration in SHG. The application of deep learning techniques specifically tailored for improving low-SNR SHG imaging has not been extensively explored. This gap presents a unique opportunity for research aimed at addressing the specific challenges associated with SHG microscopy, particularly in tissue-specific imaging under low-SNR conditions.

Image restoration enhances the image quality by eliminating noise, artifacts, and other distortions [164,309] without creating hallucinations (generation of visual structures that are not based on the actual information available in the input image [310]). Deep learning image restoration has been successfully applied to fluorescence- [164,309], super-resolution- [311,312], structured illumination- [313], and electron microscopy [165,314]. It has also been applied to multiphoton microscopy [307,308].

Three of the many different types of available image restoration techniques to remove noise are noise-to-ground truth (N2GT) [164], noise-to-noise (N2N) [315], and noise-to-void (N2V) [166]. N2GT refers to the removal of noise from an image by comparison to a reference image, also known as the ground truth image, which is assumed to be noise-free and used as a guide in the denoising process [164]. The availability of GT images is a limitation of this method [164,166]. N2N refers to removing noise from an image (low SNR) by comparing it to another noisy image (high SNR) rather than to a GT image [315,316]. This method is more widely applicable because it does not require a noise-free image [315]. One model in this category is the content-aware image restoration model (CARE) based on the U-net convolutional neural network [317]. It is among the models that require high- and low-SNR image pairs to perform image restoration [316]. N2V refers to removing noise from an image by creating a deep neural network to learn the statistical properties of the noise and the signal within one image [166]. Unlike previous methods, which require an image pair, this method does not require such a requirement and uses a single noisy image for training.

Common methods for evaluating denoised image quality include the Structural Similarity Index Metric (SSIM) and Peak Signal-to-Noise Ratio (PSNR) to ensure hallucination-free image generation. Both metrics were used to compare the similarities between the original and processed images. The PSNR is calculated by taking the ratio of the maximum signal to the mean squared error (MSE) between the original and processed images. The higher the PSNR value, the higher is the quality of the processed image. The SSIM is a metric that uses structural and textural information. It compares structural information by measuring the similarities between the original and processed images' mean value, standard deviation, and cross-covariance [318]. The value of SSIM ranges between 0 and 1, where 1 indicates perfect similarity, 0 indicates poor similarity, and -1 indicates perfect anti-correlation. The SSIM and PSNR metrics have different sensitivities to image degradation [175,181,319].

Our study uniquely addressed the tissue-specific imaging challenges of collagen and myosin within the SHG microscopy domain, investigating the effects of glycerol concentration on zebrafish fixation [320], and exploring low-laser-power imaging across diverse biological specimens, including muscle tissues from two zebrafish strains, and the intricate extracellular matrix barrier of tumor-bearing mouse mammary glands. This focus on tissue specificity coupled with our tailored application of advanced denoising techniques sets our research apart. By applying CARE 2D and N2V 2D in such a targeted manner and evaluating their effectiveness with mSSIM and PSNR metrics, our study not only highlights the adaptability and efficacy of deep learning for SHG microscopy but also emphasizes its potential for tissue-specific imaging under low-SNR conditions. This approach ensures the preservation of structural details and effective noise elimination, contributing significantly to the advancement of the field and opening new avenues for precision in biomedical imaging.

Methodology.

Tissue Preparation.

Adult wild-type and mutant Survival Motor Neuron (SMN) zebrafish (Danio rerio) were maintained at 28 °C under a light/dark cycle of 12/12 h according to the Westerfield zebrafish book [320]. Embryos were raised at 28.5 °C, collected, and staged as previously described [321]. All animal experiments were performed in compliance with the Canadian Council for Animal Care guidelines and approved by the INRS-LNBE ethics committee. Genotyping of SNM larvae was performed by high-resolution melting analysis (HRM) using genomic DNA extracted by a noninvasive genotyping protocol [322]. Larval (5-day postfertilization 5 (dpf)) SNM −/− (homozygous) and wild-type zebrafish were fixed in 4% paraformaldehyde overnight at 4° C. After fixation, the larvae were rinsed several times (1 hour) with PBS-Tween and mounted on slides in 50–100% glycerol, and finally, their muscles were imaged using SHG microscopy.

Female BALB/c mice were purchased from Charles River Laboratories. All animal experiments were conducted according to the regulations established by the Canadian Council of Animal Care under protocols approved by the McGill University Animal Care and Use Committee. The murine tumor-bearing samples used in this study were derived from orthotopic injection of 4T1 cells into nulliparous mice. 4T1 cells were provided by Dr. Peter Siegel (McGill University) and cultured in DMEM (Wisent) supplemented with 10% FBS and antibiotics. Cells were maintained at a low passage number prior to use. For both models, 1×10^5 cells were injected into the 4th mammary fat pad and tumors were allowed to grow for two weeks. Fourteen days post-injection, the mice were euthanized, and the primary tumors and surrounding stroma were removed. The samples were fixed in 10% Neutral Buffered Formalin (VWR International LLC) for 48 h at 4 °C, after which they were stored in 70% ethanol. Following fixation, naïve and tumor-bearing mammary glands were embedded in paraffin and serially sectioned (5 µm thickness). The slides were deparaffinized and rehydrated by submersion in three rounds of xylene, two rounds of 100% ethanol, one round of 95% ethanol, and one round of 70% ethanol (5 min per round). The rehydrated slides were then rinsed for 5 min in distilled water. Coverslips (VWR International LLC, No. 1) were mounted onto slides using the Permount mounting medium (Fisher). The slides were allowed to dry overnight before downstream microscopy.

SHG imaging setup.

SHG microscopy was performed using a custom-stage inverted scanning microscope, as shown in Figure 5-1. A mode-locked Ti:Sa laser (Tsunami, Spectra-Physics) pumped by a 12 W Millenia Pro laser (Spectra-Physics) was used. This laser delivered pulses of approximately 810 nm with

150 fs pulse duration, at 80 MHz repetition rate with an average power of 2.5 W. For power control, a half-wave plate and a Glan-Thompson polarizer were used to adjust the average power from 20 mW to 110 mW (0.25 to 1.38 nJ pulse energy). Given the size of the samples for imaging, sample scanning was performed using a high-speed motorized XY scanning stage (MLS203, Newton, NJ). The focus was adjusted coarsely and finely by using mechanical and piezoelectric motors (PI Nano-Z, USA). An air objective (UplanSApo 20X, NA 0.75, Olympus, Japan) was used for the illumination. A condenser was used to collect the SHG signal of the sample, which was detected using a photomultiplier tube (R6357, Hamamatsu Photonics) set at 800 V. The SHG signal was isolated using two spectral filters that were placed before the photomultiplier. A short-pass filter that blocks any wavelength higher than 720 nm (i.e., the input fundamental laser light) was employed with a bandpass filter centered at 405 nm to filter out any residual input light. A multichannel I/O board (National Instruments) and custom-written Python program were used for signal acquisition and synchronization. Given the sample size and acceleration and deceleration times of the motorized scanning stage, each SHG image had an acquisition time of a few minutes. Raw data were visualized using Fiji-ImageJ software (NIH, USA).

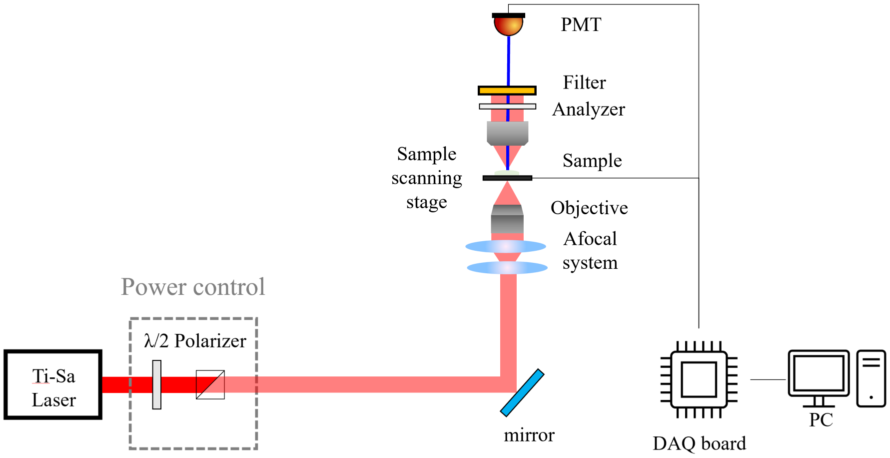

Figure 5-1: Layout of the SHG inverted microscope. The microscope and data acquisition were performed using a unified custom Python program.

Image restoration using CARE 2D and N2V 2D.

Image restoration was performed using the CARE 2D and N2V 2D models. The models were run using the Jupyter notebook provided by the ZeroCostDL4Mic toolbox [189] on Google Colaboratory. For the mammary gland cancer samples, the N2V 2D model was trained from scratch for 2000 epochs on 392 image patches (image dimensions: (500,500), patch size: (64,64)) with a batch size of 128. The CARE 2D model was trained from scratch for 300 epochs on 200 image patches (image dimensions: (500,500), patch size: (64,64)) with a batch size of 16. The reason for having different numbers of training epochs is to compensate for the limited amount of available reference data and allow the N2V 2D model to train for a longer time compared to the CARE 2D model. This extended training duration is essential for N2V 2D, as it leverages self-supervised learning, relying on inherent noise patterns within the data to improve its performance, which necessitates additional training to effectively model and remove noise. For the zebrafish samples, the N2V 2D model was trained from scratch for 2000 epochs on 800 image patches (image dimensions: (333,1333), patch size: (64,64)) with a batch size of 128. The CARE 2D model was trained from scratch for 300 epochs on 50 image patches (image dimensions: (333,1333), patch size: (64,64)) with a batch size of 16. Data augmentation was used in its default setting in all cases, and for CARE 2D, the Augmentor was used [323]. The essential Python packages include TensorFlow, Keras, CSBdeep, NumPy, and Cuda. The training was accelerated using a Tesla T4 GPU on Google servers.

Results and discussion

Fixation: evaluation of the dependence of noise as a function of glycerol content

Sample preparation is essential for any microscopic method [324]. The chemicals used in fixation can cause image deterioration in SHG microscopy for some samples, such as microtubules [123]. Moreover, there is no universal protocol for fixation and each tissue has a unique method [300]. Three glycerol concentrations were tested to determine the best fixation composition for the SHG imaging of zebrafish samples. Because of the different locations of the samples, different image sizes were obtained with a laser input power of 75 mW at the focus of the microscope objective. Figure 5-2 depicts the different samples with different glycerol concentrations that were imaged and their denoised counterparts.

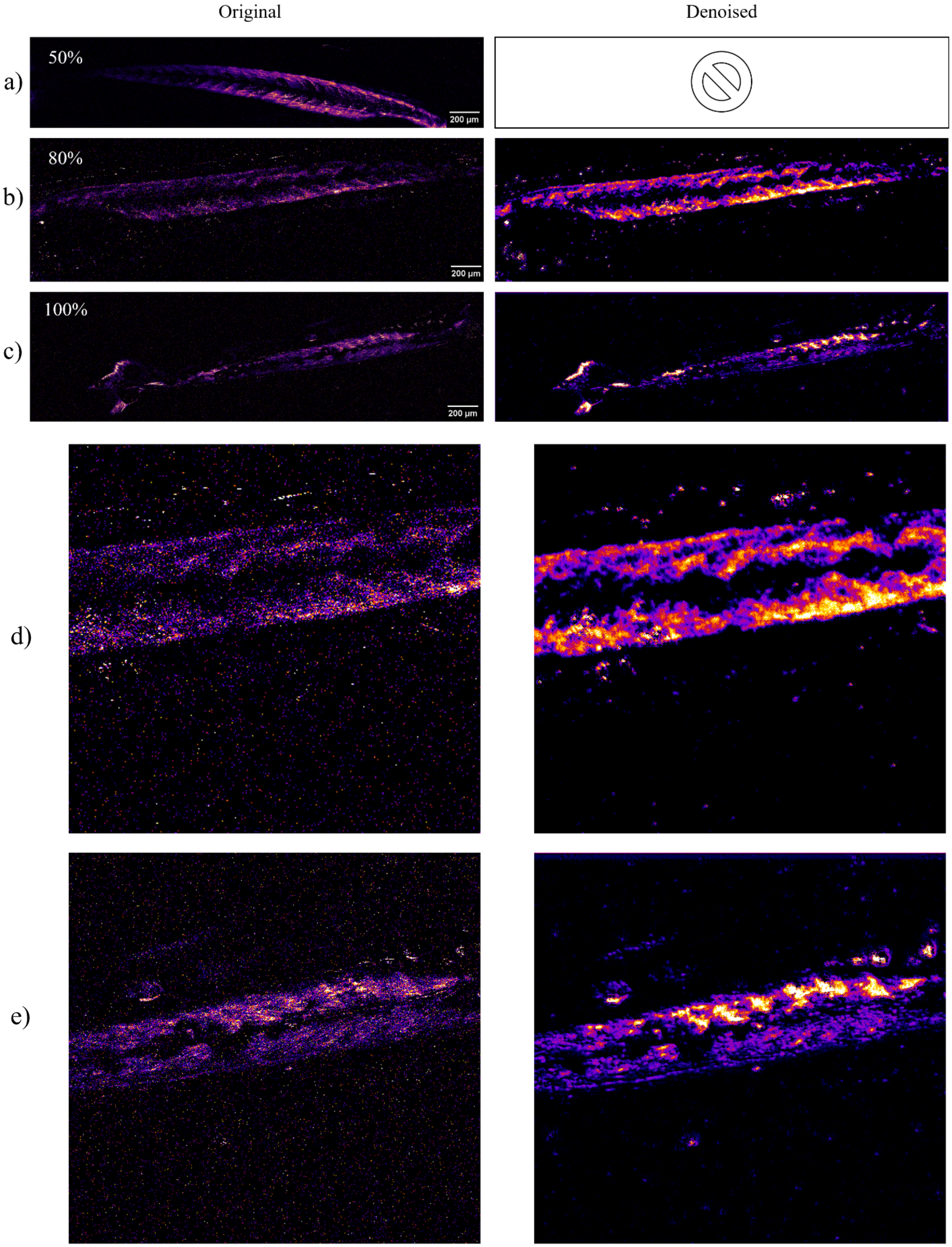

Figure 5-2: Left column: SHG images of different zebrafish samples with a) 50%, b) 80%, and c) 100% glycerol concentration in their fixation alongside zoom in (d,e) for samples b and c, respectively. As the glycerol content

in the fixation increases, the SHG image becomes noisier. Right column: Denoising based on the N2V 2D method was performed for 80 and 100% glycerol content, and it was unnecessary for 50% concentration.

Our study found a correlation between glycerol concentration and noise in the final image; the lower the glycerol concentration, the better the image quality. The minimum amount of glycerol that could be used without disturbing the fixation process is 50%. We then tested N2V 2D and CARE 2D to denoise images with higher glycerol concentrations. The CARE 2D model for these samples resulted in overfitting [188,299] during model training and was not applicable. N2V 2D could successfully restore images in both high-concentration glycerol cases and retrieve the structural information of the fish muscle, as shown in the right column. Given the amount of time and effort required for sample preparation, in some cases, deep learning tools can be used to restore the image quality instead of restarting the sample preparation to determine the perfect chemical composition and physical location of the sample. The intensity profiles for 80% and 100% glycerol are shown in Figure 5-3.

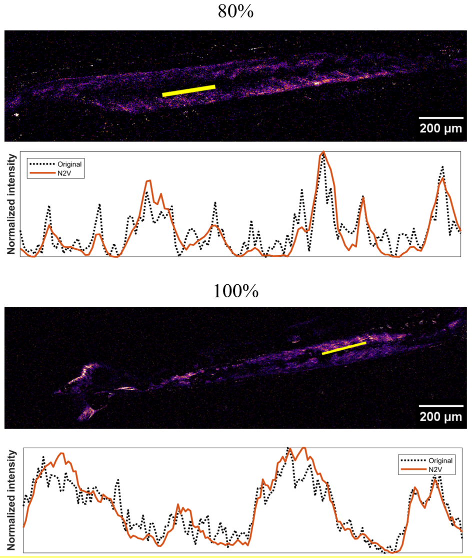

Figure 5-3: The intensity profile of 80% and 100% glycerol content fixation was imaged at 75mW input laser power for the original (black dotted line) and denoised (red solid line) images.

For the intensity profile, we plotted the intensity values of the pixels along the yellow line, as shown in Figure 5-3. From this Figure, we can see that for 80% glycerol, the model enhances the contrast of the image. A comparison with the original signal shows that it follows the same overall intensity pattern as a cleaner (omission of noise) signal. For 100% glycerol, the signal fits the intensity profile of the original, but without noisy spikes. Therefore, in cases where the chemicals in the fixation cause noise in the sample images (glycerol content in our case), N2V 2D is a perfect model for image restoration, given that sample preparation and fixation are time consuming. Moreover, it can reduce the number of animals that need to be sacrificed for sample preparation.

CARE 2D and N2V 2D models on tumor-bearing mammary glands.

We created low- and high-SNR SHG images by varying the laser input power at the focus of the objective lens. Using this approach, we obtained a less noisy (ground truth) measurement with 110 mW of input laser power at the focus of the microscope objective. The CARE 2D and N2V 2D models were applied to SHG images of the boundary of a murine mammary gland tumor, and Figure 5-4 shows the results generated by these models.

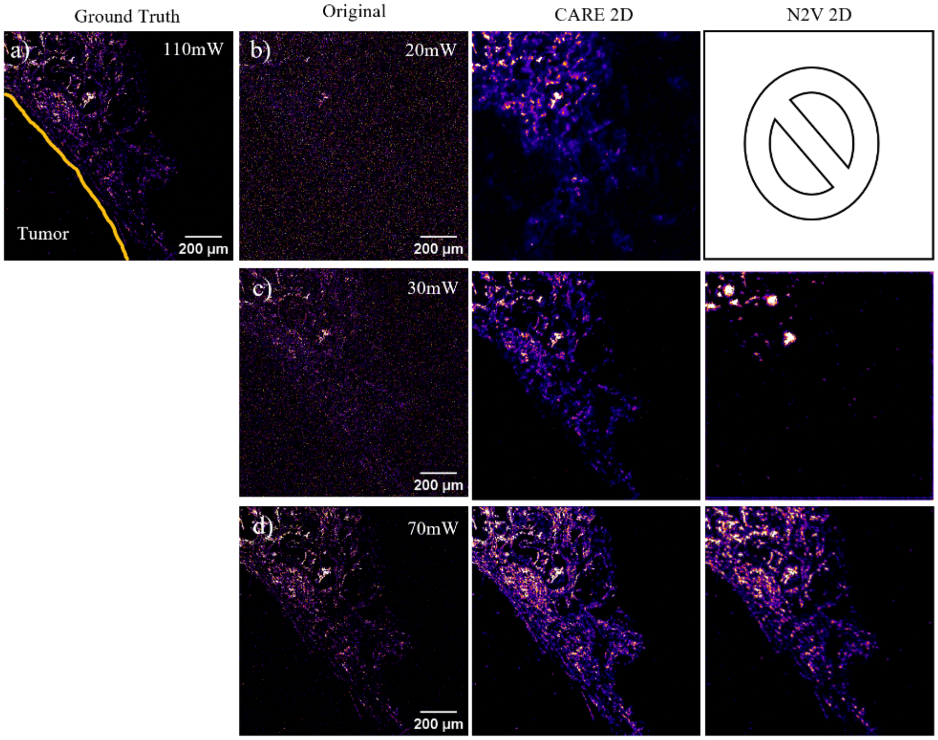

Figure 5-4: CARE 2D and N2V 2D models were applied to the collagen structure at the tumor boundary of a tumor-bearing mammary gland. a) The reference "ground-truth image is used to denoise the images using CARE 2D and for visual comparison. (b,c) present low SNR SHG images, and (d) presents a high SNR SHG image.

The original image in Figure 5-4(b) shows an extremely poor SNR. Using the CARE 2D model, we can still extract structural information about the boundary. However, this method leads to "hallucinations," in which a structure is created within the tumor area that is absent. Moreover, the N2V 2D model could not provide a clean image. The original image in Figure 5-4(c) presents a low SNR; in this case, CARE 2D provides the complete structure of the collagen boundary around the tumor, with some fine details being blurred. N2V 2D can only denoise the bright spots in the image; a silhouette of the boundary is visible but not usable for analysis. The original image in

Figure 5-4(d) presents good SNR. Here, CARE 2D enhances the crispness of the SHG images obtained, and we observe an improvement in the details and sharpness of the image. The contrast was also improved, as shown by the intricate details of the collagen boundary structure. In this case, N2V 2D also performs well, and the details of the collagen boundary structure are visible and patchy, with point-like bright spots where the SHG signal is strong. The mSSIM and PSNR parameters of the results are summarized in Table 5-1.

Table 5-1: mSSIM and PSNR metric for CARE 2D and N2V 2D model applied to the SHG imaging of the boundary of tumor-bearing mammary glands.

Model	**CARE 2D**			**N2V 2D**	
Laser power (mW)	20	30	70	30	70
Original v. GT mSSIM	0.33	0.38	0.85	0.38	0.85
Denoised v. GT mSSIM	0.34	0.79	0.89	0.55	0.80
Original v. GT PSNR (dB)	20.83	23.12	29.73	23.12	29.74
Denoised v. GT PSNR (dB)	20.83	27.57	30.01	21.81	24.44

For the CARE 2D model, we observed a negligible improvement in SSIM between the original and denoised images in the 20 mW case, and the PSNR remained the same. For 30 mW, we see the highest improvement, as the mSSIM metric almost doubles between the original and denoised images, while the PSNR has a substantial boost. For 70 mW, although some improvement in mSSIM and PSNR is observed, it is not as drastic as in the case of 30 mW. For the N2V 2D model, we see a substantial improvement in the mSSIM for the 30 mW case, but the PSNR decreases. We can see that the image did not improve in terms of details and structural information with visual inspection. For the 70 mW case, the mSSIM and PSNR of the denoised image are lower than those of the original image, and a visual inspection reveals the patchy and disjointed nature of the denoised image. In addition to the quality control metrics, we also considered a random region of interest and measured the performance of the models by plotting the intensity profile in Figure 5-4.

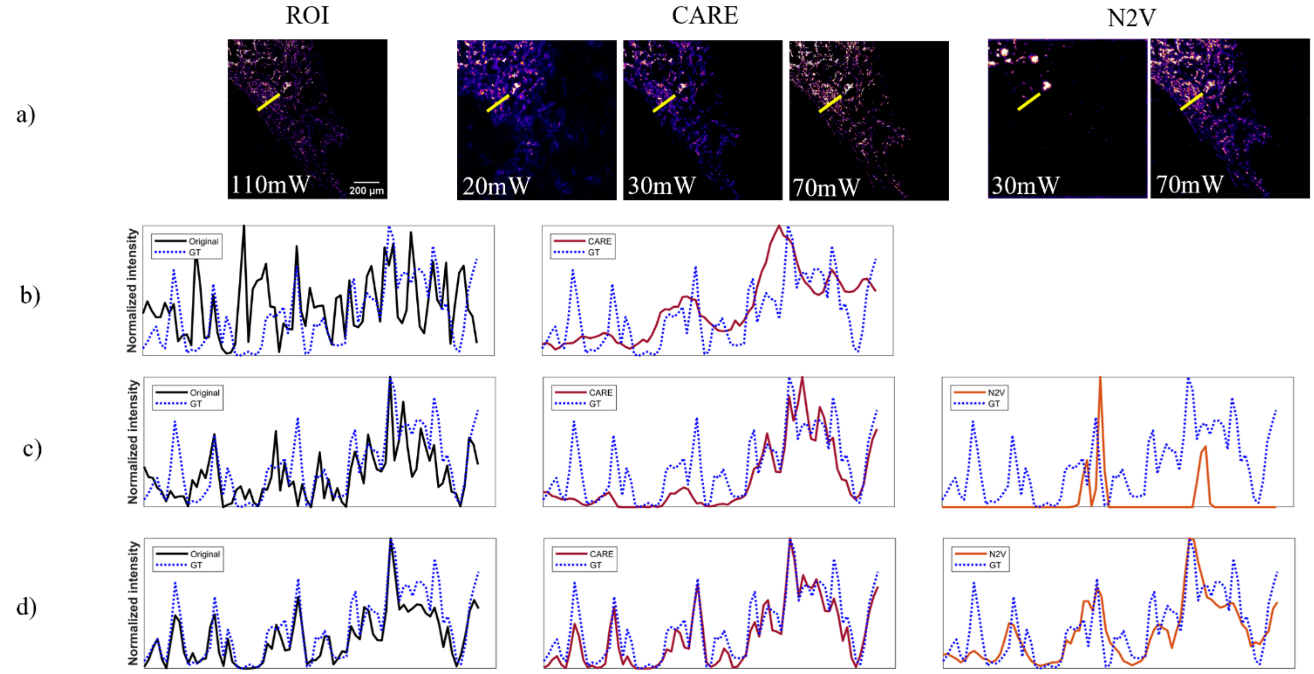

Figure 5-5: Intensity profile of a random ROI at the tumor boundary. where a) represents the visual representation of the ROI for the different power profiles. The intensity profiles for the ROIs can be seen at 20 mW (b), 30 mW (c), and 70 mW (d). The legends correspond to the original structure (black solid line), GT (blue dotted line), CARE (red solid line), and N2V (orange solid line).

For 20 mW (see Figure 5-5(a,b)), we can see that the original intensity profile contains many noise spikes, while the denoised model can smoothen these spikes and provide a profile closer to the ground truth image with overshoots in some places. CARE 2D provides a good fit that smoothens out the original signal and remains close to the ground truth intensity profile, but with some peaks that are smoothed. At 30 mW (see Figure 5-5(a,c)), the performance of CARE outshines N2V 2D, and we can see that the intensity profile for CARE resembles the ground truth image's intensity profile. N2V 2D, however, only provides some spots with high intensities in both the ROI and the intensity profile. At 70 mW (see Figure 5-5(a,d)), the performances of both models are comparable, and they both provide an intensity profile that fits close to the ground truth image. Both models exhibited enhanced contrast, characterized by more pronounced peaks and deeper valleys in the denoised images, indicating a clearer differentiation between features.

Overall, we conclude that the CARE 2D model performs better than N2V 2D because of the additional information input available during training in the form of a ground-truth image. Nevertheless, in the higher SNR cases, the performances of both models were comparable. Therefore, for exceptionally low SNR cases, CARE 2D is a better choice for denoising the detailed structures, especially in the case demonstrated in this section. For higher SNR cases, both models performed well in denoising the image and providing structural details. In the next section, we examine the performance of these models in the case of myosin, another common biological structure imaged using SHG microscopy.

CARE 2D and N2V 2D for denoising zebrafish muscle structures.

The CARE 2D and N2V 2D models were also applied to two zebrafish strains: WT and SMN. The results are shown in Figure 5-6.

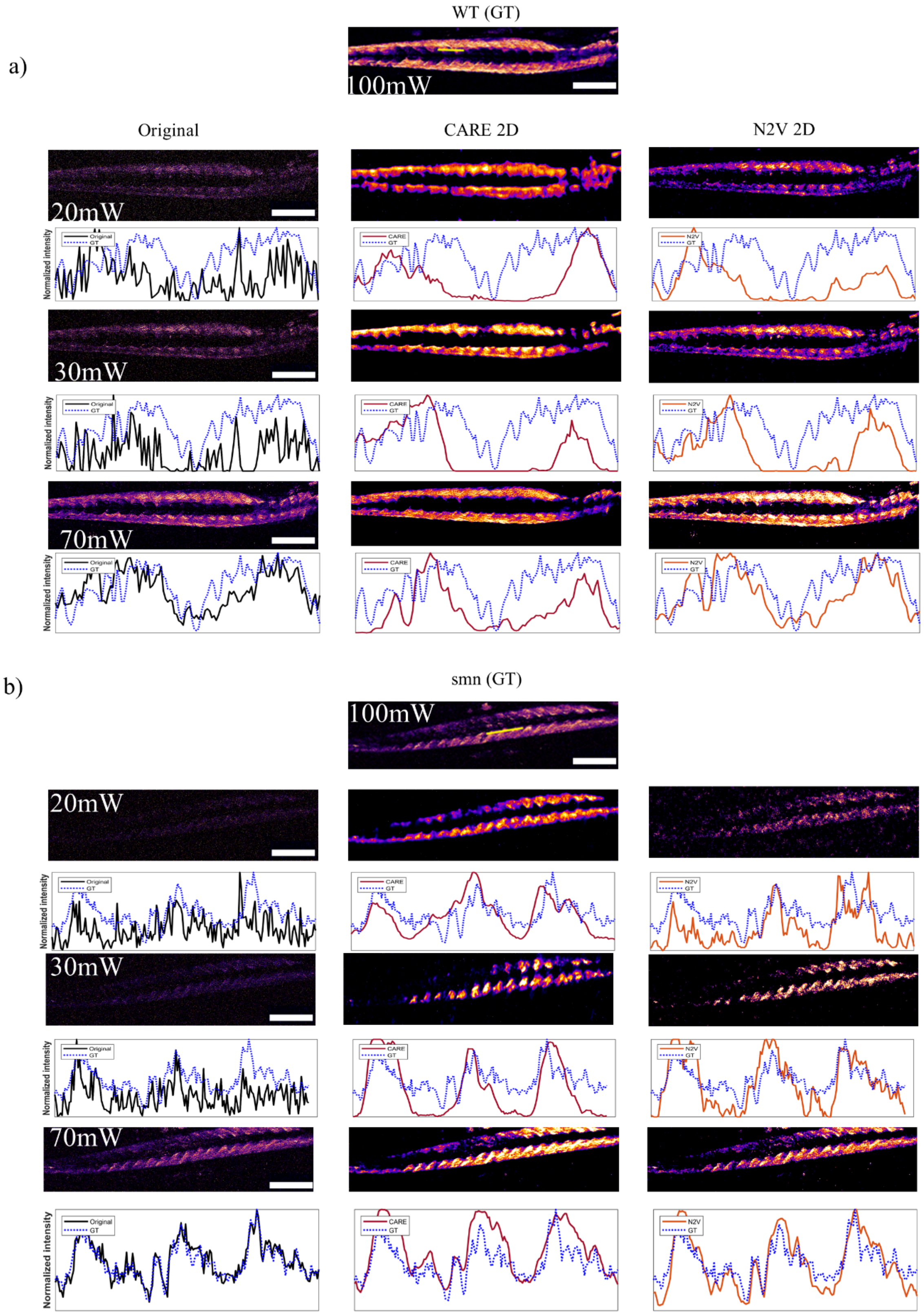

Figure 5-6: for a) wild-type (WT) and b) SMN fish along their intensity profiles from a random ROI. The ROI were identical across all samples. The legends correspond to the original structure (black solid line), GT (blue dotted line), CARE (red solid line), and N2V (orange solid line). The scale bar for all images is 200µm.

For WT samples at 20 mW and 30 mW, the predicted images appear to have improved in terms of pure SHG intensity when compared to their original counterparts. However, there was also a noticeable loss of detail in muscle structure. The CARE 2D smoothens the distinct muscle structure, resulting in a more uniform appearance. In terms of muscle structure preservation, N2V 2D outperformed CARE 2D in all the cases. While some muscle structure distinctions can still be seen at 70 mW with CARE 2D, most of them have been smoothed out. However, N2V 2D does not deliver the same SHG intensity restoration as CARE 2D, except at 70 mW. Despite this, N2V 2D is preferred in muscle structure studies as it focuses on the morphology and structural changes in different samples, as well as in intensity.

Our study also aimed to evaluate the performance of the CARE 2D and N2V 2D models for the SMN strain, which has a lower SHG intensity than the WT samples. In low-power cases, both models performed poorly with patchy and choppy muscle representations, although CARE 2D showed better performance than N2V 2D at 20 mW and 30 mW. At 70 mW, both models performed comparably, with CARE 2D delivering more SHG intensity, whereas N2V 2D preserved more muscle details. Surprisingly, N2V 2D outperformed CARE 2D in terms of muscle detail preservation and denoising of zebrafish muscle structures, even though it did not have a reference image for training. Therefore, N2V 2D is the preferred model for these applications. Based on Figure 5-6, CARE 2D matches the GT image intensity for WT samples at low power but at the cost of smoothing out most of the signal. N2V 2D, however, provides an intensity profile that is closer to the original image in terms of preserving details. At 70 mW, CARE 2D provides the same intensity value as the original image while reducing noise spikes, and N2V 2D again falls in the middle between the CARE 2D model and the original signal in terms of the intensity value while following the patterns of the original image signal. For the SMN samples, CARE 2D excels at producing the same intensity profile as the GT image at 20 mW. However, for the other samples, CARE 2D overshoots the intensity values, and N2V 2D performs better at fitting the intensity pattern of the denoised image to the GT image.

The mSSIM and PSNR metrics of the CARE 2D and N2V 2D model are summarized in Table 5-2:

Table 5-2: mSSIM and PSNR metric for CARE 2D and N2V 2D models applied to different zebrafish strains.

Laser power (mW)	Model	Sample type	Original v. GT mSSIM	Denoised v. GT mSSIM	Original v. GT PSNR (dB)	Denoised v. GT PSNR (dB)
20	CARE	WT	0.07	0.58	17.38	21.03
30	CARE	WT	0.15	0.56	17.7	20
70	CARE	WT	0.44	0.66	19.96	22.67
20	N2V	WT	0.07	0.44	17.37	19.87
30	N2V	WT	0.15	0.5	17.7	20.24
70	N2V	WT	0.44	0.6	19.96	21.26
20	CARE	smn	0.04	0.36	18.66	20.84
30	CARE	smn	0.05	0.29	18.71	20.19
70	CARE	smn	0.22	0.39	19.68	21.51
20	N2V	smn	0.04	0.15	18.66	19.33
30	N2V	smn	0.05	0.27	18.71	20.44
70	N2V	smn	0.22	0.39	19.68	21.49

From Table 5-2, we can see a significant improvement across the board, and all predicted images are better than their original counterparts, as reflected in the mSSIM and PSNR metrics. However, the loss of detail in the muscle structure is visually evident in Figure 5-6.

To summarize, Both CARE 2D and N2V 2D successfully reduced the noise in low-SNR SHG images. However, CARE 2D often outperforms N2V 2D when laser power is a major constraint, enabling details even at very low-power settings, as demonstrated in our mammary gland images (Figure 5-5). While this holds true for mammary gland tissue, N2V 2D may better retain intricate details such as striated muscle fibers in zebrafish when image noise is less severe (Figure 5-6).

These nuanced denoising outcomes across tissue types suggest that while CARE 2D excels with more homogenous patterns of stromal tissues, N2V's self-supervised learning is advantageous for handling diverse and variable patterns in muscular tissues. This observation is supported by the visual distinction in the muscle structure preserved by N2V, indicating its ability to maintain important biological details that are not fully captured by traditional metrics such as mSSIM and PSNR. The variability in performance can be tied to the representativeness of the training data, adaptability of the algorithms to different noise distributions, and different tissues.

Conclusion

Although deep learning image restoration has been explored in the context of SHG microscopy, our study provides novel insights by directly comparing the performance of CARE 2D and N2V 2D on SHG collagen and myosin images, revealing their tissue-specific strengths and weaknesses. Deep learning in image restoration has gained traction over the past few years but has not yet been thoroughly applied to SHG microscopy. SHG microscopy relies on many parameters for high-quality imaging [14], which can be tedious and time-consuming in some scenarios. As demonstrated here, deep learning image restoration can be an alternative solution to enhance SHG imaging during post-processing. Our study highlights the importance of considering a sample’s specific characteristic when choosing a denoising method. CARE 2D and N2V 2D are powerful models used in image restoration that work with (CARE 2D) and without (N2V) high-quality reference images [166,316].

We found that the glycerol concentration during fixation can lead to noisy images. At higher glycerol concentrations, N2V 2D can be used to restore SHG images despite this additional noise. Therefore, deep learning image restoration opens the possibility of fixing the significant noise and image deterioration caused by fixation chemicals. In addition, it can reduce the number of animal sacrifices required for sample preparation. Another crucial experimental aspect of SHG imaging of bio-samples is limiting the input laser power to reduce the possibility of sample damage at the cost of image SNR. This 70% decrease in the input laser power is also particularly useful for shifting the imaging from fixed to live samples. Moreover, at 30 mW, we can see the full layout of the structure at 110 mW. Given that the SHG signal is quadratically proportional to the input laser power, the input power can be significantly reduced using deep learning without loss in the SHG signal.

The nuanced denoising outcomes for 2D and N2V CARE across tissue types demonstrate their unique capabilities. While CARE 2D excels with more homogenous patterns of stromal tissues owing to its training on well-represented datasets, it can sometimes lead to oversmoothing, obscuring fine details. N2V's self-supervised learning, on the other hand, allows it to maintain important structural nuances in tissues with variable patterns like muscle, even if this approach sometimes results in lower quantitative metrics. This observation is supported by the visual distinction in the muscle structure preserved by N2V, indicating its ability to maintain important biological details that are not fully captured by traditional metrics such as mSSIM and PSNR. The variability in performance can be tied to the representativeness of the training data and adaptability of the algorithms to different noise distributions. A hybrid approach that combines reference-based learning of CARE 2D with the self-learning capabilities of N2V could potentially harness the strengths of both methods, leveraging CARE 2D's structure-preserving capabilities in consistent-pattern tissues while utilizing N2V's detail-retaining flexibility in variable-pattern tissues. An algorithm trained to classify tissue types can enable dynamic switching between CARE 2D and N2V 2D based on image characteristics, providing a more robust and versatile denoising approach.

Future research directions could include developing an adaptive framework that initially classifies tissue types and then applies the most suitable denoising techniques. Machine learning algorithms can be deployed to dynamically select between CARE 2D and N2V 2D based on the visual and noise characteristics of the tissue, potentially guided by an ensemble of metrics that include both traditional scores and assessments of structural fidelity. In summary, the optimal denoising strategy may vary not only with the tissue type but also with the specific structural features and noise characteristics present in the SHG images. Balancing quantitative assessment with qualitative visual analysis is essential to advance the application of deep learning in SHG imaging denoising. Looking ahead, we envision a composite model that synergizes CARE 2D's structural precision with N2V 2D flexible adaptation to varied noise profiles governed by real-time, sample-specific algorithmic decisions. This paradigm shift necessitates the construction of comprehensive datasets, fostering model generalization across SHG applications. The broader implications of our work suggest a transformative impact on live imaging methodologies, advocating minimal laser usage to preserve the sample integrity. Ultimately, this study lays foundational groundwork, steering future explorations towards more sophisticated and versatile imaging solutions.

Funding.

The authors acknowledge financial support from the Canada Foundation for Innovation, Fonds de recherche du Québec–Nature et Technologies, the Natural Sciences and Engineering Research Council of Canada, and the New Frontiers Research Fund. A. A. thanks the NSERC

CREATE program for the scholarship. Canadian Cancer Society (Grant #707140 to SVDR). SEJP was supported by a doctoral fellowship from Fonds de Recherche Québec Santé (FRQS) and the Epstein Fellowship in Women’s Health (Faculty of Medicine, McGill University).

Conflict of interest.

The authors declare that they have no conflicts of interest.

Data availability.

The data underlying the results presented in this paper are not publicly available at this time but may be obtained from the authors upon reasonable request.

6 ACCELERATING WHOLE-SAMPLE POLARIZATION-RESOLVED SECOND HARMONIC GENERATION IMAGING IN MAMMARY GLAND TISSUE VIA GENERATIVE ADVERSIAL NETWORKS

ACCÉLÉRATION DE L'IMAGERIE DE GÉNÉRATION HARMONIQUE SECONDE RÉSOLUE EN POLARISATION POUR L'ENSEMBLE DE L'ÉCHANTILLON DANS LE TISSU GLANDULAIRE MAMMAIRE VIA DES RÉSEAUX ANTAGONISTES GÉNÉRATIFS

Authors:

Arash Aghigh[1], Jysiane Cardot[2], Melika Saadat Mohammadi[1], Gaëtan Jargot[1], Heide Ibrahim[1], Isabelle Plante[2] and François Légaré[1]

[1] Centre Énergie Matériaux Télécommunications, Institut National de la Recherche Scientifique, Varennes, Québec, Canada.

[2] Armand-Frappier Santé Biotechnologie Research Centre, Institut National de la Recherche Scientifique Laval, Québec, Canada

Titre de la revue ou de l'ouvrage :

Biomed Opt Express. 2024 September 1; 15(9): 5251–5271. Published online: August 15, 2024. Doi: 10.1364/BOE.529779

Contribution des auteurs:

A.A conceived and wrote the article and performed the experiments. J. C. Provided samples for the experiments. M. M. assisted in data analysis. A. A., J. C., M. M., G. J., H. I. and I. P. participated in drafting, section arrangement, and revision of the manuscript. F. L. revised the manuscript critically for important intellectual content and approved the final version to be published.

6.1 Main article

Abstract: Polarization second harmonic generation (P-SHG) imaging is a powerful technique for studying the structure and properties of biological and material samples. However, conventional whole-sample P-SHG imaging is time consuming and requires expensive equipment. This paper introduces a novel approach that significantly improves imaging resolution under conditions of reduced imaging time and resolution, utilizing enhanced super-resolution generative adversarial networks (ESRGAN) to upscale low-resolution images. We demonstrate that this innovative approach maintains high image quality and analytical accuracy, while reducing the imaging time by more than 95%. We also discuss the benefits of the proposed method for reducing laser-induced photodamage, lowering the cost of optical components, and increasing the accessibility and applicability of P-SHG imaging in various fields. Our work significantly advances whole-sample mammary gland P-SHG imaging and opens new possibilities for scientific discovery and innovation.

Introduction

The mammary gland undergoes hormonal remodeling post-childbirth [325], comprising the well-studied mammary epithelium and the less-understood stroma [326], which includes adipocytes, fibroblasts, immune cells, and an extracellular matrix (ECM) of collagen, laminins, and other proteins [327,328]. The ECM plays a crucial role in gland development, especially during puberty, when stromal expansion and collagen orientation precede epithelial morphogenesis [329,330]. However, the effect of dysregulated lipid metabolism on this process remains underexplored, highlighting a gap in the understanding of mammary gland development.

SHG microscopy is the preferred method for imaging collagen in tissues because of its superior spatial resolution, reduced phototoxicity and photobleaching, focal plane selectivity, and straightforward sample preparation [2]. This label-free imaging technique enables the detection of changes in fibrillar collagen within the mammary gland, a capability that is unmatched by other imaging methods [2,158]. SHG microscopy has played a vital role in collagen research; however, relying solely on SHG intensity for orientation studies can introduce interference [232], and hindering fibril orientation imaging [52]. To address these limitations, polarization-resolved SHG microscopy (P-SHG) has emerged, offering the combined benefits of SHG microscopy and polarimetry [47,52,92,169,288]. P-SHG is extensively used in collagen-related investigations, providing precise information about fibril structures within the imaging plane, which is a valuable asset in mammary gland research [331,332]. In conventional P-SHG imaging, smaller sample areas are imaged and studied. However, this approach risks overlooking essential spatial information, especially in developmental studies, where the macroenvironment plays a crucial role. As the process shifts to imaging larger areas, the coherent nature of the SHG signal may result in the cancellation of some variations, which is a limitation acknowledged in the context of our research. In cancer boundary research the broad orientation of the collagen barrier is informative [158,333]. The same applies to understanding macroenvironmental effects on mammary gland development, where whole-sample P-SHG imaging is essential. While this approach may come with the caveat of missing some finer variations and fibers, the holistic view it offers on collagen orientation across the entire gland is essential for a comprehensive understanding of the developmental processes at play. Acknowledging the challenges associated with the cost and time of whole-sample P-SHG imaging, our study leveraged the capabilities of deep learning to overcome these barriers.

Deep learning (DL) significantly enhances SHG microscopy and image analysis by automating the interpretation and quantification of SHG signals [185,187,334,335]. DL has become a transformative force, significantly advancing tasks, such as classification, segmentation, and image restoration in SHG imaging. Highlighted studies have demonstrated its broad utility: one successfully applied a convolutional neural network (CNN) to differentiate ovarian tissue types with nearly perfect accuracy using SHG imaging [305], while another showed the effectiveness of U-Net CNN in segmenting collagen fibers, surpassing traditional techniques in handling the challenges of variable image intensity in SHG microscopy [306]. Despite the diverse applications explored, from cancer diagnosis to collagen fiber segmentation, a critical gap remains: the tailored application of deep-learning image super-resolution enhancement for P-SHG imaging. This presents an exciting avenue for future research, focusing on the development of bespoke deep-learning solutions that cater to the intricacies of P-SHG imaging. Our approach significantly improves the imaging resolution under conditions of reduced imaging time and resolution, addressing the challenges of prolonged imaging times and potential sample damage associated with conventional whole-sample P-SHG imaging by utilizing Generative Adversarial Networks (GANs).

Advanced techniques and super-resolution imaging supported by DL not only overcome technical limitations but also reduce noise, as exemplified by Generative Adversarial Network-based approaches that effectively achieve image upsampling [140]. A Generative Adversarial Network (GAN) is an artificial intelligence framework for generating new data, particularly images, audio, and text [336]. The framework operates by pitting two neural networks against each other in a competitive manner: a generator and discriminator.

The generator network uses random noise as the input and generates data that resemble the actual data. For example, in image generation, the generator attempts to create images that visually resemble the actual images. The Discriminator network then acts as a judge that attempts to distinguish between the actual data (e.g., real images) and fake data generated by the generator. It is a binary classifier that learns to identify genuine data from generated data [336]. Over time, the generator becomes better at creating indistinguishable data from the actual data, whereas the discriminator becomes better at distinguishing real data from fake data. Ideally, this process results in a generator that produces high-quality data that resembles actual data. GANs have been applied in various fields such as image synthesis, style transfer, super-resolution, image-to-image translation, and text-to-image synthesis [336].

Another advanced form of GAN is Enhanced Super-Resolution Generative Adversarial Network (ESRGAN), which is a deep learning-based approach for image super-resolution [337]. Image super-resolution is the process of increasing the image resolution while preserving or enhancing its quality. ESRGAN's architecture builds upon the idea of GANs but incorporates modifications to improve the super-resolution process [337]. One crucial aspect is the use of a perceptual loss function, which measures the difference between the high-resolution ground-truth image and the generated image in terms of perceptual features. The loss function of the discriminator measures how well the discriminator can classify real data as real and the generated data as fake. The generator loss function measures how well the generator can fool the discriminator to classify the generated data as real data. The generator aims to maximize the probability of the discriminator making a mistake.

The perceptual loss function allows ESRGAN to focus on capturing high-level features of an image, such as edges, textures, and structures, rather than relying solely on pixel-wise similarity [337]. ESRGAN generates images that appear visually plausible and realistic to human observers. The ESRGAN framework is trained using a combination of adversarial loss (to ensure realism) and perceptual loss (to maintain visual quality). This training process involves iteratively updating the generator and discriminator networks to improve the quality of the generated image over time [337].

In this study, we acquired high-quality SHG images of the whole mammary gland. We then obtained low-quality P-SHG images of the entire sample and upscaled them using the ESRGAN model. Next, to test the accuracy of the method, we obtained high-quality P-SHG images of some areas of different samples and compared the results with upscaled P-SHG image results. Quality metric assessments were performed to ensure that the integrity and structure of the original images were maintained. For simplicity, we introduce those that were implemented in this study, namely, the Peak Signal-to-Noise Ratio (PSNR), Structural Similarity Index (SSIM), Perceptual Image Quality Evaluator (PIQE), and Naturalness Image Quality Evaluator (NIQE). Multiple image quality metrics were used, because one metric is unsuitable for considering every aspect of a generated image [169]. The PSNR measures the maximum pixel value ratio to the mean squared error in an image [319]. Higher PSNR values indicate better image quality and correlate well with perceived visual quality. SSIM evaluates the luminance, contrast, and structure between two images and considers human visual perception. The SSIM ranges from -1 to 1, where 1 indicates identical images, 0 indicates no similarity, and -1 indicates anticorrelation [318]. PIQE is designed to evaluate the visual quality of images in a manner that closely aligns with human perception [184]. It incorporates various visual features such as contrast, luminance, and texture to compute a quality score that reflects perceived image quality [184]. NIQE explicitly targets the assessment of naturalness in images [183]. It computes features related to the distribution of pixel values, luminance, contrast, and other statistical properties [183]. Unlike SSIM and PSNR, which require a reference image, NIQE and PIQE do not require a reference image [183,184].

In addition, we evaluated the intensity, texture, and contrast metrics to provide a comprehensive assessment of the models and upscaled images. The intensity metrics included mean intensity, standard deviation of intensity, median intensity, and minimum and maximum intensity values. The mean intensity reflects the average pixel intensity of the image, whereas the standard deviation of the intensity measures the variation in pixel intensities [338]. The median intensity provides the middle value of pixel intensities, and the minimum and maximum intensities indicate the range of pixel values in the image [338].

Contrast metrics included root mean square (RMS) contrast and Michelson contrast [339]. The RMS contrast measures the overall contrast of the image, indicating the level of contrast enhancement, while the Michelson contrast evaluates the contrast between the maximum and minimum pixel intensities [339].

Texture analysis included gray-level co-occurrence matrix (GLCM) metrics such as dissimilarity, homogeneity, energy, and correlation [340]. Dissimilarity measures the difference between neighboring pixel values, with lower values indicating more uniform texture. Homogeneity reflects the closeness of the distribution of elements in the GLCM to the GLCM diagonal, indicating a uniform texture [340]. The energy, or angular second moment, measures textural uniformity, and the correlation measures the linear dependency of pixel values [340].

We also included advanced metrics such as the Feature Similarity Index (FSIM) for evaluating structural similarity [341], Visual Information Fidelity (VIF) for quantifying visual information preservation [342], Edge Preservation Ratio (EPR) for assessing edge retention [343], and local binary patterns (LBP) for texture analysis [344]. Histogram-based metrics such as histogram intersection, histogram correlation, and Kullback-Leibler divergence were used to compare the statistical properties of the images [345].

Methodology

Sample preparation

Sterol-CoA knockout, wild-type, and heterozygous mice were sacrificed at the following key stages of mammary gland development: prepubertal (week 4), pubertal (week 6), and adulthood (week 10). In adulthood, the female mice were cycled using an impedance meter that provided resistance to the vaginal mucosa. A peak indicated proestrus. The mice were sacrificed via CO_2 asphyxiation, followed by cervical dislocation. The mouse was pinned down on a foam pedestal, the abdomen was opened, and mammary glands were visualized. The left inguinal mammary glands were harvested immediately and placed on glass slides. The mammary gland was stretched using pliers to regain its original shape. A parafilm film was placed on the gland and flattened for a few minutes using heavy metal weight. The slides were immediately immersed in a bath of Carnoy's fixative (100% EtOH, chloroform, glacial acetic acid) for four hours at room temperature to fix the tissues. The slides were gradually rehydrated in water and alcohol baths (95%, 75%, 50%, and 25% EtOH). The slides were then stained in a carmine alum bath (2% carmine and 5% potassium aluminum sulfate dissolved in water) for three hours to dye the mammary epithelium with a violet hue. The tissues were then gradually dehydrated in alcohol baths (25%, 50%, 75%, and 95% EtOH) and incubated overnight in xylene. The colored mammary glands were then imaged using a lightbox, camera, and measurement key to compare the samples. Once digitized, the epithelial branches, number of terminal buds, and general architecture of the mammary gland were analyzed using ImageJ [346].

Imaging setup

SHG microscopy was performed using a custom laser stage inverted scanning microscope. A mode-locked fiber Ytterbium (Yb) laser (MPB Communications Inc., Montréal, CA) was used. This laser emits at 1040 nm and delivers 125 fs pulses at a repetition rate of 25 MHz with an average power of 3 W. A half-wave plate and a Glan-Thompson polarizer adjusted the average power from 20 to 125 mW (0.8 to 5 nJ pulse energy). Given the size of the samples for imaging, sample scanning was performed using a high-speed motorized XY scanning stage (MLS203; Newton, NJ, USA). The focus was adjusted coarsely and finely by using mechanical and piezoelectric motors (PI Nano-Z, USA). An air objective (UplanSApo 10X, NA 0.3, Olympus, Japan) was used for the illumination. A condenser was used to collect the SHG signal of the sample, which was detected using a photomultiplier tube (R6357, Hamamatsu Photonics) set to 800 V. The SHG signal was isolated using two spectral filters that were placed before the photomultiplier. A short-pass filter (blocking any wavelength higher than 720 nm, i.e., the input fundamental laser light) and bandpass filter centered at 515 nm were employed to filter out the residual input light. A multichannel I/O board (National Instruments) and custom-written Python program were used for signal acquisition and synchronization. Given the sample size and the acceleration and deceleration times of the motorized scanning stage, each SHG image had an acquisition time of a few minutes. Raw data were visualized using Fiji-ImageJ software (NIH, USA). The imaging configuration is shown in Figure 6-1.

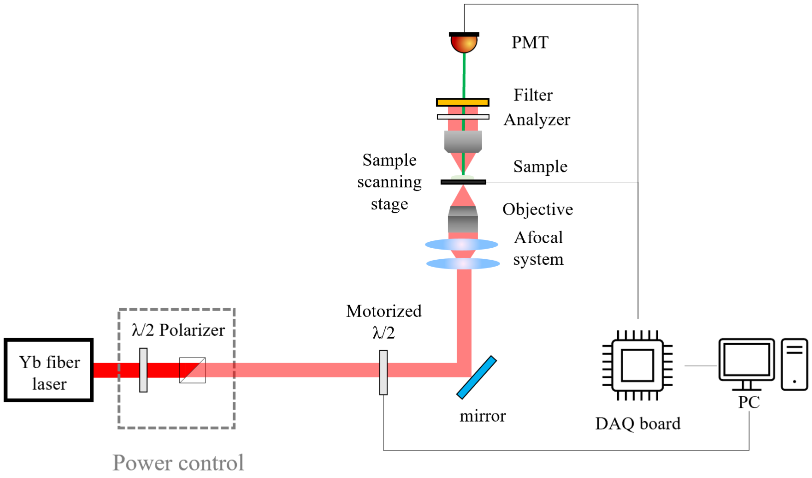

Figure 6-1: Imaging configuration for SHG and P-SHG setups. The motorized half-wave plate was removed during SHG imaging and added during the P-SHG imaging.

For low-quality P-SHG, a motorized half-wave plate was used to rotate the linear polarization of the laser beam to acquire the images. Images were captured for 18 polarization states in 10-degree steps from 0° to 170°. The motorized half-wave plate and sample scanning were synchronized using a custom-built Python program. For high-quality P-SHG imaging, random regions of interest of 1000×1000µm were imaged from different samples, and an air objective (UplanSApo 20X, NA 0.75, Olympus, Japan) was used for focusing.

Upscaling images

Image upscaling was performed using multiple models: Ultrasharp_4X [347], ESRGAN_Nomos2K [348], NMKD [348],4X-UniScaleV2_Sharp [349], and BSRGAN [350]. The upscaling was done through the ChaiNNer program, which can be found at https://github.com/chaiNNer-org/chaiNNer. Additionally, we explored guided upscaling techniques via PixTransform [351], employing high-quality SHG images as references to inform the upscaling of 18 distinct P-SHG images across a spectrum of iterations (1,000–30,000) and channel-split modes. This process was optimized for performance using an RTX 3060Ti GPU with a local computing setup.

Result and discussion

Model Performance and Selection Criteria

Upon rigorous evaluation, it became apparent that not all models performed equally. Despite the potential of each method, only Ultrasharp_4X has emerged as a viable solution that closely approximates the quality and fidelity of original high-quality SHG images (GT). This finding was critical, as our primary goal was to ensure that the upscaled images retained as much of the original detail and structural integrity as possible without introducing artifacts or distortions that could compromise analytical accuracy.

To objectively assess the performance of each upscaling method, we compiled the key metrics listed in Table 6-1.

Table 6-1: Comprehensive performance comparison of upscaling models

Method	mSSIM Ratio	NRMSE Ratio	PSNR Absolute Improvement	PSNR Percentage Improvement	Visual Inspection
UltraSharp	0.939	1.036	-0.92	-5.02%	Most true to original
BSRGAN	0.953	1.047	-0.70	-3.84%	Introduced noticeable artifacts in complex patterns
NMKD	0.691	1.164	-1.83	-10.08%	Tended to oversmooth, losing fine details

NOMOS	0.866	1.127	-1.44	-7.90%	Better detail preservation but Tended to oversmooth and artifact
PixTransform	1.335	1.100	-1.13	-6.22%	Not suitable for P-SHG application
UniScale	0.627	1.209	-2.20	-12.12%	Significant loss of detail and increased blurring

Table 6-1 provides a side-by-side comparison of each evaluated upscaled model against the key performance metrics. The mSSIM ratio reflects how well the upscaled image maintains structural similarities with the original image, with higher values indicating better preservation. Ultrasharp_4X (0.939) and BSRGAN (0.953) show excellent structural preservation, while UniScale (0.627) performs poorly. The NRMSE ratio evaluates the error level relative to the original image, where a value close to 1 indicates a minimal error. Ultrasharp_4X (1.036) and BSRGAN (1.047) perform best in this metric. The PSNR improvement quantifies the change in image quality, with values closer to zero indicating better preservation. While all models showed some degradation, BSRGAN (-0.70, -3.84%) and Ultrasharp_4X (-0.92, -5.02%) showed the least degradation.

Additionally, the Visual Inspection column assesses the ability of each model to preserve the essential details and integrity of the original image. Ultrasharp_4X demonstrated balanced performance across all metrics. Its mSSIM ratio of 0.939 indicates excellent structural preservation, whereas an NRMSE ratio of 1.036 suggests minimal error introduction. Although it shows a slight PSNR degradation (-0.92, -5.02%), this is less severe compared to the other models. Crucially, visual inspection confirmed that Ultrasharp_4X produced images most accurate to the original, preserving essential details and structural integrity without introducing noticeable artifacts.

To further evaluate the performance of each model, we conducted a detailed analysis of various image statistics and texture metrics, as presented in Table 6-2.

Table 6-2: Statistics, texture and contrast metrics comparison of upscaling models

Metric	Original	Low quality	Ultrasharp	BSRGAN	NMKD	NOMOS	PixTransform	Uniscale
Statistics - min	0	0	0	0	0	0	0	0
Statistics - max	1	1	1	1	1	1	0.816	1
Statistics - mean	0.208	0.191	0.179	0.175	0.197	0.193	0.100	0.157
Statistics - std	0.201	0.161	0.169	0.161	0.194	0.194	0.072	0.2
Statistics -median	0.133	0.137	0.118	0.125	0.129	0.122	0.078	0.082
Texture-contrast	1299.21	333.98	485.215	400.138	1228.48	995.67	127.484	1630.77
Texture-dissimilarity	20.374	6.418	8.791	7.487	19.226	15.052	6.414	20.866
Texture-homogeneity	0.110	0.646	0.357	0.410	0.131	0.203	0.239	0.174
Texture-energy	0.022	0.078	0.052	0.056	0.023	0.035	0.045	0.039
Texture-correlation	0.753	0.901	0.869	0.882	0.749	0.796	0.811	0.687
Contrast-rms	0.959	0.836	0.940	0.912	0.976	0.994	0.708	1.259
Contrast-Michelson	1.000	1.000	0.994	1.000	1.000	1.000	1.000	1.000
Constrat-mean_intensity	0.209	0.192	0.179	0.176	0.198	0.194	0.102	0.159

Contrast-intensity_var	0.040	0.026	0.028	0.026	0.037	0.037	0.005	0.040

Table 6-2 provides a detailed comparison of various metrics between the original high-quality image, low-quality image, and all the upscaled images. This comprehensive analysis allows us to evaluate how each model preserves or enhances different aspects of an image.

In terms of basic statistics, all models maintained the same minimum intensity (0.000) as the original and low-quality images. However, there were notable differences in the mean and median intensities across the models. NMKD (mean: 0.197, median: 0.129) and NOMOS (mean: 0.193, median: 0.122) maintained mean intensities closest to the original (0.208), potentially improving the overall brightness. Ultrasharp_4X (mean: 0.179, median: 0.118) and BSRGAN (mean: 0.175, median: 0.125) show slightly lower values, while PixTransform (mean: 0.100, median: 0.078) and UniScale (mean: 0.157, median: 0.082) demonstrate more significant reductions in overall brightness.

The standard deviation of the pixel intensities provides insight into image contrast. UniScale (0.200) and NMKD/NOMOS (both 0.194) closely matched or slightly reduced the standard deviation of the original image (0.201), whereas PixTransform showed a marked reduction (0.072), indicating a significant loss of contrast.

For texture metrics, we observed varying performance across the models. NMKD (contrast: 1228.485, dissimilarity: 19.226) and UniScale (contrast: 1630.773, dissimilarity: 20.866) showed remarkably high contrast values, even exceeding those of the original image (contrast: 1299.211, dissimilarity: 20.374). This could indicate over-sharpening or enhancement of the noise. Ultrasharp_4X (contrast: 485.215, dissimilarity: 8.791) and BSRGAN (contrast: 400.138, dissimilarity: 7.487) provide a more balanced improvement over the low-quality image (contrast: 333.988, dissimilarity: 6.418). NOMOS (contrast: 995.677, dissimilarity: 15.052) falls between these extremes, whereas PixTransform shows a significant reduction in contrast (127.484).

In terms of contrast metrics, NOMOS (0.994) and NMKD (0.976) achieved the highest RMS contrast, surpassing the original image (0.959). UniScale shows the highest value (1.259), which might indicate over-enhancement. Ultrasharp_4X (0.940) provided a more conservative enhancement, closely approximating the contrast of the original image. PixTransform showed the lowest RMS contrast (0.708), indicating a significant loss of overall contrast.

While Table 6-1 provides a comparison of upscaled models using fundamental image quality metrics (MSSIM, PSNR, and NRMSE), a more specialized analysis is necessary to fully understand how each upscaled image compares to the original high-quality image across various aspects of image quality. To this end, we employed a series of specialized metrics that focused on feature similarity, visual information fidelity, edge preservation, texture similarity, and intensity distribution. Table 6-3 presents the results of these analyses. These metrics offer complementary insights into how well each upscaling method preserves or enhances the different aspects of the original image quality.

Table 6-3: Specialized Image Quality Metrics for Upscaled vs. Original Image Comparison

Metric	**Original vs Low**	**Ultrasharp_4X**	**BSRGAN**	**NMKD**	**NOMOS**	**PixTransform**	**UniScale**
FSIM	0.884	0.910	0.904	0.914	0.919	0.918	0.896
VIF	0.046	0.062	0.054	0.090	0.103	0.089	0.117
EPR	0.042	0.019	0.017	0.013	0.016	0.673	0.014
LBP_Similarity	0.471	0.758	0.836	0.886	0.693	0.960	0.891
Histogram_Intersection	0.898	0.894	0.884	0.959	0.863	0.708	0.728
Histogram_Correlation	0.964	0.962	0.937	0.990	0.935	0.839	0.722
KL_Divergence	0.130	0.049	0.084	0.014	0.086	1.377	0.237

Table 6-3 provides additional insights based on the comparison metrics. FSIM scores were high across all models (ranging from 0.896 to 0.919), with NOMOS slightly outperforming the others. VIF scores show more variation, with UniScale (0.117) scoring the highest, followed by NOMOS (0.103) and NMKD (0.090). LBP_Similarity showed significant improvements for all models compared to the low-quality image (0.471), with PixTransform (0.960) and UniScale (0.891) scoring the highest.

Histogram-based metrics are particularly strong for NMKD, with high scores in Histogram_Intersection (0.959) and Histogram_Correlation (0.990), suggesting that it is highly effective at preserving the overall intensity distribution of the original image. The Kullback-Leibler

Divergence shows NMKD (0.014) and Ultrasharp_4X (0.049) outperforming other models, indicating better preservation of the original image's intensity distribution. However, it is important to note that PixTransform showed a higher KL_Divergence (1.377), suggesting less similarity to the original distribution in this aspect.

In our exploration of various upscaling techniques, we initially considered the PixTransform-guided upscaling approach, which has the potential to leverage high-quality SHG images as references for improving the upscaling process. Theoretically, this method offers a promising avenue for enhancing the resolution and detail of P-SHG images, which is critical for accurately identifying and analyzing collagen fiber orientation and other microstructural details. However, the unique characteristics of P-SHG imaging, in which image properties such as signal intensity and fiber orientation dynamically change with varying laser input angles, present unforeseen challenges. During preliminary trials, we observed that while PixTransform effectively filled in missing details in regions of low signal-to-noise ratio (SNR) or where details were obscured owing to low resolution, it did so without accounting for the critical angle-dependent variation characteristics of P-SHG images. Specifically, the guided upscaling process, in its attempt to interpolate and enhance image details based on high-quality references, inadvertently introduced artifacts and inaccuracies by "filling in the gaps" in a manner inconsistent with actual, angle-dependent SHG signal variations. This discrepancy arises from the inherent design of the model to generalize from the reference images, leading to misrepresentations where P-SHG imaging relies on precise laser angle-specific signal variations to accurately delineate fiber orientations. The resultant images, although visually improved in terms of sharpness and resolution, misrepresented the underlying biological structures by overlaying or amplifying details that did not align with the actual orientation and distribution of collagen fibers, as dictated by varying the laser angles.

Furthermore, our exploration was extended to the BSRGAN, another sophisticated upscaling model known for its impressive enhancements in various imaging contexts. Despite its capabilities, BSRGAN failed to meet the stringent requirements of accuracy and detail preservation in P-SHG image upscaling. Similar to guided upscaling attempts, BSRGAN introduced alterations that were detrimental to the integrity of our imaging technique, rendering it an unsuitable option. A visual comparison of the upscaling methods elucidates the distinctions in the performance and outcome quality, as shown in Figure 6-2.

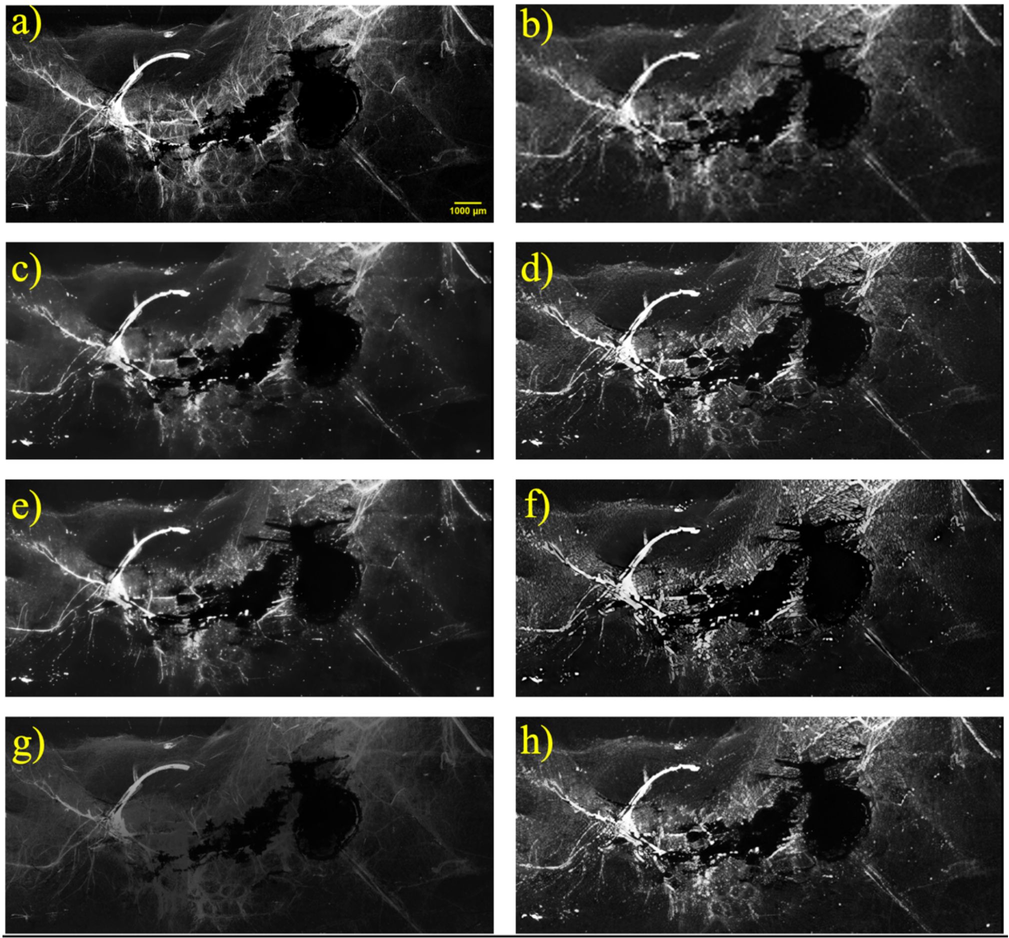

Figure 6-2: Comparative analysis of upscaled models for P-SHG imaging. This Figure illustrates the side-by-side comparison of a) original high-quality and b) low-quality SHG images against images upscaled using various models including c) BSRGAN, d) Nomos2K, e) Ultrasharp_4X, f) NMKD, g) guided upscaling via PixTransform, and h) uniscale.

This comparative analysis highlighted the necessity of selecting an upscaling model that not only enhances image resolution but also has an acute sensitivity to the nuances of scientific imaging. The challenges encountered with guided upscaling and BSRGAN further reinforce the importance of a tailored approach, particularly for specialized imaging techniques such as P-SHG, where precision and detail fidelity are non-negotiable. Implementing "Ultrasharp_4X" using the ChaiNNer program has marked a significant step toward democratizing advanced P-SHG imaging enhancement. Despite its powerful capabilities, accessibility is limited. The program was optimized for ease of use and required minimal deep learning expertise from users. Hardware requirements were clearly documented, with the existing computational resources of most modern research laboratories found to be sufficient for basic operations.

Histological images

The histological images and their corresponding SHG imaging counterparts are shown in Figure 6-3.

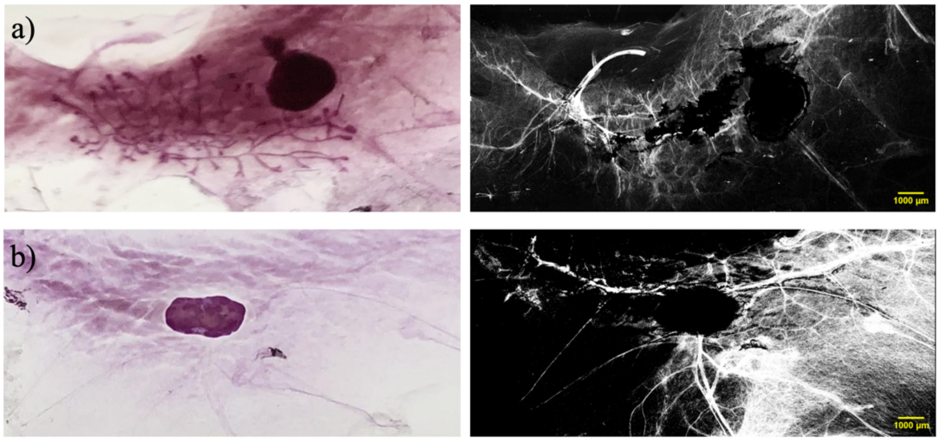

Figure 6-3: Histological and SHG Images of both samples provide a comprehensive view of tissue microstructure.

Comparing histological images with their SHG imaging counterparts can be immensely helpful in providing a comprehensive view of tissue structure and organization. This combined approach offers a more holistic understanding of tissue architecture. This integration helps during the upscaling process by providing structural guidance from the histological images, so that the enhanced SHG images maintain the structural fidelity of the tissue.

Original vs. upscaled SHG images

The original image of the sample, along with the low-quality image and its upscaled counterpart, is shown in Figure 6-4.

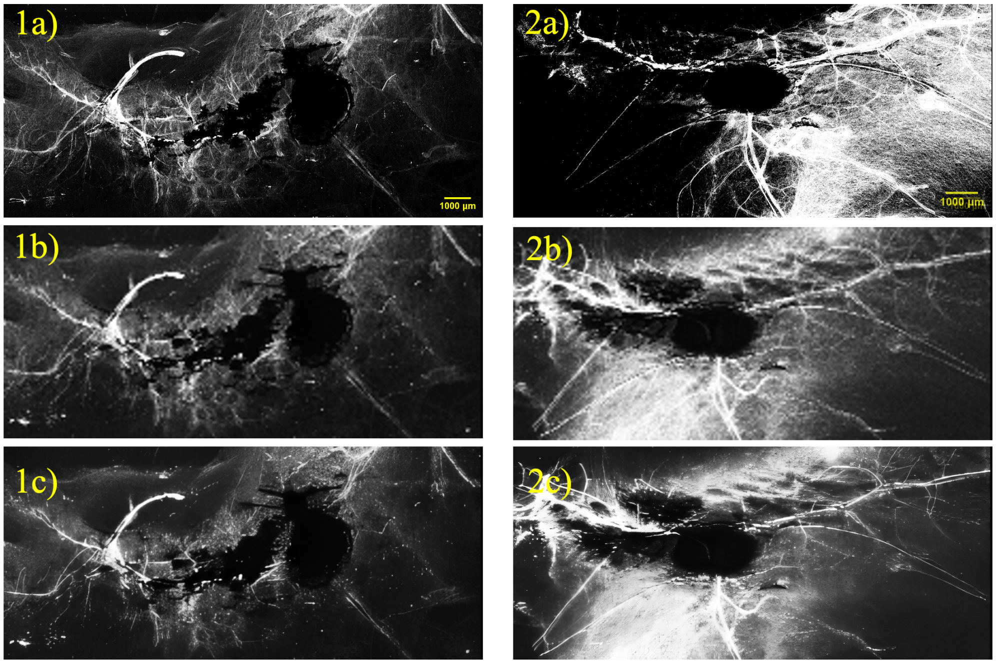

Figure 6-4: This Figure includes three categories of images: original high quality (1a,2a) , original low quality (1b,2b) and upscaled images from two different samples (1c,2c). The original high-quality images (1a,2a) had a resolution of 1800×800 pixels, low-quality images (1b,2b) had a resolution of 225×100 pixels, and upscaled images (1c,2c) had a resolution of 3600×1600 pixels.

The original high-quality images were characterized by a resolution of 1800×800 pixels, which indicated a substantial amount of detail and clarity in each image. These images were captured with high precision and provided a rich visual content. The imaging time for each image was approximately 18 min, given the speed of the scanning stage and chosen pixel size of 10µm. Although ideal for single image application, P-SHG requires 18 images in our case; therefore, if we apply the same imaging scenario, it will take over 4 h of imaging per sample, which also translates to a constant laser-sample interaction that can damage the sample. In contrast, the original low-quality images belong to a feature with a significantly reduced resolution of 225×100 pixels. This lower resolution implies a substantial loss of detail and sharpness compared with their high-quality counterparts.

However, capturing each image takes approximately 45 s, meaning that we can capture 18 images for P-SHG in the same amount of time as it takes to capture a single high-quality image for one polarization. Unfortunately, the P-SHG analysis method used does not perform well on low-resolution images; therefore, the loss of detail and sharpness encountered must be addressed. Therefore, we applied image upscaling to low-quality images using the Ultrasharp_4X model based on the ESRGAN. As mentioned, other upscaled models were also applied to the images; however, based on the results, it was decided that the Ultrasharp_4X model provided the best upscaled images in our use case. We also used high-quality images to upscale 18 low-quality images. This method did not work well because, in P-SHG, changing the laser input angle will cause changes in the SHG based on fiber alignment. We observed that the model attempted to fill in missing intensities and omit specific pixels to shape the image based on the reference image; therefore, individually upscaling each P-SHG image was optimal for our application. By applying Ultrasharp_4X twice, we could enhance the resolution of the images by 16× and obtain higher-resolution upscaled images of 3600×1600 pixels. While the upscaled images appear more detailed and visually larger than the original images, they often suffer from quality degradation owing to the interpolation and extrapolation involved in the upscaling process. Therefore, we must perform the detailed quality metric controls mentioned in the Introduction to ensure that the integrity of the information is intact.

Quality control

In the quality control section of our study on image upscaling, we meticulously assessed the effectiveness of ESRGAN in improving the quality of the low-resolution P-SHG images. Our evaluation strategy encompassed a blend of no-reference and full-reference image quality metrics, supplemented by statistical analysis through analysis of variance (ANOVA), to provide a holistic understanding of the upscaled image quality in relation to their original high-quality counterparts.

No-reference Quality Metrics

We began with no-reference quality metrics, specifically the Naturalness Image Quality Evaluator (NIQE) and the Perceptual Image Quality Evaluator (PIQE), which assess image quality without the need for a reference image. These metrics are particularly useful for evaluating the perceptual quality of the upscaled images. The findings are summarized in Table 6-4.

Table 6-4: No-reference quality metrics

Sample	Method	Source	Prediction	Ground
a	NIQE	8.940	3.186	6.707
	PIQE	40.797	23.234	46.404
b	NIQE	9.908	2.749	7.532
	PIQE	89.992	31.906	52.931

The lower scores for the predicted images across both the NIQE and PIQE metrics suggest an enhancement in the image quality post-upscaling. This indicates that our method successfully improved the perceptual quality of the images, making them more natural and visually pleasing than original high-quality (ground) images. These results confirm the effectiveness of our upscaling method, although it is important to note the potential difference between computational assessments of quality and human perception. Using PIQE and NIQE in this context makes sense because they are non-reference image quality metrics that are ideal for evaluating the quality of upscaled images when no high-quality original is available for comparison. Their application offers a method for quantitatively assessing improvements in image quality that may not be immediately apparent by visual inspection alone. Despite the concern that these metrics might be optimized for "computer perception," the lower scores for the predicted images compared with the source images suggest a successful enhancement. However, the discrepancy between these scores and human perception highlights the importance of using a combination of metrics, including full-reference metrics such as MS-SSIM, PSNR, and NRMSE, to obtain a comprehensive evaluation of image quality post-upscaling.

Full-reference Quality Metrics

Next, we assessed image quality using the full-reference metrics MS-SSIM, PSNR, and NRMSE. These metrics require a reference image for comparison and offer different perspectives on image quality, focusing on structural similarity, signal fidelity, and error. The results are summarized in Table 6-5.

Table 6-5: Full-reference quality metrics

Sample	Method	Source	Prediction
a	MS-SSIM	0.33	0.31
	PSNR	18.31	17.39
	NRMSE	0.28	0.29
b	MS-SSIM	0.01	0.01
	PSNR	9.14	9.14
	NRMSE	0.56	0.56

The similar MS-SSIM, PSNR, and NRMSE values between the source and prediction images for both samples underscores the capability of our upscaling algorithm to maintain the structural integrity and signal fidelity of the images. Although there were slight variations in some metrics, the overall similarity in the scores suggests that our method is adept at enhancing the images without compromising the original quality. Building on a detailed examination of both the no-reference and full-reference quality metrics, we further enriched our analysis by conducting ANOVA to statistically ascertain the differences in image quality across the Source, Prediction, and Ground groups. This statistical approach allowed us to rigorously test for significant variations in the image quality resulting from our upscaling process. Below, we integrate the ANOVA findings with the previously discussed quality metric evaluations.

ANOVA Results

After evaluating the image quality using both no-reference and full-reference metrics, we performed ANOVA to statistically compare these metrics across different image groups (source vs. prediction). ANOVA was used to identify any statistically significant differences in the image quality, thereby providing a quantitative basis for evaluating the efficacy of our upscaling methods. The results are presented in Table 6-6.

Table 6-6: ANOVA results

Metric Category	Metric Details	F-Value Range	P-Value Range	Highest Effect Size (η^2)
No-reference Quality Metrics	NIQE and PIQE combined	0.654	0.543	0.109
Full-reference Quality Metrics	MS-SSIM, PSNR, and NRMSE combined	0.003 to 0.006	0.948 to 0.982	0.001
Texture	Various texture metrics	0.442-1.651	0.216-0.811	0.248 (Homogeneity)
Contrast	Various contrast metrics	0.233-1.199	0.359-0.941	0.194 (RMS Contrast)

Comparison	Various comparison metrics	0.087-2.239	0.112-0.993	0.309 (Hist. Correlation)

In Table 6-6, the F-value represents the ratio of the variance between groups to the variance within groups, with larger values indicating greater differences between groups [352]. A p-value indicates the probability of obtaining test results at least as extreme as the observed results, assuming that the null hypothesis is correct [352]. A p-value less than 0.05 is typically considered statistically significant. The effect size (η^2) quantifies the magnitude of the difference between groups with values of 0.01, 0.06, and 0.14 typically considered small, medium, and large effects, respectively [353].

The ANOVA results indicated no statistically significant differences between the source and prediction groups or among upscaling methods for any set of metrics ($p > 0.05$). However, the variation in the F-values and effect sizes (η^2) suggests practical differences that warrant consideration. The no-reference quality metrics (NIQE and PIQE) showed a medium effect size ($\eta^2 \approx 0.109$), indicating a noticeable impact on perceptual image quality. In contrast, the full-reference quality metrics (MS-SSIM, PSNR, and NRMSE) show a very small effect size ($\eta^2 \approx 0.001$), suggesting high preservation of structural similarity and signal fidelity.

Among the specific metric categories, comparison metrics, particularly Histogram Correlation, showed the largest effect size ($\eta^2 = 0.309$), followed by texture metrics (homogeneity, $\eta^2 = 0.248$) and contrast metrics (RMS Contrast, $\eta^2 = 0.194$). These moderate effect sizes suggest practical differences in these aspects of image quality across the upscaling methods, despite the lack of statistical significance.

It is important to note that a lack of statistical significance does not necessarily mean that there are no meaningful differences. This may be due to several factors: our relatively small sample size, which can limit the power of statistical tests; high variability within groups; and the nature of the improvements made by our upscaling method, which may be consistent but subtle.

Despite the lack of statistical significance, the moderate effect sizes observed for some metrics suggest practical differences that warrant consideration when selecting an upscaling method for specific P-SHG imaging applications. These findings highlight the importance of considering both statistical and practical significance in evaluating imaging enhancement techniques.

Combining the no-reference and full-reference quality metrics with the ANOVA results provided a comprehensive validation of our upscaling methods. This analysis demonstrates that our

ESRGAN-based approach can enhance low-resolution images while preserving their quality. The lack of statistically significant differences, coupled with the moderate effect sizes in certain metrics, suggests that the upscaling process does not significantly alter perceived or structural image quality. This validation confirms the efficacy of the method and underscores its potential applicability in bioimaging and beyond, where maintaining the image integrity is paramount. The nuanced differences revealed by the effect size analysis provide valuable guidance for optimizing upscaling methods for specific imaging contexts, ensuring that the most critical aspects of image quality are preserved in each application.

P-SHG analysis results

Before conducting P-SHG analysis, we performed CurveAlign measurements to determine whether low-quality images could be analyzed using this method [158]. Figure 6-5 summarizes the results for the two samples.

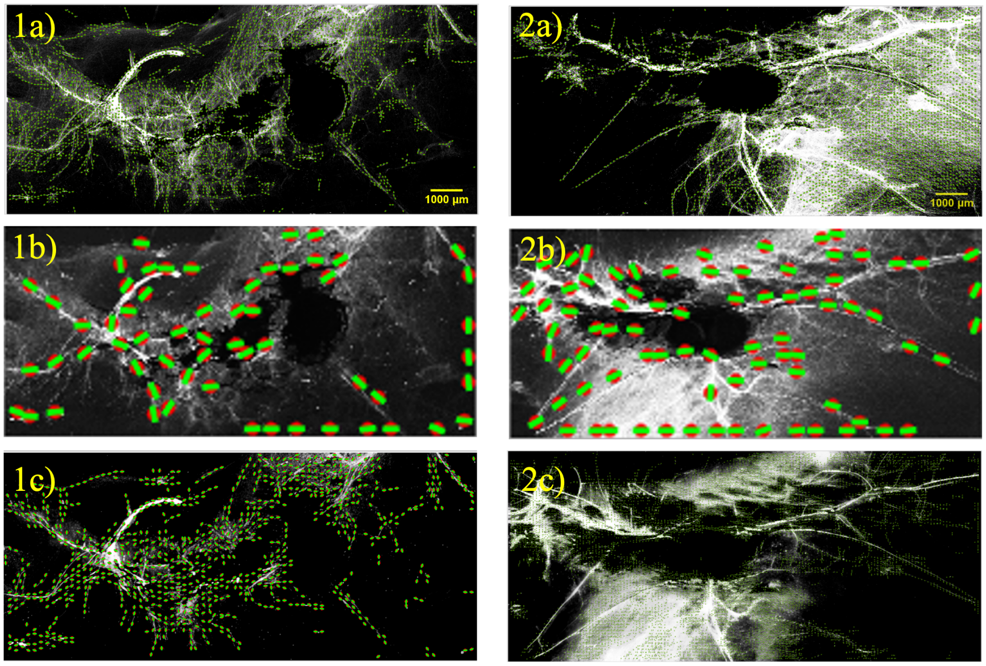

Figure 6-5: Comparative analysis using CurveAlign on samples: original high-quality (1a, 2a), low-quality (1b, 2b), and GAN-upscaled images (1c, 2c). CurveAlign accurately identifies the collagen fiber orientation in high-quality images (1a, 2a). In low-quality images (1b, 2b), the performance diminishes, with only larger recognizable fibers. However, the upscaled images (1c, 2c) show significantly improved analysis, with fiber orientation discernibility comparable to that of the original high-quality images. This demonstrates the efficacy of GAN-based upscaling in enhancing image analysis for CurveAlign.

In Figure 6-5, we present a comparative analysis using CurveAlign software on two sets of samples: original high-quality images (1a, 2a), their lower-quality versions (1b, 2b), and images enhanced via GAN-based upscaling (1c, 2c). CurveAlign proficiently identifies the orientation of collagen fibers in high-quality images (1a, 2a), demonstrating the effectiveness of the software with images of adequate resolution and clarity. However, acquiring such images required 15 min of continuous laser exposure per image, totaling 4.5 hours for the 18 images necessary for P-SHG analysis. This extended exposure can damage the samples, leading to degradation and affecting the repeatability of experiments. Additionally, fresh samples risk drying out and altering their morphology if removed from their chemical bath for more than a few minutes, potentially reducing SHG intensity or extinguishing harmonophores. Therefore, minimizing the laser exposure and expediting the imaging times are desirable.

Analysis of the lower-quality images (Figure 6-5, 1b, 2b) revealed significant limitations in both CurveAlign and our custom P-SHG algorithm. These tools struggled to accurately discern the collagen fiber orientation, identifying only a few larger fibers. This highlights the challenges that image analysis software faces with suboptimal image quality, where the loss of detail severely limits the accuracy and comprehensiveness of the P-SHG analysis. Many existing P-SHG analysis tools are optimized for higher-resolution inputs, often failing to detect finer structures or misinterpret noise as significant features when applied to low-resolution images (please refer to Supplement 1 Figure S1, and S2, respectively).

Remarkably, the GAN-upscaled images (Figure 6-5, 1c, 2c) showed a significant improvement, with CurveAlign's performance on these images being comparable to that on the original high-quality images. This comparative analysis underscores the necessity of our upscaling approach, rather than performing P-SHG analysis directly on low-resolution images. Our analysis demonstrates that the upscaled images provide a superior approximation of the original high-quality images across multiple metrics. For instance, the FSIM improved from 0.884 (low quality) to 0.910 (Ultrasharp_4X), and the LBP similarity increased from 0.471 to 0.758. Although upscaling does not recover all fine details, it strikes a balance between detail preservation and noise reduction.

The significant improvements in fiber orientation discernibility, as seen in Figure 6-5 (1c, 2c), clearly demonstrate the value of this upscaling approach. These enhancements are crucial for accurate P-SHG analysis, allowing for better differentiation of collagen structures and more reliable orientation measurements. Our approach leverages the speed of low-resolution imaging while obtaining analysis results that closely resemble those from high-resolution images, offering a pragmatic solution to the trade-off between imaging speed and analysis accuracy in P-SHG studies.In conclusion, this GAN-based upscaling approach markedly enhances the utility of lower-quality images for detailed analysis, extending the applicability of CurveAlign software and other tools to a broader spectrum of image qualities. It provides an efficient solution that combines shorter laser exposure times with image upscaling, overcoming the limitations posed by lower-quality images and technical constraints of sample preparation, and potentially opens new avenues for rapid, nondestructive P-SHG imaging in various biological applications.

Next, Images were captured at 18 polarization states, spanning 0°–170° degrees in 10-degree increments, with synchronization achieved using a custom Python program. Initially, the effort was to make the analysis software work based on low-quality images, but this was unsuccessful because there was too much loss of detail for the analysis to be accurate. The initial phase of our study attempted to conduct analyses based on low-quality images; however, this approach encountered substantial obstacles owing to the significant loss of detail, which compromised the accuracy of our analyses. To circumvent this issue, each image was individually upscaled using the Ultrasharp_4X model, thereby enhancing the resolution and clarity essential for accurate P-SHG analysis. A custom MATLAB script, inspired by the foundational work referenced in[63,158,236], was pivotal for processing upscaled P-SHG images. This script employs a spatial FFT algorithm to execute a Fourier transform on intensity measurements across different angles. For further details consult [63,236]. Figure 6-6 summarizes the results of the analysis.

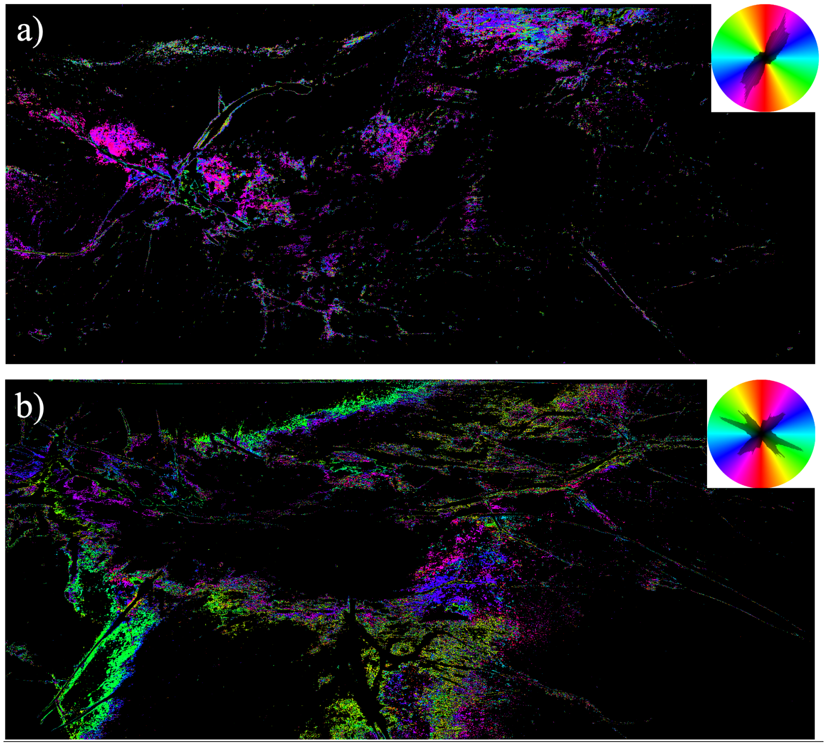

Figure 6-6: P-SHG imaging of collagen fiber orientation in mammary glands. Panels (a) and (b) display the SHG signals of two distinct tissues, visualized in a range of colors corresponding to the collagen fiber orientations relative to the polarization angle of the incident light. The color wheel insets map these orientations, with each color representing a specific angle of polarization, illustrating the complex and heterogeneous arrangement of the fibers within the samples. Notably, both images contained dark regions inside the fibers, which were attributed to areas where the intensity of the SHG signal remained static, indicating a uniform orientation of

collagen fibers over the polarization states captured. Owing to this uniformity, the spatial fast Fourier transform algorithm cannot discern variations, resulting in no color assignment in these specific regions.

Our P-SHG analysis protocol, detailed in Figure 6-6, encompasses 18 SHG images (32-bit TIFF) taken in 10-degree steps from 0°to 170°. Each angle (0-360 degrees) is denoted by a distinct color, providing a visually intuitive depiction of the fiber orientation across the sample. In addition, a fibrillar histogram accompanies the images, offering a quantitative analysis of the fiber orientations. Some areas in the analyzed images appear darker than those in the original images. Dark regions within the fiber network arise because of the uniform fiber orientation over polarization states. This results from the smoothing effect of the upscaling algorithm and impedes the ability of the FFT to detect internal variations within fibers. However, it is noteworthy that FFT remains adept at discerning the periphery of fibers and accurately identifying their borders. Importantly, the fiber borders were aligned with the interior, providing a coherent overall fiber direction. This consistency between the border and interior orientations ensures that despite the limitations in detecting internal variations, the method still effectively conveys the general directionality of the fibers. For analyses in which specific internal areas of the fiber are of interest, a targeted focus on these regions is required to overcome the limitations of these smoother, homogeneous sections (see Figure 6-7).

Furthermore, dark areas around the sample resulted from the deliberate removal of background elements and non-essential muscle structures surrounding the fibers, a step taken to enhance the clarity and focus of the analysis of the collagen fibers. Figure 6-6a. shows a network of collagen fibers with varying orientations, as indicated by the spectrum of colors present in the tissue, where each color corresponds to a different fiber orientation relative to the polarization angle of the incident light. The color wheel inset serves as a reference for interpreting these orientations. The vibrant colors suggest a diverse and complex arrangement of fibers, with pink hues indicating fibers oriented in one direction, and other colors representing different angles. Figure 6-6b. displays a collage of colors, indicating the orientation of collagen fibers. The presence of bright green and yellow hues suggests that the fibers have orientations different from those in the first image. The color intensity and distribution indicated that this sample may have a denser or more aligned collagen network than the first sample. The results, including the color wheel, orientation map, anisotropy parameter map, and histogram data, were meticulously compiled for each sample.

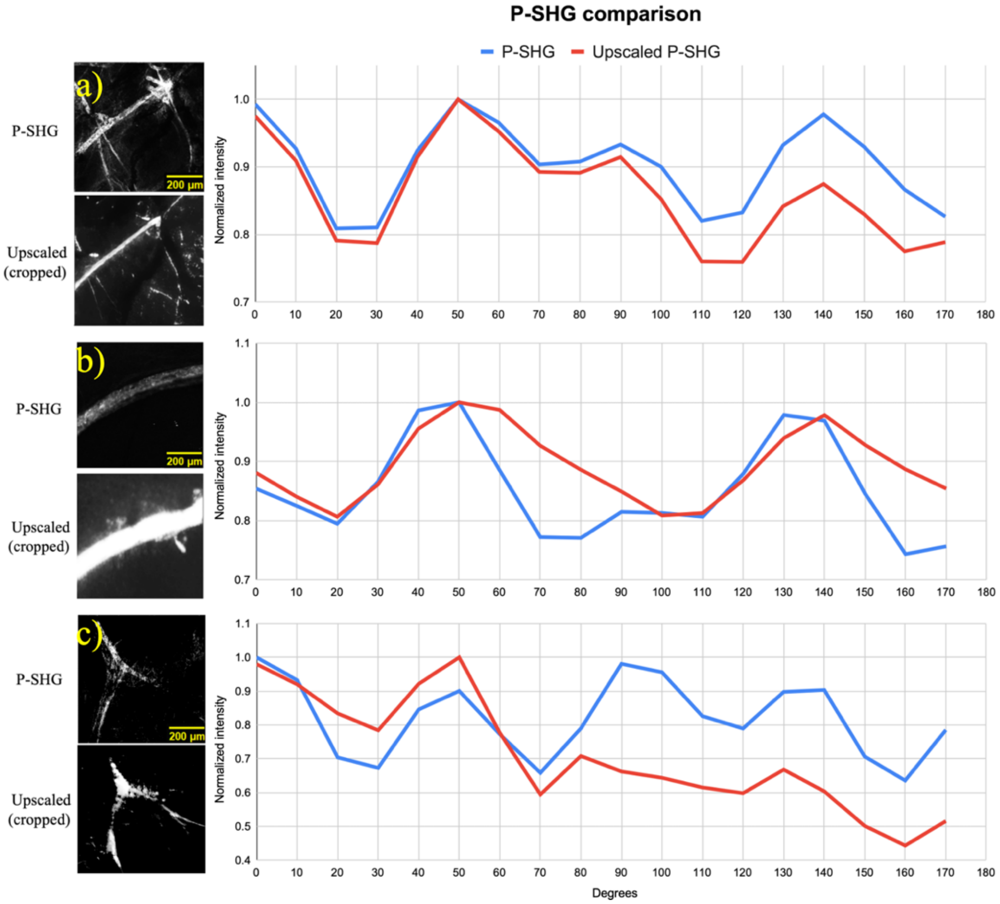

Figure 6-7: Comparative P-SHG Analysis Across Three ROIs. Each row represents a distinct region of interest (ROI) from different samples, showcasing original high-quality images (20X objective), low-quality images initially captured with a 10X objective then digitally zoomed and cropped, and their GAN-upscaled counterparts. Despite the initial lower resolution, upscaling restores detail and smoothness, yielding a fiber orientation analysis comparable to the original high-quality images. Normalized intensity vs. laser input angle graphs for each set illustrate the consistency of P-SHG responses across all imaging modalities, affirming the accuracy of collagen fiber orientation details in the upscaled images.

In Figure 6-7, we focus on the analysis of regions of interest (ROI)s extracted from different samples and their counterparts, which were enhanced through an upscaling process. This examination is pivotal for assessing the fidelity of upscaling techniques to preserve the structural and optical properties that are essential for accurate P-SHG analysis. For our analysis, images of the selected P-SHG ROIs were captured using a 20X objective. 20X is optimal for resolving the intricate patterns of collagen fiber orientation while ensuring adequate field coverage. Notably, the images earmarked for upscaling were initially obtained using a 10X objective, before being digitally zoomed and cropped. This approach was strategically employed for low-quality images to simulate the conditions in which high-resolution data were not readily available or feasible to obtain, thus mimicking a real-world scenario in which upscaling could be particularly beneficial. Upon comparing the original and upscaled (yet zoomed and cropped) P-SHG images, a key observation was the smoothness of the upscaled images. This smoothness did not detract from the structural details within the images, but rather enhanced the visual clarity, making the interpretation of collagen fiber orientations more straightforward. More importantly, when we quantified the P-SHG response by plotting the normalized intensity against the laser input angle for both the original and upscaled images, we observed remarkably consistent responses. The graph corresponding to the upscaled P-SHG images exhibited a smoother curve, an effect attributable to the upscaling process, which tended to reduce noise and interpolate between data points to create a more continuous representation of the intensity response.

Crucially, despite the smoother appearance of the graphs in the upscaled images, the overall shape and trend of the P-SHG intensity responses remained unchanged. This congruence indicates that the upscaling process, while enhancing the visual quality of the images, did not alter the fundamental biophysical properties captured by P-SHG imaging. Thus, the fidelity of fiber orientation details in the upscaled images was validated, underscoring the utility of upscaling as a viable method for improving image quality in P-SHG analysis without compromising the accuracy of collagen fiber orientation information.

Conclusion

In conclusion, our research has demonstrated significant advancements in whole-sample mammary gland P-SHG imaging, reducing the imaging time from a time-consuming 4.5 hours to a mere 13.5 minutes (more than 95% reduction). Acquiring 18 high-quality images suitable for P-SHG analysis is a time-intensive process that poses the risk of damage to samples, particularly those of considerable size. To mitigate these challenges, we propose an innovative method that involves capturing 18 low-quality images and subsequently enhancing their resolution by using a GAN-based approach. This technique not only substantially reduces the required imaging time but also ensures preservation of sample integrity during the imaging process. By leveraging the capabilities of GANs to generate high-resolution images from their lower-quality counterparts, this approach offers a promising alternative that balances the need for high-quality imaging with the imperative of minimizing potential harm to delicate samples. In our pursuit of image upscaling, we explored various models, ultimately selecting "ultrasharp_4X" based on ESRGAN owing to its remarkable similarity to the original images. Although we initially considered using high-quality images as references for upscaling, this approach led to undesirable alterations, making it unsuitable for our specific application. This method saves substantial amounts of time and offers several advantages.

One of the most noteworthy advantages of our accelerated P-SHG imaging process is the substantial reduction in the laser exposure of the sample. Laser-induced photodamage is a concern when working with delicate biological specimens, and minimizing this risk is crucial for preserving the integrity and quality of the sample. Our faster imaging method minimizes the exposure time, reduces potential harm to the sample, and allows for extended observation without compromising the biological or material properties under investigation. Using this technique, we achieved fiber orientation analysis on par with that of high-quality images captured with a 20X objective. This accelerated process was complemented by a meticulous image analysis protocol, in which each angle of polarization was represented by a specific color on a wheel, translating into an intuitive visual depiction of the fiber orientation throughout the sample. Accompanying fibrillar histograms provides quantitative analysis that enhances the interpretive depth of the study. Our results demonstrate the robustness of P-SHG responses and fidelity of collagen fiber orientation data within upscaled images. These findings were reinforced by a comparative analysis across three distinct ROIs, which confirmed that the GAN-based upscaling process preserved the integrity of the sample while enhancing the detail and smoothness of fiber alignment.

Furthermore, the expedited P-SHG imaging process allows us to reconsider the optical components of the imaging system. Because high-resolution imaging is not required in many of our applications, we can opt for more cost-effective objective objectives and imaging systems. This optimization translates to significant cost savings and lowers barriers to entry for researchers and institutions interested in utilizing the P-SHG imaging technology. This affordability and accessibility expands the potential applications of P-SHG imaging in diverse fields and communities. Our analysis confirmed the accuracy of the results obtained using accelerated imaging. By comparing the P-SHG images generated using our streamlined approach with those produced using the traditional method, we found that the results were consistent with the characteristics of the sample. Reducing the laser exposure and equipment costs ensures that P-SHG imaging can be adopted more widely, thereby advancing scientific understanding and innovation across disciplines. Our work paves the way for discoveries and breakthroughs fueled by the efficiency and accessibility of P-SHG imaging. Therefore, there are promising directions for future research. New or emerging GAN architectures can offer more precise upscaling capabilities, particularly for images with unique challenges that are not fully addressed by the current models. The development of automated analysis tools tailored for upscaled images ensures that the upscaling process enhances data interpretation. The incorporation of AI-driven methods for identifying and quantifying specific features in upscaled images can streamline the analysis of complex biological structures. In addition, the effectiveness of our method was demonstrated through mammary gland tissue imaging. Extending this approach to other tissues or conditions such as fibrotic changes in liver disease or collagen alterations in cardiovascular health could significantly broaden its applicability. This expansion would not only validates the versatility of the proposed method, but also contributes valuable insights into the structural dynamics of various diseases. Moreover, establishing guidelines for the ethical use of AI in scientific imaging will ensure the integrity of data. Developing quality standards for upscaled images will facilitate their acceptance and use in critical research endeavors.

Back matter

Funding. The authors acknowledge financial support from the Canada Foundation for Innovation, Fonds de recherche du Québec–Nature et technologies, the Natural Sciences and Engineering Research Council of Canada, and the New Frontiers Research Fund. Arash Aghigh thanks the NSERC CREATE program for the scholarship.

Conflict of interest. The authors declare that they have no conflicts of interest.

Data availability. The data, codes, and materials underlying the results presented in this paper are available for full transparency and reproducibility at DOI: 10.5281/zenodo.12788764. The ChaiNNer program can be downloaded from https://github.com/chaiNNer-org/chaiNNer. All the models used in this study can be downloaded from https://openmodeldb.info except for PixTransform which can be downloaded from https://github.com/prs-eth/PixTransform.

Ethics statement. Animal studies were conducted according to the procedures provided by the Canadian Council on Animal Care. The protocol (2005-02) was reviewed and approved by the Institutional Committee for Animal Protection of the Laboratoire National de Biologie Expérimentale (LNBE), the animal facilities based at the Institut National de Recherche Scientifique (INRS).

Supplemental document. See Supplement 1 for supporting content.

7 CONCLUSION AND FUTURE WORK

7.1 Conclusion

SHG microscopy has firmly established itself as a powerful tool for bioimaging, particularly in the study of non-centrosymmetric biological structures such as collagen, myosin, and microtubules. Integrating advanced SHG modalities, including P-SHG, I-SHG, and wide-field SHG, has significantly expanded its capabilities, enabling researchers to probe biological tissue's structural and functional aspects with unprecedented detail and precision. These advancements have positioned SHG microscopy as an essential tool in biomedical research, with potential applications spanning neuroscience, cancer diagnostics, and tissue analysis.

Recent technological advancements have improved the accessibility and versatility of SHG microscopy. On the hardware front, the shift towards more robust and cost-effective fiber and semiconductor lasers promises to broaden the user base of SHG microscopy. Concurrently, integrating machine learning and artificial intelligence in software applications is revolutionizing image analysis and enabling automated feature detection and real-time image enhancement during acquisition.

Despite these promising developments, SHG microscopy faces several challenges. The high equipment cost and the need for specialized training continue to limit its widespread adoption in routine biomedical practice. Moreover, while integrating deep learning techniques shows great potential, it is still in its early stages. Researchers are grappling with issues such as the need for large, well-annotated datasets and the risk of overfitting when working with limited data.

The application of SHG microscopy in clinical settings presents exciting prospects, particularly in areas such as cancer diagnosis and pathology. Its potential applications in drug development and personalized medicine could lead to significant breakthroughs in healthcare. However, realizing this potential will require addressing the current challenges through cost reduction, standardization of techniques, and improved data interpretation. Overcoming these limitations necessitates concerted efforts in hardware development, advanced image-processing techniques, and the establishment of standardized SHG imaging protocols. In addition to addressing technical limitations, successfully integrating SHG microscopy into routine biomedical practice will require collaborative efforts between researchers, industry, and regulatory bodies. Standardizing AI-driven SHG imaging pipelines and ensuring compliance with clinical imaging standards will be crucial for widespread adoption in pathology labs and diagnostic centers.

Developing user-friendly software solutions that enable seamless interaction between SHG imaging systems and hospital information systems can further accelerate the transition from research to clinical applications.

The emerging synergy with deep learning promises to overcome the current limitations and open new avenues for research, from automated image analysis to enhanced resolution and sensitivity. The rapid evolution of AI-driven methodologies in biomedical imaging suggests that deep learning techniques will become integral to SHG microscopy workflows in the coming years. As models become more efficient and computational hardware advances, the barriers to AI adoption in microscopy—such as computational costs and training data limitations—will gradually diminish. Refining self-supervised and few-shot learning approaches could enable deep learning models to perform effectively even in data-scarce scenarios, making AI-based image enhancement and classification more accessible to researchers across disciplines.

The research presented in the four articles of this thesis directly addressed its primary objectives. Article 1 provides crucial context and identifies areas for improvement in SHG microscopy. Articles 2 and 3 demonstrate significant advancements in image quality enhancement and automated analysis using ML techniques, whereas Article 4 shows how GANs can dramatically improve imaging speed and efficiency.

Future research should refine DL models for broader biological sample use, building on these advancements, which improve imaging quality, speed, and structural analysis capabilities. Integrating these models into clinical workflows is a priority. Further optimization of DL algorithms for specific tissue types and imaging conditions, development of integrated hardware-software solutions for real-time AI-enhanced SHG imaging, and exploration of multimodal imaging techniques combining SHG with other microscopy methods are equally important.

The broader implications of this study extend beyond SHG microscopy. By demonstrating the feasibility of AI-powered enhancements in SHG microscopy, this research contributes to a broader shift in biomedical imaging toward automation and intelligent analysis. Similar deep learning techniques can be adapted for other nonlinear optical modalities, such as THG and CARS microscopy. Furthermore, the advancements in noise reduction, image upscaling, and classification through AI can be leveraged to improve imaging accuracy in fields such as disease diagnosis, drug development, and personalized medicine.

Improved SHG microscopy techniques can lead to more accurate and earlier disease diagnosis, particularly in cancer detection. The increased efficiency and accessibility of these imaging methods could accelerate drug development, potentially reducing the time and cost of bringing new treatments to the market. Furthermore, incorporating AI with SHG microscopy could democratize access to advanced imaging technologies, enabling their use in a broader range of healthcare settings and contributing to more equitable healthcare delivery.

This thesis demonstrated the transformative potential of integrating SHG microscopy with advanced AI techniques. The findings highlight significant improvements in imaging quality and analytical capabilities, suggesting a future in which these technologies are integral to biomedical research and clinical applications. Further research should refine these methods for broader accessibility and enhanced diagnostic precision.

Future research should aim to refine machine-learning models for more diverse biological samples and explore their integration into clinical workflows. In addition, developing cost-effective and user-friendly SHG imaging systems can enhance accessibility in various healthcare settings.

7.2 Future work

7.2.1 Expanding multimodal imaging techniques

A significant opportunity lies in advancing the incorporation of AI into existing multimodal imaging techniques that combine SHG microscopy with other advanced imaging modalities. Although these combinations provide a comprehensive view of the tissue architecture and biochemical composition, adding machine learning can significantly enhance the analysis and interpretation of complex datasets. Future studies should focus on developing algorithms capable of seamlessly integrating data from these diverse modalities, offering more precise and nuanced insights into biological systems. For example, DL can improve image registration, enhance contrast, and extract subtle patterns that may not be visible using traditional methods. Moreover, AI-driven data fusion can automate the identification of correlations between structural and molecular information, facilitating a deeper understanding of complex biological processes, such as tumor progression or tissue regeneration. This integration streamlines data processing and unlocks new possibilities for personalized diagnostics and targeted therapeutic strategies by providing clinicians with a more detailed and actionable understanding of patient-specific conditions. An additional frontier in multimodal imaging involves integrating SHG with AI-driven hyperspectral and Raman imaging techniques, allowing researchers to simultaneously extract structural and biochemical information from tissues. By training deep learning models to interpret combined datasets, future studies could refine disease biomarkers and improve the predictive power of diagnostic models. This approach holds promise for oncology, where integrating SHG and biochemical data can enhance early tumor detection and classification.

7.2.2 Development of adaptive and hybrid deep learning models

The potential for developing adaptive and hybrid deep learning models is immense. These models can dynamically adjust their parameters based on real-time imaging conditions and tissue characteristics analysis, optimizing the denoising and enhancement processes. Researchers can create more versatile and practical models across various imaging scenarios by combining the strengths of CARE 2D and N2V 2D and exploring novel architectures, such as GANs. Developing deep learning models incorporating physics-based priors alongside data-driven approaches could significantly enhance SHG image reconstruction. By integrating optical physics and tissue properties knowledge into neural networks, researchers can create more interpretable AI models that are less susceptible to hallucination artifacts. This could be particularly useful in low-SNR imaging conditions, where traditional deep-learning approaches struggle to distinguish true signal from noise.

7.2.3 Enhancing classification and analysis tools

Future work should focus on refining classification algorithms to better differentiate between tissue types and conditions. Advanced techniques, such as transfer learning and ensemble methods, can improve accuracy and robustness. Additionally, developing automated analysis tools that leverage AI-driven insights can facilitate real-time diagnostics, enabling faster and more accurate decision-making in clinical settings.

7.2.4 Expanding application scope to diverse tissues

Extending the application of SHG microscopy and deep learning techniques to a broader range of tissues and conditions can validate their versatility. Research could focus on studying fibrotic changes in liver disease, collagen alterations in cardiovascular health, or structural dynamics in neurodegenerative diseases. Such studies would enhance our understanding of these conditions and provide valuable data for refining imaging and analysis techniques.

7.2.5 Ethical considerations and standardization

As AI-driven imaging has become more prevalent, establishing ethical guidelines and quality standards is essential to ensure data integrity and reliability. Future research should address the ethical implications of AI in scientific imaging to promote transparency and reproducibility. Standardizing data collection, analysis, and sharing protocols will be crucial for building trust and facilitating collaboration across the scientific community.

7.2.6 Real-time imaging and low-power applications

The enhancement of SHG microscopy for real-time and low-power imaging applications presents exciting opportunities for in vivo studies. By reducing the laser power required for high-quality imaging, researchers can minimize sample damage and extend the applicability of SHG to more delicate and dynamic biological samples. This advancement could significantly impact fields such as developmental biology and cancer research, in which observing live processes is crucial. Future studies should explore real-time AI-based denoising pipelines that operate during image acquisition, enabling researchers to obtain high-quality images with minimal Implementation of lightweight neural networks that can run on devices or embedded hardware would allow SHG microscopy to be deployed in resource-limited settings, expanding its accessibility beyond specialized research laboratories. This could open new opportunities for in-field biomedical imaging applications, such as portable SHG endoscopy for minimally invasive diagnostics.

7.2.7 Integration with clinical workflows

Finally, integrating these advanced imaging techniques with clinical workflows can revolutionize diagnostics and patient care. Developing intuitive interfaces and robust analysis tools can help clinicians quickly and accurately interpret complex imaging data. Collaboration between researchers, engineers, and healthcare professionals will ensure these technologies meet clinical needs and improve patient outcomes.

8 REFERENCES

1. A. J. M. Wollman, R. Nudd, E. G. Hedlund, and M. C. Leake, "From Animaculum to single molecules: 300 years of the light microscope," Open Biol. **5**(4), 150019 (2015).
2. A. Aghigh, S. Bancelin, M. Rivard, M. Pinsard, H. Ibrahim, and F. Légaré, "Second harmonic generation microscopy: a powerful tool for bio-imaging," Biophys. Rev. (2023).
3. M. Born and E. Wolf, *Principles of Optics: Electromagnetic Theory of Propagation, Interference and Diffraction of Light*, 7th ed. (Cambridge University Press, 1999).
4. F. S. P. Campagnola Paul J., ed., *Second Harmonic Generation Imaging* (CRC Press, 2013).
5. "Darkfield Illumination," https://www.microscopyu.com/techniques/stereomicroscopy/darkfield-illumination.
6. F. Zernike, "Phase contrast, a new method for the microscopic observation of transparent objects," Physica **9**(7), 686–698 (1942).
7. W. Lang, "Nomarski Differential Interference-Contrast Microscopy," (n.d.).
8. M. Pinsard, "Multimodal and Advanced Interferometric Second Harmonic Generation Microscopy for an Improved Characterization of Biopolymers in Cells and Tissues," phdthesis, INRS-EMT (2020).
9. M. Minsky, "Memoir on inventing the confocal scanning microscope," Scanning **10**(4), 128–138 (1988).
10. P. Davidovits and M. D. Egger, "Scanning Laser Microscope," Nature **223**(5208), 831–831 (1969).
11. C. J. R. Sheppard and T. Wilson, "The theory of the direct-view confocal microscope," J. Microsc. **124**(2), 107–117 (1981).
12. T. J. Fellers and M. W. Davidson, "Confocal Microscopy - Introduction | Olympus Life Science," https://www.olympus-lifescience.com/en/microscope-resource/primer/techniques/confocal/confocalintro/.
13. M. J. Sanderson, I. Smith, I. Parker, and M. D. Bootman, "Fluorescence Microscopy," Cold Spring Harb. Protoc. **2014**(10), pdb.top071795 (2014).
14. E. E. Hoover and J. A. Squier, "Advances in multiphoton microscopy technology," Nat. Photonics **7**(2), 93–101 (2013).

15. S. W. Hell and J. Wichmann, "Breaking the diffraction resolution limit by stimulated emission: stimulated-emission-depletion fluorescence microscopy," Opt. Lett. **19**(11), 780–782 (1994).

16. G. Moneron and S. W. Hell, "Two-photon excitation STED microscopy," Opt. Express **17**(17), 14567–14573 (2009).

17. S. T. Hess, T. P. K. Girirajan, and M. D. Mason, "Ultra-High Resolution Imaging by Fluorescence Photoactivation Localization Microscopy," Biophys. J. **91**(11), 4258–4272 (2006).

18. M. J. Rust, M. Bates, and X. Zhuang, "Sub-diffraction-limit imaging by stochastic optical reconstruction microscopy (STORM)," Nat. Methods **3**(10), 793–796 (2006).

19. M. Göppert, "Über die Wahrscheinlichkeit des Zusammenwirkens zweier Lichtquanten in einem Elementarakt," Naturwissenschaften **17**(48), 932–932 (1929).

20. T. H. Maiman, "Stimulated Optical Radiation in Ruby," Nature **187**(4736), 493–494 (1960).

21. A. L. Schawlow and C. H. Townes, "Infrared and Optical Masers," Phys. Rev. **112**(6), 1940–1949 (1958).

22. P. A. Franken, A. E. Hill, C. W. Peters, and G. Weinreich, "Generation of Optical Harmonics," Phys. Rev. Lett. **7**(4), 118–119 (1961).

23. N. Bloembergen and P. S. Pershan, "Light Waves at the Boundary of Nonlinear Media," Phys. Rev. **128**(2), 606–622 (1962).

24. R. Hellwarth and P. Christensen, "Nonlinear optical microscopic examination of structure in polycrystalline ZnSe," Opt. Commun. **12**(3), 318–322 (1974).

25. C. Sheppard, J. Gannaway, R. Kompfner, and D. Walsh, "The scanning harmonic optical microscope," IEEE J. Quantum Electron. **13**(9), 912 (1977).

26. D. A. Parry and A. S. Craig, "Quantitative electron microscope observations of the collagen fibrils in rat-tail tendon," Biopolymers **16**(5), 1015–1031 (1977).

27. M. Minary-Jolandan and M.-F. Yu, "Uncovering nanoscale electromechanical heterogeneity in the subfibrillar structure of collagen fibrils responsible for the piezoelectricity of bone," ACS Nano **3**(7), 1859–1863 (2009).

28. C. Harnagea, M. Vallières, C. P. Pfeffer, D. Wu, B. R. Olsen, A. Pignolet, F. Légaré, and A. Gruverman, "Two-Dimensional Nanoscale Structural and Functional Imaging in Individual Collagen Type I Fibrils," Biophys. J. **98**(12), 3070–3077 (2010).

29. S. Roth and I. Freund, "Second harmonic generation in collagen," J. Chem. Phys. **70**(4), 1637–1643 (1979).

30. I. Freund and M. Deutsch, "Second-harmonic microscopy of biological tissue," Opt. Lett. **11**(2), 94–96 (1986).

31. W. Denk, J. H. Strickler, and W. W. Webb, "Two-photon laser scanning fluorescence microscopy," Science **248**(4951), 73–76 (1990).

32. S. W. Hell, K. Bahlmann, M. Schrader, A. Soini, H. M. Malak, I. Gryczynski, and J. R. Lakowicz, "Three-photon excitation in fluorescence microscopy," J. Biomed. Opt. **1**(1), 71–74 (1996).

33. R. Gauderon, P. B. Lukins, and C. J. R. Sheppard, "Three-dimensional second-harmonic generation imaging with femtosecond laser pulses," Opt. Lett. **23**(15), 1209–1211 (1998).

34. P. Bianchini and A. Diaspro, "Second Harmonic Generation Microscopy (SHG)," in *Encyclopedia of Biophysics*, G. C. K. Roberts, ed., First edition (Springer, 2013), pp. 2280–2283.

35. G. Cox, E. Kable, A. Jones, I. Fraser, F. Manconi, and M. D. Gorrell, "3-Dimensional imaging of collagen using second harmonic generation," J. Struct. Biol. **141**(1), 53–62 (2003).

36. E. Hemmer, A. Benayas, F. Légaré, and F. Vetrone, "Exploiting the biological windows: current perspectives on fluorescent bioprobes emitting above 1000 nm," Nanoscale Horiz. **1**(3), 168–184 (2016).

37. D. S. James and P. J. Campagnola, "Recent Advancements in Optical Harmonic Generation Microscopy: Applications and Perspectives," BME Front. **2021**, 3973857 (2021).

38. W. R. Zipfel, R. M. Williams, R. Christie, A. Y. Nikitin, B. T. Hyman, and W. W. Webb, "Live tissue intrinsic emission microscopy using multiphoton-excited native fluorescence and second harmonic generation," Proc. Natl. Acad. Sci. U. S. A. **100**(12), 7075–7080 (2003).

39. R. W. Boyd, *Nonlinear Optics*, 4th ed. (Academic Press is an imprint of Elsevier, 2019).

40. X. Chen, O. Nadiarynkh, S. Plotnikov, and P. J. Campagnola, "Second harmonic generation microscopy for quantitative analysis of collagen fibrillar structure," Nat. Protoc. **7**(4), 654–669 (2012).

41. J. A. Squier, M. Müller, G. J. Brakenhoff, and K. R. Wilson, "Third harmonic generation microscopy," Opt. Express **3**(9), 315–324 (1998).

42. R. h. Stolen and A. Ashkin, "Optical Kerr effect in glass waveguide," Appl. Phys. Lett. **22**(6), 294–296 (1973).

43. F. Shimizu, "Frequency Broadening in Liquids by a Short Light Pulse," Phys. Rev. Lett. **19**(19), 1097–1100 (1967).

44. M. N. Islam, L. F. Mollenauer, R. H. Stolen, J. R. Simpson, and H. T. Shang, "Cross-phase modulation in optical fibers," Opt. Lett. **12**(8), 625–627 (1987).

45. M.-A. Houle, R. C. Burruss, A. Ridsdale, D. J. Moffatt, F. Légaré, and A. Stolow, "Rapid 3D chemical-specific imaging of minerals using stimulated Raman scattering microscopy," J. Raman Spectrosc. **48**(5), 726–735 (2017).

46. A. Nayak, J. Park, K. De Mey, X. Hu, T. V. Duncan, D. N. Beratan, K. Clays, and M. J. Therien, "Large Hyperpolarizabilities at Telecommunication-Relevant Wavelengths in Donor–Acceptor–Donor Nonlinear Optical Chromophores," ACS Cent. Sci. **2**(12), 954–966 (2016).

47. P. J. Campagnola and L. M. Loew, "Second-harmonic imaging microscopy for visualizing biomolecular arrays in cells, tissues and organisms," Nat. Biotechnol. **21**(11), 1356–1360 (2003).

48. W. Mohler, A. C. Millard, and P. J. Campagnola, "Second harmonic generation imaging of endogenous structural proteins," Methods **29**(1), 97–109 (2003).

49. M. Rivard, "Imagerie tissulaire par microscopie de seconde harmonique interférométrique," INRS (2016).

50. T. Yasui, Y. Tohno, and T. Araki, "Determination of collagen fiber orientation in human tissue by use of polarization measurement of molecular second-harmonic-generation light," Appl. Opt. **43**(14), 2861–2867 (2004).

51. J. Mertz and L. Moreaux, "Second-harmonic generation by focused excitation of inhomogeneously distributed scatterers," Opt. Commun. **196**(1), 325–330 (2001).

52. P. Stoller, K. M. Reiser, P. M. Celliers, and A. M. Rubenchik, "Polarization-Modulated Second Harmonic Generation in Collagen," Biophys. J. **82**(6), 3330–3342 (2002).

53. G. G. Stokes, "On the Composition and Resolution of Streams of Polarized Light from different Sources," Trans. Camb. Philos. Soc. **9**, 399 (1851).

54. R. C. Jones, "A New Calculus for the Treatment of Optical Systems. IV.," JOSA **32**(8), 486–493 (1942).

55. A. Golaraei, "Polarimetric Second-Harmonic Generation Microscopy for Histopathology," Thesis (2018).

56. E. Binshtein and M. D. Ohi, "Cryo-electron microscopy and the amazing race to atomic resolution," Biochemistry **54**(20), 3133–3141 (2015).

57. Y. Shi, "A glimpse of structural biology through X-ray crystallography," Cell **159**(5), 995–1014 (2014).

58. J. Kaneshiro, Y. Okada, T. Shima, M. Tsujii, K. Imada, T. Ichimura, and T. M. Watanabe, "Second harmonic generation polarization microscopy as a tool for protein structure analysis," Biophys. Physicobiology **16**, 147–157 (2019).

59. I. Miler, M. D. Rabasovic, M. Aleksic, A. J. Krmpot, A. Kalezic, A. Jankovic, B. Korac, and A. Korac, "Polarization-resolved SHG imaging as a fast screening method for collagen alterations during aging: Comparison with light and electron microscopy," J. Biophotonics **14**(3), e202000362 (2021).

60. C. Raoux, C. Raoux, M. Schmeltz, M. Schmeltz, M. Bied, M. Alnawaiseh, U. Hansen, G. Latour, G. Latour, and M.-C. Schanne-Klein, "Quantitative structural imaging of keratoconic corneas using polarization-resolved SHG microscopy," Biomed. Opt. Express **12**(7), 4163–4178 (2021).

61. A. Golaraei, L. B. Mostaço-Guidolin, V. Raja, R. Navab, T. Wang, S. Sakashita, K. Yasufuku, M.-S. Tsao, B. C. Wilson, and V. Barzda, "Polarimetric second-harmonic generation microscopy of the hierarchical structure of collagen in stage I-III non-small cell lung carcinoma," Biomed. Opt. Express **11**(4), 1851–1863 (2020).

62. I. Gusachenko, G. Latour, and M.-C. Schanne-Klein, "Polarization-resolved Second Harmonic microscopy in anisotropic thick tissues," Opt. Express **18**(18), 19339–19352 (2010).

63. C. Teulon, I. Gusachenko, G. Latour, and M.-C. Schanne-Klein, "Theoretical, numerical and experimental study of geometrical parameters that affect anisotropy measurements in polarization-resolved SHG microscopy," Opt. Express **23**(7), 9313–9328 (2015).

64. R. A. R. Rao, M. R. Mehta, and K. C. Toussaint, "Fourier transform-second-harmonic generation imaging of biological tissues," Opt. Express **17**(17), 14534–14542 (2009).

65. "CurveAlign – Laboratory for Optical and Computational Instrumentation," (n.d.).

66. "Transforms and Operators for Directional Bioimage Analysis: A Survey - PubMed," https://pubmed.ncbi.nlm.nih.gov/27207363/.

67. "BIG > OrientationJ," https://bigwww.epfl.ch/demo/orientationj/.

68. M. Rivard, M. Laliberté, A. Bertrand-Grenier, C. Harnagea, C. P. Pfeffer, M. Vallières, Y. St-Pierre, A. Pignolet, M. A. El Khakani, and F. Légaré, "The structural origin of second harmonic generation in fascia," Biomed. Opt. Express **2**(1), 26–36 (2010).

69. M. Pinsard, M. Schmeltz, J. van der Kolk, S. A. Patten, H. Ibrahim, L. Ramunno, M.-C. Schanne-Klein, and F. Légaré, "Elimination of imaging artifacts in second harmonic generation microscopy using interferometry," Biomed. Opt. Express **10**(8), 3938–3952 (2019).

70. S. Yazdanfar, L. H. Laiho, and P. T. C. So, "Interferometric second harmonic generation microscopy," Opt. Express **12**(12), 2739–2745 (2004).

71. M. Rivard, K. Popov, M. Laliberté, A. Bertrand-Grenier, F. Martin, H. Pépin, C. P. Pfeffer, C. Brown, L. Rammuno, and F. Légaré, "Imaging tendon and muscle with Interferometric Second Harmonic Generation microscopy (I-SHG)," in *Optics in the Life Sciences (2013), Paper NT1B.3* (Optical Society of America, 2013), p. NT1B.3.

72. C.-A. Couture, S. Bancelin, J. van der Kolk, K. Popov, M. Rivard, K. Légaré, G. Martel, H. Richard, C. Brown, S. Laverty, L. Ramunno, and F. Légaré, "The Impact of Collagen Fibril Polarity on Second Harmonic Generation Microscopy," Biophys. J. **109**(12), 2501–2510 (2015).

73. M. Pinsard, "Multimodal and Advanced Interferometric Second Harmonic Generation Microscopy for an Improved Characterization of Biopolymers in Cells and Tissues," INRS-EMT (2020).

74. R. Stolle, G. Marowsky, E. Schwarzberg, and G. Berkovic, "Phase measurements in nonlinear optics," Appl. Phys. B Laser Opt. **63**(5), 491–498 (1996).

75. M. Pinsard, L.-P. Belley, J.-M. Piau, C.-Y. Coté, H. Ibrahim, and F. Légaré, "Single-scan interferometric second harmonic generation microscopy using a kHz phase-scanner," Opt. Express **27**(26), 38435–38450 (2019).

76. C. Macias-Romero, M. E. P. Didier, P. Jourdain, P. Marquet, P. Magistretti, O. B. Tarun, V. Zubkovs, A. Radenovic, and S. Roke, "High throughput second harmonic imaging for label-free biological applications," Opt. Express **22**(25), 31102–31112 (2014).

77. C. Macias-Romero, V. Zubkovs, S. Wang, and S. Roke, "Wide-field medium-repetition-rate multiphoton microscopy reduces photodamage of living cells," Biomed. Opt. Express **7**(4), 1458–1467 (2016).

78. M. D. Peterson, P. L. Hayes, I. S. Martinez, L. C. Cass, J. L. Achtyl, E. A. Weiss, and F. M. Geiger, "Second harmonic generation imaging with a kHz amplifier [Invited]," Opt. Mater. Express **1**(1), 57–66 (2011).

79. D. Oron, E. Tal, and Y. Silberberg, "Scanningless depth-resolved microscopy," Opt. Express **13**(5), 1468–1476 (2005).

80. A. Vaziri and C. V. Shank, "Ultrafast widefield optical sectioning microscopy by multifocal temporal focusing," Opt. Express **18**(19), 19645–19655 (2010).

81. E. E. Hoover, J. J. Field, D. G. Winters, M. D. Young, E. V. Chandler, J. C. Speirs, J. T. Lapenna, S. M. Kim, S.-Y. Ding, R. A. Bartels, J. W. Wang, and J. A. Squier, "Eliminating the scattering ambiguity in multifocal, multimodal, multiphoton imaging systems," J. Biophotonics **5**(5–6), 425–436 (2012).

82. L.-C. Cheng, C.-Y. Chang, C.-Y. Lin, K.-C. Cho, W.-C. Yen, N.-S. Chang, C. Xu, C. Y. Dong, and S.-J. Chen, "Spatiotemporal focusing-based widefield multiphoton microscopy for fast optical sectioning," Opt. Express **20**(8), 8939–8948 (2012).

83. H. Zhao, H. Zhao, H. Zhao, H. Zhao, R. Cisek, R. Cisek, A. Karunendiran, A. Karunendiran, D. Tokarz, B. A. Stewart, B. A. Stewart, V. Barzda, and V. Barzda, "Live imaging of contracting muscles with wide-field second harmonic generation microscopy using a high power laser," Biomed. Opt. Express **10**(10), 5130–5135 (2019).

84. M. Sivaguru, S. Durgam, R. Ambekar, D. Luedtke, G. Fried, A. Stewart, and K. C. Toussaint, "Quantitative analysis of collagen fiber organization in injured tendons using Fourier transform-second harmonic generation imaging," Opt. Express **18**(24), 24983–24993 (2010).

85. K. Gelse, E. Pöschl, and T. Aigner, "Collagens--structure, function, and biosynthesis," Adv. Drug Deliv. Rev. **55**(12), 1531–1546 (2003).

86. P. J. Campagnola, A. C. Millard, M. Terasaki, P. E. Hoppe, C. J. Malone, and W. A. Mohler, "Three-dimensional high-resolution second-harmonic generation imaging of endogenous structural proteins in biological tissues," Biophys. J. **82**(1 Pt 1), 493–508 (2002).

87. G. Cox, "Biological applications of second harmonic imaging," Biophys. Rev. **3**(3), 131 (2011).

88. I. Rocha-Mendoza, D. R. Yankelevich, M. Wang, K. M. Reiser, C. W. Frank, and A. Knoesen, "Sum Frequency Vibrational Spectroscopy: The Molecular Origins of the Optical Second-Order Nonlinearity of Collagen," Biophys. J. **93**(12), 4433–4444 (2007).

89. A. E. Tuer, S. Krouglov, N. Prent, R. Cisek, D. Sandkuijl, K. Yasufuku, B. C. Wilson, and V. Barzda, "Nonlinear Optical Properties of Type I Collagen Fibers Studied by Polarization Dependent Second Harmonic Generation Microscopy," J. Phys. Chem. B **115**(44), 12759–12769 (2011).

90. P. Stoller, B.-M. Kim, A. M. Rubenchik, K. M. Reiser, and L. B. Da Silva, "Polarization-dependent optical second-harmonic imaging of a rat-tail tendon," J. Biomed. Opt. **7**(2), 205–214 (2002).

91. S.-W. Chu, S.-Y. Chen, G.-W. Chern, T.-H. Tsai, Y.-C. Chen, B.-L. Lin, and C.-K. Sun, "Studies of χ(2)/χ(3) Tensors in Submicron-Scaled Bio-Tissues by Polarization Harmonics Optical Microscopy," Biophys. J. **86**(6), 3914–3922 (2004).

92. G. Latour, I. Gusachenko, L. Kowalczuk, I. Lamarre, and M.-C. Schanne-Klein, "In vivo structural imaging of the cornea by polarization-resolved second harmonic microscopy," Biomed. Opt. Express **3**(1), 1–15 (2012).

93. H. Lodish, A. Berk, S. L. Zipursky, P. Matsudaira, D. Baltimore, and J. Darnell, "Myosin: The Actin Motor Protein," Mol. Cell Biol. 4th Ed. (2000).

94. S. Schürmann, F. von Wegner, R. H. A. Fink, O. Friedrich, and M. Vogel, "Second harmonic generation microscopy probes different states of motor protein interaction in myofibrils," Biophys. J. **99**(6), 1842–1851 (2010).

95. "Myosin filament structure in vertebrate smooth muscle," J. Cell Biol. **134**(1), 53–66 (1996).

96. R. Craig and J. L. Woodhead, "Structure and function of myosin filaments," Curr. Opin. Struct. Biol. **16**(2), 204–212 (2006).

97. S. V. Plotnikov, A. C. Millard, P. J. Campagnola, and W. A. Mohler, "Characterization of the Myosin-Based Source for Second-Harmonic Generation from Muscle Sarcomeres," Biophys. J. **90**(2), 693–703 (2006).

98. C. Greenhalgh, N. Prent, C. Green, R. Cisek, A. Major, B. Stewart, and V. Barzda, "Influence of semicrystalline order on the second-harmonic generation efficiency in the anisotropic bands of myocytes," Appl. Opt. **46**(10), 1852–1859 (2007).

99. C. Odin, T. Guilbert, A. Alkilani, O. P. Boryskina, V. Fleury, and Y. L. Grand, "Collagen and myosin characterization by orientation field second harmonic microscopy," Opt. Express **16**(20), 16151–16165 (2008).

100. M. Rivard, C.-A. Couture, A. K. Miri, M. Laliberté, A. Bertrand-Grenier, L. Mongeau, and F. Légaré, "Imaging the bipolarity of myosin filaments with Interferometric Second Harmonic Generation microscopy," Biomed. Opt. Express **4**(10), 2078–2086 (2013).

101. S. J. Wallace, J. L. Morrison, K. J. Botting, and T. W. Kee, "Second-harmonic generation and two-photon-excited autofluorescence microscopy of cardiomyocytes: quantification of cell volume and myosin filaments," J. Biomed. Opt. **13**(6), 064018 (2008).

102. F. Tiaho, G. Recher, and D. Rouède, "Estimation of helical angles of myosin and collagen by second harmonic generation imaging microscopy," Opt. Express **15**(19), 12286–12295 (2007).

103. V. Nucciotti, C. Stringari, L. Sacconi, F. Vanzi, L. Fusi, M. Linari, G. Piazzesi, V. Lombardi, and F. S. Pavone, "Probing myosin structural conformation in vivo by second-harmonic generation microscopy," Proc. Natl. Acad. Sci. U. S. A. **107**(17), 7763–7768 (2010).

104. A. Buttgereit, C. Weber, C. S. Garbe, and O. Friedrich, "From chaos to split-ups--SHG microscopy reveals a specific remodelling mechanism in ageing dystrophic muscle," J. Pathol. **229**(3), 477–485 (2013).

105. Stufflebeam, Robert, "Neurons, Synapses, Action Potentials," https://mind.ilstu.edu/curriculum/neurons_intro/.

106. S. Fowler, R. Roush, and J. Wise, *Concepts of Biology*, Open Textbook Library (Open Textbook Library, 2013).

107. F. Zhang, L.-P. Wang, E. S. Boyden, and K. Deisseroth, "Channelrhodopsin-2 and optical control of excitable cells," Nat. Methods **3**(10), 785–792 (2006).

108. G. J. Stuart and L. M. Palmer, "Imaging membrane potential in dendrites and axons of single neurons," Pflugers Arch. **453**(3), 403–410 (2006).

109. P. J. Campagnola, H. A. Clark, W. A. Mohler, A. Lewis, and L. M. Loew, "Second-harmonic imaging microscopy of living cells," J. Biomed. Opt. **6**(3), 277–286 (2001).

110. B. A. Nemet, V. Nikolenko, and R. Yuste, "Second harmonic imaging of membrane potential of neurons with retinal," J. Biomed. Opt. **9**(5), 873–881 (2004).

111. D. A. Dombeck, L. Sacconi, M. Blanchard-Desce, and W. W. Webb, "Optical recording of fast neuronal membrane potential transients in acute mammalian brain slices by second-harmonic generation microscopy," J. Neurophysiol. **94**(5), 3628–3636 (2005).

112. M. Nuriya, J. Jiang, B. Nemet, K. B. Eisenthal, and R. Yuste, "Imaging membrane potential in dendritic spines," Proc. Natl. Acad. Sci. U. S. A. **103**(3), 786–790 (2006).

113. J. Jiang, K. B. Eisenthal, and R. Yuste, "Second harmonic generation in neurons: electro-optic mechanism of membrane potential sensitivity," Biophys. J. **93**(5), L26-8 (2007).

114. M. Nuriya and M. Yasui, "Membrane potential dynamics of axons in cultured hippocampal neurons probed by second-harmonic-generation imaging," J. Biomed. Opt. **15**(2), 020503 (2010).

115. J. Jiang and R. Yuste, "Second-harmonic generation imaging of membrane potential with photon counting," Microsc. Microanal. Off. J. Microsc. Soc. Am. Microbeam Anal. Soc. Microsc. Soc. Can. **14**(6), 526–531 (2008).

116. P. W. Baas, J. S. Deitch, M. M. Black, and G. A. Banker, "Polarity orientation of microtubules in hippocampal neurons: uniformity in the axon and nonuniformity in the dendrite," Proc. Natl. Acad. Sci. U. S. A. **85**(21), 8335–8339 (1988).

117. G. M. Alushin, G. C. Lander, E. H. Kellogg, R. Zhang, D. Baker, and E. Nogales, "High-resolution microtubule structures reveal the structural transitions in αβ-tubulin upon GTP hydrolysis," Cell **157**(5), 1117–1129 (2014).

118. P. W. Baas and S. Lin, "Hooks and comets: The story of microtubule polarity orientation in the neuron," Dev. Neurobiol. **71**(6), 403–418 (2011).

119. L. C. Kapitein and C. C. Hoogenraad, "Building the Neuronal Microtubule Cytoskeleton," Neuron **87**(3), 492–506 (2015).

120. T. Horio and T. Murata, "The role of dynamic instability in microtubule organization," Front. Plant Sci. **5**, 511 (2014).

121. D. A. Dombeck, K. A. Kasischke, H. D. Vishwasrao, M. Ingelsson, B. T. Hyman, and W. W. Webb, "Uniform polarity microtubule assemblies imaged in native brain tissue by second-harmonic generation microscopy," Proc. Natl. Acad. Sci. U. S. A. **100**(12), 7081–7086 (2003).

122. A. C. Kwan, D. A. Dombeck, and W. W. Webb, "Polarized microtubule arrays in apical dendrites and axons," Proc. Natl. Acad. Sci. U. S. A. **105**(32), 11370–11375 (2008).

123. V. Van Steenbergen, W. Boesmans, Z. Li, Y. de Coene, K. Vints, P. Baatsen, I. Dewachter, M. Ameloot, K. Clays, and P. Vanden Berghe, "Molecular understanding of label-free second harmonic imaging of microtubules," Nat. Commun. **10**(1), 3530 (2019).

124. A. Akhmanova and C. C. Hoogenraad, "Microtubule plus-end-tracking proteins: mechanisms and functions," Curr. Opin. Cell Biol. **17**(1), 47–54 (2005).

125. A. C. Kwan, "Second-Harmonic Generation Imaging of Microtubules," Second Harmon. Gener. Imaging 151–167 (2013).

126. S. Bancelin, C.-A. Couture, M. Pinsard, M. Rivard, P. Drapeau, and F. Légaré, "Probing microtubules polarity in mitotic spindles in situ using Interferometric Second Harmonic Generation Microscopy," Sci. Rep. **7**(1), 6758 (2017).

127. W. H. Stoothoff, B. J. Bacskai, and B. T. Hyman, "Monitoring tau-tubulin interactions utilizing second harmonic generation in living neurons," J. Biomed. Opt. **13**(6), 064039 (2008).

128. D. Raanan, M. S. Song, W. A. Tisdale, and D. Oron, "Super-resolved second harmonic generation imaging by coherent image scanning microscopy," Appl. Phys. Lett. **120**(7), 071111 (2022).

129. W. Wang, B. Wu, B. Zhang, Z. Zhang, X. Li, S. Zheng, Z. Fan, and J. Tan, "Second harmonic generation microscopy using pixel reassignment," J. Microsc. **281**(1), 97–105 (2021).

130. J. M. Bueno, F. J. Ávila, R. M. Martínez-Ojeda, and P. Artal, "Adaptive-Optics Polarization-Sensitive Second Harmonic Generation Microscopy," in *2020 22nd International Conference on Transparent Optical Networks (ICTON)* (2020), pp. 1–4.

131. J. Moon, S. Kang, J. H. Hong, S. Yoon, and W. Choi, "Synthetic aperture phase imaging of second harmonic generation field with computational adaptive optics," (2023).

132. B. A. Grubbs, N. P. Etter, W. E. Slaughter, A. M. Pittsford, C. R. Smith, and P. D. Schmitt, "A Low-Cost Beam-Scanning Second Harmonic Generation Microscope with Application for Agrochemical Development and Testing," Anal. Chem. **91**(18), 11723–11730 (2019).

133. E. Pshenay-Severin, H. Bae, K. Reichwald, G. Matz, J. Bierlich, J. Kobelke, A. Lorenz, A. Schwuchow, T. Meyer-Zedler, M. Schmitt, B. Messerschmidt, and J. Popp, "Multimodal nonlinear endomicroscopic imaging probe using a double-core double-clad fiber and focus-combining micro-optical concept," Light Sci. Appl. **10**(1), 207 (2021).

134. Y. LeCun, Y. Bengio, and G. Hinton, "Deep learning," Nature **521**(7553), 436–444 (2015).

135. I. Goodfellow, Y. Bengio, and A. Courville, *Deep Learning*, Illustrated edition (The MIT Press, 2016).

136. L. Alzubaidi, J. Zhang, A. J. Humaidi, A. Al-Dujaili, Y. Duan, O. Al-Shamma, J. Santamaría, M. A. Fadhel, M. Al-Amidie, and L. Farhan, "Review of deep learning: concepts, CNN architectures, challenges, applications, future directions," J. Big Data **8**(1), 1–74 (2021).

137. S. K. Melanthota, D. Gopal, S. Chakrabarti, A. A. Kashyap, R. Radhakrishnan, and N. Mazumder, "Deep learning-based image processing in optical microscopy," Biophys. Rev. **14**(2), 463–481 (2022).

138. W. S. McCulloch and W. Pitts, "A logical calculus of the ideas immanent in nervous activity," Bull. Math. Biophys. **5**(4), 115–133 (1943).

139. F. Rosenblatt, "The perceptron: A probabilistic model for information storage and organization in the brain," Psychol. Rev. **65**(6), 386–408 (1958).

140. P. Pradhan, S. Guo, O. Ryabchykov, J. Popp, and T. W. Bocklitz, "Deep learning a boon for biophotonics?," J. Biophotonics **13**(6), e201960186 (2020).

141. N. F. Sopelsa Neto, S. F. Stefenon, L. H. Meyer, R. Bruns, A. Nied, L. O. Seman, G. V. Gonzalez, V. R. Q. Leithardt, and K.-C. Yow, "A Study of Multilayer Perceptron Networks Applied to Classification of Ceramic Insulators Using Ultrasound," Appl. Sci. **11**(4), 1592 (2021).

142. Y. Le Cun, L. D. Jackel, B. Boser, J. S. Denker, H. P. Graf, I. Guyon, D. Henderson, R. E. Howard, and W. Hubbard, "Handwritten digit recognition: applications of neural network chips and automatic learning," IEEE Commun. Mag. **27**(11), 41–46 (1989).

143. Z. C. Lipton, J. Berkowitz, and C. Elkan, "A Critical Review of Recurrent Neural Networks for Sequence Learning," (2015).

144. J. Mao, W. Xu, Y. Yang, J. Wang, Z. Huang, and A. Yuille, "Deep Captioning with Multimodal Recurrent Neural Networks (m-RNN)," (2015).

145. R. Socher, A. Perelygin, J. Wu, J. Chuang, C. D. Manning, A. Ng, and C. Potts, "Recursive Deep Models for Semantic Compositionality Over a Sentiment Treebank," in *Proceedings of the 2013 Conference on Empirical Methods in Natural Language Processing*, D. Yarowsky, T. Baldwin, A. Korhonen, K. Livescu, and S. Bethard, eds. (Association for Computational Linguistics, 2013), pp. 1631–1642.

146. K. Cho, B. van Merriënboer, C. Gulcehre, D. Bahdanau, F. Bougares, H. Schwenk, and Y. Bengio, "Learning Phrase Representations using RNN Encoder–Decoder for Statistical Machine Translation," in *Proceedings of the 2014 Conference on Empirical Methods in Natural*

Language Processing (EMNLP), A. Moschitti, B. Pang, and W. Daelemans, eds. (Association for Computational Linguistics, 2014), pp. 1724–1734.

147. S. Albelwi and A. Mahmood, "A Framework for Designing the Architectures of Deep Convolutional Neural Networks," Entropy **19**(6), 242 (2017).

148. I. Goodfellow, J. Pouget-Abadie, M. Mirza, B. Xu, D. Warde-Farley, S. Ozair, A. Courville, and Y. Bengio, "Generative Adversarial Nets," in *Advances in Neural Information Processing Systems* (Curran Associates, Inc., 2014), **27**.

149. M. Abedi, L. Hempel, S. Sadeghi, and T. Kirsten, "GAN-Based Approaches for Generating Structured Data in the Medical Domain," Appl. Sci. **12**(14), 7075 (2022).

150. L. Mescheder, A. Geiger, and S. Nowozin, "Which Training Methods for GANs do actually Converge?," (2018).

151. J. A. Nichols, H. W. Herbert Chan, and M. A. B. Baker, "Machine learning: applications of artificial intelligence to imaging and diagnosis," Biophys. Rev. **11**(1), 111–118 (2018).

152. F. Xing, Y. Xie, H. Su, F. Liu, and L. Yang, "Deep Learning in Microscopy Image Analysis: A Survey," IEEE Trans. Neural Netw. Learn. Syst. **29**(10), 4550–4568 (2018).

153. H. Lee, R. Grosse, R. Ranganath, and A. Y. Ng, "Convolutional deep belief networks for scalable unsupervised learning of hierarchical representations," in *Proceedings of the 26th Annual International Conference on Machine Learning* (ACM, 2009), pp. 609–616.

154. Y. V. Kistenev, V. V. Nikolaev, O. S. Kurochkina, A. V. Borisov, D. A. Vrazhnov, and E. A. Sandykova, "Application of multiphoton imaging and machine learning to lymphedema tissue analysis," Biomed. Opt. Express **10**(7), 3353–3368 (2019).

155. M. J. Huttunen, A. Hassan, C. W. McCloskey, S. Fasih, J. Upham, B. C. Vanderhyden, R. W. Boyd, and S. Murugkar, "Automated classification of multiphoton microscopy images of ovarian tissue using deep learning," J. Biomed. Opt. **23**(6), 1–7 (2018).

156. K. Mirsanaye, L. Uribe Castaño, Y. Kamaliddin, A. Golaraei, R. Augulis, L. Kontenis, S. J. Done, E. Žurauskas, V. Stambolic, B. C. Wilson, and V. Barzda, "Machine learning-enabled cancer diagnostics with widefield polarimetric second-harmonic generation microscopy," Sci. Rep. **12**(1), 10290 (2022).

157. B. Shen, S. Liu, Y. Li, Y. Pan, Y. Lu, R. Hu, J. Qu, and L. Liu, "Deep learning autofluorescence-harmonic microscopy," Light Sci. Appl. **11**(1), 76 (2022).

158. A. Aghigh, S. E. J. Preston, G. Jargot, H. Ibrahim, S. V. Del Rincón, and F. Légaré, "Nonlinear microscopy and deep learning classification for mammary gland microenvironment studies," Biomed. Opt. Express **14**(5), 2181–2195 (2023).

159. A. Mikołajczyk and M. Grochowski, "Data augmentation for improving deep learning in image classification problem," in *2018 International Interdisciplinary PhD Workshop (IIPhDW)* (2018), pp. 117–122.

160. Z. Gao, L. Wang, L. Zhou, and J. Zhang, "HEp-2 Cell Image Classification With Deep Convolutional Neural Networks," IEEE J. Biomed. Health Inform. **21**(2), 416–428 (2017).

161. C. L. Chen, A. Mahjoubfar, L.-C. Tai, I. K. Blaby, A. Huang, K. R. Niazi, and B. Jalali, "Deep Learning in Label-free Cell Classification," Sci. Rep. **6**(1), 21471 (2016).

162. K. J. Halupka, B. J. Antony, M. H. Lee, K. A. Lucy, R. S. Rai, H. Ishikawa, G. Wollstein, J. S. Schuman, and R. Garnavi, "Retinal optical coherence tomography image enhancement via deep learning," Biomed. Opt. Express **9**(12), 6205–6221 (2018).

163. Y. Ma, X. Chen, W. Zhu, X. Cheng, D. Xiang, and F. Shi, "Speckle noise reduction in optical coherence tomography images based on edge-sensitive cGAN," Biomed. Opt. Express **9**(11), 5129–5146 (2018).

164. C. Belthangady and L. A. Royer, "Applications, promises, and pitfalls of deep learning for fluorescence image reconstruction," Nat. Methods **16**(12), 1215–1225 (2019).

165. T.-O. Buchholz, A. Krull, R. Shahidi, G. Pigino, G. Jékely, and F. Jug, "Chapter 13 - Content-aware image restoration for electron microscopy," in *Methods in Cell Biology*, T. Müller-Reichert and G. Pigino, eds., Three-Dimensional Electron Microscopy (Academic Press, 2019), **152**, pp. 277–289.

166. A. Krull, T.-O. Buchholz, and F. Jug, "Noise2Void - Learning Denoising from Single Noisy Images," (2019).

167. H. E. Kim, A. Cosa-Linan, N. Santhanam, M. Jannesari, M. E. Maros, and T. Ganslandt, "Transfer learning for medical image classification: a literature review," BMC Med. Imaging **22**(1), 69 (2022).

168. K. Weiss, T. M. Khoshgoftaar, and D. Wang, "A survey of transfer learning," J. Big Data **3**(1), 9 (2016).

169. S. G. Stanciu, F. J. Ávila, R. Hristu, and J. M. Bueno, "A Study on Image Quality in Polarization-Resolved Second Harmonic Generation Microscopy," Sci. Rep. **7**(1), 15476 (2017).

170. S. A. Barman, R. A. Welikala, A. R. Rudnicka, and C. G. Owen, "Chapter 8 - Image quality assessment," in *Computational Retinal Image Analysis*, E. Trucco, T. MacGillivray, and Y. Xu, eds., The Elsevier and MICCAI Society Book Series (Academic Press, 2019), pp. 135–155.

171. M. Pedersen, "Full-Reference Image Quality Metrics: Classification and Evaluation," Found. Trends® Comput. Graph. Vis. **7**(1), 1–80 (2011).

172. V. Kamble and K. M. Bhurchandi, "No-reference image quality assessment algorithms: A survey," Optik **126**(11–12), 1090–1097 (2015).

173. A. Mittal, A. K. Moorthy, and A. C. Bovik, "No-Reference Image Quality Assessment in the Spatial Domain," IEEE Trans. Image Process. **21**(12), 4695–4708 (2012).

174. A. Rubel, O. Ieremeiev, V. Lukin, J. Fastowicz, and K. Okarma, "Combined No-Reference Image Quality Metrics for Visual Quality Assessment Optimized for Remote Sensing Images," Appl. Sci. **12**(4), 1986 (2022).

175. Z. Wang, A. C. Bovik, H. R. Sheikh, and E. P. Simoncelli, "Image quality assessment: from error visibility to structural similarity," IEEE Trans. Image Process. **13**(4), 600–612 (2004).

176. Z. Wang and A. C. Bovik, "Mean squared error: Love it or leave it? A new look at Signal Fidelity Measures," IEEE Signal Process. Mag. **26**(1), 98–117 (2009).

177. U. Sara, M. Akter, and M. S. Uddin, "Image Quality Assessment through FSIM, SSIM, MSE and PSNR—A Comparative Study," J. Comput. Commun. **07**(03), 8–18 (2019).

178. Z. Wang, E. P. Simoncelli, and A. C. Bovik, "Multiscale structural similarity for image quality assessment," in *The Thrity-Seventh Asilomar Conference on Signals, Systems & Computers, 2003* (2003), **2**, pp. 1398-1402 Vol.2.

179. M. P. Sampat, Z. Wang, S. Gupta, A. C. Bovik, and M. K. Markey, "Complex Wavelet Structural Similarity: A New Image Similarity Index," IEEE Trans. Image Process. **18**(11), 2385–2401 (2009).

180. J. Nilsson and T. Akenine-Möller, "Understanding SSIM," (2020).

181. V. Mudeng, M. Kim, and S. Choe, "Prospects of Structural Similarity Index for Medical Image Analysis," Appl. Sci. **12**(8), 3754 (2022).

182. J.-F. Pambrun and R. Noumeir, "Limitations of the SSIM quality metric in the context of diagnostic imaging," in *2015 IEEE International Conference on Image Processing (ICIP)* (2015), pp. 2960–2963.

183. A. Mittal, R. Soundararajan, and A. C. Bovik, "Making a “Completely Blind” Image Quality Analyzer," IEEE Signal Process. Lett. **20**(3), 209–212 (2013).

184. Venkatanath N, Praneeth D, Maruthi Chandrasekhar Bh, S. S. Channappayya, and S. S. Medasani, "Blind image quality evaluation using perception based features," in *2015 Twenty First National Conference on Communications (NCC)* (IEEE, 2015), pp. 1–6.

185. G. Hall, W. Liang, and X. Li, "Fitting-free algorithm for efficient quantification of collagen fiber alignment in SHG imaging applications," Biomed. Opt. Express **8**(10), 4609–4620 (2017).

186. B. Qiu, Z. Huang, X. Liu, X. Meng, Y. You, G. Liu, K. Yang, A. Maier, Q. Ren, and Y. Lu, "Noise reduction in optical coherence tomography images using a deep neural network with perceptually-sensitive loss function," Biomed. Opt. Express **11**(2), 817–830 (2020).

187. S. Lee, M. Negishi, H. Urakubo, H. Kasai, and S. Ishii, "Mu-net: Multi-scale U-net for two-photon microscopy image denoising and restoration," Neural Netw. **125**, 92–103 (2020).

188. M. J. Anzanello and F. S. Fogliatto, "Learning curve models and applications: Literature review and research directions," Int. J. Ind. Ergon. **41**(5), 573–583 (2011).

189. L. von Chamier, R. F. Laine, J. Jukkala, C. Spahn, D. Krentzel, E. Nehme, M. Lerche, S. Hernández-Pérez, P. K. Mattila, E. Karinou, S. Holden, A. C. Solak, A. Krull, T.-O. Buchholz, M. L. Jones, L. A. Royer, C. Leterrier, Y. Shechtman, F. Jug, M. Heilemann, G. Jacquemet, and R. Henriques, "Democratising deep learning for microscopy with ZeroCostDL4Mic," Nat. Commun. **12**(1), 2276 (2021).

190. F. Helmchen and W. Denk, "Deep tissue two-photon microscopy," Nat. Methods **2**(12), 932–940 (2005).

191. A. C. Millard, P. J. Campagnola, W. Mohler, A. Lewis, and L. M. Loew, "Second harmonic imaging microscopy," in *Biophotonics. Pt. B*, G. Marriott and I. Parker, eds., Methods in Enzymology No. v. 361 (Academic Press, 2003), **361**, pp. 47–69.

192. P. W. Smith, M. A. Duguay, and E. P. Ippen, *Mode-Locking of Lasers* (Elsevier Science & Technology Books, 1974).

193. W. E. Lamb, "Theory of an Optical Maser," Phys. Rev. **134**(6A), A1429–A1450 (1964).

194. J. W. Strutt, *The Theory of Sound*, Cambridge Library Collection - Physical Sciences (Cambridge University Press, 2011), **1**.

195. N. Bloembergen, "Nonlinear Optics: past, present and future," in *Guided Wave Nonlinear Optics*, D. B. Ostrowsky and R. Reinisch, eds., NATO ASI Series (Springer Netherlands, 1992), pp. 1–9.

196. B. R. Masters and P. T. C. So, eds., *Handbook of Biomedical Nonlinear Optical Microscopy* (Oxford University Press, 2008).

197. M. Göppert-Mayer, "Über Elementarakte mit zwei Quantensprüngen," Ann. Phys. **401**(3), 273–294 (1931).

198. A. E. Siegman, *Lasers* (University Science Books, 1986).

199. E. Fukada and I. Yasuda, "Piezoelectric Effects in Collagen," Jpn. J. Appl. Phys. **3**(2), 117 (1964).

200. S. B. Lang, "Pyroelectric Effect in Bone and Tendon," Nature **212**(5063), 704–705 (1966).

201. A. Schuldt, "Seeing the wood for the trees: Concept of confocal microscopy, Realization of confocal microscopy," Nat. Cell Biol. **11**(S1), S12–S13 (2009).

202. S. W. Hell, K. Bahlmann, M. Schrader, A. Soini, H. M. Malak, I. Gryczynski, and J. R. Lakowicz, "Three-photon excitation in fluorescence microscopy," J. Biomed. Opt. **1**(1), 71–74 (1996).

203. W. R. Zipfel, R. M. Williams, and W. W. Webb, "Nonlinear magic: multiphoton microscopy in the biosciences," Nat. Biotechnol. **21**(11), 1369–1377 (2003).

204. P. Campagnola, "Second Harmonic Generation Imaging Microscopy: Applications to Diseases Diagnostics," Anal. Chem. **83**(9), 3224–3231 (2011).

205. G. Hall, K. B. Tilbury, K. R. Campbell, K. W. Eliceiri, and P. J. Campagnola, "Experimental and simulation study of the wavelength dependent second harmonic generation of collagen in scattering tissues," Opt. Lett. **39**(7), 1897–1900 (2014).

206. S.-W. Chu, I.-H. Chen, T.-M. Liu, P. C. Chen, C.-K. Sun, and B.-L. Lin, "Multimodal nonlinear spectral microscopy based on a femtosecond Cr:forsterite laser," Opt. Lett. **26**(23), 1909–1911 (2001).

207. I. Gusachenko, V. Tran, Y. G. Houssen, J.-M. Allain, and M.-C. Schanne-Klein, "Polarization-Resolved Second-Harmonic Generation in Tendon upon Mechanical Stretching," Biophys. J. **102**(9), 2220–2229 (2012).

208. S. Bancelin, "Quantitative Imaging of Collagen by Second Harmonic Generation," Ecole Polytechnique (2014).

209. F. S. Pavone and P. J. Campagnola, eds., *Second Harmonic Generation Imaging* (CRC Press, 2013).

210. F. Légaré, C. Pfeffer, and B. R. Olsen, "The role of backscattering in SHG tissue imaging," Biophys. J. **93**(4), 1312–1320 (2007).

211. E. Hase, T. Minamikawa, K. Sato, D. Yonekura, M. Takahashi, and T. Yasui, "Observation of Tendon Healing with Second-harmonic-generation (SHG) Microscopy," Trans. Jpn. Soc. Med. Biol. Eng. **54**(6), 253–260 (2016).

212. Laboratoires Servier, *Collagen Trimerlabel* (2019).

213. N. Morishige, Y. Takagi, T. Chikama, A. Takahara, and T. Nishida, "Three-Dimensional Analysis of Collagen Lamellae in the Anterior Stroma of the Human Cornea Visualized by Second Harmonic Generation Imaging Microscopy," Invest. Ophthalmol. Vis. Sci. **52**(2), 911–915 (2011).

214. M. Rivard, K. Popov, C.-A. Couture, M. Laliberté, A. Bertrand-Grenier, F. Martin, H. Pépin, C. P. Pfeffer, C. Brown, L. Ramunno, and F. Légaré, "Imaging the noncentrosymmetric structural organization of tendon with Interferometric Second Harmonic Generation microscopy," J. Biophotonics **7**(8), 638–646 (2014).

215. L. Mostaço-Guidolin, N. L. Rosin, and T.-L. Hackett, "Imaging Collagen in Scar Tissue: Developments in Second Harmonic Generation Microscopy for Biomedical Applications," Int. J. Mol. Sci. **18**(8), 1772 (2017).

216. J. M. Bueno, F. J. Ávila, and P. Artal, "Second Harmonic Generation Microscopy: A Tool for Quantitative Analysis of Tissues," in *Microscopy and Analysis*, S. G. Stanciu, ed. (InTech, 2016).

217. S.-W. Teng, H.-Y. Tan, J.-L. Peng, H.-H. Lin, K. H. Kim, W. Lo, Y. Sun, W.-C. Lin, S.-J. Lin, S.-H. Jee, P. T. C. So, and C.-Y. Dong, "Multiphoton autofluorescence and second-harmonic generation imaging of the ex vivo porcine eye," Invest. Ophthalmol. Vis. Sci. **47**(3), 1216–1224 (2006).

218. Y. Ogura, Y. Tanaka, E. Hase, T. Yamashita, and T. Yasui, "Texture analysis of second-harmonic-generation images for quantitative analysis of reticular dermal collagen fibre in vivo in human facial cheek skin," Exp. Dermatol. **28**(8), 899–905 (2019).

219. M. Han, G. Giese, and J. Bille, "Second harmonic generation imaging of collagen fibrils in cornea and sclera," Opt. Express **13**(15), 5791–5797 (2005).

220. A. T. Yeh, M. J. Hammer-Wilson, D. C. Van Sickle, H. P. Benton, A. Zoumi, B. J. Tromberg, and G. M. Peavy, "Nonlinear optical microscopy of articular cartilage," Osteoarthritis Cartilage **13**(4), 345–352 (2005).

221. M.-A. Houle, C. Couture, S. Bancelin, J. van der Kolk, É. Auger, C. Brown, K. Popov, L. Ramunno, and F. Légaré, "Analysis of forward and backward Second Harmonic Generation images to probe the nanoscale structure of collagen within bone and cartilage," J. Biophotonics (2015).

222. P. Stoller, P. M. Celliers, K. M. Reiser, and A. M. Rubenchik, "Quantitative second-harmonic generation microscopy in collagen," Appl. Opt. **42**(25), 5209–5219 (2003).

223. S. E. J. Preston, M. Bartish, V. R. Richard, A. Aghigh, C. Gonçalves, J. Smith-Voudouris, F. Huang, P. Thebault, A. Cleret-Buhot, R. Lapointe, F. Légaré, L.-M. Postovit, R. P. Zahedi, C. H. Borchers, W. H. Miller, and S. V. Del Rincón, "Phosphorylation of eIF4E in the stroma drives the production and spatial organisation of collagen type I in the mammary gland," Matrix Biol. J. Int. Soc. Matrix Biol. S0945-053X(22)00092–0 (2022).

224. H. Lodish, A. Berk, S. L. Zipursky, P. Matsudaira, D. Baltimore, and J. Darnell, *Molecular Cell Biology*, 4th ed. (W. H. Freeman, 2000).

225. E. Ralston, B. Swaim, M. Czapiga, W.-L. Hwu, Y.-H. Chien, M. G. Pittis, B. Bembi, O. Schwartz, P. Plotz, and N. Raben, "Detection and imaging of non-contractile inclusions and sarcomeric anomalies in skeletal muscle by second harmonic generation combined with two-photon excited fluorescence," J. Struct. Biol. **162**(3), 500–508 (2008).

226. C. P. Pfeffer, B. R. Olsen, F. Ganikhanov, and F. Légaré, "Imaging skeletal muscle using second harmonic generation and coherent anti-Stokes Raman scattering microscopy," Biomed. Opt. Express **2**(5), 1366–1376 (2011).

227. G. Cox, N. Moreno, and J. Feijó, "Second-harmonic imaging of plant polysaccharides," J. Biomed. Opt. **10**(2), 024013 (2005).

228. Z.-Y. Zhuo, C.-S. Liao, C.-H. Huang, J.-Y. Yu, Y.-Y. Tzeng, W. Lo, C.-Y. Dong, H.-C. Chui, Y.-C. Huang, H.-M. Lai, and S.-W. Chu, "Second harmonic generation imaging – A new method for unraveling molecular information of starch," J. Struct. Biol. **171**(1), 88–94 (2010).

229. R. Cisek, D. Tokarz, M. Steup, I. J. Tetlow, M. J. Emes, K. H. Hebelstrup, A. Blennow, and V. Barzda, "Second harmonic generation microscopy investigation of the crystalline ultrastructure

of three barley starch lines affected by hydration," Biomed. Opt. Express **6**(10), 3694–3700 (2015).

230. R. Cisek, D. Tokarz, S. Krouglov, M. Steup, M. J. Emes, I. J. Tetlow, and V. Barzda, "Second Harmonic Generation Mediated by Aligned Water in Starch Granules," J. Phys. Chem. B **118**(51), 14785–14794 (2014).

231. BP-Aegirsson, "Wikiwand-Second-harmonic generation," https://wikiwand.com/en/Second_harmonic_generation.

232. M. Rivard, M. Laliberté, A. Bertrand-Grenier, C. Harnagea, C. P. Pfeffer, M. Vallières, Y. St-Pierre, A. Pignolet, M. A. El Khakani, and F. Légaré, "The structural origin of second harmonic generation in fascia," Biomed. Opt. Express **2**(1), 26–36 (2010).

233. C. P. Brown, M.-A. Houle, K. Popov, M. Nicklaus, C.-A. Couture, M. Laliberté, T. Brabec, A. Ruediger, A. J. Carr, A. J. Price, H. S. Gill, L. Ramunno, and F. Légaré, "Imaging and modeling collagen architecture from the nano to micro scale," Biomed. Opt. Express **5**(1), 233–243 (2013).

234. M. Pinsard, S. Laverty, H. Richard, J. Dubuc, M.-C. Schanne-Klein, and F. Légaré, "Maturation of the Meniscal Collagen Structure Revealed by Polarization-Resolved and Directional Second Harmonic Generation Microscopy," Sci. Rep. **9**(1), 18448 (2019).

235. S. Psilodimitrakopoulos, V. Petegnief, G. Soria, I. Amat-Roldan, D. Artigas, A. M. Planas, and P. Loza-Alvarez, "Estimation of the effective orientation of the SHG source in primary cortical neurons," Opt. Express **17**(16), 14418–14425 (2009).

236. G. Ducourthial, J.-S. Affagard, M. Schmeltz, X. Solinas, M. Lopez-Poncelas, C. Bonod-Bidaud, R. Rubio-Amador, F. Ruggiero, J.-M. Allain, E. Beaurepaire, and M.-C. Schanne-Klein, "Monitoring dynamic collagen reorganization during skin stretching with fast polarization-resolved second harmonic generation imaging," J. Biophotonics **12**(5), e201800336 (2019).

237. R. Hristu, S. G. Stanciu, D. E. Tranca, and G. A. Stanciu, "Improved quantification of collagen anisotropy with polarization-resolved second harmonic generation microscopy," J. Biophotonics **10**(9), 1171–1179 (2017).

238. A. E. Tuer, M. K. Akens, S. Krouglov, D. Sandkuijl, B. C. Wilson, C. M. Whyne, and V. Barzda, "Hierarchical model of fibrillar collagen organization for interpreting the second-order susceptibility tensors in biological tissue," Biophys. J. **103**(10), 2093–2105 (2012).

239. T. Verbiest, S. van Elshocht, S. Sioncke, M. Kauranen, A. Persoons, and K. U. Leuven, "Circular-difference effects in second-harmonic generation from thin films," in 1999 Technical Digest Series (Optical Society of America, 1999), p. SaD3.

240. M. Schmeltz, C. Teulon, G. Latour, D. Ghoubay, V. Borderie, C. Aimé, and M.-C. Schanne-Klein, "Implementation of artifact-free circular dichroism SHG imaging of collagen," Opt. Express **27**(16), 22685–22699 (2019).

241. M. Schmeltz, C. Teulon, M. Pinsard, U. Hansen, M. Alnawaiseh, D. Ghoubay, V. Borderie, G. Mosser, C. Aimé, C. Aimé, F. Légaré, G. Latour, G. Latour, and M.-C. Schanne-Klein, "Circular dichroism second-harmonic generation microscopy probes the polarity distribution of collagen fibrils," Optica **7**(11), 1469–1476 (2020).

242. M. Pinsard, "Multimodal and Advanced Interferometric Second Harmonic Generation Microscopy for an Improved Characterization of Biopolymers in Cells and Tissues," (2020).

243. N. Mazumder, J. Qiu, M. R. Foreman, C. M. Romero, C.-W. Hu, H.-R. Tsai, P. Török, and F.-J. Kao, "Polarization-resolved second harmonic generation microscopy with a four-channel Stokes-polarimeter," Opt. Express **20**(13), 14090–14099 (2012).

244. J. Qiu, N. Mazumder, H.-R. Tsai, C.-W. Hu, and F.-J. Kao, "Stokes vector formalism based second harmonic generation microscopy," in *Single Molecule Spectroscopy and Superresolution Imaging V* (SPIE, 2012), **8228**, pp. 69–76.

245. N. Mazumder, L. Y. Xiang, J. Qiu, and F.-J. Kao, "Investigating starch gelatinization through Stokes vector resolved second harmonic generation microscopy," Sci. Rep. **7**(1), 45816 (2017).

246. N. Mazumder and F.-J. Kao, "Stokes polarimetry-based second harmonic generation microscopy for collagen and skeletal muscle fiber characterization," Lasers Med. Sci. **36**(6), 1161–1167 (2021).

247. L. Kontenis, M. Samim, A. Karunendiran, S. Krouglov, B. Stewart, and V. Barzda, "Second harmonic generation double stokes Mueller polarimetric microscopy of myofilaments," Biomed. Opt. Express **7**(2), 559–569 (2016).

248. M. Samim, S. Krouglov, and V. Barzda, "Double Stokes Mueller polarimetry of second-harmonic generation in ordered molecular structures," JOSA B **32**(3), 451–461 (2015).

249. M. Pinsard, M. Schmeltz, J. van der Kolk, S. A. Patten, H. Ibrahim, L. Ramunno, M.-C. Schanne-Klein, and F. Légaré, "Elimination of imaging artifacts in second harmonic generation microscopy using interferometry," Biomed. Opt. Express **10**(8), 3938–3952 (2019).

250. M. Rivard, C.-A. Couture, A. K. Miri, M. Laliberté, A. Bertrand-Grenier, L. Mongeau, and F. Légaré, "Imaging the bipolarity of myosin filaments with Interferometric Second Harmonic Generation microscopy," Biomed. Opt. Express **4**(10), 2078–2086 (2013).

251. S. Bancelin, C.-A. Couture, K. Légaré, M. Pinsard, M. Rivard, C. Brown, and F. Légaré, "Fast interferometric second harmonic generation microscopy," Biomed. Opt. Express **7**(2), 399–408 (2016).

252. P. T. C. So, E. Y. S. Yew, and C. Rowlands, "High-Throughput Nonlinear Optical Microscopy," Biophys. J. **105**(12), 2641–2654 (2013).

253. Y. Shao, H. Liu, W. Qin, J. Qu, X. Peng, H. Niu, and B. Z. Gao, "Addressable, large-field second harmonic generation microscopy based on 2D acousto-optical deflector and spatial light modulator," Appl. Phys. B **108**(4), 713–716 (2012).

254. N. D. Kirkpatrick, E. Chung, D. C. Cook, X. Han, G. Gruionu, S. Liao, L. L. Munn, T. P. Padera, D. Fukumura, and R. K. Jain, "Video-rate resonant scanning multiphoton microscopy," Intravital Print **1**(1), 10.4161/intv.21557 (2012).

255. H. Zhao, H. Zhao, H. Zhao, H. Zhao, R. Cisek, R. Cisek, A. Karunendiran, A. Karunendiran, D. Tokarz, B. A. Stewart, B. A. Stewart, V. Barzda, and V. Barzda, "Live imaging of contracting muscles with wide-field second harmonic generation microscopy using a high power laser," Biomed. Opt. Express **10**(10), 5130–5135 (2019).

256. E. Shaffer, P. Marquet, and C. Depeursinge, "Real time, nanometric 3D-tracking of nanoparticles made possible by second harmonic generation digital holographic microscopy," Opt. Express **18**(16), 17392–17403 (2010).

257. E. Shaffer, C. Moratal, P. Magistretti, P. Marquet, and C. Depeursinge, "Label-free second-harmonic phase imaging of biological specimen by digital holographic microscopy," Opt. Lett. **35**(24), 4102–4104 (2010).

258. J. Wu, N. Ji, and K. K. Tsia, "Speed scaling in multiphoton fluorescence microscopy," Nat. Photonics **15**(11), 800–812 (2021).

259. Neuron description, *English: Neuron Description.* (2019).

260. P. W. Baas and S. Lin, "Hooks and comets: The story of microtubule polarity orientation in the neuron," Dev. Neurobiol. **71**(6), 403–418 (2011).

261. V. van Steenbergen, W. Boesmans, Z. Li, Y. Coene, K. Vints, P. Baatsen, I. Dewachter, M. Ameloot, K. Clays, and P. Vanden Berghe, "Molecular understanding of label-free second harmonic imaging of microtubules," Nat. Commun. **10**(1), 3530 (2019).

262. C.-H. Yu, N. Langowitz, H.-Y. Wu, R. Farhadifar, J. Brugues, T. Y. Yoo, and D. Needleman, "Measuring Microtubule Polarity in Spindles with Second-Harmonic Generation," Biophys. J. **106**(8), 1578–1587 (2014).

263. W. H. Stoothoff, B. J. Bacskai, and B. T. Hyman, "Monitoring tau-tubulin interactions utilizing second harmonic generation in living neurons," J. Biomed. Opt. **13**(6), 064039 (2008).

264. K. Brittain, M. Harvey, R. Cisek, S. Pillai, S. D. Christie, and D. Tokarz, "Second harmonic generation microscopy of otoconia," Biomed. Opt. Express **13**(6), 3593–3600 (2022).

265. M. Alata, V. Piazza, C. Jaramillo-Restrepo, J. R. Eguibar, C. Cortes, and V. H. Hernandez, "H-ABC tubulinopathy revealed by label-free second harmonic generation microscopy," Sci. Rep. **12**(1), 14417 (2022).

266. V. Nikolenko, B. Watson, R. Araya, A. Woodruff, D. Peterka, and R. Yuste, "SLM microscopy: scanless two-photon imaging and photostimulation using spatial light modulators," Front. Neural Circuits **2**, (2008).

267. A. Hanninen, M. W. Shu, and E. O. Potma, "Hyperspectral imaging with laser-scanning sum-frequency generation microscopy," Biomed. Opt. Express **8**(9), 4230–4242 (2017).

268. V. Kučikas, M. P. Werner, T. Schmitz-Rode, F. Louradour, and M. A. M. J. van Zandvoort, "Two-Photon Endoscopy: State of the Art and Perspectives," Mol. Imaging Biol. (2021).

269. K. Mirsanaye, L. U. Castaño, Y. Kamaliddin, A. Golaraei, R. Augulis, L. Kontenis, S. J. Done, E. Žurauskas, B. C. Wilson, and V. Barzda, *Machine Learning-Enabled Cancer Diagnostics with Widefield Polarimetric Second-Harmonic Generation Microscopy* (2021), p. 2021.05.26.445874.

270. L. Bejarano, M. J. C. Jordão, and J. A. Joyce, "Therapeutic Targeting of the Tumor Microenvironment," Cancer Discov. **11**(4), 933–959 (2021).

271. E. A. Brett, M. A. Sauter, H.-G. Machens, and D. Duscher, "Tumor-associated collagen signatures: pushing tumor boundaries," Cancer Metab. **8**(1), 1–5 (2020).

272. S. Xu, H. Xu, W. Wang, S. Li, H. Li, T. Li, W. Zhang, X. Yu, and L. Liu, "The role of collagen in cancer: from bench to bedside," J. Transl. Med. **17**(1), 309 (2019).

273. M. W. Conklin, J. C. Eickhoff, K. M. Riching, C. A. Pehlke, K. W. Eliceiri, P. P. Provenzano, A. Friedl, and P. J. Keely, "Aligned collagen is a prognostic signature for survival in human breast carcinoma," Am. J. Pathol. **178**(3), 1221–1232 (2011).

274. K.-S. Hsu, J. M. Dunleavey, C. Szot, L. Yang, M. B. Hilton, K. Morris, S. Seaman, Y. Feng, E. M. Lutz, R. Koogle, F. Tomassoni-Ardori, S. Saha, X. M. Zhang, E. Zudaire, P. Bajgain, J. Rose, Z. Zhu, D. S. Dimitrov, F. Cuttitta, N. J. Emenaker, L. Tessarollo, and B. St. Croix, "Cancer cell survival depends on collagen uptake into tumor-associated stroma," Nat. Commun. **13**(1), 7078 (2022).

275. K. Song, Z. Yu, X. Zu, G. Li, Z. Hu, and Y. Xue, "Collagen Remodeling along Cancer Progression Providing a Novel Opportunity for Cancer Diagnosis and Treatment," Int. J. Mol. Sci. **23**(18), 10509 (2022).

276. W. Han, S. Chen, W. Yuan, Q. Fan, J. Tian, X. Wang, L. Chen, X. Zhang, W. Wei, R. Liu, J. Qu, Y. Jiao, R. H. Austin, and L. Liu, "Oriented collagen fibers direct tumor cell intravasation," Proc. Natl. Acad. Sci. **113**(40), 11208–11213 (2016).

277. D. Chen, H. Chen, L. Chi, M. Fu, G. Wang, Z. Wu, S. Xu, C. Sun, X. Xu, L. Lin, J. Cheng, W. Jiang, X. Dong, J. Lu, J. Zheng, G. Chen, G. Li, S. Zhuo, and J. Yan, "Association of Tumor-Associated Collagen Signature With Prognosis and Adjuvant Chemotherapy Benefits in Patients With Gastric Cancer," JAMA Netw. Open **4**(11), e2136388 (2021).

278. J. N. Ouellette, C. R. Drifka, K. B. Pointer, Y. Liu, T. J. Lieberthal, W. J. Kao, J. S. Kuo, A. G. Loeffler, and K. W. Eliceiri, "Navigating the Collagen Jungle: The Biomedical Potential of Fiber Organization in Cancer," Bioengineering **8**(2), 17 (2021).

279. A. Ray, Z. M. Slama, R. K. Morford, S. A. Madden, and P. P. Provenzano, "Enhanced Directional Migration of Cancer Stem Cells in 3D Aligned Collagen Matrices," Biophys. J. **112**(5), 1023–1036 (2017).

280. K. M. Riching, B. L. Cox, M. R. Salick, C. Pehlke, A. S. Riching, S. M. Ponik, B. R. Bass, W. C. Crone, Y. Jiang, A. M. Weaver, K. W. Eliceiri, and P. J. Keely, "3D collagen alignment limits protrusions to enhance breast cancer cell persistence," Biophys. J. **107**(11), 2546–2558 (2014).

281. S. I. Fraley, P. Wu, L. He, Y. Feng, R. Krisnamurthy, G. D. Longmore, and D. Wirtz, "Three-dimensional matrix fiber alignment modulates cell migration and MT1-MMP utility by spatially and temporally directing protrusions," Sci. Rep. **5**(1), 14580 (2015).

282. R. Oldenbourg and G. Mei, "New polarized light microscope with precision universal compensator," J. Microsc. **180**(Pt 2), 140–147 (1995).

283. H. Lim, "Harmonic Generation Microscopy 2.0: New Tricks Empowering Intravital Imaging for Neuroscience," Front. Mol. Biosci. **6**, 99 (2019).

284. P. P. Provenzano, K. W. Eliceiri, J. M. Campbell, D. R. Inman, J. G. White, and P. J. Keely, "Collagen reorganization at the tumor-stromal interface facilitates local invasion," BMC Med. **4**(1), 38 (2006).

285. P. P. Provenzano, D. R. Inman, K. W. Eliceiri, J. G. Knittel, L. Yan, C. T. Rueden, J. G. White, and P. J. Keely, "Collagen density promotes mammary tumor initiation and progression," BMC Med. **6**(1), 11 (2008).

286. B. L. Wen, M. A. Brewer, O. Nadiarnykh, J. Hocker, V. Singh, T. R. Mackie, and P. J. Campagnola, "Texture analysis applied to second harmonic generation image data for ovarian cancer classification," J. Biomed. Opt. **19**(9), 096007 (2014).

287. K. R. Campbell, R. Chaudhary, M. Montano, R. V. Iozzo, W. A. Bushman, and P. J. Campagnola, "Second-harmonic generation microscopy analysis reveals proteoglycan decorin is necessary for proper collagen organization in prostate," J. Biomed. Opt. **24**(6), 066501 (2019).

288. R. Cisek, A. Joseph, M. Harvey, and D. Tokarz, "Polarization-Sensitive Second Harmonic Generation Microscopy for Investigations of Diseased Collagenous Tissues," Front. Phys. **9**, (2021).

289. A. Golaraei, L. Kontenis, R. Cisek, D. Tokarz, S. J. Done, B. C. Wilson, and V. Barzda, "Changes of collagen ultrastructure in breast cancer tissue determined by second-harmonic generation double Stokes-Mueller polarimetric microscopy," Biomed. Opt. Express **7**(10), 4054–4068 (2016).

290. G. Wang, G. Wang, G. Wang, Y. Sun, Y. Sun, Y. Sun, S. Jiang, G. Wu, G. Wu, W. Liao, Y. Chen, Z. Lin, Z. Liu, S. Zhuo, and S. Zhuo, "Machine learning-based rapid diagnosis of human borderline ovarian cancer on second-harmonic generation images," Biomed. Opt. Express **12**(9), 5658–5669 (2021).

291. Y. Liu, A. Keikhosravi, G. S. Mehta, C. R. Drifka, and K. W. Eliceiri, "Methods for Quantifying Fibrillar Collagen Alignment," Methods Mol. Biol. Clifton NJ **1627**, 429–451 (2017).

292. M. Sandler, A. Howard, M. Zhu, A. Zhmoginov, and L.-C. Chen, "MobileNetV2: Inverted Residuals and Linear Bottlenecks," (2019).

293. Y. Liu, A. Keikhosravi, C. A. Pehlke, J. S. Bredfeldt, M. Dutson, H. Liu, G. S. Mehta, R. Claus, A. J. Patel, M. W. Conklin, D. R. Inman, P. P. Provenzano, E. Sifakis, J. M. Patel, and K. W. Eliceiri, "Fibrillar Collagen Quantification With Curvelet Transform Based Computational Methods," Front. Bioeng. Biotechnol. **8**, (2020).

294. M. Abadi, A. Agarwal, P. Barham, E. Brevdo, Z. Chen, C. Citro, G. S. Corrado, A. Davis, J. Dean, M. Devin, S. Ghemawat, I. Goodfellow, A. Harp, G. Irving, M. Isard, Y. Jia, R. Jozefowicz, L. Kaiser, M. Kudlur, J. Levenberg, D. Mane, R. Monga, S. Moore, D. Murray, C. Olah, M. Schuster, J. Shlens, B. Steiner, I. Sutskever, K. Talwar, P. Tucker, V. Vanhoucke, V. Vasudevan, F. Viegas, O. Vinyals, P. Warden, M. Wattenberg, M. Wicke, Y. Yu, and X. Zheng, "TensorFlow: Large-Scale Machine Learning on Heterogeneous Distributed Systems," (2016).

295. L. Gole, J. Yeong, J. C. T. Lim, K. H. Ong, H. Han, A. A. Thike, Y. C. Poh, S. Yee, J. Iqbal, W. Hong, B. Lee, W. Yu, and P. H. Tan, "Quantitative stain-free imaging and digital profiling of collagen structure reveal diverse survival of triple negative breast cancer patients," Breast Cancer Res. **22**(1), 42 (2020).

296. S. E. J. Preston, M. Bartish, V. R. Richard, A. Aghigh, C. Gonçalves, J. Smith-Voudouris, F. Huang, F. Légaré, L.-M. Postovit, R. Lapointe, R. P. Zahedi, C. H. Borchers, W. H. Miller Jr., and S. V. del Rincón, "Phosphorylation of eIF4E in the stroma drives the production and spatial organisation of collagen type I in the mammary gland," (2022).

297. K. Maharana, S. Mondal, and B. Nemade, "A review: Data pre-processing and data augmentation techniques," Glob. Transit. Proc. **3**(1), 91–99 (2022).

298. A. P. Piotrowski and J. J. Napiorkowski, "A comparison of methods to avoid overfitting in neural networks training in the case of catchment runoff modelling," J. Hydrol. **476**, 97–111 (2013).

299. N. Srivastava, G. Hinton, A. Krizhevsky, I. Sutskever, and R. Salakhutdinov, "Dropout: a simple way to prevent neural networks from overfitting," J. Mach. Learn. Res. **15**(1), 1929–1958 (2014).

300. G. Borile, D. Sandrin, A. Filippi, K. I. Anderson, and F. Romanato, "Label-Free Multiphoton Microscopy: Much More Than Fancy Images," Int. J. Mol. Sci. **22**(5), 2657 (2021).

301. H. Yokota, J. Kaneshiro, and Y. Uesu, "Optical Second Harmonic Generation Microscopy as a Tool of Material Diagnosis," Phys. Res. Int. **2012**, e704634 (2012).

302. G. H. Patterson and D. W. Piston, "Photobleaching in Two-Photon Excitation Microscopy," Biophys. J. **78**(4), 2159–2162 (2000).

303. K. König, P. T. C. So, W. W. Mantulin, and E. Gratton, "Cellular response to near-infrared femtosecond laser pulses in two-photon microscopes," Opt. Lett. **22**(2), 135–136 (1997).

304. K. König, H. Liang, M. W. Berns, and B. J. Tromberg, "Cell damage by near-IR microbeams," Nature **377**(6544), 20–21 (1995).

305. G. Wang, H. Zhan, T. Luo, B. Kang, X. Li, G. Xi, Z. Liu, and S. Zhuo, "Automated Ovarian Cancer Identification Using End-to-End Deep Learning and Second Harmonic Generation Imaging," IEEE J. Sel. Top. Quantum Electron. **29**(4: Biophotonics), 1–9 (2023).

306. A. E. Woessner and K. P. Quinn, "Improved segmentation of collagen second harmonic generation images with a deep learning convolutional neural network," J. Biophotonics **15**(12), e202200191 (2022).

307. R. Houhou, E. Quansah, T. Meyer-Zedler, M. Schmitt, F. Hoffmann, O. Guntinas-Lichius, J. Popp, and T. Bocklitz, "Comparison of denoising tools for the reconstruction of nonlinear multimodal images," Biomed. Opt. Express **14**(7), 3259–3278 (2023).

308. A. Fast, A. Lal, A. F. Durkin, G. Lentsch, R. M. Harris, C. B. Zachary, A. K. Ganesan, and M. Balu, "Fast, large area multiphoton exoscope (FLAME) for macroscopic imaging with microscopic resolution of human skin," Sci. Rep. **10**(1), 18093 (2020).

309. Z. Liu, L. Jin, J. Chen, Q. Fang, S. Ablameyko, Z. Yin, and Y. Xu, "A survey on applications of deep learning in microscopy image analysis," Comput. Biol. Med. **134**, 104523 (2021).

310. M. E. Helou and S. Süsstrunk, "BIGPrior: Towards Decoupling Learned Prior Hallucination and Data Fidelity in Image Restoration," (2022).

311. C. Qiao, D. Li, Y. Guo, C. Liu, T. Jiang, Q. Dai, and D. Li, "Evaluation and development of deep neural networks for image super-resolution in optical microscopy," Nat. Methods **18**(2), 194–202 (2021).

312. C. Qiao, D. Li, Y. Liu, S. Zhang, K. Liu, C. Liu, Y. Guo, T. Jiang, C. Fang, N. Li, Y. Zeng, K. He, X. Zhu, J. Lippincott-Schwartz, Q. Dai, and D. Li, "Rationalized deep learning super-resolution microscopy for sustained live imaging of rapid subcellular processes," Nat. Biotechnol. 1–11 (2022).

313. L. Jin, B. Liu, F. Zhao, S. Hahn, B. Dong, R. Song, T. C. Elston, Y. Xu, and K. M. Hahn, "Deep learning enables structured illumination microscopy with low light levels and enhanced speed," Nat. Commun. **11**(1), 1934 (2020).

314. H. Wieslander, C. Wählby, and I.-M. Sintorn, "TEM image restoration from fast image streams," PLoS ONE **16**(2), e0246336 (2021).

315. J. Lehtinen, J. Munkberg, J. Hasselgren, S. Laine, T. Karras, M. Aittala, and T. Aila, "Noise2Noise: Learning Image Restoration without Clean Data," (2018).

316. M. Weigert, U. Schmidt, T. Boothe, A. Müller, A. Dibrov, A. Jain, B. Wilhelm, D. Schmidt, C. Broaddus, S. Culley, M. Rocha-Martins, F. Segovia-Miranda, C. Norden, R. Henriques, M. Zerial, M. Solimena, J. Rink, P. Tomancak, L. Royer, F. Jug, and E. W. Myers, "Content-aware image restoration: pushing the limits of fluorescence microscopy," Nat. Methods **15**(12), 1090–1097 (2018).

317. O. Ronneberger, P. Fischer, and T. Brox, "U-Net: Convolutional Networks for Biomedical Image Segmentation," (2015).

318. D. Rouse and S. Hemami, "Understanding and simplifying the structural similarity metric," in (2008), pp. 1188–1191.

319. A. Horé and D. Ziou, "Image Quality Metrics: PSNR vs. SSIM," in *2010 20th International Conference on Pattern Recognition* (2010), pp. 2366–2369.

320. M. Westerfield, *THE Zebrafish Book a Guide for the Laboratory Use of Zebrafish Danio** (n.d.).

321. C. B. Kimmel, W. W. Ballard, S. R. Kimmel, B. Ullmann, and T. F. Schilling, "Stages of embryonic development of the zebrafish," Dev. Dyn. Off. Publ. Am. Assoc. Anat. **203**(3), 253–310 (1995).

322. G. J. Espinoza, J. M. Poland, and J. R. A. Bremer, "Genotyping live fish larvae: Non-lethal and noninvasive DNA isolation from 3–5 day old hatchlings," BioTechniques **63**(4), 181–186 (2017).

323. M. D. Bloice, P. M. Roth, and A. Holzinger, "Biomedical image augmentation using Augmentor," Bioinformatics **35**(21), 4522–4524 (2019).

324. L. Silvestri, I. Costantini, L. Sacconi, and F. S. Pavone, "Clearing of fixed tissue: a review from a microscopist's perspective," J. Biomed. Opt. **21**(8), 081205 (2016).

325. H. Macias and L. Hinck, "Mammary Gland Development," Wiley Interdiscip. Rev. Dev. Biol. **1**(4), 533–557 (2012).

326. S. K. Biswas, S. Banerjee, G. W. Baker, C.-Y. Kuo, and I. Chowdhury, "The Mammary Gland: Basic Structure and Molecular Signaling during Development," Int. J. Mol. Sci. **23**(7), 3883 (2022).

327. J. J. Campbell and C. J. Watson, "Three-dimensional culture models of mammary gland," Organogenesis **5**(2), 43 (2009).

328. L. G. Griffith and M. A. Swartz, "Capturing complex 3D tissue physiology in vitro," Nat. Rev. Mol. Cell Biol. **7**(3), 211–224 (2006).

329. P. Schedin and R. C. Hovey, "Editorial: The Mammary Stroma in Normal Development and Function," J. Mammary Gland Biol. Neoplasia **15**(3), 275–277 (2010).

330. W. V. Ingman, J. Wyckoff, V. Gouon-Evans, J. Condeelis, and J. W. Pollard, "Macrophages promote collagen fibrillogenesis around terminal end buds of the developing mammary gland," Dev. Dyn. Off. Publ. Am. Assoc. Anat. **235**(12), 3222–3229 (2006).

331. B. Lloyd-Lewis, "Multidimensional Imaging of Mammary Gland Development: A Window Into Breast Form and Function," Front. Cell Dev. Biol. **8**, 203 (2020).

332. H. Katsuno-Kambe, J. L. Teo, R. J. Ju, J. Hudson, S. J. Stehbens, and A. S. Yap, "Collagen polarization promotes epithelial elongation by stimulating locoregional cell proliferation," eLife **10**, e67915 (2021).

333. J. N. Ouellette, C. R. Drifka, K. B. Pointer, Y. Liu, T. J. Lieberthal, W. J. Kao, J. S. Kuo, A. G. Loeffler, and K. W. Eliceiri, "Navigating the Collagen Jungle: The Biomedical Potential of Fiber Organization in Cancer," Bioengineering **8**(2), 17 (2021).

334. Y. V. Kistenev, V. V. Nikolaev, O. S. Kurochkina, A. V. Borisov, D. A. Vrazhnov, and E. A. Sandykova, "Application of multiphoton imaging and machine learning to lymphedema tissue analysis," Biomed. Opt. Express **10**(7), 3353–3368 (2019).

335. M. J. Huttunen, A. Hassan, C. W. McCloskey, S. Fasih, J. Upham, B. C. Vanderhyden, R. W. Boyd, and S. Murugkar, "Automated classification of multiphoton microscopy images of ovarian tissue using deep learning," J. Biomed. Opt. **23**(6), 1–7 (2018).

336. I. Goodfellow, J. Pouget-Abadie, M. Mirza, B. Xu, D. Warde-Farley, S. Ozair, A. Courville, and Y. Bengio, "Generative Adversarial Nets," (n.d.).

337. X. Wang, K. Yu, S. Wu, J. Gu, Y. Liu, C. Dong, C. C. Loy, Y. Qiao, and X. Tang, "ESRGAN: Enhanced Super-Resolution Generative Adversarial Networks," (2018).

338. "Intensity measurements — Microscopy for Beginners reference guide," https://www.bioimagingguide.org/03_Image_analysis/Intensity.html.

339. E. Peli, "Contrast in complex images," JOSA A **7**(10), 2032–2040 (1990).

340. N. Iqbal, R. Mumtaz, U. Shafi, and S. M. H. Zaidi, "Gray level co-occurrence matrix (GLCM) texture based crop classification using low altitude remote sensing platforms," PeerJ Comput. Sci. **7**, e536 (2021).

341. "FSIM: A Feature Similarity Index for Image Quality Assessment," https://ieeexplore.ieee.org/document/5705575.

342. "Image information and visual quality | IEEE Journals & Magazine | IEEE Xplore," https://ieeexplore.ieee.org/document/1576816.

343. "Edge preservation ratio for image sharpness assessment," https://ieeexplore.ieee.org/document/7578241.

344. Z. Pan, S. Hu, X. Wu, and P. Wang, "Adaptive center pixel selection strategy in Local Binary Pattern for texture classification," Expert Syst. Appl. **180**, 115123 (2021).

345. W. Zhao and R. Chellappa, eds., "CHAPTER 19 - NEAR REAL-TIME ROBUST FACE AND FACIAL-FEATURE DETECTION WITH INFORMATION-BASED MAXIMUM DISCRIMINATION," in *Face Processing* (Academic Press, 2006), pp. 619–646.

346. I. Plante, M. K. G. Stewart, and D. W. Laird, "Evaluation of mammary gland development and function in mouse models," J. Vis. Exp. JoVE (53), 2828 (2011).

347. "4x UltraSharp," https://openmodeldb.info/models/4x-UltraSharp.

348. "Model Database - Upscale Wiki," https://upscale.wiki/w/index.php?title=Model_Database&oldid=1571.

349. "4x UniScaleV2 Sharp," https://openmodeldb.info/models/4x-UniScaleV2-Sharp.

350. "Official Research Models - Upscale Wiki," https://upscale.wiki/wiki/Official_Research_Models.

351. R. de Lutio, S. D’Aronco, J. D. Wegner, and K. Schindler, "Guided Super-Resolution as Pixel-to-Pixel Transformation," (2019).

352. T. K. Kim, "Understanding one-way ANOVA using conceptual figures," Korean J. Anesthesiol. **70**(1), 22–26 (2017).

353. G. M. Sullivan and R. Feinn, "Using Effect Size—or Why the P Value Is Not Enough," J. Grad. Med. Educ. **4**(3), 279–282 (2012).

9 SUPPLEMENTARY INFORMATION FOR ARTICLE 2

Supplemental Document

Biomedical Optics EXPRESS

Nonlinear microscopy and deep learning classification for mammary gland microenvironment studies: supplement

Arash Aghigh,[1] Samuel E. J. Preston,[2,3] Gaëtan Jargot,[1] Heide Ibrahim,[1] Sonia V Del Rincón,[2,3] and François Légaré[1,*]

[1] *Centre Énergie Matériaux Télécommunications, Institut National de la Recherche Scientifique, Varennes, Québec, Canada*
[2] *Department of Experimental Medicine, Faculty of Medicine, McGill University, Montréal, Québec, Canada*
[3] *Gerald Bronfman Department of Oncology, Segal Cancer Centre, Lady Davis Institute and Jewish General Hospital, McGill University, Montreal, Quebec, Canada*
[*] *francois.legare@inrs.ca*

Supplement DOI: https://doi.org/10.6084/m9.figshare.22360006

Parent Article DOI: https://doi.org/10.1364/BOE.487087

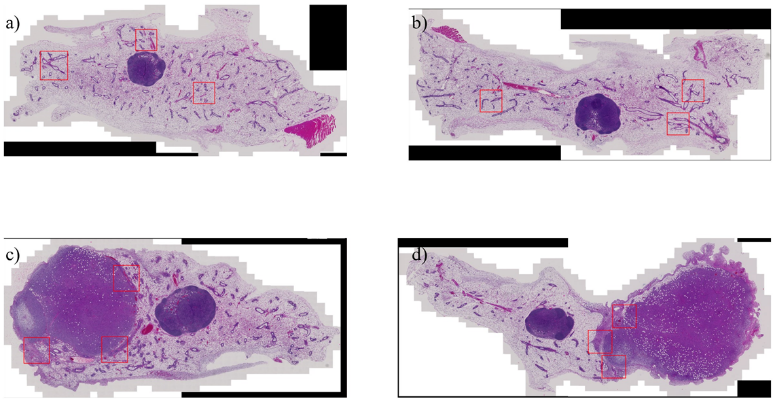

Figure S1. H&E images of the whole mammary gland with and without tumor. (a) and (b) are naïve mammary glands. (c) and (d) are tumor bearing. The red rectangles show the regions of interest studied using SHG microscopy for [1].

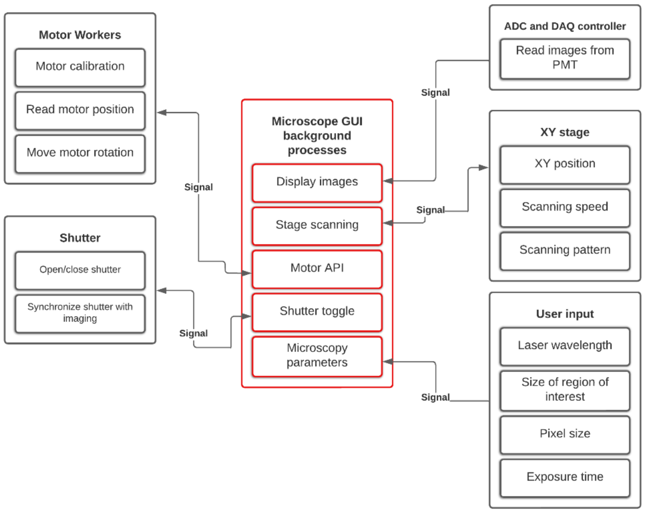

Figure S2. Microscope program and how the centralized program controls the signal acquisition and synchronization in this experiment. After inputting the necessary information, every aspect of the imaging is automated.

MS-SSIM analysis of all the samples with increasing R^2

Table S1: R^2 minimum and MS-SSIM between P-SHG and CurveAlign images for sample 1

R^2 minimum	P-SHG vs CurveAlign MS-SSIM
0.3	0.24
0.4	0.25
0.5	0.27
0.7	0.27

Table S2: R^2 minimum and MS-SSIM between P-SHG and CurveAlign images for sample 2

R^2 minimum	P-SHG vs CurveAlign MS-SSIM
0.3	0.14
0.4	0.25
0.5	0.26
0.7	0.27

Table S3: R^2 minimum and MS-SSIM between P-SHG and CurveAlign images for sample 3

R^2 minimum	P-SHG vs CurveAlign MS-SSIM
0.3	0.32
0.4	0.39
0.5	0.42
0.7	0.46

Table S4: R^2 minimum and MS-SSIM between P-SHG and CurveAlign images for sample 4

R^2 minimum	P-SHG vs CurveAlign MS-SSIM
0.3	0.16
0.4	0.16
0.5	0.24
0.7	0.32

Table S5: R^2 minimum and MS-SSIM between P-SHG and CurveAlign images for sample 5

R^2 minimum	P-SHG vs CurveAlign MS-SSIM
0.3	0.23
0.4	0.24
0.5	0.25
0.7	0.3

References

1. S. E. J. Preston, M. Bartish, V. R. Richard, A. Aghigh, C. Gonçalves, J. Smith-Voudouris, F. Huang, F. Légaré, L.-M. Postovit, R. Lapointe, R. P. Zahedi, C. H. Borchers, W. H. Miller Jr., and S. V. del Rincón, "Phosphorylation of eIF4E in the stroma drives the production and spatial organisation of collagen type I in the mammary gland," (2022).

10 SUPPLEMENTARY INFORMATION FOR ARTICLE 4

Access to all supplementary materials for Article 4 is in the following repository: 10.5281/zenodo.12788764.